Doctoral theses at NTNU, 2020:144

Kristine Bakken

In situ Characterization of Ferroelectric Oxide Thin Films during Aqueous Chemical Solution Deposition

Doctoral thesis

ISBN 978-82-326-4636-4 (printed ver.)
ISBN 978-82-326-4637-1 (electronic ver.)
ISSN 1503-8181

NTNU
Norwegian University of
Science and Technology

NTNU
Norwegian University of Science and Technology
Thesis for the Degree of
Philosophiae Doctor
Faculty of Natural Sciences
Department of Materials Science and Engineering

Doctoral theses at NTNU, 2020:144

NTNU

Kristine Bakken

In situ Characterization of Ferroelectric Oxide Thin Films during Aqueous Chemical Solution Deposition

Thesis for the Degree of Philosophiae Doctor

Trondheim, May 2020

Norwegian University of Science and Technology
Faculty of Natural Sciences
Department of Materials Science and Engineering

NTNU
Norwegian University of
Science and Technology

NTNU
Norwegian University of Science and Technology

Thesis for the Degree of Philosophiae Doctor

Faculty of Natural Sciences
Department of Materials Science and Engineering

ISBN 978-82-326-4636-4 (printed ver.)
ISBN 978-82-326-4637-1 (electronic ver.)
ISSN 1503-8181

Doctoral theses at NTNU, 2020:144

Printed by NTNU Grafisk senter

Preface

This thesis has been submitted to the Norwegian University of Science and Technology (NTNU) in partial fulfilment of the requirements for the Degree of Philosophiae Doctor. The work presented in this thesis was performed in the Functional Materials and Materials Chemistry (FACET) research group at the Department of Material Science and Engineering (IMA) from August 2016 to March 2020. During this time, synchrotron experiments were performed at the BM01 end-station, Swiss-Norwegian Beamlines (SNBL) at the European Synchrotron Radiation Facility (ESRF) in Grenoble (France). Near-normal reflection infrared spectra were recorded at the Institute of Physics at the Czech Academy of Sciences in Prague (Czech Republic). The work was supervised by Prof. Mari-Ann Einarsrud (main advisor), Prof. Tor Grande (co-advisor) and Assoc. Prof. Julia Glaum (co-advisor).

This work was part of the "From aqueous solutions to oxide thin films and hierarchical structures" (FASTS) project. Funding for this work was provided by the Norwegian Research Council under the Toppforsk program to the project (250403/F20).

The experiments, data processing and interpretations presented in this thesis were done by the author, with certain contributions from others. Dr. Anders Bank Blichfeld designed of the *in situ* X-ray diffraction heating setup and developed the procedure for data processing (outlined in Appendix C). He contributed during the acquirement of the *in situ* X-ray diffraction data and did the data processing for the results shown in Figure 4.20 and 4.15. Furthermore, he designed the front plate for the *in situ* infrared spectroscopy setup (Figure 3.6). $K_xNa_{1-x}NbO_3$ (KNN) precursor solutions, powders and films were prepared by MSc Nikolai Helth Gaukås. MSc Viviann Hole deposited the interdigitated electrodes for the electrical characterization of the multilayer films and performed the measurements shown in Figure 4.33. The TEM sample preparation and imaging were done by MSc Inger-Emma Nylund. Dr. Evgeniya Khomyakova prepared a BCZT thin film, which was investigated with *in situ* X-ray diffraction (shown in Figure 4.6). The *in situ* powder X-ray diffraction measurements on $BaTiO_3$ precursor powders with variable CO_2 partial pressure were conducted with the help of Dr. Kristin Høydalsvik Wells. Near-normal incident infrared spectroscopy measurements of $BaTiO_3$-based thin films and phonon modelling were conducted under the guidance of Dr. Stanislav Kamba and Dr. Veronica Goian.

Parts of this thesis are in preparation for publication:

K. Bakken*, A. B. Blichfeld, D. Chernyshov, T. Grande, J. Glaum, M.-A. Einarsrud, "Mechanisms for texturing in $BaTiO_3$ thin films from aqueous chemical solution deposition", Submitted to *Journal of Sol-Gel Science and Technology* (2020).
Included in Appendix B.
*Contributions to the work include preparation of samples, design and execution of the experiments, data processing and analysis, literature review and writing the drafted manuscript.

A. B. Blichfeld, **K. Bakken***, D. Chernyshov, J. Glaum, T. Grande and M.-A. Einarsrud, "Experimental setup for high-temperature *in situ* studies of crystallization of thin films with atmosphere control". Drafted manuscript.
Included in Appendix C.
*Contributions to this work include preparing $BaTiO_3$ thin films, conducting experiments, providing the discussion related to the $BaTiO_3$ synthesis and feedback on the drafted manuscript.

Other work, omitted from this thesis:

T. M. Raeder, **K. Bakken***, J. Glaum, M.-A. Einarsrud and T. Grande, "Enhanced in-plane ferroelectricity in $BaTiO_3$ thin films fabricated by aqueous chemical solution deposition", *AIP Advances* **8** (2018) 105228.
*Contributions to the work include investigation of the synthesis by producing powders and recording infrared spectra and X-ray diffraction patterns of the powders and literature review, data analysis and discussions related to the decomposition reactions and phase evolution during synthesis.

E. Khomyakova, S. Wenner, **K. Bakken***, T. Grande, J. Glaum, M.-A. Einarsrud, "On the formation mechanism of BCZT thin films by aqueous chemical solution deposition", Submitted to *Journal of the European Ceramic Society* (2020).
*Contributions to this work include discussions of the results and providing feedback to the drafted manuscript.

Trondheim, March 2020
Kristine Bakken

Acknowledgement

In the fall of 2010, I matriculated in the Materials Science and Engineering Master of Technology program at NTNU, and over the past decade NTNU has become somewhat of a second home. I get nostalgic thinking back on all the memories and amazing people, and the small moments that lead to me decided that I wanted to get into research and do a PhD. This has been a dream and a goal of mine for a while. It has been both challenging and hard at times, but I feel truly grateful for the opportunity to achieve this milestone. However, I did not get here alone, and there are so many to thank.

During my master's I was lucky enough to be supervised by Prof. Mari-Ann Einarsrud, and then again during my PhD, and I couldn't have asked for a better advisor. You have this amazing ability to make every one of you students feel like they are your top priority. You also inspire and set the bar high, which I know I have grown from, and I appreciate that I have been allowed to find my own solutions. I have enjoyed all the discussions and your guidance, and I'm thankful for all your hard work. To my co-advisors Prof. Tor Grande and Assoc. Prof. Julia Glaum, thank you for making time for me and for all your help, feedback and suggestions on my work. I'm grateful for the active role and the interest you have taken, like suggesting new directions for the experimental work, especially on that first beamtime when I felt overwhelmed and needed to be told what to do. Moreover, to all my advisors, thank you for seeing my potential and for giving me the chance to prove myself, it means more than you know, and it has been a pleasure working with all of you!

I am also forever grateful to Dr. Anders Bank Blichfeld, my unofficial mentor. I have learned so much from you, and I consider myself lucky to have had the opportunity to work with one of the very best. Thank you for having the patience to answer all my questions and for taking the time to actually teach me and not just explain, especially on the beamtimes when I was tired and needed to be told at least twice. This thesis would look very different without your kind guidance on everything from software to what do on the beamtimes. It not often you meet the perfect combination of engineer and scientist and I know that tales will be told in the hallways of KI about your awsome problem solving abilities for years to come.

By working on this project, I have been part of the Toppforsk team, and I appreciate all the contributions for the incredible people that have been associated with the FASTS project, both directly and indirectly. Thanks to my office mates Dr. Ola Gjønnes Grendal and PhD Candidate Trygve Magnus Ræder for sharing the day-to-day struggles, the (mainly) constructive discussions and for helping each

other with all the small challenges. Thank you to all my colleagues and friends in the FACET group and at the department. The social and work environment we have is something special and I feel lucky to have been part of that. I have enjoyed the seminars, the iSCREAM, department parties, Christmas lunches and the general "team work" attitude that exists in KI and KII. Thanks to my fellow PhD Candidates/friends who got through the courses with me and made the day-to-day of PhD life a little easier. To the people in KI, thank you for the way to strong coffee, the lunch breaks and discussions on all of life's small and big problems. No names mentioned, but all of you appreciated.

The technical staff and lab engineers in KI and KII also deserve a thanks, especially Dr. Kristin Høydalsvik Wells and Magnus Bentzen Følstad for their support and help with the experimental work. The same goes for Dr. Dmitry Chernyshov and the beamline staff at SNBL (ESRF) for all their help with the data acquisition and development of the methods. During my PhD I spent 3 months at the Institute of Physics at the Czech Academy of Sciences in Prague. I want to thank my host Dr. Stanislav Kamba for taking such good care of me, and the people at Department of Dielectrics such as Dr. Veronica Goian, Dr. Martin Kempa and Dr. Victor Bovtun for all their help and kindness during my stay.

I would also like to thank the friends who have pretended to understand what I was doing for years, but still supported me and acted like they were interested, you know who you are. In particular I want to thank Emil and Per Arne who are the reason I applied to NTNU in the first place, but most importantly Jeanette, who has been there for me always. Jeanette, thank you for all the shared memories, life experiences and for listening when I have something or someone to complain about. Du er min favoritt skrulling og jeg vet hvor du bor!

Finally, a special thanks goes to my parents and my favourite brother for their unconditional love and support. It means the world to me and this would not have been possible without you. I wholeheartedly appreciate that you are always there when I need you and all your unnecessary worrying, (I'm fine, I promise!).

Summary

Ferroelectric materials are used in a wide range of applications, including capacitors and non-linear optical devices. Utilization of ferroelectric thin films is especially desirable due to the possibility to tailor the ferroelectric properties by control of the crystallographic texture of the films. Chemical solution deposition (CSD) of oxide films is a simple and environmentally friendly processing route, but insight into the decomposition and crystallization processes is crucial to tailor the film properties. The aim of this thesis was to obtain a fundamental understanding of the mechanisms involved in decomposition, nucleation, growth and texture during thermal processing of ferroelectric films deposited by aqueous CSD by *in situ* X-ray diffraction (XRD) and infrared (IR) spectroscopy.

A new heating setup for synchrotron XRD was utilized in this work and the crystallization of $BaTiO_3$-based and KNN thin films from aqueous CSD were studied by this *in situ* XRD technique. A 2D detector was used to monitor the development of crystallographic texture during annealing, but also for more in-depth texture analysis at ambient temperature. A diffuse reflection (DRIFTS) cell for *in situ* IR spectroscopy was adapted for studying the decomposition reactions during thermal annealing, accompanied by *ex situ* characterization of powders from the same precursor solutions.

$BaTiO_3$ precursor films were prepared by spin coating of aqueous solutions on several different substrates. According to the *in situ* IR spectroscopy, pyrolysis and removal of the organic compounds in $BaTiO_3$ precursor films occurred in the temperature range 400-500 °C, leaving only amorphous $BaCO_3$-like and Ti-rich $BaTiO_3$-like phases in the films. Upon further annealing, a metastable oxycarbonate phase with the proposed stoichiometry $BaO_x(CO_3)_{1-x}$ was formed, which has a crystal structure close to the calcite-type $BaCO_3$ polymorph. A high partial pressure of CO_2 was observed to stabilize the oxycarbonate phase, but also lead to the formation of the aragonite-type $BaCO_3$ as a stable secondary phase. A transformation path from the precursor to crystalline films was outlined for the $BaTiO_3$-based films. Homogenous nucleation of $BaTiO_3$ by reaction of the oxycarbonate phase and Ti-rich phases occurred above 530 °C, but the nucleation temperature of $BaTiO_3$ was influenced by the heating rate and type of substrate, while the microstructure depended solely on the heating rate during the nucleation stage. Films with modified chemical compositions were also investigated, and zirconium substitution was observed to increase the nucleation temperature and reduce the decomposition and texture formation kinetics, while the effect of calcium substitution was neglectable.

Mechanisms for development of crystallographic texture of the $BaTiO_3$-based films were proposed. In a single layer deposited by CSD, texture was found to depend on the intermediate phases present in the film as a result of decomposition and pyrolysis of the precursors. Prolonged annealing below the nucleation threshold (500 °C) resulted in $BaCO_3$-like and Ti-rich $BaTiO_3$-like phases in the film, which gave a crystalline film with high degree of texture. The degree of texture was enhanced by a low heating rate during $BaTiO_3$ nucleation. Texture analysis was performed on the single layered films, and in general the texture of the films adhered to the substrate orientation in case of crystalline substrates. Texture could also be induced in films prepared by multiple depositions by CSD, where repeated annealing between each deposition caused Ostwald ripening of favourably oriented grains in the already crystalline layers, as consecutive layers were deposited, independent of the substrate.

In case of high annealing temperatures (>1000 °C) and high heating rates (> 1 °C/s), the formation of epitaxy was observed in the $BaTiO_3$ thin films with *in situ* XRD, although transmission electron microscopy revealed that these films were relaxed by formation of dislocations at the substrate film interface. The observed lattice parameters showed that the films have no-uniform strain, which arise both from lattice and thermal mismatch, especially for multilayer films. A possible formation mechanism for epitaxy was suggested, where the high heating rate is important in order to limit homogenous nucleation in the films before exceeding the threshold where cube-on-cube growth is favoured. Electrical characterization confirmed that multilayer cube-on-cube grown films were ferroelectric, with remnant polarization in the range 3.9-6.5 $\mu m/cm^2$ and cohesive fields in the range 4.5-6.5 kV/cm for an applied field of 20 kV/cm.

$K_xNa_{1-x}NbO_3$ (KNN) films deposited by CSD were also investigated. In these films, the choice of niobium precursor affected the nucleation temperature, lattice parameter and secondary phase formation. KNN films based on a malic acid complexed niobium precursor nucleated at higher temperature and without formation of the secondary $K_4Nb_6O_{17}$ phase, which was seen for the oxalate complexed niobium KNN films. However, all single layer KNN films were observed to be phase pure after annealing at 700-800 °C. No texture was seen in the single layer films, but texture formation by repeated annealing was suggested by the same mechanisms as for the $BaTiO_3$-based films.

Finally, the importance of *in situ* characterization tools for studying the complex decomposition and crystallization process in oxide thin films from aqueous CSD was highlighted, and a set of generalized guidelines for film fabrication were outlined.

Contents

Preface **I**

Acknowledgement **III**

Summary **V**

1 Background **1**
1.1 Motivation . . . 1
1.2 Aim of work . . . 3

2 Introduction **5**
2.1 Ferro- and piezoelectricity . . . 5
2.1.1 Ferro- and piezoelectric thin films . . . 6
2.1.2 Applications of ferroelectric devices . . . 8
2.2 Chemical solution deposition of thin films . . . 9
2.2.1 Precursor solution chemistry . . . 10
2.2.2 Film annealing . . . 12
2.3 Barium titanate and related materials . . . 14
2.3.1 Barium titanate . . . 14
2.3.2 Solid solutions of $BaTiO_3$ with related perovskites . . . 16
2.3.3 Barium carbonate . . . 18
2.4 Chemical solution deposition of $BaTiO_3$-based thin films . . . 20
2.4.1 Transformation paths . . . 20
2.4.2 Structure of the oxycarbonate phase . . . 23
2.4.3 Solid solutions of $BaTiO_3$ . . . 24
2.4.4 Aqueous CSD of $BaTiO_3$-based films . . . 24
2.4.5 Microstructure and properties of $BaTiO_3$-based films from CSD 25
2.5 Potassium sodium niobate . . . 26
2.6 *In situ* characterization methods . . . 27
2.6.1 Infrared spectroscopy of powders and films . . . 27
2.6.2 Synchrotron X-ray diffraction of films . . . 28

3 Materials and methods **29**
3.1 Synthesis . . . 29
3.1.1 Preparation of solutions . . . 29

3.1.2 Fabrication of films . . . 32
3.1.3 Preparation of powders . . . 34
3.2 Characterization . . . 34
3.2.1 *In situ* synchrotron X-ray diffraction of thin films . . . 34
3.2.2 X-ray powder diffraction . . . 37
3.2.3 *In situ* infrared spectroscopy of thick films . . . 38
3.2.4 *Ex situ* infrared spectroscopy of powders and thin films . . . 39
3.2.5 Electrical characterization . . . 41
3.2.6 Scanning electron microscopy . . . 42
3.2.7 Transmission electron microscopy . . . 42

Results **45**

4 Barium titanate based films **47**
4.1 *In situ* synchrotron X-ray diffraction of thin films . . . 47
4.1.1 Single step annealing . . . 47
4.1.2 Multi-step annealing of $BaTiO_3$ thin films on (100) $SrTiO_3$ . . . 54
4.1.3 Rietveld refinements . . . 54
4.1.4 Annealing of a $BaTiO_3$ thin film in CO_2 rich atmosphere . . . 58
4.2 Crystallographic texture . . . 59
4.2.1 Preferential orientation of $BaTiO_3$ films on various substrates 59
4.2.2 Preferential orientation of cations substituted $BaTiO_3$ films on (100) STO . . . 61
4.3 Epitaxy . . . 64
4.4 *In situ* infrared spectroscopy during decomposition of thick films . . . 70
4.4.1 $BaTiO_3$ thick films . . . 70
4.4.2 Cation substituted $BaTiO_3$ thick films . . . 74
4.5 Transmission electron microscopy . . . 76
4.5.1 Epitaxial $BaTiO_3$ thin film on (100) STO . . . 76
4.5.2 Polycrystalline $BaTiO_3$ thin film on (100) STO . . . 78
4.5.3 Textured $BaTiO_3$ thin film on (100) STO . . . 78
4.6 Ferroelectric properties . . . 79
4.6.1 $BaTiO_3$ thin films . . . 79
4.6.2 Cation substituted $BaTiO_3$ thin films . . . 81
4.7 Infrared spectroscopy of $BaTiO_3$-based thin films and phonon modelling 84

5 Barium titanate based powders **87**
5.1 The precursor powders . . . 87
5.2 Precursor powder annealing and decomposition . . . 88
5.2.1 X-ray diffraction of the phase evolution . . . 88
5.2.2 Infrared spectroscopy of the phase evolution . . . 91
5.2.3 Thermal analysis of the phase evolution . . . 93
5.3 *In situ* X-ray powder diffraction in variable CO_2 atmosphere . . . 96

6 Potassium sodium niobate films **103**
6.1 *In situ* synchrotron X-ray diffraction of KNN thin films 103
6.2 *In situ* infrared spectroscopy of KNN thick films 105

Discussion **109**

7 Tailoring of high quality films by aqueous chemical solution deposition **111**
7.1 Barium titanate based thin films 111
7.1.1 Precursor chemistry, decomposition and pyrolysis reactions . . 111
7.1.2 Crystallization: texture and microstructure of the films 118
7.1.3 Epitaxy and cube-on-cube growth in the films 123
7.1.4 Ferroelectric behaviour 125
7.2 KNN thin films 127
7.2.1 Effect of niobium precursor 127
7.2.2 Effect of salt flux 127
7.2.3 Texture and epitaxy in the KNN films 128
7.3 Possibilities and challenges with the *in situ* characterization tools . . 129
7.4 How to make phase pure textured perovskite thin films by aqueous chemical solution deposition 131

8 Conclusion **137**

9 Outlook **139**

References **141**

Appendices **159**

A Additional Results **161**
A.1 X-ray diffraction results 161
A.1.1 Powder X-ray diffraction 161
A.1.2 Synchrotron X-ray diffraction 166
A.2 Infrared spectroscopy 172
A.2.1 *In situ* infrared spectroscopy of $BaTiO_3$-based films 172
A.2.2 Near-normal infrared spectroscopy of thin films and phonon modelling 175
A.3 Electrical characterization 180
A.4 Electron microscope imaging 181

B Scientific Paper Draft 1 **183**

C Scientific Paper Draft 2 **203**

1 Background

1.1 Motivation

Piezoelectricity was first reported in 1880 by Pierre and Jacques Curie, identified for several single crystals such as quartz, topaz, sugar, tourmaline and Rochelle salt ($NaKC_4H_4O_6{\cdot}4H_2O$). [1] All these crystals lack centro-symmetry, which is an important prerequisite for piezoelectricity. In the non-centrosymmetric structure, atomic displacements, caused by an applied mechanical stress, will generate charges. The material will also exhibit mechanical strain as a response to applied electrical potential, called the converse-piezoelectric effect. [2] Certain piezoelectric crystals are also ferroelectric, meaning that the net polarization is present without applying an external field. The polarization can be reversed (switch direction) with an applied electric field, but this behaviour is only present in the material below the Curie temperature. When heated above the Curie temperature, the material becomes paraelectric as a phase transition to a centrosymmetric crystal structure occur, but the material will regain its properties upon cooling. The piezoelectric effect is illustrated in Figure 1.1 for a ferroelectric crystal.

Piezo- and ferroelectric materials are used in a wide range of applications, mainly as sensors, actuators and transducers. Microphones, microscale high precision positioning systems, voltage generators, sonars, medical ultrasound imaging, capacitators, memory devices and quartz watches are a few of the most common applications. [1, 3, 4] In a quartz watch, the crystal will vibrate with a certain frequency

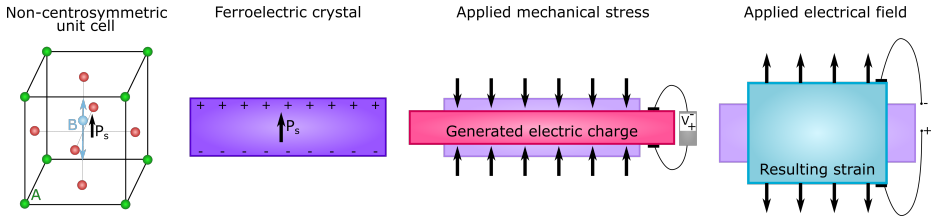

Figure 1.1: Polarization arising from atomic displacement in a non-centrosymmetric unit cell, which gives a net polarization in a ferroelectric crystal. Ferroelectric materials generate charge when a mechanical stress is applied (direct piezoelectric effect), or exhibit strain as an electrical field is applied (converse piezoelectric effect).

when connected to the watch battery, which is used by the electronics to monitor the time. [1] Medical ultrasound imaging relies on piezoelectric transducers which generates acoustic waves. Such non-invasive imaging is an important aspect of medical diagnostics. [1] Another example of how ferroelectricity can be exploited is ferroelectric random-access memory (FeRAM) for information storage. In FeRAM, a thin film of a ferroelectric material is used to store information as either 0 or 1 by utilizing the two directions of the net polarisation in a ferroelectric crystal. [5]

Today, the most widely used ferroelectric material is $PbZr_xTi_{x-1}O_3$ (PZT), as the ferroelectric properties are superior to most other material systems, but also the ease of which the functional properties can be adjusted through doping and cation substitution. However, the high lead-content in PZT, more than 60 wt%, is of increasing concern, both in an environmental and health perspective. [3] Therefore, research on lead-free materials has increased in the last decades, in an effort to replace PZT. Perovskites based on $K_xNa_{1-x}NbO_3$ (KNN), $BaTiO_3$ and bismuth alkali titanates ($Bi_xK_{1-x}TiO_3$ and $Bi_xNa_{1-x}TiO_3$) are promising alternatives, especially for implantable devices where toxicity and biocompatibility are of utmost importance. [3]

For several of the common applications, it is beneficial to use the piezo- or ferroelectric material as a thin film, as the piezo- and ferroelectric response is enhanced in films with texture or epitaxy. Smaller devices, lower operating voltage, higher speed and lower processing temperatures are some additional advantages. [5] Flexible energy harvesters, nanogenerators and *in vivo* sensors are new possible applications where ferroelectric thin films are attractive. Hence, sustainable and simple deposition routes to high quality films with a high degree of crystallographic texture need to be developed in order to fully utilize the potential of the materials. [3, 4]

Chemical solution deposition (CSD) is a well-suited, inexpensive and flexible method for fabrication of oxide thin films on an industrial scale. [6, 7] The synthesis is simple, as a stable precursor solution with the desired metal ions is deposited onto a substrate by e.g. spin coating before the film is annealed. Depending on the precursor solution chemistry and the heating profile used, different pyrolysis and crystallization reactions occur. [6, 7] Lead-based ferroelectric films based on PZT are industrially produced by CSD, but synthesis routes for other ferroelectric material classes have also been developed. [6, 7] However, the use of aqueous precursor solutions is not extensively reported in literature, even if it removes the need for toxic organic solvents and simplifies the process as inert atmosphere is not required.

Thin films fabricated with CSD are typically measured *ex situ* with X-ray diffraction (XRD) to characterize the phase purity and degree of texture of the films. The decomposition process is typically not emphasized but characterization of annealed powders derived from the precursor solution are on occasion reported, which is both time consuming and may not be representative for the film decomposition. However, both the properties and microstructure of the thin films from CSD are reported to be heavily influenced by the synthesis procedure. [4] Hence, in order to produce high quality thin films from CSD, a thorough understanding of the complex decomposition and crystallization reactions is desired to optimize the film processing conditions.

1.2 Aim of work

The principal aim of this thesis was to obtain a fundamental understanding of mechanisms governing decomposition, nucleation, growth and texture development during annealing of ferroelectric thin films from aqueous chemical solution deposition by *in situ* XRD and infrared (IR) spectroscopy.

In situ XRD is well-suited for studying the crystallization during film annealing, while *in situ* IR spectroscopy is useful for investigating the decomposition reaction of the films prior to crystallization. One of the goals in this work was to utilize the development of the *in situ* characterization tools in the FASTS project, which this PhD work was part of. *In situ* XRD was conducted at synchrotron facilities, with a custom made heating setup developed in the FASTS project. A procedure for conducting the measurements was established during the beamtimes and improved iteratively by post analyses of the obtained data. A protocol for data processing and texture analysis was established. This work also involved the adaption of a diffuse reflection (DRIFTS) cell for the *in situ* IR spectroscopy measurements of thin films, which was achieved by deposition of thick films on a reflective substrate.

$BaTiO_3$-based materials were chosen as the main material system as $BaTiO_3$ is technologically important due to the dielectric and ferroelectric properties. The chemistry of $BaTiO_3$ is also less complex compared to $BaTiO_3$-based materials with cation substitution. Calcium substitution, forming $Ba_{1-x}Ca_xTiO_3$ (BCT), increases the Curie temperature. BCT is also the end member of the more complex $Ba_{1-x}Ca_xZr_yTi_{1-y}O_3$ (BCZT) system, with significantly enhanced ferroelectric response. [4] Moreover, an intermediate phase is formed during preparation of $BaTiO_3$ by CSD [6], which is observable in both XRD and IR spectroscopy, a feature that was particularly suited for development of both the IR and XRD *in situ* characterization tools.

Lastly, previous work on KNN films has shown the potential for epitaxy and a high degree of texture in these films. [8, 9] Based on this, KNN films were also characterized by *in situ* IR and XRD, as a second material system was beneficial for suggesting generalized decomposition, crystallization and texture mechanisms for oxide thin films from aqueous CSD.

2 Introduction

2.1 Ferro- and piezoelectricity

Dielectrics are electrical insulators which respond with a displacement of the bound charges (ions or electrons) when these materials are subjected to an applied electrical field. The charge displacement causes a change in the dipole moments and polarizes the material. A subgroup of dielectric materials are piezoelectrics, where an applied electrical field causes mechanical strain in the material, or conversely the material will generate an electric polarization in response to an external mechanical stress. Piezoelectrics have non-centrosymmetric crystal structure, limiting the crystal structure to 20 of the crystallographic point groups (those without inversion symmetry). [2] A further subgroup of piezoelectrics is pyroelectrics, where the internal strain caused by the spontaneous electrical polarization in the crystal results in a change in the crystal structure to one of lower symmetry, which is reversible upon heating. These crystals have a net polarization in their primitive unit cell. Only 10 of the point groups can accommodate net polarization as a consequence of Neumann's principle stating that "a macroscopic physical property must at least have the point group symmetry of the crystal". [2] Ferroelectrics are pyroelectrics where the spontaneous polarization can be reversibly changed between two polarization states by an applied electrical field, making it possible to align neighbouring domains. The transition from randomly oriented domains in a paraelectric phase, to an ordered ferroelectric structure occurs at a temperature termed the Curie temperature (T_C). [2]

The piezoelectric coefficient, d, is the tensor expressing the resulting polarization (P) from an applied mechanical stress (σ) in a piezoelectric material, $P = d\sigma$, or the induced strain (ϵ) from an applied electrical field (E); $\epsilon = dE$. The piezoelectric coefficient depends on the material and crystal symmetry and is an important figure of merit, especially the d_{33}-value. The electromechanical coupling coefficient, k, is also an important figure of merit, as it describes the effectiveness of conversion between electrical to mechanical energy for a piezoelectric material. [2]

The perovskite structure

Several technologically important ferroelectric materials, including the $PbZr_xTi_{x-1}O_3$ (PZT) system, the $K_xNa_{1-x}NbO_3$ (KNN) system and $BaTiO_3$-based materials, take the perovskite structure (ABO_3). [3] This structure consists of corner-sharing BO_6-

octahedra with the larger A-ions 12-coordinated at the corners of the unit cell. This structure can accommodate all the 10 polar point groups. [3] The perovskite simple cubic unit cell (space group $Pm\bar{3}m$) can be distorted in various ways, often accompanied by tilting of the BO_6-octahedra. Ferroelectricity develops as the centrosymmetric cubic perovskite is cooled below the Curie temperature and a phase transition to a crystal structure with lower symmetry takes place, usually to accommodate displacement of the B-cation. Distortion of the cubic unit cell into tetragonal, orthorhombic, rhombohedral, monoclinic and triclinic cells is often observed. [3] Most perovskites structures have a sequence of phase transitions with reducing symmetry with decreasing temperature. [3]

Ferroelectric domains and hysteresis

Ferroelectric domains are finite regions where the amplitude and direction of the spontaneous polarization is homogenous. [10] The domains are separated by domain walls, which are electric interfaces acting as energy barriers for the motion of domains. The domains walls are defined by the angle between the polarizations of each domain, such as 180° and 90° domain walls in tetragonal crystals. The domains form when the material is cooled from above the Curie temperature as a mechanism to minimize the elastic, electrostatic, domain wall and surface energy, in the absence of an electrical field or mechanical load. [10]

Dielectrics exhibit a linear polarization to an applied electrical field, but this behaviour does not hold for ferroelectrics, even though reversal of an electric field can eventually reverse the saturation polarization. Ferroelectric materials show hysteresis in their polarization-electric field curves (PE-loops), as shown in Figure 2.1. Hysteresis is caused by the energy required to move domains walls between domains that have different polarization directions. To change the net polarization of a crystal, the relative sizes of the various domains need to be altered. This requires domain wall motion between domains having different orientations, which costs energy. [2] The shape of the hysteresis loop reveals information of the domain reorientation and is therefore used to characterize ferroelectrics as soft or hard dependent on how difficult they are to pole and unpole.

The PE-loop of an ideal ferroelectric material is shown in Figure 2.1. Starting from an unpoled state at the origin (point O) the polarisation increases with increasing electrical field until the domain alignment is complete (point B) and the polarization reaches the saturation polarization P_s (point C). When the electric field is removed (point D), there will be a certain remnant polarization (P_r), since not all domains are able to switch back to their original state. A negative cohesive field (E_c) is required in order to reach zero polarization. The hysteresis remains in the poled ferroelectric material unless it is heated above the Curie temperature, which will "reset" the domain pattern in an unpoled state.

2.1.1 Ferro- and piezoelectric thin films

Polycrystalline oxide ceramics and films require the material to be ferroelectric in order to exhibit piezoelectricity, since all the individual polarization directions in

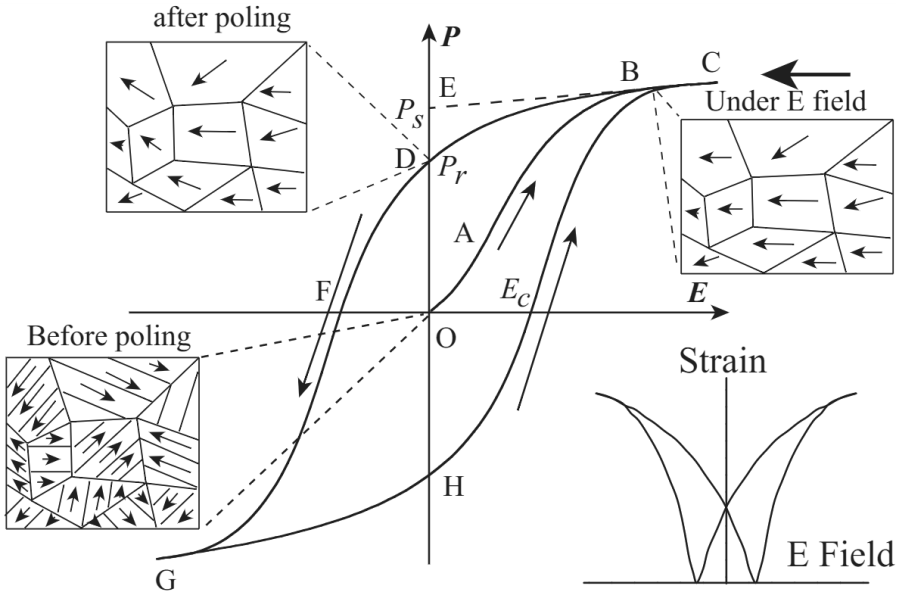

Figure 2.1: The PE-loop of an ideal ferroelectric material illustrating the alignment of the domains with an applied electrical field. Figure from [11], reprinted with permission from John Wiley and Sons.

the different grains need to be aligned to create a net piezoelectric response. [12] Increased piezoelectric response is usually found in oxide films with crystallographic texture or epitaxy [4]. The reduced dimensions of thin films compared to bulk ferroelectric ceramics are also highly advantageous from a device point of view. [3,5]

Preferred orientation, texture and epitaxy

Polycrystalline ceramic films can have randomly distributed dipole orientations in the different grains, but often the orientation distribution is not random and a preferred orientation for the polar axis exist, which gives the film crystallographic texture. The extreme case is an epitaxial film, where all unit cells are oriented and adhere to the substrate lattice, where the epitaxial strain, ϵ_m, arising in the film lattice is determined by the lattice mismatch:

$$\epsilon_m = \frac{a_{sub} - a_{film}}{a_{film}} \tag{2.1}$$

where a_{sub} and a_{film} refers to the lattice parameter of the substrate and film, respectively. Epitaxy occurs as the film lattice distorts to achieve row-matching, which means that the crystal lattice of the film and substrate must be compatible and lattice mismatch minimal. Although, complete row-matching can only be supported in a thin layer of a few unit cells. Above a critical thickness the film will relax by introducing dislocations. [13] Periodic edge dislocations at the substrate interface

caused by terminations of a lattice planes is one way to dissipate the strain, where the periodicity, p, is a function of the Burgers vector, $\vec{b}$ (for a cubic lattice this is simply the lattice parameter), and the strain from the lattice mismatch;

$$p = \frac{|\vec{b}|}{\epsilon_m} \tag{2.2}$$

Preferred orientation, or texture, in ceramic films often relates to the substrate lattice and arise in a layer close to the substrate which then progress upwards into the film. However, there is no requirement for an orientation relationship with the substrate, as texture can evolve from a randomly initial deposited film, by reorientation or homoepitaxial growth of consecutive deposited layers. [13]

Grain size and porosity effect on ferroelectric response

The grain size can have a detrimental effect on the ferroelectric response, e.g. the polarization arising from an applied electric field, in piezoelectric ceramics. [4] Grains that are too large reduce the ferroelectric response by excessive back switching. Too small grains on the other hand, might cause suppression of ferroelectricity due to reduced lattice distortions and low permittivity layers at the grain boundaries. [4] When the grain size approach nanoscale, the grains might become unstable as spontaneous polarization is compensated by charges at the grain boundaries, which these small grains can not support and therefore change to a nonpolar lattice. [14] The grain size in thin films are often dependent on the deposition method, nucleation mechanism and type of substrate. The processing temperatures are typically significantly lower than the bulk sintering temperatures, so grain growth in thin films is often limited. [15] Porosity will also serve as a limitation for the ferroelectric response and is generally unwanted, but the inclusion of pores will depend on the processing and microstructure. [14]

2.1.2 Applications of ferroelectric devices

Ferroelectrics are mainly used as sensors, actuators and transducers [3], where some common applications include pressure and strain sensors, ultrasonic imaging for medical purposes or non-destructive material testing, sonar, non-volatile memory devices, microelectronics and capacitors. [3–5, 15] Ferroelectric sensors detect mechanical stress by monitoring the dielectric displacement, where the piezoelectric coefficient is the most important material property. Ferroelectric actuators can act as high precision positioning systems, making dielectric displacement and strain response to electrical fields crucial for device design. While for the transducers, the coupling coefficients are most important.

Utilizing a ferroelectric material as a thin film offers several advantages compared to bulk ceramics, such as lowered operating voltage, higher speed, lower processing temperatures and minimization of devices. [5] Furthermore, the reduced size enables new possible applications such as flexible energy harvestors, nanogenerators and *in vivo* sensors. Flexible energy harvestors will enable energy to be converted

and utilized from a large number of vibrations such as human motion, breathing, heartbeats, seismic vibrations, acoustic waves, water flow, wind, blood flow, etc., and are therefore a promising source of renewable energy. [16, 17]

For biomedical applications, the material is required to be non-toxic and biocompatible, where the lead-free ferroelectric systems such as $BaTiO_3$-based materials [17, 18] and $K_xNa_{1-x}NbO_3$-based materials [19, 20] have shown great promise. The low Curie temperature of many lead-free ferroelectrics limits the replacement of lead-based ferroelectric materials, which is not a concern for biomedical applications. Ferroelectric thin films are of particular interest for cell simulation, tissue engineering, regenerative medicine and implantable nanogenerators, power supplies and sensors. [18]

2.2 Chemical solution deposition of thin films

Chemical solution deposition (CSD) is one of many methods well-suited for fabrication of oxide thin films. CSD offers many advantages compared to more traditional synthesis methods, such as atomic layer deposition (ALD), pulsed laser deposition (PLD) and molecular beam epitaxy (MBE). Controlling the composition and changing stoichiometry are easily done by CSD and the precursor solutions ensure intimate mixing of the cations, which result in chemically homogenous films. Moreover, the CSD method is cost and time effective and scalable for industrial production. [6,7,21] A wide range of chemical precursors and solvents can be used, and a range of synthesis parameters can be varied, making CSD a versatile synthesis method. The leading lead-based ferroelectric films, PZT, are industrially produced by CSD today, but synthesis routes for other dielectric and ferroelectric films have also been developed. [6, 7]

The CSD method is illustrated in Figure 2.2. The first step is preparing a stable precursor solution with the desired metal ions by mixing metal salts in correct stoichiometry in a solvent. Additives such as wetting agents, complexing agents and flux might also be added if necessary.

After preparing the stable precursor solution, the film is deposited onto the substrate. The most common deposition methods are spin coating, dip coating and spray coating. Spin coating is illustrated in Figure 2.2, where a few droplets of the precursor solution are placed on the surface of a substrate and then the substrate is rotated to create a homogenous film of uniform thickness. [6, 7] The substrate is usually held in place by vacuum at the back side, and a syringe is typically used to deposit only a few droplets of the precursor solution. The rotation speed (typically 1000-8000 rpm), the duration of the rotation (ranging from seconds to minutes), the concentration and the viscosity of the precursor solution will influence the final oxide film thickness. [6, 7] For the dip coating technique, the substrate is emerged in the precursor solution and withdrawn at a certain speed. The withdrawal speed, viscosity, gravitational forces and surface tension all influence the final film thickness. [6, 7] The precursor solution is transformed into an aerosol for spray coating. Small droplets are then transferred to the substrate either by gravity or electrostatic field. The droplet size and spray time will determine the film thickness. [6, 7]

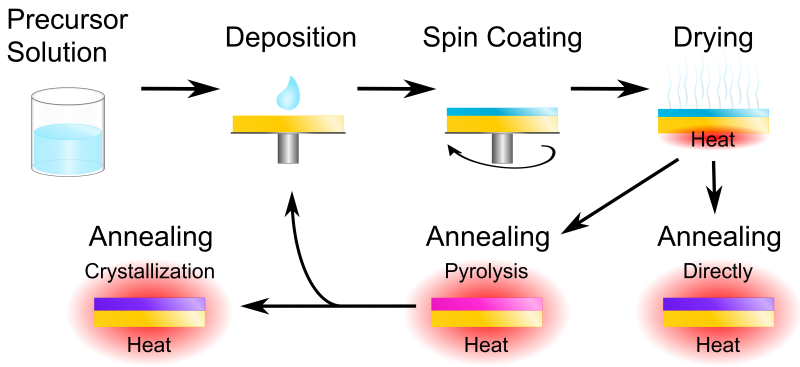

Figure 2.2: Illustration of the chemical solution deposition process for thin film fabrication.

After film deposition, conversion of the as-deposited amorphous film into a crystalline film is done by a heat treatment, either on a hot plate, conventional furnace or by rapid thermal processing (RTP). Dependent on the temperature program used for annealing, pyrolysis and crystallization reactions can take place. For intermediate temperatures, pyrolysis occur, where the as-deposited amorphous film is decomposed and organic species removed. [6,7] Nucleation events often start during pyrolysis, while complete crystallization is achieved only at higher temperatures. The typical thickness after deposition of a layer by chemical solution deposition is 10-30 nm (dependent on the concentration of the precursor solution). [6] However, a thickness of 0.5-2 mm is often required for many applications. [6] Thicker films can be prepared by repeated deposition, either after pyrolysis with a final crystallization step at the end, or by fully crystallizing each layer (Figure 2.2).

2.2.1 Precursor solution chemistry

Organic solvents

Typically, 2-methoxyethanol, methanol and modifying ligands such as acetic acid and acetyl acetone are used as solvents. [6] Synthesis based on 2-methoxyethanol are extensively reported, as these precursor solutions often are highly stable. Ageing effects are usually negligible, which gives good control and reproducibility. [7] However, these solutions require a long preparation time, and the toxicity of the solvent is a concern. [7] The use of methanol as solvent with acetic acid or acetylacetone as chelating agents is also reported. These chemicals are less toxic than the 2-methoxyethanol based precursor solutions, and also requires shorter processing time. However, the methanol-based precursor solutions are typically sensitive to humidity, giving quick ageing. [7]

Although application of organic solvents has successfully yielded thin films of a wide variety of chemistries, the use of these raises a series of health and envi-

ronmental concerns. The stability of the solutions can also be an issue, as these solvents are usually sensitive towards hydrolysis and needs to be handled in inert atmosphere. Therefore, the use of aqueous or diol-based precursor solutions have been investigated to avoid these issues. [6]

Aqueous solutions

Aqueous CSD is not extensively reported in literature, since water-based solutions raises additional challenges. Organic solvents wet typically used substrates better than water, but that can be remedied by adding organic additives (such as surfactants) to reduce surface tension of water. Another approach is to chemically clean the substrates prior to deposition by chemical etching or the use of UV and ozone plasma. [7] However, using water as the solvent reduces the cost and also avoids the use of hazardous organic substances, making the process more environmentally-friendly. Moreover, the use of inert atmosphere is not necessary for aqueous processing. [7]

The aqueous precursor solution reported in literature generally consist of dissolved chelating carbonic acids (oxalic acid or citric acid) and other coordinating ligands such as ethylenediamine (EDTA), along with compounds of the desired metal ions. [7] Several common synthesis routes exist and are classified as aqueous, including the nitrate route, the citrate route and Pechini based synthesis. [6, 7]

In the Pechini route, metal nitrates are dissolved in water and citric acid is added to chelate the metal ions. Further, polyhydroxyalcohol, usually ethylene glycol, is added and the citric acid metal chelates react with the ethylene glycol to form polyesters. The citrate route is similar, except no polyhydroxyalcohol is added. The metal nitrates are simply added in stoichiometric rations, in water and then citric acid is used to form chelated citrate species, which reduces the amount of organics in the solution. A modified version of the Pechini method is also reported, where the metal ions are not limited to nitrates, but also hydroxides, alkoxides, acetates, chlorides and citrates are used. [6, 7] Although not as frequently reported, preparation of aqueous solutions for CSD without polyester formation can be achieved, where the pH is optimized for cation solubility. [6, 22]

Gelation of the film after deposition

The post-deposition behaviour of the films can be divided in to three main categories; formation of a chemical gel, formation of a physical gel and non-gelling, dependent on the precursor solution chemistry. A chemical gel, (also called polymeric gel), is formed immediate after deposition by evaporation of the solvent, where polymerization or polycondensation result in a long-range network structure in which the precursor species are forced to interact. Chemical cross-lining of the precursor species lead to a gelled film, where the reactions taking place are irreversible. [6] A physical gel forms by aggregation of oligomers or particles caused by van der Waals forces or steric interactions. These films can typically be redissolved in the solvent, but physical gels often become chemical with time or at elevated temperatures due to condensation. [6] Non-gelling precursor solutions typically have a solvent with a

high boiling temperature, low volatility and limited polymerization. Films of this type of precursor solution usually have to be dried in order to prevent dewetting of the film and pyrolysis reactions can start at the solvent boiling temperature. [6]

2.2.2 Film annealing

Thin films from CSD are generally amorphous after deposition, and the transformation into a crystalline film is accomplished by thermal annealing. During the annealing different reactions occur, dependent on the processing parameters and precursor chemistry. Thermolysis is the removal of organics by the formation of volatile organic species in the absence of oxygen, while pyrolysis is the formation of volatile organic molecules such as CO or CO_2 through combustion. Dehydration can also occur, where -OH groups are eliminated. Oxidation of the metal ions or formation of metal carbonates are also common reactions. [6]

The temperature program used is either direct heating or with a hold step at low temperatures for pyrolysis. The pyrolysis step normally ensure removal of most of the organic compounds at low temperature (200-500 °C) before crystallization at a higher temperature (above 500 °C). By direct heating, the removal of organics and nucleation occur simultaneously for the typical heating rates used (20-50 °C/s). However, the specific transformation pathway, e.g. which phases formed during the decomposition and how the crystalline phase nucleate, is a function of the precursor chemistry and the temperature profile. [6, 7]

Nucleation and growth of crystalline thin films

The crystallization of films from CSD typically results from a nucleation and growth process. The thermodynamic driving force governs the transformation from the amorphous to the crystalline film and will to a large degree control which nucleation events occur and the resulting microstructure of the crystalline film. Nuclei forming on an interface often results in a columnar microstructure, whereas homogeneous nucleation throughout the film often gives a microstructure consisting of randomly oriented equiaxed grains. [6] The thermodynamic driving force for crystallization is the difference in free energy (ΔG_v) between the amorphous and crystalline phase, (Figure 2.3(a)). The total change in Gibbs free energy for formation of a nucleus contains a contribution from the reduction of free energy by formation of the new phase and also an increase in free energy from the formation of a new surface:

$$\Delta G = \frac{4}{3}\pi r^3 \Delta G_v + 4\pi r^2 \gamma \tag{2.3}$$

where ΔG_v is the thermodynamic driving force per volume, γ is the surface energy per area and r is the radius of the nucleus. [23] The nuclei are unstable below a critical radius ($r*$), meaning they form and redissolve repeatedly. Nuclei are only stable if they exceed a critical radius, corresponding to the barrier for nucleation. The following energy barriers and their dependence on the driving force (ΔG_v) can

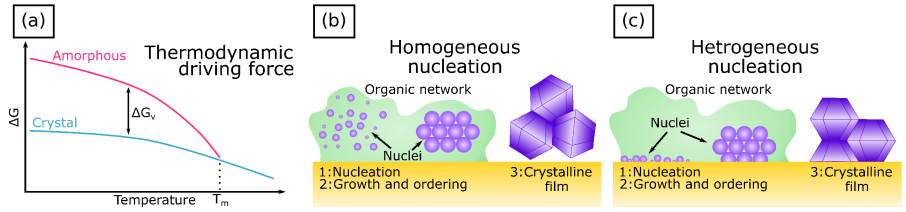

Figure 2.3: (a) The difference in Gibbs free energy between the amorphous and the crystalline phase is the thermodynamic driving force for nucleation (adapted from [6]). Illustration of the nucleation and growth process for films from chemical solution deposition for (b) homogenous nucleation giving polycrystalline films and (c) heterogeneous nucleation giving textured films.

---

be derived for homogeneous and heterogeneous nucleation respectively;

$$\Delta G^*_{homo} = \frac{16\pi\gamma^3}{3(\Delta G_v)^2} \tag{2.4}$$

$$\Delta G^*_{het} = \frac{16\pi\gamma^3}{3(\Delta G_v)^2} f(\theta) \tag{2.5}$$

where $f(\theta)$ is a function related to the contact angle θ, with values in the range 0-1. Hence, nucleation at an interface (Figure 2.3(c)) lowers the nucleation barrier compared to homogenous nucleation (Figure 2.3(b)). The values of γ and θ and the temperature will therefore determine where nucleation occurs in the film. [6, 23]

The crystallization temperature is usually only a fraction of the melting temperature, giving a large driving force and favouring the formation of a high number of nuclei. [6, 24] With slow heating, the nucleation and growth start at low temperatures and continue as the temperature increases. Under these circumstances, homogeneous is just as probable as heterogeneous nucleation, which often results in more than one type of nucleation event and can lead to polycrystalline randomly textured films. [6, 7] A high heating rate may delay the nucleation and growth to higher temperatures and can therefore be beneficial in preparation of oriented films since the mobility of the ions increases with increasing temperature. [6] Nucleation at higher temperatures also implies a lower driving force for crystallization, which in turn makes heterogeneous nucleation at the substrate more probable due to the lower nucleation barrier. The substrate has a substantial effect on the state of the residual stress and the domain structure of the ferroelectric film. [7] When the substrate has a high degree of lattice matching with the film, the $f(\theta)$ term will decrease and hence lower the barrier for heterogeneous nucleation at the substrate, making it possible to grow columnar and epitaxial films. [24]

Thermodynamics does not necessarily provide information about the transformation pathway, which will have a major effect on the nucleation and growth process. Intermediate phases can alter the nucleation into a non-classical regime by acting

as nucleation sites or growth templates for the crystalline phase. Certain intermediate phases, like the metastable fluorite phase in the PZT system, lower the driving force for crystallization, making perovskite nucleation only favourable at the substrate interface. [6] These films have a columnar microstructure, with homoepitaxy between each deposited layer. Since the transformation path influences nucleation, the decomposition and pyrolysis reactions can determine the degree of texture in the crystalline film. [6]

Crystallographic texture or preferential orientation is often desired in an oxide thin film, as functional properties, such as ferroelectricity, are typically more pronounced in textured films. Ricote *et al.* [25] demonstrated that in order to achieve thin films with a preferential orientation by CSD, a high heating rate (on the order of several C/min) was necessary. To preserve the orientation as the thickness of the film was increased, each layer should be fully crystallized in order to act as seeds for the consecutive deposited layers. Orientation can also be achieved by a topotactic transformation pathway, where the pyrolysis products give rise to an oriented nucleation process of the crystalline material, which may also be in relation to the substrate. [26]

2.3 Barium titanate and related materials

2.3.1 Barium titanate

Barium titanate ($BaTiO_3$) was the first discovered ferroelectric perovskite and has been of technical interest since the 1940-50 due to its high permittivity and high dielectric coefficients and is therefore also one of the most researched perovskites. [4, 27] $BaTiO_3$ has the tetragonal perovskite structure at room temperature, where the ferroelectricity arises from the spontaneous polarization due to the displacement of the titanium ion inside the oxygen octahedra, giving a dipole moment in each unit cell. [2] The phase transitions of $BaTiO_3$ are illustrated in Figure 2.4(a), along with the lattice distortions and changes in lattice parameters, but the cubic ($Pm\bar{3}m$) to tetragonal (P4mm) phase transition around 125 °C is of particular interest as this corresponds to the Curie temperature. [2, 4]

The cubic-tetragonal phase transition is a source of discussion in literature, as evidence for both a displacive and order-disorder type phase transition are reported. A displacive type phase transition involves the dynamical equilibrium between freezing and softening of a soft phonon mode. [2] A soft mode is a lattice vibration where the restoring forces associated with this motion becomes negligible when cooled towards the phase transition. Without the restoring forces, the crystal can become mechanically unstable with respect to the atomic displacements and will transform to a lower symmetry structure, in which the atomic displacements are frozen (static) compared to the high temperature phase. [2] The atoms in the lattice vibrate around their equilibrium positions in certain patterns derived from the lattice symmetry. The phonon modes of $BaTiO_3$ are shown in Figure 2.5. The soft mode in $BaTiO_3$ is a transverse optical phonon mode associated with titanium displacement relative to the oxygen octahedra (Figure 2.5(a)), which freeze at the zone centre where the

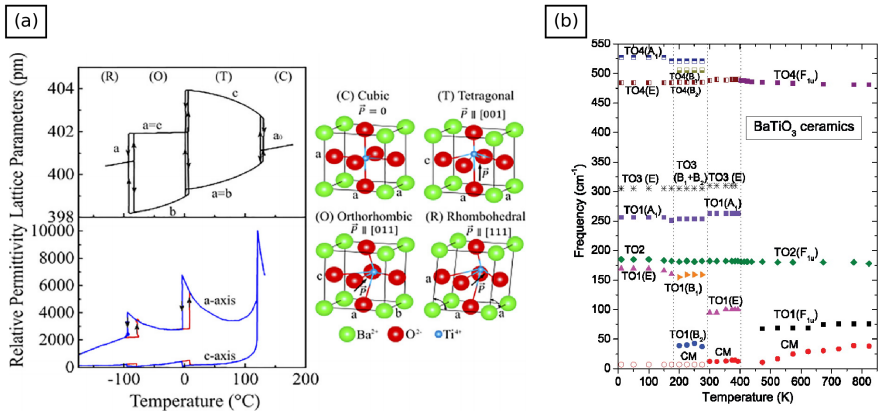

Figure 2.4: (a) Abnormalities in the dielectric permittivity and lattice parameters as a function of temperature, with illustration of the different crystal structures and the polarisation direction arising from the phase transitions. From [4], based on data from [28]. Reprinted with permission from AIP Publishing and John Wiley and Sons. (b) Temperature dependence of the polar TO phonon modes in $BaTiO_3$ ceramics. Figure from [29], reprinted with permission from Taylor & Francis.

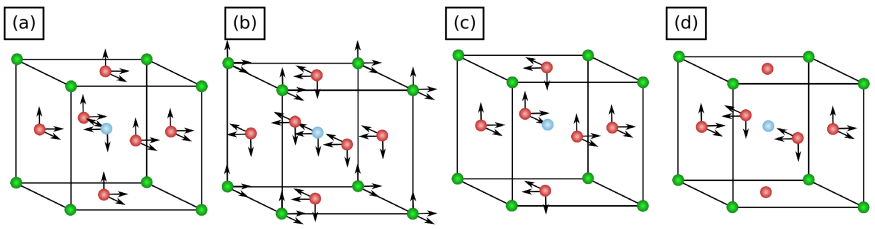

Figure 2.5: Illustration of the lattice vibrations of cubic perovskites ($Pm\bar{3}m$), exemplified by $BaTiO_3$ at the Γ-point. (a) T_{1u} transversal optical mode with displacement of the Ti-ion relative to the oxygen octahedra, which is the mode that softens at the Curie temperature. (b) T_{1u} transversal optical mode with displacement of the Ba-lattice relative to the Ti-O octahedra. (c) T_{1u} transversal optical mode with change in the octahedra shape. All these modes (a-c) results in a change in the dipole moment and are therefore infrared active. Additionally, they are triply degenerated, as the displacement can occur in three symmetry equivalent directions. (d) T_{2u} transversal optical mode with a displacement of an oxygen plane, which does not result in a change in the dipole moment, and therefore is not infrared active.

wavelength is close to infinite, meaning that the atomic displacement freezes in every unit cell. [2, 30] This Ti-vibration continues to freeze, become a static atomic displacement, during cooling, until the rhombohedral structure is reached.

The order-disorder phase transition proposed for $BaTiO_3$ also involves the displacement of the titanium atom, which is microscopically located in one of eighth potential minima along the [111] directions. In the rhombohedral structure, complete long range order of the Ti displacement is assumed, e.g. they are all displaced to the same minima. [31, 32] As the temperature is increased a correlation is lost in one of the three [111] direction at each phase transition. In the cubic phase the Ti will occupy all eight of the local minima along the [111] directions randomly, representing the disordered phase. Neither model is able to fully account for the behaviour of the system at the phase transitions, but a combination of both models has been proposed, where interactions between the soft mode and the off-centre displacement of Ti contribute to the ferroelectric phase transition. [32–34]

Only three of the phonon modes shown in Figure 2.5 are infrared (IR) active. The $BaTiO_3$ transversal ($T_{1u} = A_1^3 + E^4$) phonon mode will gradually broaden and then split in two bands when the symmetry is reduced from cubic to tetragonal, orthorhombic and rhombohedral, due to different bond lengths (force constants) when the symmetry decrease. [35] This can be seen from Figure 2.4(b) where the transversal optical modes of bulk $BaTiO_3$ are shown as a function of temperature. The mode denoted TO1 is the soft mode responsible for the ferroelectric phase transition at the Curie temperature.

$BaTiO_3$ is chemically, thermally and mechanically very stable [36–38], with a high dielectric constant (K), but also low loss characteristics [36], making barium titanate attractive for applications such as capacitors. [39] The properties of bulk $BaTiO_3$ are summarized and compared to lead-based piezoelectric materials in Table 2.1. Cation substitution has shown to improve the ferroelectric properties of $BaTiO_3$, expanding the possible applications for this material (Section 2.3.2). Although barium titanate exhibit good piezoelectric properties, the low Curie temperature limits the use. The dielectric constant also shows a strong dependence on grain size in bulk $BaTiO_3$-based materials. The dielectric constant increases with decreasing grain sizes until nanosized grains are reached, then the dielectric constant drops. [15] This loss of ferroelectric properties below a critical size is proposed due to a lattice transition from tetragonal to cubic symmetry globally. [40] Although, locally orthorhombic structures have been identified, as the orthorhombic-tetragonal phase transition is reported to shift up to room temperature with decreasing grain size. [41] The critical size is dependent on the fabrication method [40], but grain sizes in the range 10-100 nm are reported to induce a paraelectric state at room temperature in $BaTiO_3$. [4]

2.3.2 Solid solutions of $BaTiO_3$ with related perovskites

The properties of $BaTiO_3$ changes when put into solid solutions with other perovskites, such as $SrTiO_3$ and $BaZrO_3$. $Ba_xSr_{1-x}TiO_3$ (BST) has a high dielectric constant, low leakage current and low dielectric frequency dispersion. [50–52] $BaZr_xTi_{1-x}O_3$ (BZT) also has a high dielectric constant and low dielectric loss, but also better capacitance tunability compared to BST, because Zr^{4+} is chemically more stable than Ti^{4+}. [53] The average grain size in BZT bulk ceramics is typically smaller than for $BaTiO_3$. [54] Moreover, Zr-substitution increases the orthorhom-

Table 2.1: Comparison of the dielectric and piezoelectric properties of $BaTiO_3$ and selected lead-based piezoelectric materials.

Properties		**$BaTiO_3$**	**$PbTiO_3$**	**Pure PZT**	**Soft PZT**	**Hard PZT**
Curie Temperature	T_C [°C]	125	470	360	193	300
Dielectric constant	K (1 kHz)	1500	190	800	3500	1000
Piezoelectric strain constants	d_{33} [pC/N]	190	56	220	590	220
	d_{15} [pC/N]	270	68	-93	-270	-37
Piezoelectric voltage constants	g_{33} [mVm/N]	14	33	35	20	25
	g_{15} [mVm/N]	20	32	-14	-9.1	-4.2
Electromechanical coupling coeff.	k_{33}	0.49	0.45	0.67	0.75	0.70
	k_{15}	0.48	-	0.31	0.39	0.30
Mechanical quality factor, Q_M		100	1300	-	65	1000

References: $BaTiO_3$ [4, 12], $PbTiO_3$ [42, 43], Pure PZT [12, 44], Soft PZT [12] and Hard PZT [12]

Table 2.2: Overview of the structure and lattice parameters of $BaTiO_3$-based materials at ambient temperature.

Stoichiometry	**Symmetry**	**a [Å]**	**c [Å]**
$BaTiO_3$ [45]	P4mm	3.99716	4.03699
$BaTiO_3$ [46]	P4mm	3.9932	4.0347
$Ba_{0.90}Ca_{0.10}TiO_3$ [45]	P4mm	3.98015	4.02684
$Ba_{0.90}Ca_{0.10}TiO_3$ [47]	P4mm	3.984	4.025
$Ba_{0.85}Ca_{0.15}Zr_{0.1}Ti_{0.9}O_3$ [48]	R3m	4.00669	
	P4mm	3.99999	4.01584
$Ba_{0.9}Ca_{0.10}Zr_{0.20}Ti_{0.8}O_3$ [49]	$Pm\bar{3}m$	4.04119	

bic to tetragonal phase transition temperature, and decreases the Curie temperature. [54] For about 15 mol% zirconium these phase transitions merge around room temperature, which increases the dielectric and piezoelectric coefficient. [54–56] A further increase of the zirconium content decreases T_C further and above 25 at% zirconium the material shows relaxor behaviour. [54,56,57] For very high Zr-content in BZT, antiferroelectric behaviour is reported. [58]

Calcium substitution in $BaTiO_3$

Calcium substitution on the A-site in $BaTiO_3$ (BCT) affects the phase transitions. The Curie temperature is somewhat increased for low substitution levels, where a maximum T_C of 136 °C was observed for 8 at% Ca, but T_C decreased for higher Ca-content. [59] Increased Curie temperature by solid solutions are rare for the $BaTiO_3$ system, but was explained by the stabilization of the Ti off-centring by the polar displacements of Ca, analogous Pb in PZT. [60] The Ca-substitution is also responsible for inducing diffuse phase transitions, but there seems to be a certain dependency on the fabrication methods for these observations. [60] Furthermore,

Ca-substitution suppresses the rhombohedral and orthorhombic phase transitions, stabilizing the tetragonal phase. [4] The smaller size of Ca^{2+} compared to Ba^{2+} (1.34 Å versus 1.61 Å [61]) reduce the unit cell volume, while the large off-centring of Ca stabilize the tetragonal phase compared to $BaTiO_3$. [60]

Calcium and zirconium substitution in $BaTiO_3$

A compound that lately has received much well deserved attention is the solid solution $zBaZr_xTi_{1-x}O_3$-(1-z)$Ba_yCa_{1-y}TiO_3$ (BCZT), between rhombohedral BZT and tetragonal BCT, which has a polymorphic phase boundary at approximately z=0.5 (for x=0.2 and y=0.7). [62] One of the first works on BCZT was conducted by Liu *et al.*, reporting excellent piezoelectric properties, with a very high piezoelectric constant of 620 pC/N [63], higher than values for conventionally used PZT materials. [4, 17] Although, the promising piezoelectric properties seem to be highly dependent on processing, precursor materials and microstructure judging from the wide range of values reported in literature. [4, 17]

The most important feature of the BCZT system is the convergence point between the rhombohedral, orthorhombic, trigonal and cubic phase. There is a certain degree of controversy about this region, as both the existence of a quadruple point (conflicting with Gibbs phase rule) and the existence of two adjacent triple points are reported in literature. [4] Various crystal structures or coexistence of several crystal structures are observed in the convergence region, dependent on the characterization method, but the consensus seems to be that the transitions in this region are smeared, making measurements of any phase transition related parameter difficult. [4] However, the energy barriers in the convergence region are reported to be low for rotation of the polarization between the tetragonal, orthorhombic and rhombohedral structures, giving enhanced piezoelectric and dielectric properties. [17]

The experimental observations of piezoelectric properties for different regions of the BZT-BCT phase diagram are summarized in Figure 2.6, where the highest piezoelectric coefficients are observed for compositions at the phase boundary between the orthorhombic and tetragonal phases. Zr-substitution generally enhances the ferroelectric properties but leads to decreased Curie temperature, as the highest Curie temperature reported in the BCZT system is for BCT (8 at% Ca). [4]

2.3.3 Barium carbonate

The thermodynamic stability of $BaCO_3$ poses a common synthesis challenge for producing $BaTiO_3$, especially from an aqueous solution. The stability of $BaCO_3$ relative to $BaTiO_3$ increases with a high partial pressure of CO_2 in the atmosphere (Figure 2.7(a)), and analogously with the activity (concentration) of CO_2 in water. [64] Moreover, the solubility of $BaCO_3$ in water is limited [66], which combined with the thermodynamic stability make carbonate secondary phases a prevailing challenge for wet chemical synthesis routes of $BaTiO_3$.

At room temperature $BaCO_3$ has an aragonite-type (Pmcn) structure, where the carbonate ions are located in between layers of Ba^{2+}, but by increasing the temperature, two phase transitions are known. First to the calcite-type ($R\bar{3}m$) structure

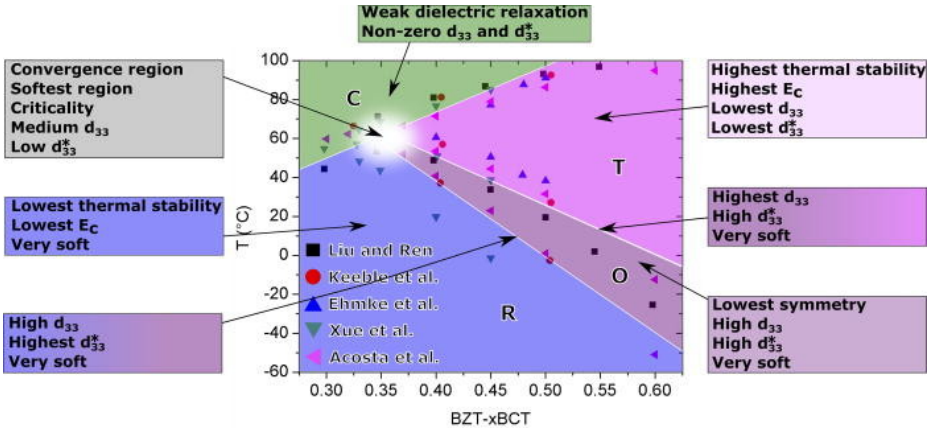

Figure 2.6: BZT-BCT phase diagram with summary of the experimentally observed piezoelectric properties of the different crystal symmetries. Figure from [4], reprinted with permission from AIP Publishing.

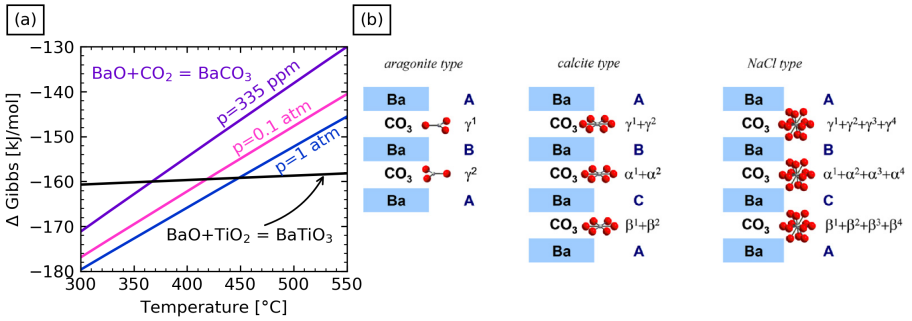

Figure 2.7: (a) The Gibbs free energy of formation of $BaCO_3$ versus $BaTiO_3$, based on data from [64]. (b) Packing of CO_3^{-2} ions for the different $BaCO_3$ polymorphs. Reproduced from Ischenko *et al.* [65]. Copyright © 2007 Elsevier Masson SAS.

above 800 °C and to the NaCl-type ($F\bar{3}mH$) structure above 970 °C. Although lower transition temperatures are reported for cooling. [67–69] The relative orientation and rotation of the carbonate anions in the different structures are illustrated in Figure 2.7(b), showing the smearing of the carbonate anion over the symmetry equivalent positions due to thermally activated rotation.

The calcite-type structure is not stable below 750 °C, but there are some reports that impurities in $BaCO_3$ can stabilize the high temperature modification at significantly lower temperatures. The calcite structure can be obtained in a metastable state at ambient temperature when doped with up to 10 at% of $BaSO_4$ [70] and heating a mixture of the alkaline earth carbonates ($BaCO_3$, $SrCO_3$ and $CaCO_3$) above 750 °C gives the calcite structure, which remained unchanged after cooling

Table 2.3: Infrared vibrational frequencies of the different modes of various carbonate related compounds.

Carbonate type	ν_1 **(ss)** [cm^{-1}]	ν_2 **(oop)** [cm^{-1}]	ν_3 **(as)** [cm^{-1}]	ν_4 **(ip)** [cm^{-1}]
Free $CO_3{}^{-2}$ ion [71]	-	879	1415	680
Aragonite ($BaCO_3$) [72, 73]	1059	856	1435	697
Aragonite ($CaCO_3$) [71]	1080	856	1460	704
Calcite ($CaCO_3$) [71]	-	879	1432	706
Oxycarbonate [65, 74]	1064	876	1390-1435	693
Oxycarbonate [75]	1059	874	1436	693
Oxycarbonate [76]	1059	875	not reported	693

ss = symmetric stretching
oop = out-of-plane bending
as = asymmetric stretching
ip = in-plane stretching

to ambient temperature. [67] The infrared vibrational frequencies for various carbonate related compounds are summarized in Table 2.3, where the oxycarbonate frequencies are listed for comparison as this phase will be reviewed in Section 2.4.2.

2.4 Chemical solution deposition of $BaTiO_3$-based thin films

2.4.1 Transformation paths

Several wet chemical synthesis routes are reported for $BaTiO_3$ powders and films in literature, which in general can be divided into two categories based on the reported transformation pathway to achieve the crystalline $BaTiO_3$. Either $BaTiO_3$ is formed by the solid state reaction between $BaCO_3$ and TiO_2 or through the formation of an intermediate metastable oxycarbonate phase. Which transformation path a certain synthesis route follows seems to be dependent on the nature and chemistry of the precursor compounds. A summary of typical precursors and solvents used for CSD fabrication of $BaTiO_3$ films is presented in Table 2.4. The transformation path is indicated for the works where this was reported.

Solid state reaction of $BaCO_3$ and TiO_2

A well-known reaction scheme for fabricating $BaTiO_3$ is through the solid state reaction of $BaCO_3$ and TiO_2, which is commonly used for producing powders. [91–96] The solid state reaction is reported for powders to occur in two stages, the first being formation of contact points between $BaCO_3$ and TiO_2. Followed by diffusion of Ba^{2+} to TiO_2, where Ti-rich barium titanium oxides are common intermediate phases, usually accompanied by unreacted $BaCO_3$. [92, 96] The particle sizes are of importance as this process is dependent on diffusion, and typically high temperature is required (700-1000 °C). [94, 95]

Table 2.4: Summary of most common synthesis routes of $BaTiO_3$-based thin films from CSD, the transformation path is listed based on what the authors reported.

Precursors		**Solvent**	**Transformation path**	**Ref**
Barium	**Titanium**			
Acetate	4-Isopropoxide^{S}	2-methoxyethanol	Not reported	[77]
Acetate^{S}	4-Isopropoxide^{S}	Ethanol+Water	$BaCO_3$+TiO_2	[78]
Diaminoetoxide	4-Butoxide^{S}	2-butoxyethanol	$BaCO_3$+TiO_2	[79]
Hydroxide	4-Butoxide^{S}	Butanol+ EG	Not reported	[80]
Acetate	4-Butoxide^{S}	Methanol	$BaCO_3$+TiO_2	[81]
Acetate	4-Butoxide^{S}	2-methoxyethanol	Oxycarbonate	[82, 83]
Propionate	4-Butoxide^{S}	CCA+Butanol	Not reported	[84]
Acetate	4-Butoxide^{U,S}	CCA	Oxycarbonate	[24, 85]
Propionate	4-Butoxide^{U,S}	CCA	Oxycarbonate	[24, 85]
2-methylpropionate	4-Butoxide^{U,S}	CCA	$BaCO_3$+TiO_2	[24, 85]
2-ethylhexanoate	4-Butoxide^{U,S}	CCA	$BaCO_3$+TiO_2	[24]
Acetate	4-Isopropoxide^{S}	Propanol + Water	Not reported	[86]
Methoxypropoxide	Methoxypropoxide	Butanol + Water	Oxycarbonate	[87, 88]
Hydroxide^{S}	4-Butoxide^{S}	Butanol + Water	Not reported	[89]
Acetate^{S}	4-Butoxide^{S}	Butanol + Water	Not reported	[89]
Hydroxide^{S}	4-Isopropoxide^{S}	Ethanol + Water	Not reported	[90]

CCA = Corresponding carboxylic acid
EG = Ethylene Glycol
S = Stabilized with acetyl acetone or acetic acid
U = Unstabilized

The formation of $BaCO_3$ (aragonite) during the annealing step in the CSD process has been observed by several authors [24,78,79,81,85,97]. Both $BaCO_3$ and TiO_2 usually form from decomposition of the precursors in the temperature range 300-400 °C [81, 97] and then react at higher temperatures ($\sim$ 600 °C) to form $BaTiO_3$. [24] Hasenkox *et al.* observed that titanium alkoxides decomposed at lower temperatures than barium carboxylates, which led to an amorphous mixture of finely dispersed TiO_2 and barium carboxylates in the film before crystallization. [24]

Ashiri proposed a reaction mechanism with the simultaneous decomposition of $BaCO_3$ and nucleation and growth of $BaTiO_3$ for thin films from CSD. [86] Below 600 °C, the film consisted of $BaCO_3$ and TiO_2 grains. Above 600 °C, $BaTiO_3$ grains started to nucleate, which decreased the density of the $BaCO_3$ grains as they dissolved. The $BaTiO_3$ grains formed in the vicinity of the dissolving $BaCO_3$ grains by reaction with TiO_2 and release of CO_2. [86] The $BaTiO_3$ grains grew by coalescence with increasing temperature, giving a crystalline film with grains in different shapes and sizes at first. Further growth and coarsening resulted in a film with fairly even thickness. [86]

Formation of an intermediate oxycarbonate phase

Several works report on the formation of an intermediate metastable carbon rich oxycarbonate phase during CSD of $BaTiO_3$ thin films. [24, 82, 83, 85, 87, 88] Crystallization shifted towards higher temperature is reported when $BaTiO_3$ forms by decomposition of the intermediate phase. This phase is also observed during wet chemical synthesis of $BaTiO_3$ powders. [65, 74–76, 98–102]

Hasenkox *et al.* reported that the formation of the intermediate phase was dependent on the type of barium precursor [24], while Halder *et al.* observed that the minimum crystallization temperature of $BaTiO_3$ was 600 °C, independent of the formation of the intermediate oxycarbonate phase. [79] The oxycarbonate formation has been linked to the presence of "carbonate like" linkage in the barium carboxylates [79], or to the formation of a mixed metal complex.

Formation of a mixed metal citric acid complex has been reported in the Pechini synthesis routes based on Ti-isopropoxide/butoxide, ethylene glycol, citric acid (non-aqueous and aqueous) and barium carbonate/nitrate. [75,98–100,103,104] The formation of the mixed metal complex was observed to inhibit the formation of TiO_2 and $BaCO_3$, so $BaTiO_3$ formed through the intermediate oxycarbonate phase, rather than through the solid state reaction. Formation of such a mixed metal complex might be a key aspect of the oxycarbonate forming synthesis routes, even when different precursors are used. Oxycarbonate formation is typically observed for Pechini related synthesis [75, 98–100], when (Ba,Ti)-organic complexes were used directly [65, 74, 76] or when using Ba- and Ti-precursors based on the same type of alkoxide group [105].

Arima *et al.* [100], Kakihana *et al.* [101] and Fang *et al.* [102] investigated the precursor chemistry of the Pechini synthesis route with citric acid and ethylene glycol in more detail with Raman spectroscopy and ^{13}C-NMR. They reported on the formation of a mixed metal complex, where citric acid simultaneously stabilized both barium and titanium. [100] The fundamental coordination of the structure of the mixed

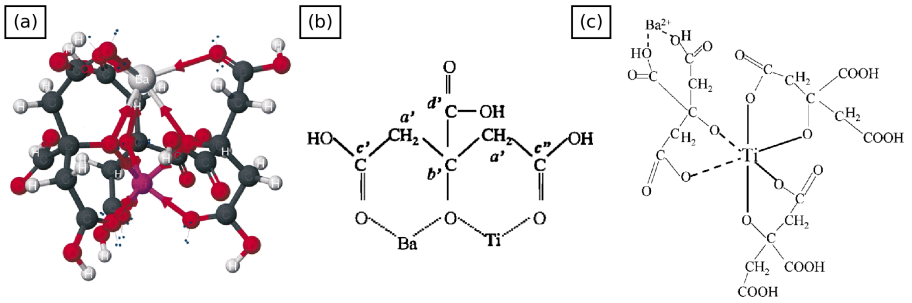

Figure 2.8: The proposed structure of the mixed metal complex according to (a&b) Kakihana *et al.* [101], reprinted with permission from Kakihana *et al.* [101]. Copyright (2020) American Chemical Society. (c) Proposed structure according to Fang *et al.* [102], reprinted with permission from John Wiley and Sons.

metal complex remained unchanged during the polymerization process. [101] Barium and titanium were observed in stoichiometric ratios in the complexes, and excess of either cation in the solution did not change the metal ratio in the complex. Cation excess was proposed to give formation of individual cation complexes. [101] The simultaneous presence of barium and titanium prompts a rearrangement of the citric acid to form a mixed metal complex with the formula $BaTi(C_6H_6O_7)_3{\cdot}4H_2O$, where the proposed structure is shown in Figure 2.8(a&b). [101] Drying of the precursor solution resulted in the dehydrated $BaTi(C_6H_6O_7)_3$ complex, which transformed to the oxycarbonate phase through the formation of $BaTiO(C_5H_4O_4)_{2-x}(CO_3)_x$. [101] Fang *et al.* [102] concluded that the metal complex was mostly related to the chelation between citric acid and titanium and the barium ions are merely interacting with the complex. The proposed structure of the complex by Fang *et al.* is shown in Figure 2.8(c). The nature of the mixed metal complex would probably vary with the different solvents and cation precursors, but it seems to be the cause of the oxycarbonate formation.

2.4.2 Structure of the oxycarbonate phase

The composition of the oxycarbonate phase is widely discussed in the literature. Gopalakrishnamurthy *et al.* first reported on this phase in their work on thermolysis of barium titanyl oxalate in 1975, and proposed that the compound had the stoichiometry $Ba_2Ti_2O_5CO_3$. [106] This stoichiometry has been supported by the findings of other authors [24, 85, 103, 107–110] which also observed that the diffuse XRD patterns could not be ascribed to any other expected phase, demonstrating that the intermediate phase is somewhat crystalline. Others, such as Vasyl'kiv *et al.* [111] and Hasenkox *et al.* [24] have described the interphase as a mixture of finely dispersed $BaCO_3$ and TiO_2 particles, whereas Cho *et al.* [110] concluded that the phase was hexagonal $BaCO_3$ stabilized with Ti^{3+} and oxygen vacancies.

Gablenz *et al.* reported that an intermediate metastable carbon rich phase was

a crystalline oxycarbonate phase with the stoichiometry $Ba_2Ti_2O_5CO_3$, based on experimental results and DFT calculations. [76] Durán *et al.* [75, 99] also came to the same conclusion. Both argue that the IR spectra of powders calcined at 400-800 °C reveal a change in the out-of-plane vibration mode for the carbonate ions corresponding to a transition from carbonate to oxycarbonate (the frequencies were listed in Table 2.3). Both works propose the same structure of the oxycarbonate, based on the work of Tsay *et al.* [98]. The proposed structure has $CO_3{}^{2-}$-groups that differ from those in $BaCO_3$, located in interlayers in the $BaTiO_3$ perovskite structure. Durán *et al.* also hypothesized that the mechanism behind the $BaTiO_3$ formation can change not only with the heating rate regime but also with the previous thermal history of polymeric precursors. [75]

Ischenko *et al.* [65,74] reported that the global stoichiometry of the oxycarbonate phase was consistent with the proposed structure by Gablenz *et al.* [76], Durán *et al.* [75, 99] and Tsay *et al.* [98]. However, Ischencko *et al.* observed that the sample was not homogeneous, but consisted of Ba-rich and Ti-rich nanosized regions, where there was no clear single crystallinity in the Ti-rich areas. [74] The Ba-rich areas had a structure close to the high temperature calcite-type polymorph of $BaCO_3$ and contained no titanium. [65, 74] Ischenko *et al.* suggested that the Ba-rich areas consisted of $BaO_x(CO_3)_{1-x}$, where the substitution of O^{2-} and $CO_3{}^{2-}$ stabilized the calcite structure. [65, 74] The Ti-rich areas were suggested to be oxygen deficient Ba_xTiO_{2+x}, where x was in the range 0.2-0.4. [74] Ischenko *et al.* proposed a general reaction for the transformation pathway through the intermediate oxycarbonate phase:

$$\text{(Ba,Ti)-precursor complex} \longrightarrow Ba_yTiO_{2+y} + BaO_x(CO_3)_{1-x} \longrightarrow BaTiO_3 \tag{2.6}$$

The oxycarbonate phase was also observed to form preferably in the presence of titanium [65, 74]. Hence, a second stabilizing mechanism was proposed; topotaxial formation of calcite-type structural domains of $BaCO_3$ by templating with oxygen-deficient Ti-rich $BaTiO_3$-like structures. [65]

2.4.3 Solid solutions of $BaTiO_3$

Thin films of $BaTiO_3$ solid solutions with other perovskites fabricated from CSD are reported to follow the same transformation path as outlined for $BaTiO_3$. Similar precursors and solvents are commonly used. Both formation of oxycarbonate and ordinary carbonates are reported for solid solutions with STO [24, 80, 82, 83, 85, 88, 112–115], BCT and BZT [116–126]. All showing similar decomposition and crystallization as described for $BaTiO_3$.

2.4.4 Aqueous CSD of $BaTiO_3$-based films

Few descriptions on the preparation of $BaTiO_3$ thin films by aqueous CSD are reported in literature. Ræder *et al.* [127] might have been the first to fabricate $BaTiO_3$ films using a water-based approach, with citric acid as a complexing agent for Ti (from Ti-isporopoxide) and Ba complexed with EDTA and citric acid. Based

on this work, Khomyakova *et al.* recently developed a CSD synthesis for BCZT thin films. [128] Hardy *et al.* prepared BZT films using a simliar approach. [129, 130] Ti-isporopoxide was stabilized with citric acid and Zr-propoxide was dissolved in propanol, stabilized with citric acid and hydrogen peroxide to form a stable Zr-complex, mixed with $BaCO_3$ and aqueous ammonia to regulate the pH.

2.4.5 Microstructure and properties of $BaTiO_3$-based films from CSD

$BaTiO_3$ based thin films produced by CSD generally have polycrystalline or columnar microstructures, where the latter results from homoepitaxial growth of consecutive layers. [6,24,78,79,81,85,124] As formation of the perovskite phase occurs either through the solid state reaction of $BaCO_3$ and TiO_2 or through the decomposition of an oxycarbonate phase, nucleation will occurs homogeneously throughout the film. Columnar microstructure was observed by Hasenkox *et al.* [24] and Hoffmann *et al.* [85] to be dependent on the precursor concentration, as homoepitaxial growth could only be supported in thin layers on Pt/Si. Highly oriented columnar $BaTiO_3$ films on $LaTiO_3$ (LAO) were prepared by Schwartz *et al.* [81] by utilizing a $BaTiO_3$ seed layer annealed at high temperature (1100 °C) and annealing of the final film at high temperature for 30-120 min. Textured films were also prepared on Si substrates, using $La(NO_3)_3$ buffer layers to increase adhesion and a heating rate of 300 °C/min, resulting in films with equiaxed grains. [131] Highly oriented $BaTiO_3$ films following the substrate orientation were also reported on Pt coated (100), (110) and (111) MgO substrates. [132] The films were dense and seemingly free of grain boundaries and TEM investigation showed an epitaxial orientation relationship between the films and substrates. [132] Epitaxial $BaTiO_3$ films on Si-substrates with a 2 nm (100) STO interface layer are also reported, with dense but grain-like microstructure after annealing at 600 °C for 1 h. [133] Moreover, epitaxial BCZT was grown with a columnar grains on a $La_{0.5}Sr_{0.5}CoO_3/CeO_2/Y_{0.15}Zr_{0.85}O_{1.93}$/Si layered structure [62] and with a grain-like microstructure on $La_{0.7}Sr_{0.3}MnO_3$ coated STO [134]. Preparation of textured BCZT films have also been reported. [117, 120, 121, 135]

The capacitor tunability of $BaTiO_3$ films was reported to be 37 % (100 kHz). [79] Remnant polarization in the range 0.9-3.0 $\mu C/cm^2$ [132] has been observed, but the cohesive field reported vary from the range 6.6-13.7 kV/cm [132] to the range 23-120 kV/cm [77, 80], possibly caused by measurements conditions and leakage contributions. Characterization of $BaTiO_3$ films from CSD with interdigitated electrodes gave 6 % tunability for an applied field of 83 kV/cm when the film was crystallized at 750 °C, but this increased to 21 % tunability after annealing at 1100 °C for the same field bias, due to increased grain size. [136] The high temperature annealing also increased the extension of hysteresis loop of the dielectric constant from the range 200-300 to the range 700-1200 [136], where the latter is comparable to bulk values (Table 2.1). BCZT films from CSD are reported to have d_{33}-values in the range 50-141 pm/V [4], which is far from the 620 pC/N observed in bulk BCZT ceramics by Liu *et al.* [63], but the properties are reportedly highly dependent on the synthesis route, type of substrate and deposition conditions. [4]

2.5 Potassium sodium niobate

Potassium sodium niobate (KNN or $K_xNa_{1-x}NbO_3$) is a solid solution between the two orthorhombic perovskites $KNbO_3$ and $NaNbO_3$. [3] $KNbO_3$ is ferroelectric and displays the same phase transition sequence as $BaTiO_3$, while $NaNbO_3$ is antiferroelectric. [3] The most pronounced piezoelectric response is generally observed near the morphotropic phase boundary, around x=0.5. [3] The Curie temperature of KNN is reported to be 413 °C [137], and d_{33}-values are in the range 80-160 pC/N. [3, 138] For most processing routes of KNN materials (powders, ceramics, films, etc.), the volatility of the alkali metals is a challenge, where alkali excess is typically added to compensate for alkali evaporation. [3] Alkali evaporation usually leads to the formation of Nb-rich phases, such as $K_4Nb_6O_{17}$, K_2NbO_{11} and K_3NbO_4 for the K_2O-Nb_2O_5 binary system and Na_3NbO_4 and $Na_2Nb_8O_{11}$ for the Na_2O-Nb_2O_5 binary system. [139]

KNN films from chemical solution deposition

KNN thin films from CSD are in general fabricated with alkali acetate or ethoxide and Nb-pentaethoxide precursors in 2-metoxyethanol and mainly deposited on Pt/Si, with 0-30 % alkali excess. [140–148] These films typically have a polycrystalline microstructure, and varying degree of texture. Both (100) [148] and (110) [144, 149] preferred orientation are reported on (111) Pt/Si and (100) preferred orientation is reported on (100) STO [147,150]. Epitaxial KNN films were also achieved on (100) STO, when each deposited layer was pyrolysed at 450 °C, followed by a final crystallization at 800 °C. [150] Secondary phases are generally reported with low annealing temperatures or insufficient alkali excess, resulting in poor piezoelectric performance. [140, 143, 147–149] A remnant polarization of 1-10 $\mu C/cm^2$ and cohesive fields in the range 30-170 kV/cm have been observed. [140, 144–149] The piezoelectric coefficient was reported to be 18-46 pC/N [144,146], but 6 % Li-doping increased the d_{33}-value to 192 pC/N [145].

Aqueous CSD fabrication of KNN films has also been reported. Lu *et al.* [151] prepared KNN films on Pt/Si, from alkali acetates and niobium oxide mixed in water with citric acid, ethylene glycol and EDTA as complexing agents. The addition of EDTA was reported to suppress the alkali volatility, giving polycrystalline films with larger grains and higher saturation polarizations. [151] Zhang *et al.* [152] used a similar route based on citric acid complexed niobium with alkali acetate and PVP (polyvinylpyrrolidone). PVP was shown to promote (100) texture in the polycrystalline films and decreased the amount of secondary phases, resulting in a remnant polarization of 21 $\mu C/cm^2$ and a cohesive field of 31 kV/cm. [152] An alkali nitrate based synthesis route with oxalate or malic acid complexed niobium has also been reported [8,9], where the niobium complex is prepared in water and then the nitrates are dissolved directly in the solution. Gaukås *et al.* [9] prepared polycrystalline KNN films with (100) preferred orientation on (100) STO, columnar grains and PE-loops showing switching, although influenced by leakage. Only multilayer KNN films prepared by a malic acid complexed niobium precursor annealed in air were found to be

phase pure, while the malic acid based KNN films in O_2 and the oxalate based KNN films showed the presence of secondary phases. [9] Pham *et al.* [8] prepared highly textured KNN films on STO based on the oxalate complexed niobium precursor, with the addition of a salt flux (25 % excess KCl/NaCl). Films on (111) STO were found to be epitaxial, while on (100) and (110) STO an epitaxial layer was observed at the substrate interface, but the films were mainly polycrystalline. [8]

2.6 *In situ* characterization methods

2.6.1 Infrared spectroscopy of powders and films

Most modern IR spectrometers can be adapted to conduct *in situ* characterization. *In situ* measurements are frequently utilized to characterize catalytic and surface reactions [153–160], often with a diffuse reflection (DRIFTS) cell, where the sample is used as a loose powder with minimum sample preparation. [161] The DRIFTS cells are designed to separate optically diffuse reflection from specular reflection, hence, small particles sizes or dilution in a non-absorbent matrix (KBr) will increase the diffuse signal. [161] *In situ* studies with an attenuated total reflection (ATR) cell for liquid flow or electrochemical reactions are also reported. [161–165] Heating cells and cryostats compatible with near-normal incident angle measurements also exist for continuous studies of temperature dependent lattice dynamics in thin films and ceramics. [29,166,167] The geometries for *in situ* IR measurements of thin films and bulk ceramics are illustrated in Figure 2.9, while the DRIFTS setup is shown in Figure 3.6.

Innocenzi *et al.* [168] performed *in situ* IR measurements in combination with synchrotron small angle X-ray scattering to study the solvent evaporation and self-assembly of mesoporous films from a sol-gel synthesis at ambient temperature. [168] A liquid droplet was deposited onto a IR non-absorbent substrate (diamond or ZnSe) so the IR measurements could be done in a transmission geometry, where a mirror was positioned below the substrate to reflect the signal onto the IR detector, while the XRD measurements were done in a reflective geometry. [168] However, *in situ* IR spectroscopy characterization has not been reported for annealing of powders or films were decomposition reactions occur during the measurements.

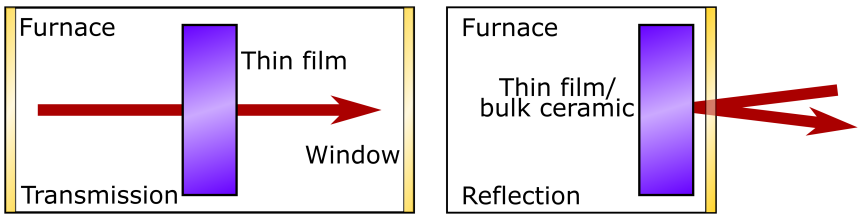

Figure 2.9: Illustrations of sample geometries for transmission and near-normal reflection *in situ* IR spectroscopy of thin films and ceramics.

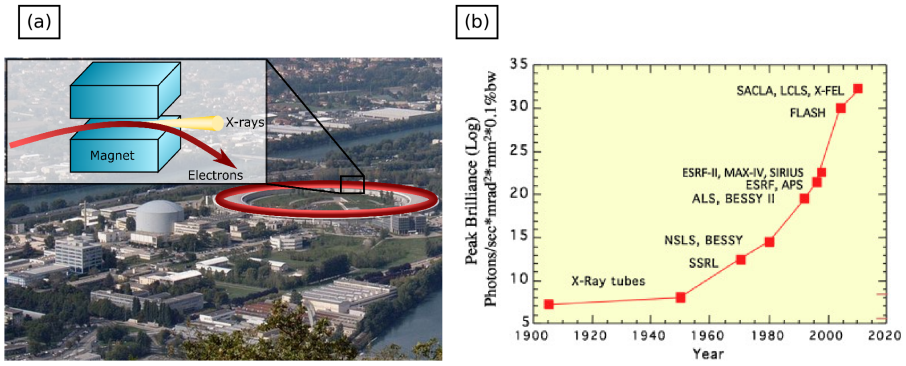

Figure 2.10: (a) Picture of the ESRF synchrotron facility at Grenoble (France), with an illustration of the generation of X-rays by the accelerated electrons. (b) Evolution of the brilliance at different synchrotron facilities. From [169], reprinted with permission from Elsevier.

2.6.2 Synchrotron X-ray diffraction of films

XRD is probably the most important characterization tool for crystalline materials. X-rays can be produced at synchrotron facilities, as the bending of the electron path by magnets cause emission of intense electromagnetic radiation (Figure 2.10(a)). The electrons can be generated over a wide energy range, with intensity 6-7 orders of magnitude higher than what is available in laboratory setups. [170] Synchrotrons also offer higher brilliance (quality) which gives higher signal-to-noise ratio, flexible beam energy, higher polarization and flux. The evolution of the brilliance at various synchrotron facilities is shown in Figure 2.10(b). High brilliance means that the sample volume can be reduced, and the acquisition time to obtain an XRD pattern can be in the order of seconds, making synchrotrons especially suitable for *in situ* experiments. [170] Moreover, the infrastructure at a beamline is usually more specialized for a certain type of measurements, which enables more advanced and sophisticated characterization to be conducted.

Thin films can either be investigated with X-rays in a transmission or reflection geometry. *In situ* growth of thin films investigated by synchrotron XRD are reported for PLD [171], magnetron sputtering [172–177] and thermal co-evaporation [178], all in a reflection geometry. *In situ* post-deposition annealing of oxide films grown by molecular-beam-epitaxy (MBE) [179] and *in situ* characterization of the piezoelectric response from crystalline PZT films from CSD [180] have also been investigated. Total-scattering XRD of crystalline thin films on amorphous substrates have been reported in a transmission [181] and reflection [182] geometry. Grazing incident wide-angel X-ray scattering during deposition and annealing at 70 °C of halide perovskite films have also been reported. [183] A setup for *in situ* annealing of PZT thin films on Pt/Si substrates from CSD has been described, where IR lamps were used, mimicking film annealing in RTP units. [184, 185].

3 Materials and methods

3.1 Synthesis

3.1.1 Preparation of solutions

The aqueous precursor solutions were made by varying selected complexing agents. For the barium titanate based precursor solution, separate solutions for each of the cations were prepared and then the final precursor solution was made by mixing the appropriate cation solutions in stoichiometric ratios. The potassium sodium niobate precursor solutions were mixed directly. All chemicals used for preparing the solutions are listed in Table 3.1.

Table 3.1: Chemicals used for preparing the aqueous solutions.

Chemical Name	**Chemical Formula**	**Purity [%]**	**Producer**
Barium nitrate	$Ba(NO_3)_2$	99.9	Sigma-Aldrich, St. Louis, MO, USA
Titanium isopropoxide	$Ti[OCH(CH_3)_2]_4$	97	Sigma-Aldrich, St. Louis, MO, USA
Calcium nitrate hydrate	$Ca(NO_3)_2{\cdot}4H_2O$	99	Sigma-Aldrich, St. Louis, MO, USA
Zirconium oxynitrate hydrate	$ZrO(NO_3)_2{\cdot}xH_2O$	99	Sigma-Aldrich, St. Louis, MO, USA
Ammonium niobate (V) oxalate hydrate	$NH_4NbO(C_2O_4)_2{\cdot}xH_2O$	99.99	Sigma-Aldrich, St. Louis, MO, USA
Potassium nitrate	KNO_3	99	Alfa Aesar, Haverhill, MA, USA
Potassium chloride	KCl	99.95	Merck, Darmstadt, Germany
Sodium nitrate	$NaNO_3$	99	Sigma-Aldrich, St. Louis, MO, USA
Sodium chloride	NaCl	99.95	Merck, Darmstadt, Germany
Citric Acid	$C_6H_8O_7$	99.5	Sigma-Aldrich, St. Louis, MO, USA
EDTA	$C_{10}H_{16}N_2O_8$	98	Sigma-Aldrich, St. Louis, MO, USA
Aqueous ammonia solution	NH_3 (aq)	30	Sigma-Aldrich, St. Louis, MO, USA
DL-malic acid	$C_4H_6O_5$	99	Sigma-Aldrich, St. Louis, MO, USA

Barium solutions

The Ba-solutions were prepared by heating deionized water under stirring to 60 °C and dissolving the complexing agent EDTA. Aqueous ammonia solution was added to fully deprotonate the EDTA. $Ba(NO_3)_2$ was dried for 24 h at 200 °C before weighing and then added to the EDTA solution. Citric acid was added as a second

Table 3.2: Overview of the concentrations of the different cation solutions and the prepared concentrations.

Cation solutions	Prepared Concentrations		
	A	B	C
Ba	0.52 M	0.33 M	0.39 M
Ti	0.53 M	0.44 M	0.75 M
Ca	0.39 M		
Zr	0.18 M		

complexing agent and the solution was left to stir at 60 °C until transparent (5-10 min). Afterwards the pH was adjusted to neutral by the addition of aqueous ammonia solution. The molar ratios for Ba^{2+} relative to the additives were 1:1 EDTA, 1:5 ammonia and 1:2 citric acid. The concentration of the Ba-solution was determined by adding deionized water until a certain volume was achieved.

Titanium solution

The Ti-solution were prepared by heating deionized water and citric acid to 80 °C under stirring. Titanium isopropoxide was added to the solution, which was then left under stirring at 80 °C for more than 12 h to become transparent. The pH was adjusted to neutral by addition of aqueous ammonia solution. The molar ratio of Ti^{4+} relative to citric acid was 1:3. The concentration of the Ti-solution was determined by thermogravimetric analysis from the residual weight after heating to 1000 °C.

Calcium solution

The Ca-solution was prepared similar to the Ba-solutions. Deionized water was heated to 60 °C under stirring and EDTA was added, followed by aqueous ammonia solution, $Ca(NO_3)_2{\cdot}4H_2O$ and citric acid. The solution was left to stir at 60 °C to become transparent (5-10 min). Afterwards the pH was adjusted to neutral by the addition of aqueous ammonia solution. The molar ratios for Ca^{2+} compared to the additives were 1:1 EDTA, 1:5 ammonia and 1:2 citric acid. The concentration of the Ca-solution was determined by thermogravimetric analysis from the residual weight after heating to 800 °C.

Zirconium solution

The Zr-solution was made by dissolving citric acid in deionized water and heated to 70 °C under stirring. $ZrO(NO_3)_2$ was added and the pH was adjusted to neutral by aqueous ammonia solution. The molar ratio of Zr^{4+} relative to citric acid was 1:2. The concentration of the Zr-solution was determined by thermogravimetric analysis from the residual weight after heating to 1200 °C.

Table 3.3: Overview over the prepared precursor solutions, their concentrations and which cation solutions were mixed.

Precursor Solutions	Prepared Concentrations and Mixed Cation Solutions			
	A	B	C	D
BT	0.26 M Ba-A+Ti-A	0.25 M Ba-B+Ti-B	0.25 M Ba-C+Ti-C	0.13 M Ba-C+Ti-C
BCT	0.25 M Ba-C+Ca-A+Ti-C	0.13 M Ba-C+Ca-A+Ti-C		
BCZT	0.23 M Ba-C+Ca-A+Zr-A+Ti-C	0.11 M Ba-C+Ca-A+Zr-A+Ti-C	0.3 M BCZT-C	

Barium titanate based precursor solutions

The Ba-solutions and Ti-solutions were mixed in stoichiometric ratios to prepare the $BaTiO_3$ (BT) precursor solutions. After mixing the precursor solutions were stable for more than two years for concentrations lower than 0.26 M, while a 0.40 M precursor solution was only stable for 6 months and a 0.5 M precursor solution gelled after 2 h. The calcium-substituted $BaTiO_3$ (BCT) precursor solutions were prepared by mixing Ba-solution, Ca-solution and Ti-solution in the stoichiometry of $Ba_{0.92}Ca_{0.08}TiO_3$. The calcium- and zirconium-substituted $BaTiO_3$ (BCZT) precursor solutions were prepared by mixing Ba-solution, Ca-solution Zr-solution and Ti-solution in the stoichiometry of $Ba_{0.85}Ca_{0.15}Zr_{0.1}Ti_{0.9}O_3$. Different concentrations than directly achieved by mixing were prepared either by evaporation or dilution. For one BCZT thin film the BCZT precursor solution (BCZT-C) was prepared differently. The calcium and zirconium solutions used for the BCZT-C solution were prepared by dissolving $Ca(NO_3)_2{\cdot}4H_2O$ and $ZrO(NO_3)_2$ directly in deionized water without any additives. An overview of the precursor solutions and concentrations are listed in Table 3.3.

KNN precursor solutions

$K_{0.5}Na_{0.5}NbO_3$ (KNN) precursor solutions based on a oxalic acid-complex (KNN-Ox) were prepared by dissolving $NH_4NbO(C_2O_4)_2{\cdot}xH_2O$ in deionized water heated to 70 °C under stirring before dried $NaNO_3$ and KNO_3 were added in equal molar ratios to give a 5 % alkali metal excess. The nitrates were dried at 200 °for 24 h before weighting. The solution was then left on a hotplate at 70 °C under stirring for 2 h. The concentration of niobium was 0.25 M, determined by thermogravimetric analysis from the residual weight after heating to 800 °C.

The solution with a malic acid-complex (KNN-MA) was prepared by dissolving a niobic acid precipitate in deionized water with 0.33 M DL-malic acid under stirring at 70 °C. The molar ratio was 1:2 between niobium and the malic acid. The pH was adjusted to neutral by aqueous ammonia solution, before dried $NaNO_3$ and KNO_3 were added in equal molar ratios to give 5 % alkali metal excess. The nitrates were dried at 200 °for 24 h before weighting. The concentration of niobium was 0.14 M,

determined by thermogravimetric analysis from the residual weight after heating to 800 °C. Oxalate and malic acid precursor solutions with the addition of a salt flux (KNN-Oxsf and KNN-MAsf) were prepared by dissolving 1:1 NaCl and KCl salts in molar ratio to the precursor solutions giving 35 % alkali metal excess in total.

3.1.2 Fabrication of films

Substrates

Various 1x1 cm^2 substrates were used for the thin film fabrication, listed in Table 3.4. All substrates were washed with ethanol (96 %) and ISO 5 clean room wipes before they were cleaned with oxygen plasma (Femto, Diener Electronic GmbH+Co, Ebhausen, Germany) for 2 min to enhance wetting prior to the film deposition.

Table 3.4: Overview of substrates used for film fabrication with lattice parameters and thermal expansion coefficients.

Substrate	**Orientation**	**Lattice**	**Thermal exp. coeff. [1/K]**	**Producer**
Single crystal $SrTiO_3$ (STO)	(100),(110),(111)	$Pm\bar{3}m$, a=3.9045 Å	$9.0{\cdot}10^{-6}$	Crystal-GMBH, Berlin, Germany
Single crystal MgO	(100)	$Fm\bar{3}m$, a=4.203 Å	$12.8{\cdot}10^{-6}$	Crystal-GMBH, Berlin, Germany
Single crystal $LaAlO_3$ (LAO)	(100)	$Pm\bar{3}m$, a*=3.7896 Å	$9.2{\cdot}10^{-6}$	Crystal-GMBH, Berlin, Germany
Platinized silicon (Pt/Si)	Polycrystalline	$Fm\bar{3}m$, a=3.92 Å (Pt)	$2.6{\cdot}10^{-6}$ (Si)	SINTEF, Oslo, Norway
Fused silica (FS)	Amorphous	-	$\sim 0.5{\cdot}10^{-6}$	Crystal-GMBH, Berlin, Germany

*Pseudocubic
References: For STO, LAO and MgO the values given were from the supplier data sheet [186], for Pt/Si the lattice parameter was given for Pt [187] and the thermal expansion for Si [188] and for FS the thermal expansion coefficient was from [189].

Chemical solution deposition of thin films

Thin films were prepared by aqueous chemical solution deposition (CSD), which was illustrated in Figure 2.2. The precursor solution was deposited onto the substrate through a syringe with a 0.2 µm cellulose acetate membrane filter and then spin coated (WS-400B-6NPP-LITE/AS, Laurell Technologies, Montgomery, PA, USA) at 3500 rpm for 30 s. Afterwards the films were dried on a hotplate for 4 min at 180 °C.

The thin films were annealed either *in situ* during the synchrotron X-ray diffraction (XRD) or *ex situ*. The films prepared *ex situ* were heated on a rapid heating plate (RHP) which was a replica of the setup used during *in situ* synchrotron XRD measurements, described in detail in Blichfeld *et al.* [190], (Appendix C). The RHP

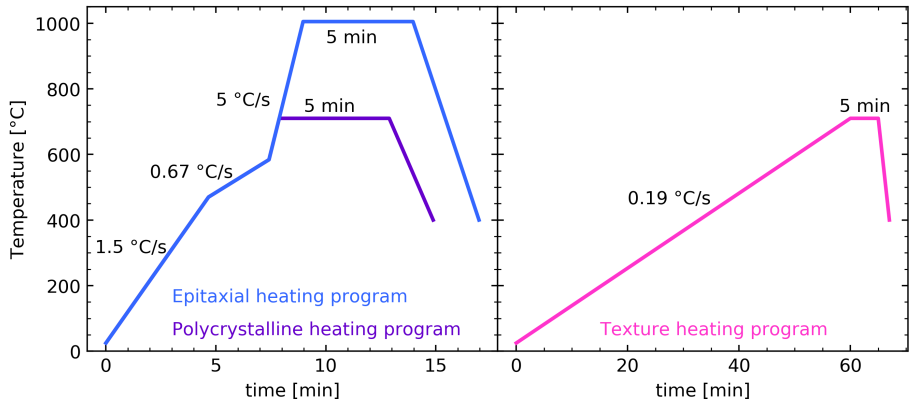

Figure 3.1: Schematics over the *ex situ* heating programs used for thin film annealing.

consists of a flat heating element (850 W, BACH RC GmbH, Seefeld, Germany) incorporated in a ceramic insulation block placed on steel rods in an aluminium box. The films were placed on a silicon wafer on top of the heating plate, and a second piece of the ceramic insulation block was used as a lid to stabilize temperature. A thermocouple was positioned inside the heating plate to control the temperature and the film temperature was measured by a second thermocouple positioned on the film surface. The temperature was controlled with a PID control unit (2408/2116, Eurotherm, Ashburn, VA, USA).

For *ex situ* multi-layer films three different heating programs were used (Figure 3.1), developed based on the results from the *in situ* characterization after annealing single layered films. The different heating programs are referred to as the polycrystalline heating program (Poly HP), the texture heating program (Tex HP) and the epitaxial heating program (Epi HP). For all the films, each layer was fully crystallized before the next was deposited when multi-layer films were prepared.

Preparation of thick films

Thicker films were prepared for the *in situ* infrared (IR) spectroscopy measurements to ensure strong enough signal from the films. These thick films were made by dispersing precursor powders (described in Section 3.1.3) in deionized water and depositing droplets directly onto Pt/Si substrates. The droplets were flattened by draining most of the liquid off the substrate edge, leaving a thick wet precursor film, which was left to dry in ambient temperature for 30-60 min before the IR measurements.

3.1.3 Preparation of powders

To prepare powders, the $BaTiO_3$-based precursor solutions were dried at temperatures between 150 and 200 °C for 12-24 h, resulting in a sponge-like brown material, which was crushed in an agar mortar to yield the precursor powers. For the KNN precursor powders the KNN-Ox precursor solution was dried at 100 °C and the KNN-MA precursor solution was dried at 200 °C, both for 24 h followed by crushing in an agar mortar. Calcination of powders was done in a muffle furnace with heating and cooling rates of 200 °C/h. Temperature and hold time were varied dependent on the purpose of the calcination. Thermogravimetric analysis (TGA, STA 449C, Netzsch, Selb, Germany) of the precursor powders were done in synthetic air, using a heating rate of either 0.2 °C/s or 0.02 °C/s.

3.2 Characterization

Figure 3.2 show an overview over the *in situ* thin film characterization methods during the annealing step in the CSD process, where IR spectroscopy was used to study the decomposition of the amorphous precursor phases and XRD was used to study the crystallization process. *Ex situ* characterization was done to supplement the *in situ* data.

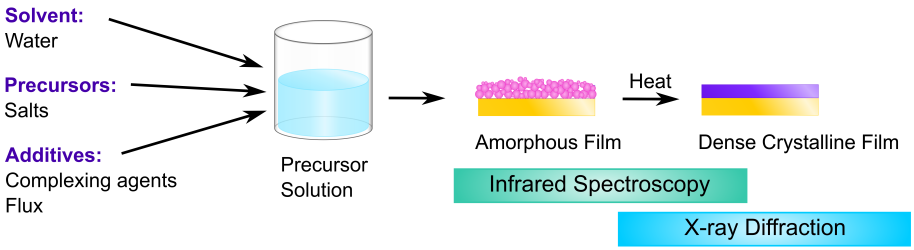

Figure 3.2: Overview of the *in situ* characterization methods used during film synthesis from aqueous CSD.

3.2.1 *In situ* synchrotron X-ray diffraction of thin films

In situ synchrotron XRD was conducted at the BM01 end-station, Swiss-Norwegian Beamlines (SNBL) at ESRF (The European Synchrotron Radiation Facility, Grenoble, France) over four separate beamtimes. At the first beamtime the wavelength was 0.78449 Å and the film surface temperature was recorded manually. For the following beamtimes the wavelengths were 0.77624 Å, 0.78242 Å and 0.78006 Å, and the film surface temperature was recorded and saved for each frame.

A Pilatus 2M 2D-detector [191] was used to be able to detect azimuthal distribution of the diffracted intensity and to reveal texture information. The wavelength was chosen to minimize the fluorescence of strontium (from the substrates). The beam size was 250 x 500 μm (height x width) for most experiments.

Thin film preparation

The films for *in situ* annealing were prepared by spin coating and drying (as described in Section 3.1.2). For the $BaTiO_3$ films precursor solutions BT-A and BT-B was used, for BCT films precursor solution BCT-A was used and for BCZT precursor solutions BCZT-A and BCZT-C were used. The KNN films were made from the KNN-Ox, KNN-MA, KNN-Oxsf and KNN-MAsf precursor solutions. Crystalline $BaTiO_3$ single- and multi-layer thin films were also prepared as described in Section 3.1.2 for texture analysis.

The heating setup

The heating setup is described in detail in Blichfeld *et al.* [190], (Appendix C). The setup consists of a flat SiC heating element (850 W, Bach Resistor Ceramics GmbH, Seefeld, Germany) incorporated in a ceramic insulation block placed on steel rods in an aluminium box (Figure 3.3). The film was placed on a silicon wafer on top of the heating plate and held in place by a thermocouple, which measured the film surface temperature. A second thermocouple was positioned inside the heating plate and the temperature was controlled by a PID control unit (2408/2116, Eurotherm, Ashburn, VA, USA). A schematic overview of the two types of temperature profiles used during the *in situ* XRD annealing is presented in Figure 3.4.

The films were measured in grazing incidence to limit the signal from the substrate and they were aligned such that the beam footprint was centred in the film. During the *in situ* annealing measurements the incident angle was increased from 1° to 2° during data acquisition, so that each frame was an average of this angle range. This was done to capture more reflections, and to compensate for any misalignment. To compensate for thermal expansion of the insulating ceramic block and SiC heater, the whole heating setup was shifted stepwise downwards with respect to the normal to the film, in order to keep the same position for the beam footprint during the *in situ* annealing experiments. The height steps and the exposure time were optimized for each experiment individually, based on the temperature profile.

For the experiment with controlled atmosphere a lid was placed on top of the aluminium box, which had two large Kapton tape windows to allow the full beam onto the sample (Figure 3.3(c)). A gas mixing setup was connected to the heating cell and gases were mixed in the molar ratios 45:15:40 for N_2:O_2:CO_2 respectively. The cell was purged for 1h with the gas mixture before starting the measurement.

For the texture analysis the films were aligned such that the beam focused at the centre of the films. The films were measured at ambient temperature and with an increasing tilt angle ($\Delta\omega$=0.1°) relative to the beam (Figure 3.3(d)). Exposure time was 1 s for each ω step.

Data processing and analysis

A procedure for handling the thermal expansion and the height offset is described in Blichfeld *et al.* [190], (Appendix C). The signal from the substrate and thermal expansion data was combined to calculate the real sample to detector distance

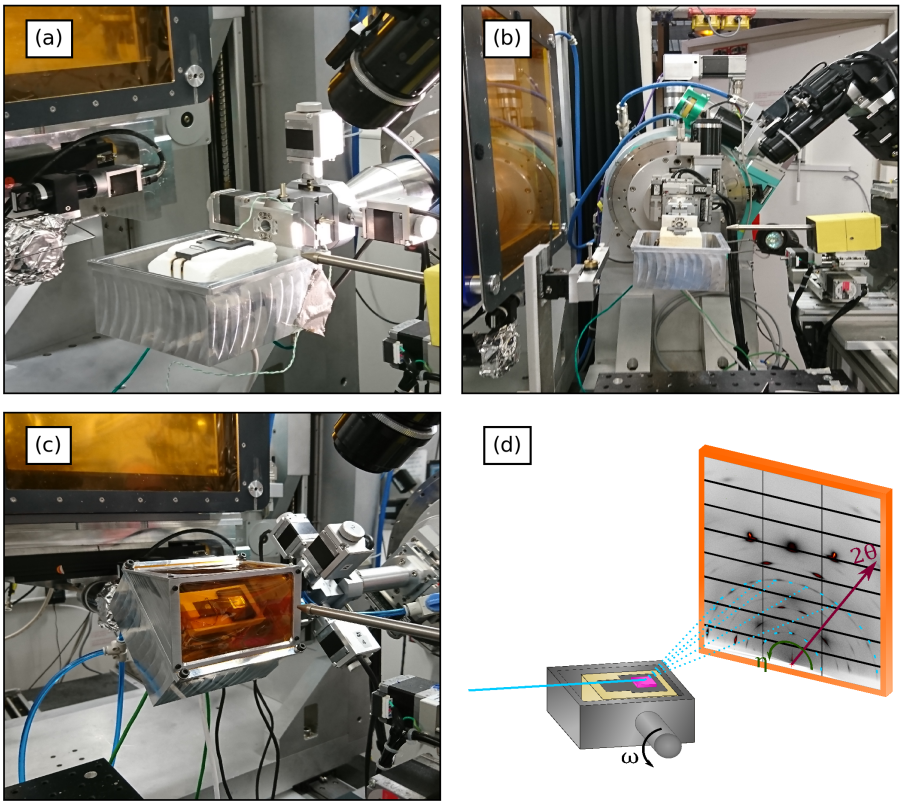

Figure 3.3: (a) Picture showing the *in situ* XRD heating setup. (b) Side view of the heating setup. (c) Picture of the heating setup with the lid for atmosphere control. (d) Schematics of the beam direction relative to the film and detector showing the different angles; ω (tilt), η (azimuthal) and 2ϑ (diffraction).

for each measurement height, and the diffractograms were shifted based on these calibrations. The integration and data processing were done in Jupyter Notebook utilizing the pyFAI package. Rietveld refinements were done for the *in situ* data on 1D diffractograms using the MAUD software (Materials Analysis Using Diffraction v2.78) to find the lattice parameters. [192]

For the texture refinements the diffractograms were integrated with the BUBBLE software (v 2018.11.28) from SNBL [191] with azimuthal slicing of 5°, to preserve the texture information. The substrate reflections were masked and a background function subtracted prior to refinements. Rietveld refinements were preformed using the MAUD software (v 2.93) with the E-WIMV model to account for texture. No symmetry was imposed and the refinements were run to convergence. The calculated orientation distribution function (ODF) was exported from MAUD and pole figures based on the ODFs were calculated with the MTEX package (v 5.2.4) for MATLAB

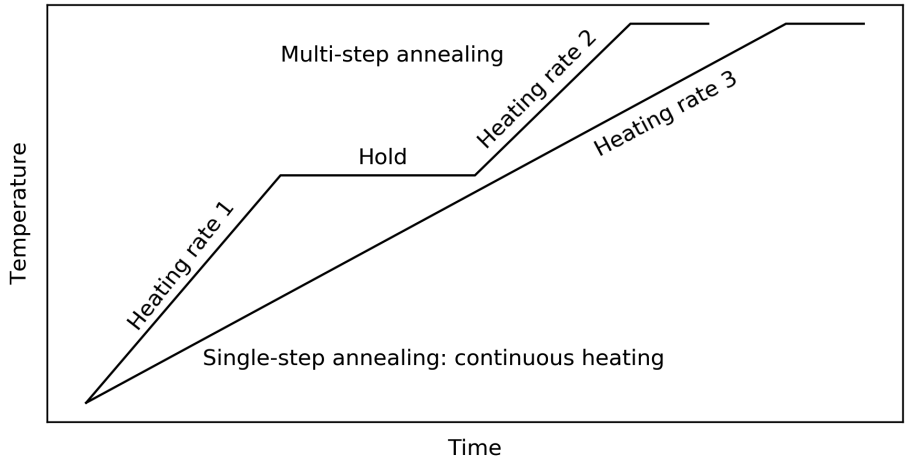

Figure 3.4: Schematic illustration of the two types of temperature profiles used during the *in situ* XRD experiments.

(v R2018a) assuming cubic structure for the films.

Texture was also visualized by slicing the data in two orthogonal angular directions; tilt (ω) and azimuthal (η) (Figure 3.3(d)). These data were measured with stepwise increasing tilt. The ω-series was integrated to 1D diffractograms with the BUBBLE software without any mask. The azimuthal series was made by summing the ω-series into one single 2D diffractogram and integrated with azimuthal slicing and a step size of 0.5°.

3.2.2 X-ray powder diffraction

Powder X-ray diffraction (XRD) was performed on both a D8 A25 DaVinci X-ray diffractometer and a D8 Focus X-ray Diffractometer (Bruker, Billerica, MA, USA) both with CuKα radiation (λ = 1.54 Å). Both diffractometers are equipped with LynxEye^{TM} SuperSpeed Detectors. On the D8 A25 DaVinci instrument, diffractograms were recorded with a step size of 0.0112° and variable divergence slit, which gives a constant illuminated length of 6 mm. On the D8 Focus instrument diffractograms were recorded with a step size of 0.016° and constant divergence slit of 0.6 mm. Conventional grazing incident XRD was performed on the thin films with a D8 A25 DaVinci X-ray diffractometer (Bruker, Billerica, MA, USA) with CuKα radiation (λ = 1.54 Å) equipped with a LynxEye^{TM} SuperSpeed Detector. The diffractograms were recorded with an incident angle of 2°, with a step size of 0.0278°, no rotation and a variable divergence slit, which gives a constant illuminated length of 6 mm.

In situ XRD on precursor powders with controlled atmosphere was performed on a D8 Advance Diffractometer (Bruker, Billerica, MA, USA) with CuKα radiation

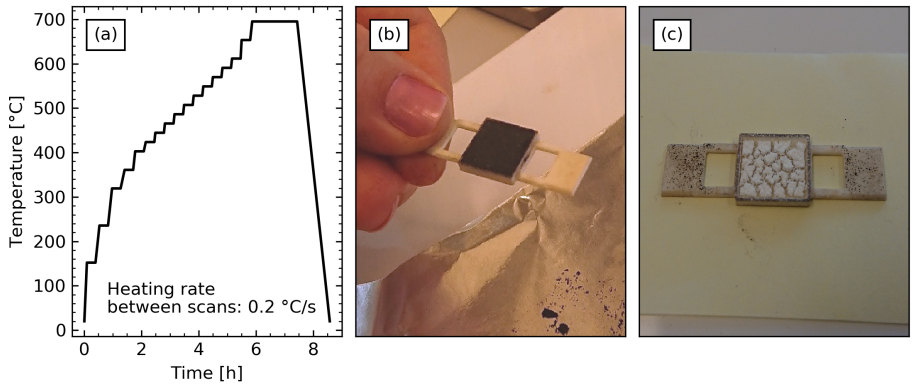

Figure 3.5: (a) Heating profile during gas XRD measurements. (b) Picture of a prepared sample of $BaTiO_3$ precursor powder before measurement. (c) Picture of the sample after heating in synthetic air.

($\lambda = 1.54$ Å) equipped with a Våntec-1^{TM} SuperSpeed detector. The samples were prepared in a radiant heater sample holder of alumina, shown in Figure 3.5(b&c). A gas mixing system was connected to be able to vary partial pressure of CO_2 in synthetic air. The sample chamber was closed and purged with the desired gas mixture for 1 h before measurements were started. The diffractograms were recorded with a step size of 0.033 °and 0.5 s scantime per step. One diffractogram was recorded at ambient temperature before heating started and three diffractograms were record at ambient temperature after cooling. The heating profile for all samples is shown in Figure 3.5(a), where the diffractograms were recorded during a hold step at selected temperatures and the heating rate in between hold steps was 0.2 °C/s. For the *in situ* XRD with variable CO_2 partial pressure, precursor powders based on the BT-B precursor solution were used. Rietveld refinements of the powder XRD patterns were done with the TOPAS software (v5, Bruker, Billerica, MA, USA).

3.2.3 *In situ* infrared spectroscopy of thick films

A procedure for measuring the decomposition reactions during annealing of films from aqueous CSD by *in situ* IR was developed. Fourier-transform infrared spectroscopy (FTIR, Vertex 80v, Bruker, Billerica, MA, USA) was done with a Praying Mantis^{TM} Diffuse Reflection Accessory (Harrick Scientific Products Inc., Pleasantville, NY, USA) and a Praying Mantis^{TM} High Temperature Reaction Chamber (Harrick Scientific Products Inc., Pleasantville, NY, USA). A specialized front plate was designed for the FTIR instrument so the reaction chamber could be water cooled, have synthetic air atmosphere and be connected to a PID control unit (2408/2116, Eurotherm, Ashburn, VA, USA) while the FTIR instrument was under vacuum (Figure 3.6(a)). Figure 3.6(b) shows a schematic illustration of the diffuse reflectance cell and the reaction chamber. The height of the reaction chamber was

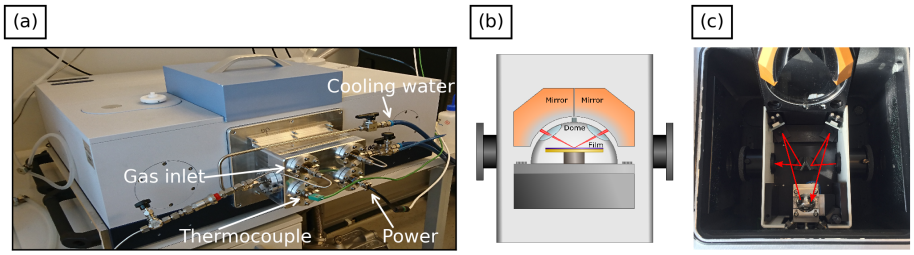

Figure 3.6: (a) Picture of the FTIR instrument showing the front plate designed to enable *in situ* measurements and (b) a schematic illustration of geometry of the reaction chamber inside the diffuse reflectance cell. (c) Picture of the reaction chamber (seen from above) where the beam path is indicated.

adjusted to maximize the throughput signal prior to measurements, as were all the mirrors in the diffuse reflectance cell. The incident angle was in the range 40-50° relative to the film surface.

A clean Pt/Si substrate was used as background and measured at room temperature under the same conditions as the films. The measurements were done in the reflectance mode in the range 400-4000 cm^{-1}, with a resolution of 4 cm^{-1} and using a 6 mm aperture. The number of averaged scans depended on the heating rate; for 0.05 °C/s 80 scans were averaged, for 0.2 °C/s 40 scans were averaged and for 0.5 and 1 °C/s 20 scans were averaged.

The heating programs used for the different *in situ* IR experiment of thick $BaTiO_3$-based film are shown are Figure 3.7. Sample BT-2 was measured without the dome for atmosphere control. The dome significantly reduced the throughput signal and caused a high noise level at low wavenumbers, so measuring without it resulted in better resolution of the absorption bands and increased signal to noise ratio, especially at low wavenumbers. However, the reactions taking place during decomposition depend on an oxygen containing atmosphere, which meant that the instrument could not be evacuated.

For the *in situ* IR experiments, thick films were made from precursor powders of the BT-C, BCT-A and BCZT-A precursor solutions for the $BaTiO_3$-based films and the KNN films were made from the KNN-Ox, KNN-MA, KNN-Oxsf and KNN-MAsf precursor powders.

3.2.4 *Ex situ* infrared spectroscopy of powders and thin films

IR spectroscopy and modelling of phonon modes for thin films on single crystal substrates were done at the Institute of Physics at the Czech Academy of Science (Prague, Czech Republic). A Bruker IFS 113v FTIR instrument (Bruker, Billerica, MA, USA) was used to record the reflection spectra at near normal incident with 5 mm aperture and 2 cm^{-1} resolution. A metallic mirror was used as the back-

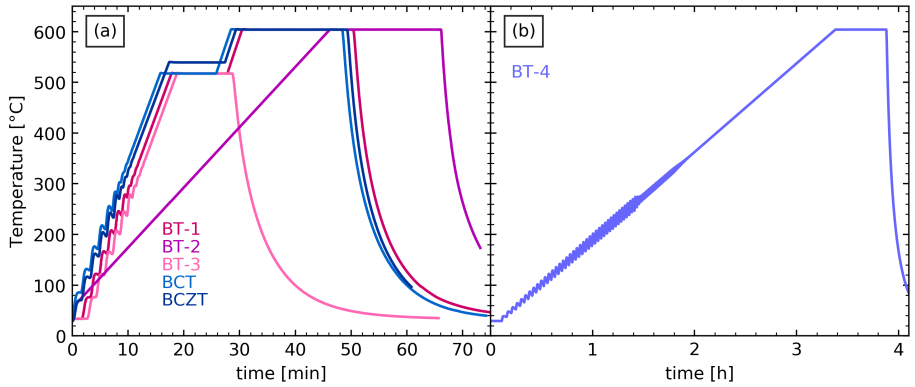

Figure 3.7: Temperature profiles for the $BaTiO_3$-based thick films during the *in situ* IR measurements.

---

ground. Separate measurements were performed for the low and high wavenumber regions and the data was later merged using the OPUS software (Bruker, Billerica, MA, USA). For the 20-1000 cm^{-1} range, a Hg lamp was used as source, 128 scans were averages for the sample, while 64 scans were averaged for the background measurement. For the high wavenumber region, 400-7000 cm^{-1}, a Globar source and a Ge/KBr beamsplitter were used, 74 scans were averaged for the sample and 32 scans were averaged for the background.

The reflection spectra were fitted manually, where the phonon modes for the substrates were expressed as damped harmonic oscillators according to the Lyddane-Sachs-Teller (LST) relation:

$$\epsilon(\omega) = \epsilon_\infty \prod_n \frac{\omega_{LO,n}^2 - \omega^2 - i\gamma_{LO,n}\omega}{\omega_{TO,n}^2 - \omega^2 - i\gamma_{TO,n}\omega} \tag{3.1}$$

where the $\omega_{LO,n}$ and $\omega_{TO,n}$ are the frequencies and γ_n are the damping coefficients for the phonon modes in the substrates. Then the phonon modes for the films were found according to:

$$\epsilon(\omega) = \epsilon_\infty + \sum_n \frac{S_n}{(\omega_n^2 - \omega^2)^2 + i\gamma_n^2\omega^2} \tag{3.2}$$

where S_n is a coefficient, ω_n the phonon mode frequency and γ_n is the damping coefficient of the phonon mode. Equations 3.1 and 3.2 are taken from Brüesch (1986). [193] The ϵ_∞ values were determined based on the reflection value in the IR spectra above 4000 cm^{-1}, where the reflection had a constant value. The reflection spectra were calculated from the dielectric function according to;

$$R = \frac{1 + \sqrt{\epsilon_{re}^2 + \epsilon_{im}^2} - \sqrt{2\epsilon_{re} + 2\sqrt{\epsilon_{re}^2 + \epsilon_{im}^2}}}{1 + \sqrt{\epsilon_{re}^2 + \epsilon_{im}^2} + \sqrt{2\epsilon_{re} + 2\sqrt{\epsilon_{re}^2 + \epsilon_{im}^2}}} \tag{3.3}$$

IR spectroscopy was performed on a series of calcined $BaTiO_3$, BCT and BCZT precursor powders. The spectra were collected using a FTIR instrument (Vertex 80v, Bruker, Billerica, MA, USA) and a Platinum ATR diamond system. The spectra were recorded in the range 400-4000 cm^{-1}, where 32 scans were averaged for each sample with a resolution of 4 cm^{-1}, and the aperture was set to 5 mm. The ATR diamond was cleaned with isopropanol between each sample.

3.2.5 Electrical characterization

Electrode deposition on thin films

Interdigitated electrodes (IDE) were deposited on $BaTiO_3$-based multi-layer crystalline thin films on (100) STO. The films were cleaned for 2 min in an acetone ultrasound bath, followed by immediate rinsing with isopropanol and blow drying with N_2. The films were further cleaned with oxygen plasma (Femto, Diener Electronic GmbH+Co, Ebhausen, Germany) for 1 min. The films were dried on a hotplate at 150 °C for 5 min, before a ma-N440 negative photoresist (micro resist technology GmbH, Berlin, Germany) was spin coated on for 30 s at 3000 rpm (WS-400B-6NPP-LITE/AS, Laurell Technologies, Montgomery, PA, USA), and soft baked at 95 °C for 5 min on a hotplate. Exposure was done by a mask aligner (MLA 150, Heidelberg Instruments Mikrotechnik GmbH, Heidelberg, Germany) with an exposure dose of 3600 mJ/cm^2. Development of the photoresist was performed with the corresponding developer ma-D322s (micro resist technology GmbH, Berlin, Germany) and the surface was activated by 1 min oxygen plasma before deposition. Electrodes of 5 nm titanium and 20 nm platinum were deposited by e-beam evaporation (ATC series, AJA international Inc., North Scituate, MA, USA). Lift-off was done by placing the films in an acetone ultrasound bath for 30 s and rinsed with first isopropanol, then water and blow drying with N_2. Afterwards the electrodes were annealed in air at 600 °C for 2 h in a muffle furnace with a heating and cooling rate of 200 °C/s. The quality of the electrodes was checked with an optical microscope (Nikon SMZ460/SMZ800, Tokyo, Japan) and images of the films were used to calculate distances between the fingers for each electrode. Typical distances between electrodes were 6-8 µm and typical electrode thickness was 2-3 µm. Several electrodes were deposited on each film and the electrode pattern and orientation relative to the substrate crystallographic directions is shown in Figure 3.8.

Electrical measurements of thin films

Electrical characterization of the thin films was preformed at room temperature with a piezoelectric evaluation system (PES, aixPES, aixACCT, Aachen, Germany). Measurements were done for all electrode orientations for each film. Both Polarization-Voltage (PV) and Capacitance-Voltage (CV) loops were recorded. For the PV loops the voltage was chosen to corresponded to approximately 20 kV/cm, and the electric field was calculated by dividing by the effective electrode spacing, given by:

$$a' = \frac{a + 4tln(2)}{\pi} \tag{3.4}$$

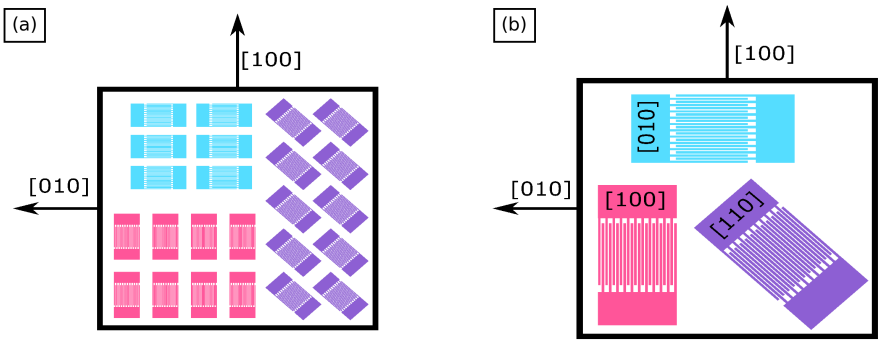

Figure 3.8: (a) Schematic illustration of the electrode pattern deposited relative to the substrate crystallographic direction, where the [001] direction is out-of-plane. (b) Close up of the 3 different electrode orientations relative to the substrate crystallographic directions.

---

where a is the distance between electrodes and t is the film thickness. [194] CV-loops where recorded with triangular signal pulses with a base frequency of 0.1 Hz and small signal frequency of 1 kHz. The voltage amplitude corresponded to approximately 20 kV/cm and the small signal voltage was in the range 0.2-0.4 kV/cm. Several PV-loops were recorded before measuring the CV-loops, followed by another PV-loop. Only the last CV- and PV-loops are reported. For one film the voltage was increased stepwise up to a value corresponding to approximately 200 kV/cm, where a PV-loop and CV-loop was recorded for each step.

3.2.6 Scanning electron microscopy

Scanning electron microscopy (SEM) of thin films was performed using a field-emission FE-SEM Zeiss Ultra 55 LE microscope (Carl Zeiss AG, Oberkochen, Germany) with an in-lens detector. No coating was applied to the samples prior to imaging, but the samples were covered with aluminium foil or conducting carbon tape in the areas surrounding the imaged area to reduce charging. Microstructure was investigated by imaging the film surface, while for film thickness a cross-section of the film was imaged after fracturing the films.

3.2.7 Transmission electron microscopy

Transmission electron microscopy (TEM) was performed on crystalline 15-layer films prepared as described in Section 3.1.2. One cross-sectional TEM specimen was made from each film using a focused ion beam (Helios G4 UX, Thermo Fisher Scientific, Waltham, MA, USA). The chosen area was first coated with a carbon protection layer applied in two steps, first a thin layer using the electron beam, then a thicker layer using the ion beam. The lift-out and initial thinning of the

sample was done using the ion beam at 30 kV, while the final thinning steps were done at 5 kV and lastly at 2 kV to make the damage layer caused by the ion beam as thin as possible. All the TEM investigations were performed on a double-corrected cold FEG microscope (JEM ARM200F, JEOL Ltd., Tokyo, Japan) with an acceleration voltage of 200 kV. All the diffraction patterns were acquired using a selected area aperture with a diameter covering approximately 160 nm in real space. The HAADF-STEM images were acquired using a beam convergence angle of 27 mrad, and inner and outer collection angle of 119 mrad and 471 mrad, respectively.

Results

4 Barium titanate based films

Barium titanate based films were prepared and characterized by *in situ* tools developed in the FASTS project. The crystallization process and the mechanisms for the development of texture and epitaxy in $BaTiO_3$ thin films were investigated by *in situ* XRD. The effect of cation substitution and the influence of the substrate on the phase evolution and crystallization were also explored. The precursor decomposition and pyrolysis reactions were studied with *in situ* IR spectroscopy of thick films. Crystalline films of $BaTiO_3$ were also characterized *ex situ* by TEM, and the in-plane ferroelectric properties of the films were determined using interdigitated electrodes. Finally, the phonon modes of thin films on different substrates were modelled from near normal IR spectra.

4.1 *In situ* synchrotron X-ray diffraction of thin films

4.1.1 Single step annealing

$BaTiO_3$ thin films on (100) STO

The phase evolution and crystallization of a $BaTiO_3$ thin film on (100) STO are shown by the 2D contour plot in Figure 4.1. Before nucleation of $BaTiO_3$ at 570 °C an intermediate oxycarbonate phase was observed, seen from the diffuse diffraction line at 2ϑ=13.4° corresponding to the (012) diffraction line of the calcite type polymorph of $BaCO_3$ ($R\bar{3}mH$) [65,69,74] The intensity of the diffraction peak at 2ϑ=13.4° decreased at the onset of crystallization of $BaTiO_3$. The features at 2ϑ=10.3°, 15.6°, 29.4° and 37.5° in Figure 4.1 are caused by diffuse scattering from the STO substrate, which could not be masked. The apparent negative intensity at 2ϑ=23.0° and 36.1° are effects of gaps in the detector, which shift slightly in position from frame to frame.

Figure 4.2(a) shows a 1D diffractogram of the $BaTiO_3$ film after cooling to room temperature, along with the calculated diffractogram from Rietveld refinement. Cubic $BaTiO_3$ ($Pm\bar{3}m$, ICSD card #01-074-4539) was used in the refinement to find the lattice parameter. The calculated lattice parameter of $BaTiO_3$ at 710 °C was 4.0204(3) Å and at ambient temperature 3.9983(9) Å. Figure 4.2(b) shows a 2D diffractogram of the $BaTiO_3$ film, where the film texture is evident as there are

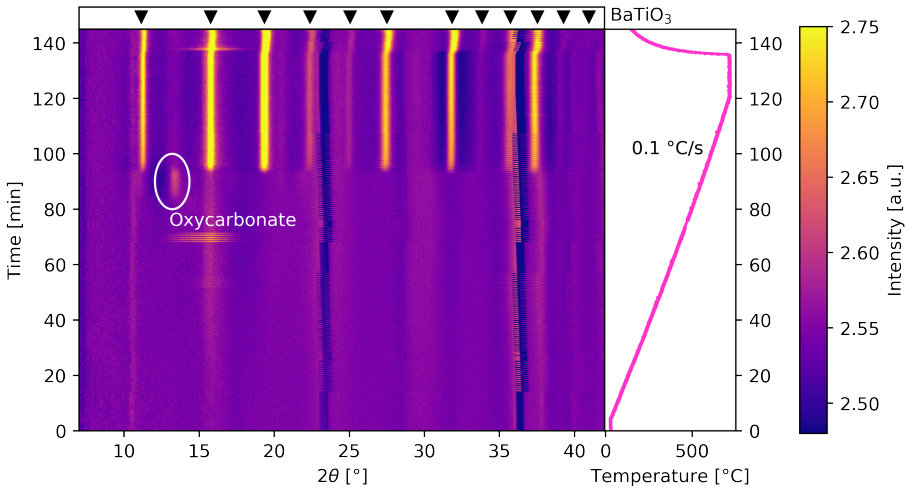

Figure 4.1: *In situ* diffractograms for a $BaTiO_3$ thin film on (100) STO as a function of time with the corresponding temperature profile. The intermediate oxycarbonate phase forming before the perovskite is indicated. Any features before the oxycarbonate are a result of the gaps in the detector, the data treatment or diffuse scattering from the substrate. The wavelength was 0.77624 Å.

district diffraction spots instead of full diffraction rings. The high degree of (100) preferred orientation is seen as the intense diffraction spot in the centre of the (100) ring with hardly any distribution of this reflection along the diffraction ring. The (311) and (310) reflections from STO are also visible in the 2D diffractogram. The films diffraction spots were equally positioned at slightly lower 2ϑ and with limited intensity distribution along the diffraction ring, further demonstrating the high degree of (100) preferred orientation. The SEM image of the film (Figure 4.2(c)) shows small spherical inter-necked grains approximately 50 nm in size, with an incomplete coverage of the STO substrate.

A summary of the crystallization behaviour as a function of heating rate for single step annealing of $BaTiO_3$ thin films on (100) STO is presented in Figure 4.3(a). For fast heating (> 3 °C/s) no texture was observed and the oxycarbonate phase and the $BaTiO_3$ perovskite nucleated simultaneously. For ultrafast heating (> 10 °C/s), $BaTiO_3$ nucleated directly without formation of any secondary or intermediate crystalline phases. These heating rates are in the range of what is commonly employed during RTP annealing of thin films. The maximum heating rate to obtain texture was $\sim$3 °C/s, inferred from the increasing degree of texture observed at lower heating rates. In the case of the textured films, the oxycarbonate phase nucleated first, followed by nucleation of $BaTiO_3$.

The oxycarbonate phase normally remained for some time after the initial nucleation of $BaTiO_3$. The nucleation temperatures for both phases generally increased with increasing heating rate, and the temperature range for the presence of oxycar-

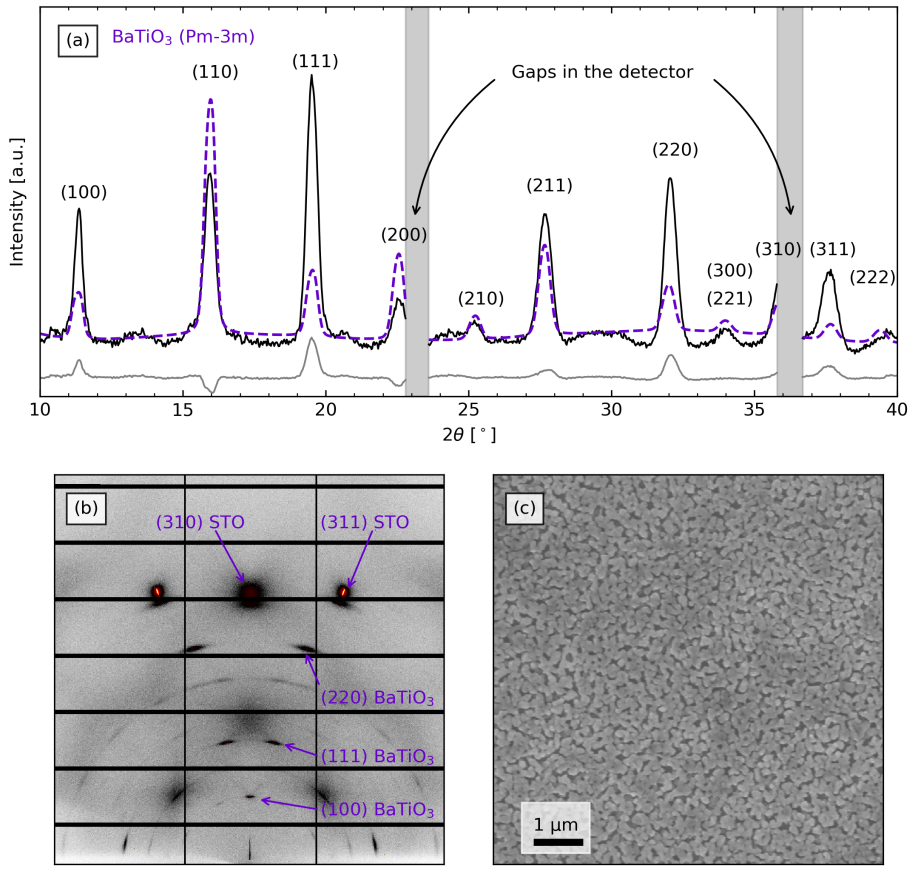

Figure 4.2: (a) Room temperature 1D diffractogram and Rietveld refinement of a $BaTiO_3$ thin film on (100) STO heated to 710 °C with a heating rate of 0.1 °C/s, (b) 2D diffractogram the same film showing the resulting film texture and (c) microstructure of the film.

bonate (marked by vertical lines) decreased with faster heating. For all the films with heating rates < 3 °C/s, the preferential orientation was the same as presented in Figure 4.2(b) for the film heated with 0.1 °C/s. For heating rates < 0.1 °C/s, the intensity of the diffraction spots increased compared to the diffractogram in Figure 4.2(b), and for heating rates > 0.1 °C/s the intensity of the spots decreased shifting towards the presence of complete rings due to the polycrystalline nature of the films.

The microstructure of $BaTiO_3$ thin films on (100) STO after single step annealing with different heating rates are shown in Figure 4.3(b-d). Even though there is a large difference in the heating rate used during annealing in Figure 4.3(b&c), 0.03 °C/s and 1.6 °C/s respectively, both films possessed a certain degree of crystallographic texture and the resulting microstructure was similar, consisting of small

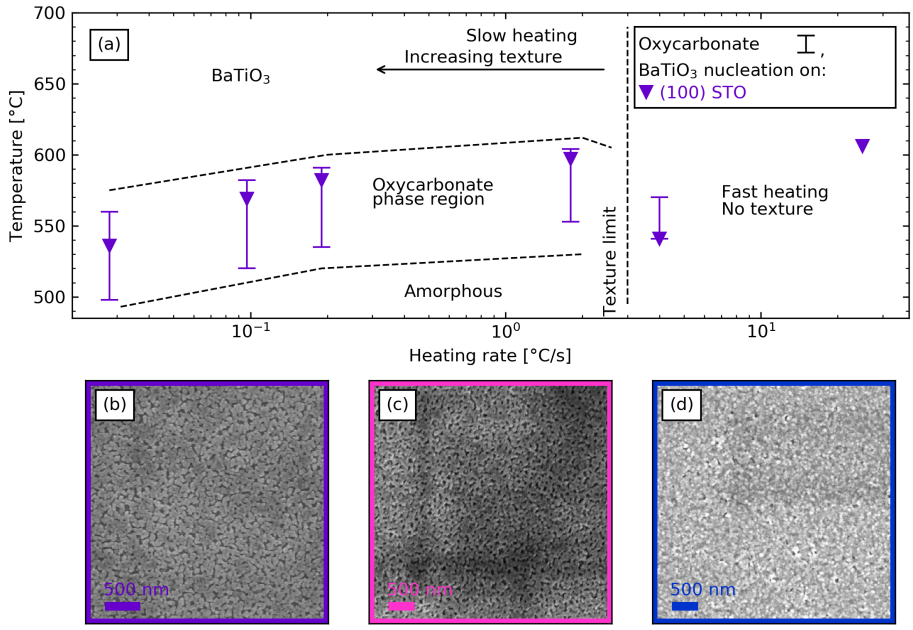

Figure 4.3: (a) Nucleation temperature for $BaTiO_3$ and temperature region for the presence of oxycarbonate (vertical lines) as a function of heating rate during single step annealing of thin films on (100) STO. Film microstructure (top view) of $BaTiO_3$ thin films on (100) STO after single step annealing with a heating rate of (b) 0.03 °C/s, (c) 1.6 °C/s and (d) 20 °C/s.

spherical grains approximately 50 nm in size. Necking was observed between the grains and the coverage was incomplete for a single layer. For the film heated with a heating rate of 20 °C/s, the microstructure consisted of even smaller grains of 15-20 nm. The coverage of the substrate was significantly higher, but some minor pinholes remained (Figure 4.3(d)). The single layered films were 25-35 nm thick after crystallization.

The azimuthal intensity distribution of the (100) diffraction express the degree of preferential orientation in the films. The normalized azimuthal intensities of the (100) reflections along the diffraction ring for the films from single step annealing on (100) STO are shown in Figure 4.4. The film heated with the highest heating rate of 20 °C/s was polycrystalline, and the intensity of the (100) diffraction ring was so low that when normalized it was not visible in the azimuthal map (Figure 4.4).The film heated with a heating rate of 1.6 °C/s had a certain degree of texture as well as full diffraction rings. The intensity of the centred (100) reflection increases as a lower heating rate was used along with the disappearance of the full diffraction rings, demonstrating clearly how the degree of preferential orientation increases as the heating rate decreases.

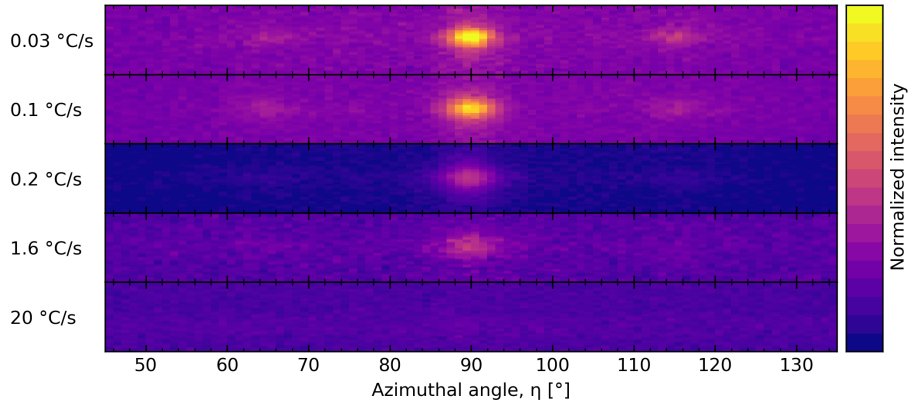

Figure 4.4: Normalized azimuthal intensity distribution for the (100) $BaTiO_3$ diffraction for the films on (100) STO from single step annealing showing the degree of (100) preferential orientation in the films as a function of heating rate.

$BaTiO_3$ thin films on various substrates

The crystallization behaviour of $BaTiO_3$ was relatively unaffected by the orientation of the STO substrate, as shown in Figure 4.5(a), where the nucleation temperature for both oxycarbonate and $BaTiO_3$ and the temperature range for the presence of the oxycarbonate were practically indistinguishable for all the films on STO. Both the films on (110) STO and (111) STO had the same degree of texture as the corresponding films on (100) STO, but the diffraction pattern reflects the different orientations, as shown in Figure 4.5(b&c). For the film on Pt/Si, the $BaTiO_3$ nucleation temperature was higher compared to the corresponding film on STO, and the oxycarbonate nucleation temperature and decomposition were unaffected by the heating rate, which contrasts with the strong heating rate dependence for both $BaTiO_3$ and oxycarbonate formation observed using STO. The diffraction pattern of the film on Pt/Si is shown in Figure 4.5(d), where all the diffraction spots, and the most intense rings derive from the substrate. A $BaTiO_3$ film on fused silica was also studied by *in situ* XRD for single step annealing with a heating rate of 0.2 ° C/s. $BaTiO_3$ nucleated above 588 °C on fused silica, which is ∼10 °C higher than the nucleation temperature for the corresponding film on STO. The strong diffuse scattering from the substrate dominate the angular range where the Bragg reflections due to the presence of the oxycarbonate phase are strongest (the diffraction pattern of this film is shown in Figure 4.5(e)), so it was not possible to determine if there was formation of any oxycarbonate phase.

Figure 4.5(f-i) shows the microstructure of the surface a single layer of $BaTiO_3$ films on different substrates. The microstructure of the films on (110) and (111) STO (Figure 4.5(f&g)) was the same type as found on (100) STO (Figure 4.2(c)), with internecked grains 40-60 nm in size. The microstructure of the $BaTiO_3$ film on Pt/Si (heating rate 2 °C/s) resembled the microstructure of the corresponding

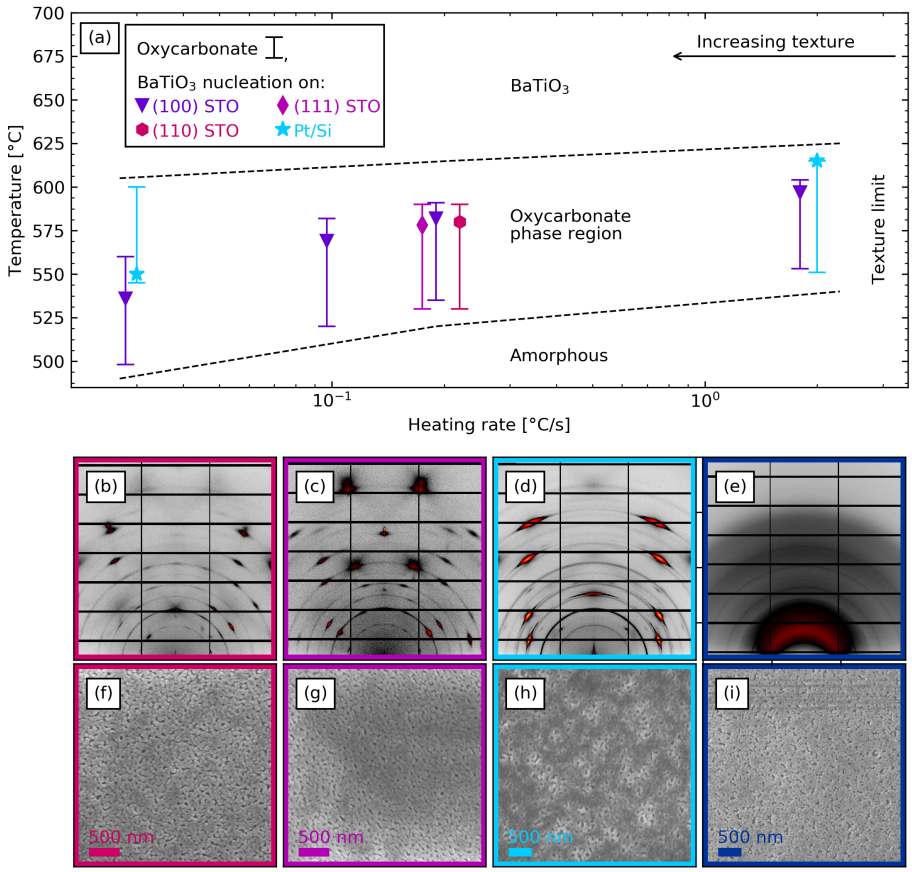

Figure 4.5: (a) Nucleation temperature for $BaTiO_3$ and temperature region for the presence of oxycarbonate (vertical lines) as a function of heating rate during single step annealing of thin films on STO and Pt/Si substrates. Diffraction pattern of a $BaTiO_3$ thin film after single step annealing on (b) (110) oriented STO heated with 0.2 °C/s, (c) (111) oriented STO heated with 0.2 °C/s, (d) Pt/Si substrate heated with 2 °C/s and (e) fused silica substrate heated with 0.2 °C/s, all films heated to ∼700 °C. Microstructure of the film surface for the same $BaTiO_3$ thin films on (f) (110) STO, (g) (111) STO, (h) Pt/Si and (i) fused silica taken at ambient temperatures.

---

film on STO (1.6 °C/s, Figure 4.3(c)), only the pinholes in the film were larger and the grains were 30-40 nm in size. The microstructure of a $BaTiO_3$ film on fused silica (heating rate 0.2 °C/s) is shown in Figure 4.5(i), which was similar to the microstructure of the corresponding films on STO, with necking between grains and incomplete coverage. The grains were in the range 30-50 nm, hence the heating rate was more important for the film microstructure than the type of substrate.

Cation substitution of $BaTiO_3$ thin films on (100) STO

The crystallization behaviour of BCT and BCZT thin films are compared to the pure $BaTiO_3$ thin films in Figure 4.6. Calcium substitution increased the nucleation temperature of the oxycarbonate and perovskite to some extent, and the temperature range for the presence of the oxycarbonate was somewhat reduced compared to $BaTiO_3$. Zirconium substitution increases the oxycarbonate nucleation temperature significantly compared to $BaTiO_3$, whereas the perovskite nucleation temperature was relatively unaffected. The texture of the BCT film was of the same type as shown in Figure 4.2(b) for the corresponding $BaTiO_3$ film, and the degree of (100) preferred orientation was similar. However, the BCZT film (0.2 °C/s) shown in Figure 4.6 was polycrystalline, which demonstrates the large influence of zirconium substitution on the crystallization behaviour, whereas it is relatively unaffected by calcium substitution. However, texture was possible in the BCZT films, as a BCZT film heated 0.03 °C/s had a high degree of preferred orientation (not included in Figure 4.6 due to loss of beam). The microstructure of both polycrystalline and textured $BaTiO_3$, BCT and BCZT thin films are shown in (Appendix A.4), where the microstructure was relatively unaffected by the cations substitution, which demonstrates that the microstructure is determined by the heating rate, in contrast to the nucleation temperature and degree of texture. However, the overall crystallization behaviour is similar for the $BaTiO_3$, BCT and BCZT thin films.

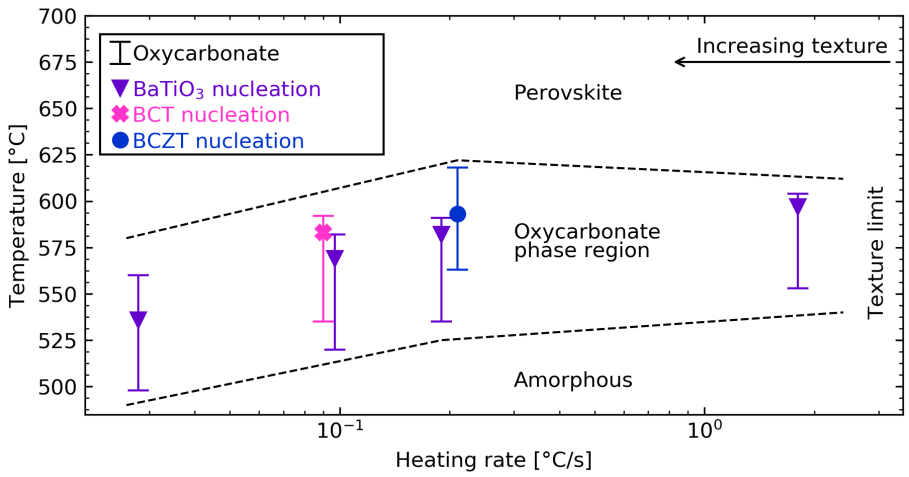

Figure 4.6: Perovskite nucleation temperature and temperature region for the presence of oxycarbonate (vertical lines) as a function of heating rate during single step annealing of $BaTiO_3$, BCT and BCZT thin films on (100) STO.

4.1.2 Multi-step annealing of $BaTiO_3$ thin films on (100) $SrTiO_3$

The temperature profiles of $BaTiO_3$ thin films on (100) STO investigated *in situ* during multi-step annealing are shown in Figure 4.7(a&b). Heating continuously with a fast heating rate (Film I in Figure 4.7(a)), resulted in direct nucleation of the perovskite at a relatively high temperature. The resulting film was polycrystalline, which can be seen from the diffractogram in Figure 4.7(c). The microstructure consists of small spherical grains with complete film coverage (Figure 4.7(d)). The nucleation behaviour changed by introducing an intermediate dwell period at a certain temperature. If the hold step was in the temperature range where nucleation of $BaTiO_3$ takes place (Film II in Figure 4.7(a)), the oxycarbonate formed before nucleation of $BaTiO_3$ and remained present until the temperature was increased due to the relative stability of the oxycarbonate in this temperature region. However, if the temperature during the hold step was significantly below the nucleation thresholds (Film III in Figure 4.7(a)), the oxycarbonate phase was not formed, and the perovskite nucleated directly in the second heating period with the fast heating rate used through the nucleation temperature region. Film III prepared by the temperature profile in Figure 4.7(a) has some degree of texture, which can be seen from the 2D diffractogram in Figure 4.7(c). The texture developed even though a much higher heating rate was used than the heating rate limit for texture observed for the single-step annealing ($\sim$3 °C/s). Hence, the time spent below the nucleation threshold temperature influences the degree of preferential orientation of the films. This is further illustrated by the films with a low heating rate before the hold step in Figure 4.7(b), where all the films were highly textured (Figure 4.7(c)), independent of the heating rate used during crystallization. Full coverage of the substrate and spherical grains of 15-20 nm are evident in the microstructure of the films with a high heating rate during nucleation (Film I, II, III and V in Figure 4.7(d)). For the films with low heating rate during nucleation (Film IV and VI), the surface coverage was incomplete, the grains were 45-60 nm and intergrown with some degree of necking, resembling the microstructure of the single step annealed film (Figure 4.2(c)). The films prepared by the multi-step annealing showed (100) preferred orientation, the same as for the single step annealed films.

4.1.3 Rietveld refinements

The temperature dependence of the cubic lattice parameter of $BaTiO_3$, determined by Rietveld refinements of the *in situ* XRD patterns of the thin films on (100) STO for both single and multi-step annealing, is shown in Figure 4.8. The data can be divided into two regimes. For the films with the lowest heating rates during nucleation (0.03 and 0.1 °C/s), $BaTiO_3$ nucleated with a lattice parameter slightly below the bulk value with no changes upon further heating. The films with a medium heating rate (0.2 °C/s and 1.6 °C/s) nucleated with a larger lattice parameter relative to bulk $BaTiO_3$, which decreased upon further heating converging towards a value below the bulk value in the same range as the films with lower heating rates. It should be noted that a direct comparison between the film and bulk lattice parameters is

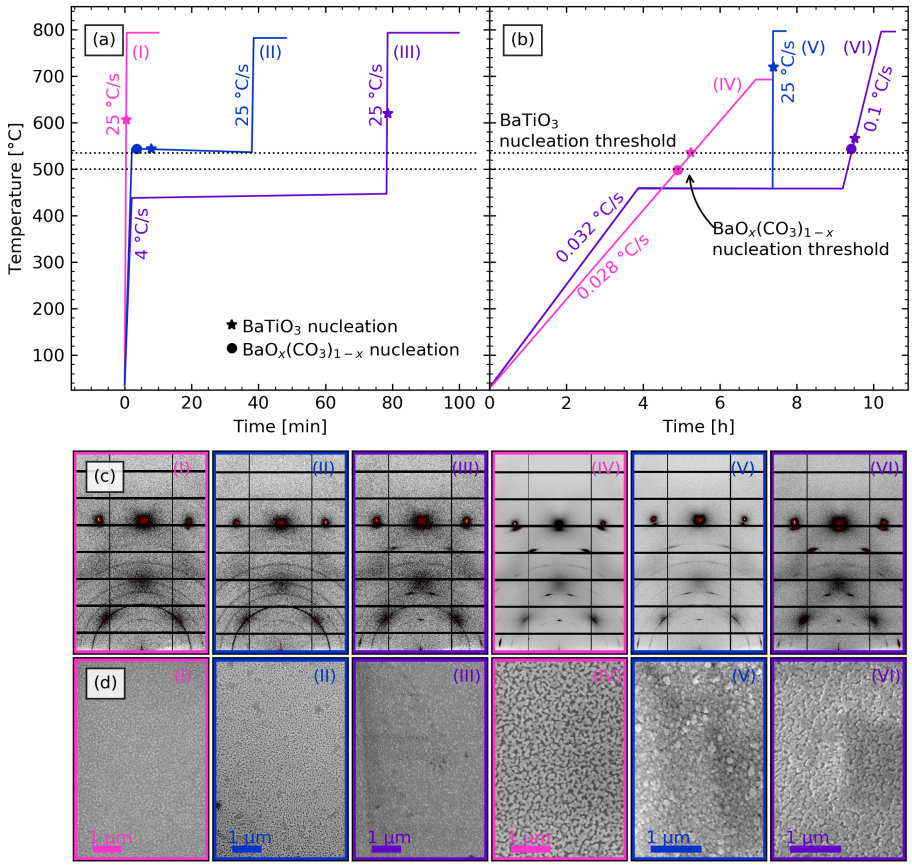

Figure 4.7: Multi-step annealing temperature profile and nucleation temperatures of$BaTiO_3$ and oxycarbonate for (a) thin films with a short annealing time below the nucleation thresholds and (b) long annealing time below the nucleation thresholds. (c) High temperature diffractograms of the films with multi-step annealing at ∼800 ° C and (d) microstructure of the films after cooling.

not straight forward due to both finite size effects and strain in the films. Moreover, texture is present in all the films included in Figure 4.8 and the microstructure was the same type as presented in Figure 4.2(c) for the film with a heating rate of 0.1 ° C/s, with necking between grains, incomplete coverage and grains in the range 40-60 nm.

The lattice parameters from the Rietveld refinements and texture evaluated from the 2D diffractograms of the $BaTiO_3$-based thin films on various substrates are summarized in Table 4.1. The texture evident from the 2D diffractograms was the same for all films on (100) STO, shown in Figure 4.2(b) for the single-step annealed film with a heating rate of 0.1 °C/s. The intensity of the (100) diffraction spots on

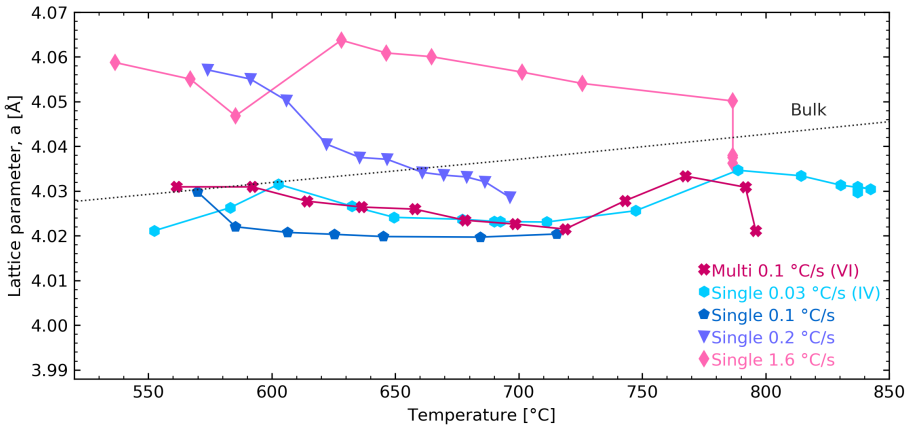

Figure 4.8: Lattice parameters from Rietveld refinements as a function of temperature during both single step and multi-step annealing of $BaTiO_3$ thin films on (100) STO. Bulk values for the lattice parameter of $BaTiO_3$ based on thermal expansion data from Taylor [46] are included as the stippled line.

the 2D diffraction rings decreased for faster heating rates, demonstrating reduced texture with increased heating rate in accordance with the azimuthal distribution plot in Figure 4.4. The lattice parameter of the films on (100) STO were in general smaller for films with high degree of preferential orientation, demonstrating that the texture influences the lattice parameter of the film. The lattice parameters of the films on (110) and (111) STO were comparable to the lattice parameters of the films on (100) STO (Table 4.1), but the preferential orientation adheres to the substrate orientation. The films on Pt/Si had significantly lower lattice parameters than the films on STO (Table 4.1), which can be explained by a different strain in these films. Both films on Pt/Si were polycrystalline with full diffraction rings, but for the film with a heating rate of 0.03 °C/s there were $BaTiO_3$ diffraction spots on the diffraction rings, showing that there is a certain degree of preferred orientation also for $BaTiO_3$ films on Pt/Si.

The room temperature lattice parameters of $BaTiO_3$ on (100) STO, MgO and LAO were all in the same range. Both difference in thermal expansion coefficient and lattice mismatch (Table 3.4) contribute to the strain in the films affecting the observed lattice parameters. It is noteworthy that the lattice parameters found for fused silica and LAO are the same, as fused silica will not impose strain from lattice mismatch, but solely from difference in the thermal expansion coefficient. The lattice parameters of the BCT and BCZT films were also in the same range, although slightly larger than for $BaTiO_3$, which is in contrast with the bulk values listed in Table 2.2.

Table 4.1: Summary of the results from Rietveld refinements of $BaTiO_3$-based thin films on various types of substrates, prepared using different heating profiles.

Heating profile	**Heating rate [°C/s]**	**Substrate**	**Lattice parameter [Å]**	**Texture**
Multi-step(VI)	0.1	(100) STO	4.0211(8) (792 °C)	Strong (100)
Multi-step (III)	20	(100) STO	4.0453(3) (794 °C)	Weak (100)
Multi-step (II)	20	(100) STO	4.0467(6) (782 °C)	No texture
Multi-step (V)	20	(100) STO	4.0491(1) (797 °C)	Weak (100)
Single-step (IV)	0.03	(100) STO	4.0298(6) (842 °C)	Strong (100)
Single-step	0.1	(100) STO	4.0204(3) (710 °C) 3.9983(9) (RT)	Strong (100)
Single-step	0.2	(100) STO	4.0256(6) (697 °C)	Strong (100)
Single-step	1.6	(100) STO	4.0375(4) (787 °C)	Weak (100)
Single-step (I)	20	(100) STO	4.0502(1) (793 °C)	No texture
Single-step	0.2	(110) STO	4.0276(9) (698 °C)	Strong (110)
Single-step	0.2	(111) STO	4.0235(2) (702 °C)	Strong (111)
Single-step	2	Pt/Si	3.9832(4) (711 °C)	No texture
Single-step	0.03	Pt/Si	3.9775(8) (695 °C)	Textured
Single-step	0.2	Fused Silica	4.0194(2) (RT)	No texture
Single-step	0.2	(100) MgO	4.0097(7) (RT)	Strong (100)
Single-step	0.2	(100) LAO	4.0191(1) (RT)	Strong (100)
BCT (Single)	0.1	(100) STO	4.0062(3) (RT)	Strong (100)
BCZT (Single)	0.2	(100) STO	4.0001(5) (RT)	No texture
BCZT (Single)	0.03	(100) STO	4.0054(6) (RT	Strong (100)

4.1.4 Annealing of a $BaTiO_3$ thin film in CO_2 rich atmosphere

The stability of carbonates is generally sensitive towards the partial pressure of CO_2 in the atmosphere (Section 2.3.3). The oxycarbonate observed during the decomposition of the $BaTiO_3$ thin films was also stabilized by a high CO_2 partial pressure in the surrounding atmosphere. The 2D contour plot in Figure 4.9 shows how oxycarbonate in 40 % CO_2 atmosphere was formed at the same temperature as for annealing in air. The oxycarbonate phase remained stable up to at least 630 °C in 40 % CO_2 significantly higher than the nucleation temperature of $BaTiO_3$ in air (for intermediate heating rates) where the oxycarbonate usually decomposes below 600 °C (Figure 4.3). In ambient atmosphere, only the diffraction line at 2ϑ=13.4° was visible from the oxycarbonate phase (Figure 4.1), but in CO_2 rich atmosphere several strong diffraction lines from the oxycarbonate were observed (Figure 4.9). This demonstrate that the weak reflections from the oxycarbonate phase observed in air reflects the metastable nature and poor crystallinity of this phase. However, the quality of the diffractograms in a CO_2 rich atmosphere were not sufficient to do refinements on the structure of the oxycarbonate phase.

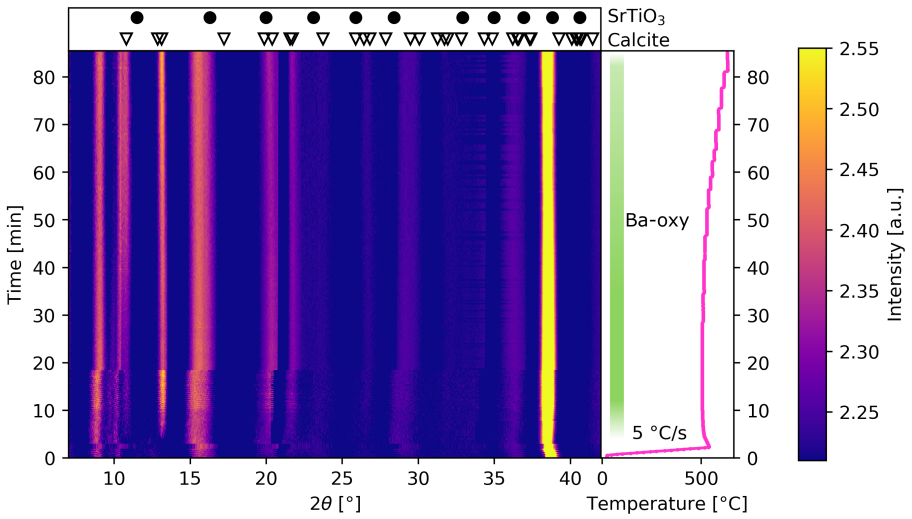

Figure 4.9: 2D contour plot of the *in situ* diffractograms of a $BaTiO_3$ precursor thin film on (100) STO as a function of time in a 40 % CO_2 atmosphere. The corresponding temperature profile is given to the right. $BaCO_3$ (calcite) and STO substrate diffraction lines are marked on the top. Apparent negative peaks, or peaks not indexed are a result of the data treatment and diffuse scattering from the substrate. The wavelength was 0.78242 Å.

4.2 Crystallographic texture

4.2.1 Preferential orientation of $BaTiO_3$ films on various substrates

(100) oriented STO

The degree of preferential orientation of $BaTiO_3$ thin films on (100) STO increased with decreasing heating rate as shown in Figure 4.3. The diffractogram of a highly textured $BaTiO_3$ thin film on (100) STO was displayed in Figure 4.2(b). Figure 4.10(a&b) shows the experimental and calculated diffractograms when a texture component was included in the Rietveld refinements and the substrate reflections had been masked. However, the model underestimates the (100) centred diffraction spot. A cubic symmetry is concluded from the pole figures calculated from the orientation distribution functions (ODF) from the texture refinement, see Figure 4.10(c). Distortions in the pole figures relative to the theoretical pole figures could be due to tetragonality, experimental errors or a slight misalignment of the film relative to the beam.

To further study the crystallographic texture of $BaTiO_3$ on (100) STO, a series of diffractograms were recorded and the diffraction from a $BaTiO_3$ thin film on (100) STO (Film VI in Figure 4.7(b)) is presented in two perpendicular angular directions, tilt (ω) and azimuthal (η) in Figure 4.11. The tilt series (Figure 4.11(a)) demonstrates that the $BaTiO_3$ reflections had a spatial extension in this angular direction as the $BaTiO_3$ diffraction signature were horizontal lines, while the substrate reflections were distinct spots. In the azimuthal direction (Figure 4.11(b)) both the $BaTiO_3$ and substrate reflections are distinct diffraction spots. Although there are a series of spots in the azimuthal direction for the $BaTiO_3$ film, it is far from single crystalline like the substrate, where only a few reflections are captured by the detector for this measurement configuration. The cubic lattice parameter of $BaTiO_3$ calculated from the (310) and (311) Bragg reflections were 4.0005±0.0025 Å and 4.0068±0.0025 Å, respectively.

(110) and (111) oriented STO

The experimental and calculated diffraction patterns of BaTiO3 thin films on (110) and (111) STO are shown in Figures 4.12(a&b) and 4.13(a&b) respectively, where the calculated patterns are from Rietveld refinements with texture components. Pole figures calculated from the texture refinement are presented in Figures 4.12(c) and 4.13(c) for the films on (110) and (111) STO, respectively. Both the diffraction patterns and pole figures reflect the change in orientation of the STO substrate, meaning that the film texture adhere to the substrate orientation. Distortions in the pole figures relative to the theoretical pole figures are could be due to tetragonality, experimental errors or a slight misalignment of the film relative to the beam.

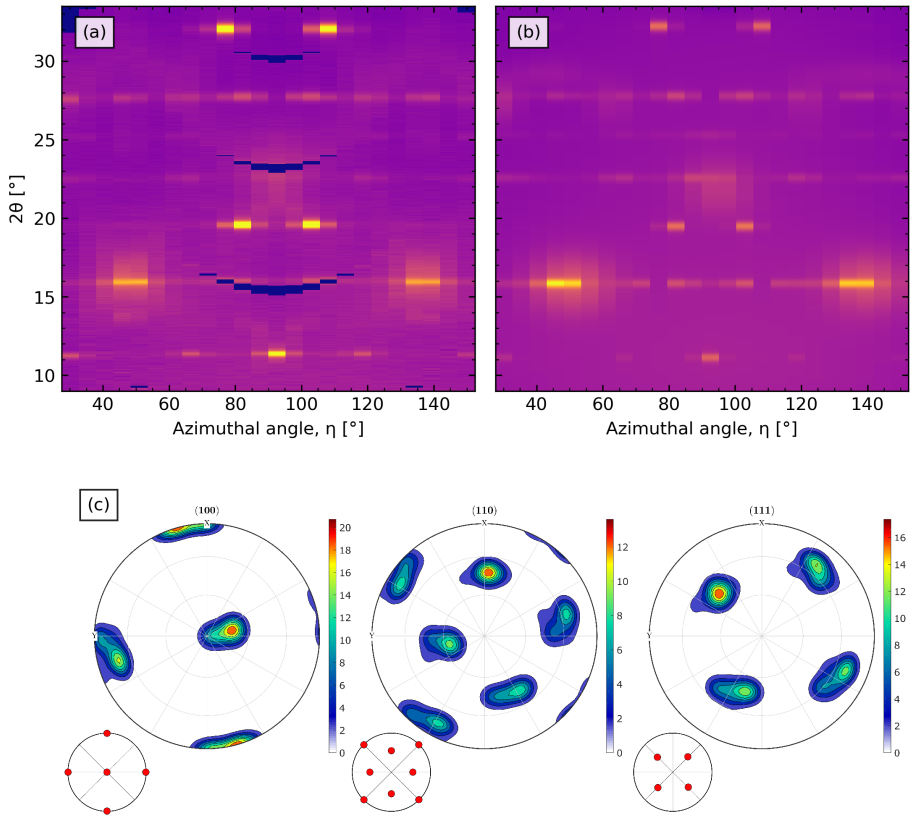

Figure 4.10: The (a) experimental and (b) calculated 2D diffractograms from a Rietveld refinement with an E-WIMV texture component for a single-layer crystalline $BaTiO_3$ thin film on (100) STO after single step annealing with 0.1 °C/s to 710 °C. (c) Pole figures calculated from ODFs from the Rietveld refinement of the same film with the illustration of the theoretical pole figures for the different orientations. The wavelength was 0.77624 Å.

(100) oriented MgO and LAO

The $BaTiO_3$ film texture on (100) MgO and LAO were found to be cubic, with similar diffraction patterns and pole figures as for $BaTiO_3$ on (100) STO, showing that the film texture adheres to the substrate orientation even on different crystal lattices. The experimental and calculated diffraction patterns of $BaTiO_3$ thin films MgO and LAO with the calculated pole figures can be found in in Appendix A.1.2 (Figure A.8 and A.9).

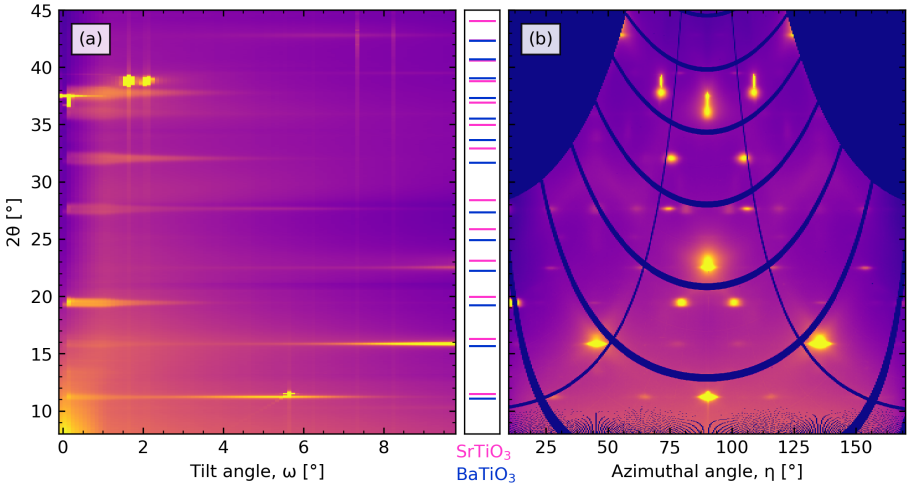

Figure 4.11: Diffraction from a single-layer highly textured $BaTiO_3$ thin film on (100) STO (Film VI) is presented in two perpendicular angular directions; (a) tilt (ω) and (b) azimuthal (η). The wavelength was 0.78242 Å.

4.2.2 Preferential orientation of cations substituted $BaTiO_3$ films on (100) STO

Cation substitution with calcium and zirconium did not alter the film texture relative to the $BaTiO_3$ film on (100) STO (Figure 4.10) and cubic symmetry was observed for both the BCT and BCZT films. The experimental and calculated diffraction patterns with the calculated pole figures for the BCT and BCZT thin films on (100) STO are displayed in Appendix A.1.2 (Figure A.10 and A.11). The pole figures of the textured BCT film had split intensity spots which arise because the film axes are rotated relative to the reference system or caused by tetragonality. However, from the diffractogram there is no sign of such axes rotation or tetragonal splitting. Zr-substitution influences both the thermodynamics and kinetics of the crystallization behaviour of BCZT compared to $BaTiO_3$ and BCT, as a lower heating rate and higher temperature is necessary to achieve textured BCZT films. However the mechanisms for the texture formation were the same, independent of substitution. The experimental diffraction pattern of BCZT (Figure A.11(a)) shows that there was also a textured oxycarbonate phase present, which was not captured by the model used in the refinement.

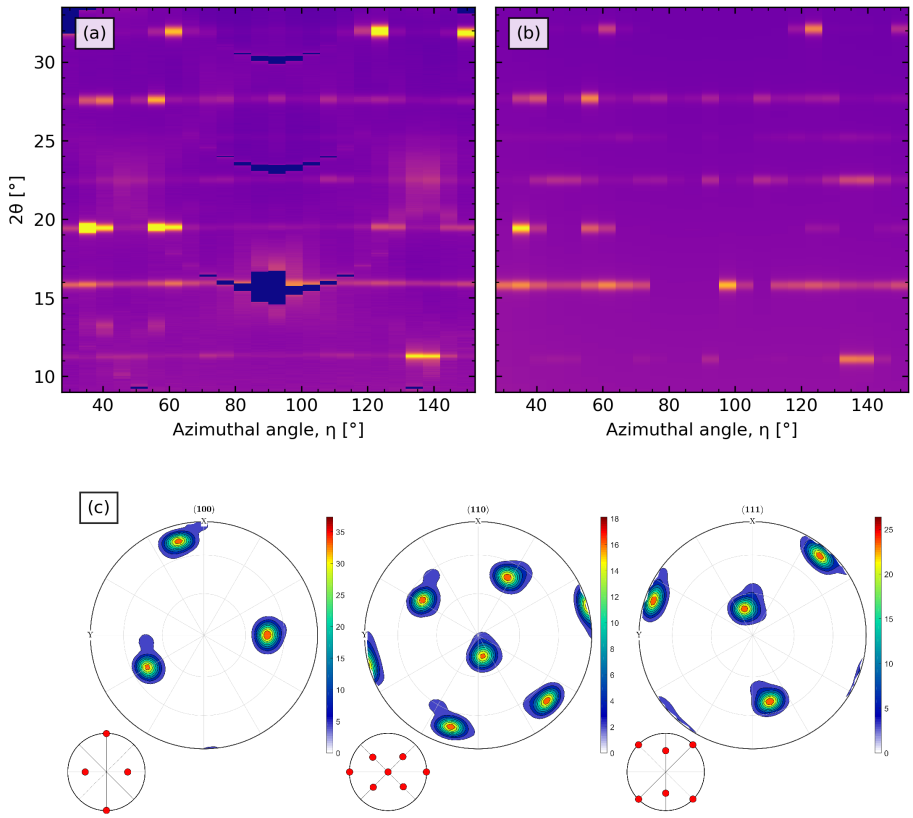

Figure 4.12: The (a) experimental and (b) calculated 2D diffractograms from a Rietveld refinement with an E-WIMV texture component for a single-layer crystalline $BaTiO_3$ thin film on (110) STO after single step heating with 0.2 °C/s to 698 °C. (c) Pole figures calculated from ODFs from the Rietveld refinement of the same film with the illustration of the theoretical pole figures for the different orientations. The wavelength was 0.77624 Å.

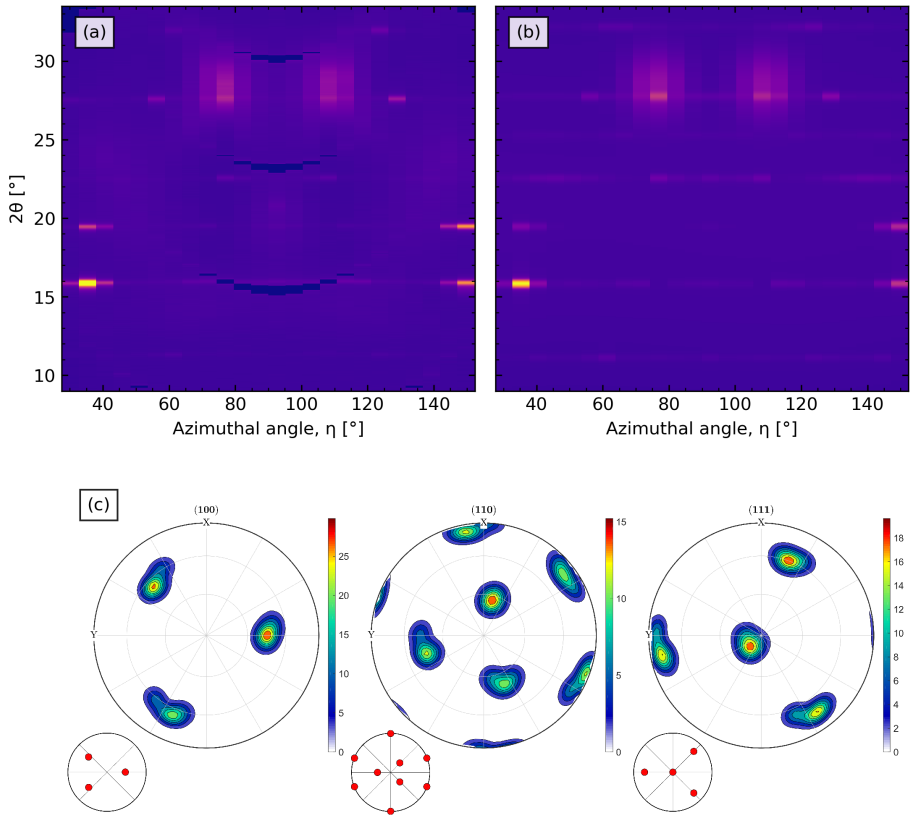

Figure 4.13: The (a) experimental and (b) calculated 2D diffractograms from a Rietveld refinement with a E-WIMV texture component for a single-layer crystalline $BaTiO_3$ thin film on (111) STO after single step heating with 0.2 °C/s to 702 °C. (c) Pole figures calculated from ODFs from the Rietveld refinement of the same film with the illustration of the theoretical pole figures for the different orientations. The wavelength was 0.77624 Å.

4.3 Epitaxy

The preparation of epitaxial $BaTiO_3$ thin films were demonstrated by Ræder *et al.* [127], but the mechanism for achieving epitaxy was not fully investigated. Preparation of thin films with a high degree of preferential orientation was reported in Sections 4.1-4.2, but none of these films were epitaxial. Therefore three films were heated *in situ* to the maximum temperature of the heating setup ($\sim$ 1000 °C) with different heating programs, shown in Figure 4.14(a), while Figure 4.14(b-d) display the resulting microstructure of the films.

The phase evolution of Film VII is shown in Figure 4.15. The fast heating at low temperatures resulted in direct nucleation of polycrystalline $BaTiO_3$, but quickly most of the $BaTiO_3$ Bragg reflections vanished as the film evolved into an epitaxial film during the annealing at the maximum temperature. The epitaxy can be seen from the appearance of a strong reflection at 36.7°, right next to the (311) STO reflection. The microstructure of this film (Figure 4.14(b)) appears as a continuous layer seemingly without grain boundaries, but with pinholes with faceted edges.

The epitaxy of Film VII is further illustrated by considering the reflections in two perpendicular angular directions (Figure 4.16). In the tilt direction (Figure 4.16(a)) only a few of the substrate and film reflections are seen, demonstrating the film epitaxy. The film reflections are wider than the substrate reflections, showing

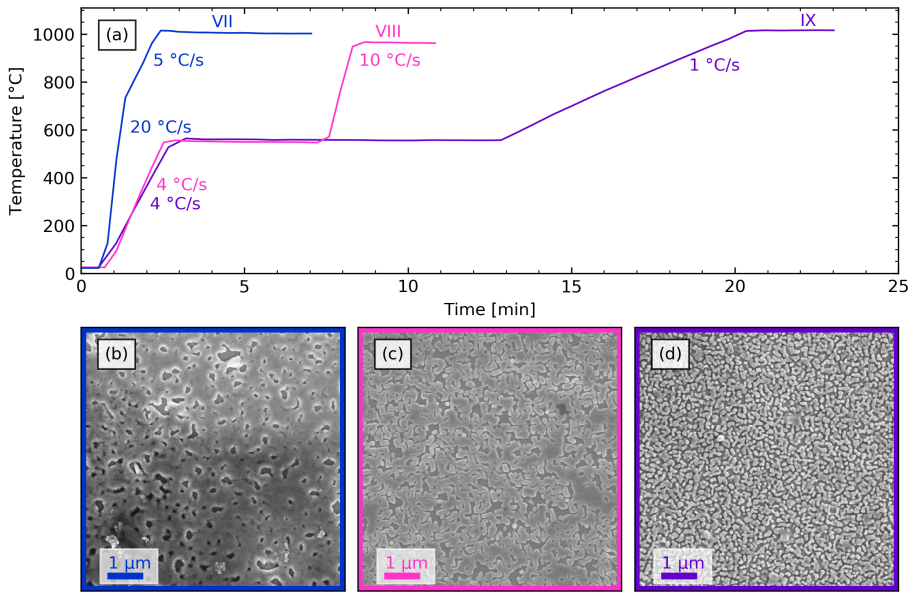

Figure 4.14: (a) Temperature profiles for $BaTiO_3$ thin films on (100) STO heated *in situ* to investigate conditions for epitaxy. Microstructure (top view) of (b) Film VII, (c) Film VIII and (d) Film IX.

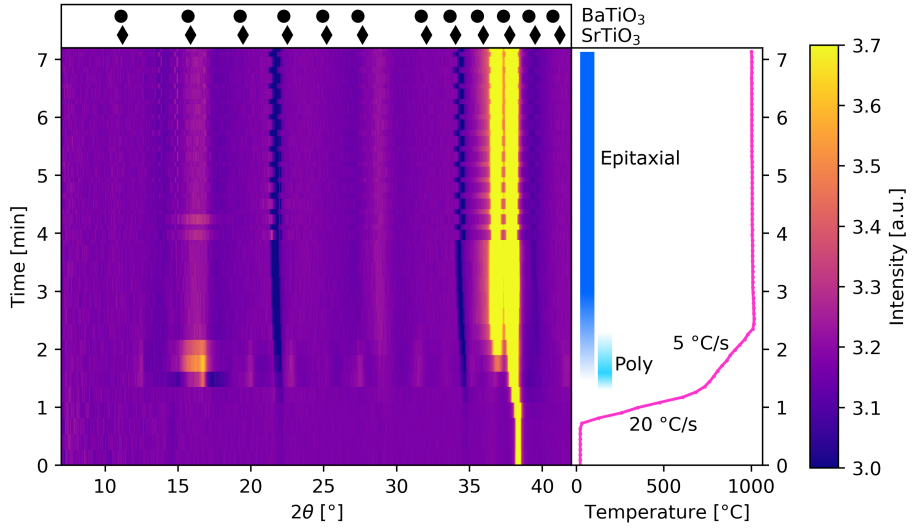

Figure 4.15: 2D contour plot of the *in situ* diffractograms for a $BaTiO_3$ thin film (VII) on (100) STO as a function of time. The corresponding temperature profile with the film development is illustrated to the right. The apparent negative peaks are due to gaps in the detector. The wavelength was 0.78242 Å.

---

that the film is not perfectly single crystalline as the substrate. In the azimuthal direction, it is harder to distinguish between the film and substrate reflections, but the epitaxy is clear from the distinct (100) reflection at azimuthal angles of 90° and 2ϑ=11.1°. The cubic lattice parameters calculated from the (310) and (311) reflections were 3.9522±0.0025 Å and 4.0171±0.0025 Å, respectively.

Cross sections of the (310) and (311) reflections of Film VII and the (100) STO substrate are shown in Figure 4.17 at various tilt angles. The Bragg reflections (vertical lines in the centre) are surrounded by a cylindrical reflection object. This type of reflection object was observed for both the epitaxial films investigated *in situ*. The additional reflections correspond to a periodicity of 16.8 and 17.1 nm calculated from the (311) reflection (left and right reflection, respectively), arising from some type of periodic feature in the films.

Another film (VIII) was heated with a lower heating rate to form oxycarbonate and see how that effected the formation of epitaxy. The phase evolution of Film VIII is shown in Figure 4.18. Oxycarbonate formed before nucleation of polycrystalline $BaTiO_3$ as the temperature was increased. The polycrystalline $BaTiO_3$ started to transform to an epitaxial layer, but due to the slightly lower maximum temperature (∼965 °C), the transformation was incomplete and reflections from polycrystalline $BaTiO_3$ can still be seen after holding at this temperature, although the intensity of these reflections was low. The microstructure of Film VIII (Figure 4.14(c)) shows the film was continuous, but with holes, similar to Film VII.

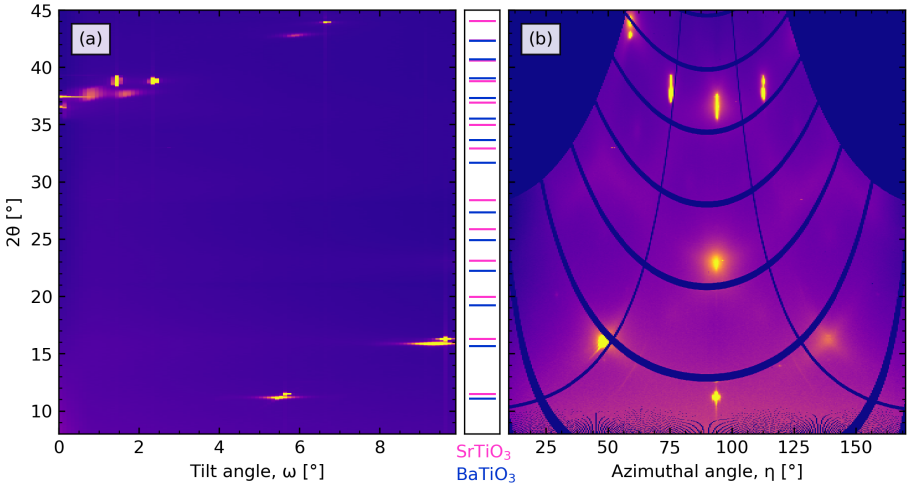

Figure 4.16: The reflections of a epitaxial $BaTiO_3$ thin film (VII) on (100) STO is presented in two perpendicular angular directions; (a) tilt (ω) and (b) azimuthal (η). The wavelength was 0.78242 Å.

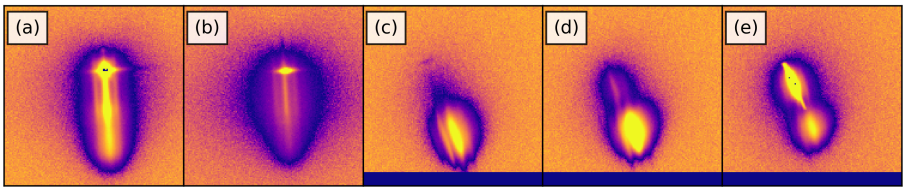

Figure 4.17: Cross sections of the (310) and (311) reflections for an epitaxial $BaTiO_3$ thin film (Film VII) on (100) STO. (a) (311) reflection at ω=0.25°, (b) (311) reflection at ω=0.75°, (c) (310) reflection at ω=1.25°, (d) (310) reflection at ω=1.75°and (e) (310) reflection at ω=2.25°.

The diffraction reflection of Film VIII in two perpendicular angular directions is displayed in Figure 4.19. In the tilt direction the reflections of the film and the substrate were almost non-distinguishable, demonstrating the epitaxy of the film, but there were also some weak horizontal lines since this film also contained polycrystalline $BaTiO_3$. The azimuthal direction also shows that the film was mostly epitaxial. The diffraction rings of the polycrystalline $BaTiO_3$ cannot be seen in the azimuthal plot (Figure 4.19(b)) due to the intensity difference. The low 2ϑ reflections, such as the (100) reflection, seen in Figure 4.16 for Film VII, were not observed for Film VIII (Figure 4.19) because of the lower angular range for the tilt series. Hence, only the diffuse scattering of the low 2ϑ reflections can be observed in Figure 4.19(b).

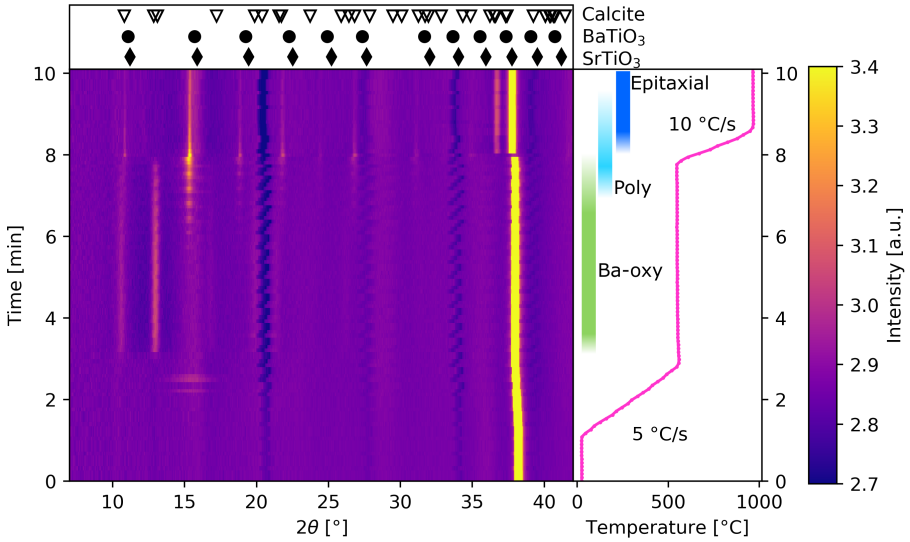

Figure 4.18: 2D contour plot of the *in situ* diffractograms for a $BaTiO_3$ thin film (VIII) on (100) STO as a function of time. The corresponding temperature profile with the film development is illustrated to the right. The apparent negative peaks are due to gaps in the detector. The wavelength was 0.78242 Å

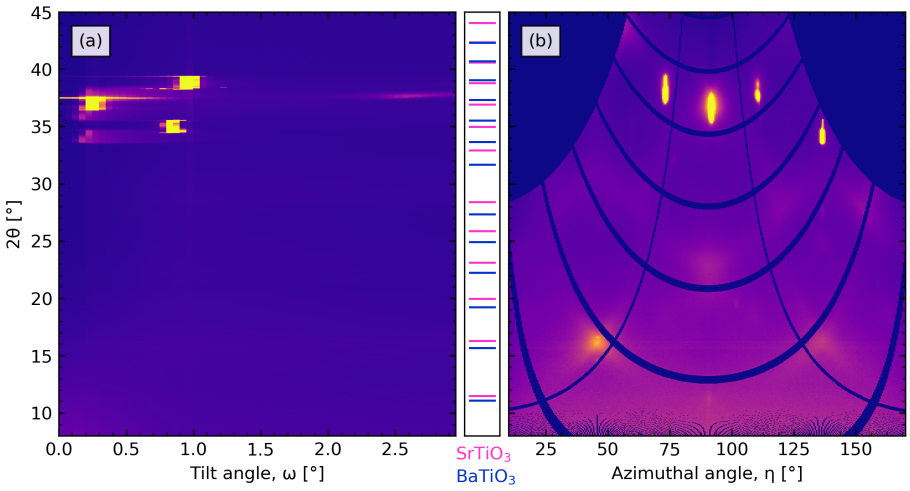

Figure 4.19: The reflections of a epitaxial $BaTiO_3$ thin film (VIII) on (100) STO is presented in two perpendicular angular directions; (a) tilt (ω) and (b) azimuthal (η). The wavelength was 0.78242 Å.

The phase evolution of Film IX prepared to study the effect of the heating rate during crystallization with respect to the formation of epitaxial films is shown in Figure 4.20. Oxycarbonate formed during the hold period at 560 °C, followed by formation of polycrystalline $BaTiO_3$. A lower heating rate was used compared to Films VII and VIII and the polycrystalline $BaTiO_3$ film did not transform to an epitaxial film, again demonstrating that the kinetics plays a key role in the formation of epitaxial thin films from CSD. The microstructure of Film IX (Figure 4.14(d)) was polycrystalline, consisting of ∼50 nm grains distributed on the substrate.

The microstructure of 6-layered $BaTiO_3$ thin films on different orientations of STO substrates heated with the epitaxial heating program (Figure 3.1) are shown in Figure 4.21. The films were ∼60 nm thick and different surface morphologies arise for the different substrate orientations. On (100) STO (Figure 4.21(a)), the film was a continuous layer with pinholes that had faceted edges. Deposition on (110) oriented STO (Figure 4.21(b)), resulted in a film where the termination of lattice planes can be seen as lines going across the film. Pinholes with sharp edges showing the facets were also present in the films, but these were smaller compared to the (100) film. On (111) STO (Figure 4.21(c)), the film growth mechanism was clearly by island growth as the film was covered by small circular heights. The microstructure of the BCT film (Figure 4.21(d)) was the same as for $BaTiO_3$, demonstrating again that the Ca-substitution does not change the crystallization behaviour. However, the Zr-substitution as previously observed, does influence the crystallization, resulting in a rougher appearance of the BCZT thin film (Figure 4.21(e)). As the nucleation temperature for BCZT was shown to be higher than for $BaTiO_3$, the kinetics for the texture development was also slower for BCZT. Given how important both the annealing temperature and the heating rate are in order to achieve epitaxy, the rough microstructure observed for the BCZT film can be rationalized by a too low temperature and heating rate to obtain a completely epitaxial film.

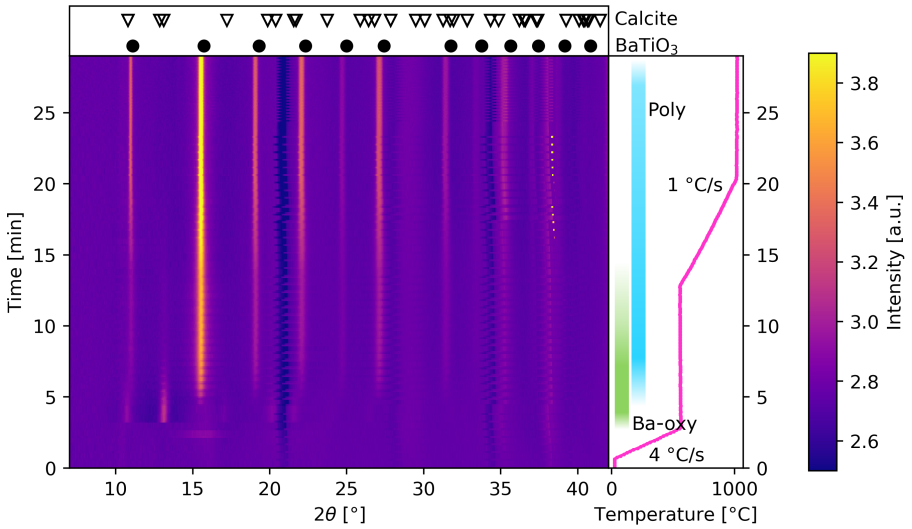

Figure 4.20: 2D contour plot of the *in situ* diffractograms for a $BaTiO_3$ thin film (IX) on (100) STO as a function of time. The corresponding temperature profile with the film development is illustrated to the right. The apparent negative peaks are due to gaps in the detector. The wavelength was 0.78242 Å

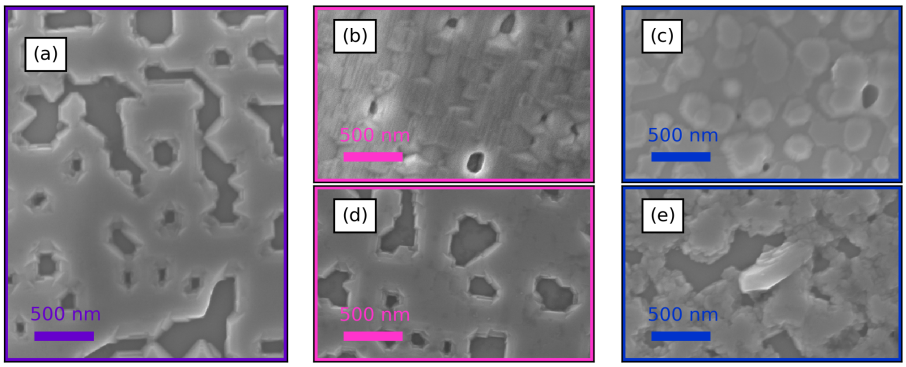

Figure 4.21: Microstructure of ∼ 60 nm thin films heated with the epitaxial heating program, $BaTiO_3$ films on (a) (100) STO, (b) (110) STO, (c) (111) STO and (d) BCT film and (e) BCZT film on (100) STO

4.4 *In situ* infrared spectroscopy during decomposition of thick films

4.4.1 $BaTiO_3$ thick films

BT-1: Medium heating rate with hold step for oxycarbonate formation

Figure 4.22 shows the *in situ* IR spectra of a $BaTiO_3$ precursor thick film during annealing with a medium heating rate of 0.5 °C/s and a hold step at 520 °C to obtain formation of oxycarbonate. Below 500 °C the film was amorphous and displayed the same type of organic functional groups as the powders (Figure 5.5). Absorption bands from $Ba(NO_3)_2$ (asymmetric stretching mode ∼1400 cm^{-1}), symmetric (1240-1450 cm^{-1}) and asymmetric (1590-1750 cm^{-1}) stretching modes for the carboxylic acid groups from both EDTA, citric acid, and their derivatives and C-N stretching mode (1020-1250 $^{-1}$) from the EDTA derivatives can all be identified at low temperatures. [71, 195, 196] Carbonate bands belonging to the oxycarbonate phase were evident in the IR spectra between 500 and 600 °C. Above 600 °C, only a broad feature was observed at low wavenumbers. However, the IR spectrum taken of the same thick film after cooling, and without the dome (RT after), showed the characteristic perovskite signature, confirming that $BaTiO_3$ was formed during heating. The bands in the range 2100-2500 cm^{-1} are assigned to dissolved CO_2 and NO_2 gas forming during the decomposition [197], which due to the dome remains in the film, as these bands were not seen in the powders (Section 5.2.2). The IR spectra in the temperature region for the presence of the oxycarbonate phase are shown in detail in Figure 4.23. A shift in the carbonate frequencies was observed for both the out-of-plane (oop) band and asymmetrical stretching (as) band with increasing temperature from that of the aragonite-type $BaCO_3$ (861 and 1430 cm^{-1}) to that of the calcite-type $BaCO_3$ (871 and 1402 cm^{-1}). [71] Broad bands developed at the start of the hold period which became sharper with prolonged annealing and the frequencies shifted towards the calcite value. The wide as-band was also accompanied by a shoulder at 1580 cm^{-1} for most of the films and an additional shoulder at 1280 cm^{-1} were also observed in some cases. It is proposed that the shoulders correspond to $RCOO^-$ symmetric (∼1280 cm^{-1}) and asymmetric (∼1580 cm^{-1}) stretching bands, which were also present in the precursor film and remained to such high temperature before completely decomposing. The bands could also be assigned to a splitting of the asymmetric stretching band of the $CO_3{}^{2-}$-ion bonded to Ti^{4+}. The shoulder seen in Figure 4.23 emerged at the same time as the carbonate band developed and disappeared as the oxycarbonate decomposed, indicating that the presence of this carbon containing compound is related to the oxycarbonate phase.

BT-2: Heating without the dome and no vacuum

To better compare how the perovskite absorption band develops compared to the carbonate band, a $BaTiO_3$ precursor thick film (BT-2) was heated without the dome with a medium heating rate of 0.5 °C/s. The *in situ* IR spectra of sample BT-2 in

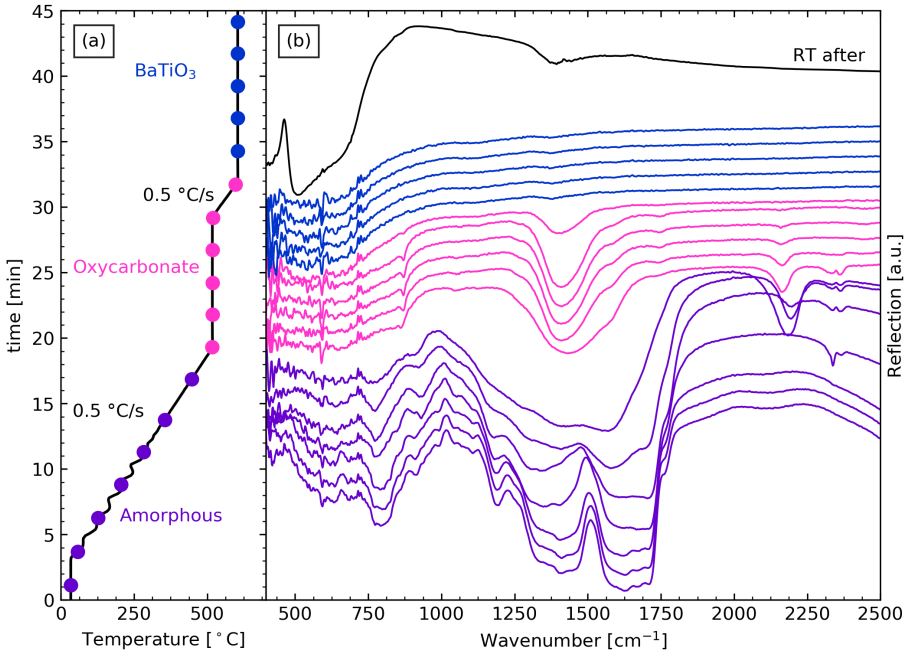

Figure 4.22: (a) Temperature profile and (b) *in situ* IR spectra during annealing of a $BaTiO_3$ precursor film (BT-1) with a medium heating rate and a hold step for oxycarbonate formation.

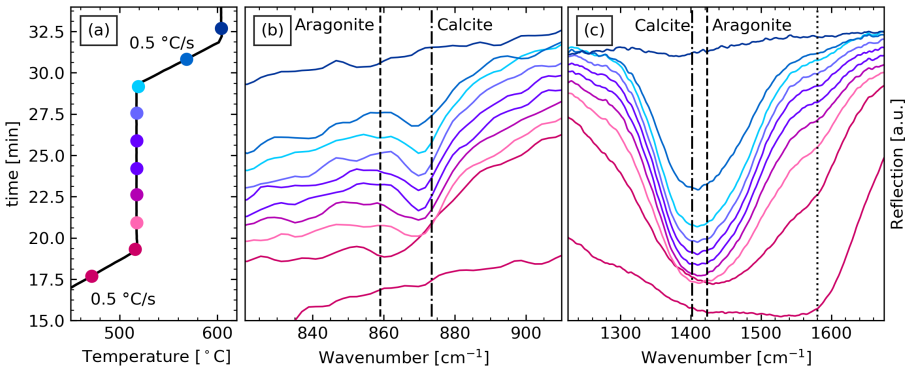

Figure 4.23: (a) Temperature profile of a $BaTiO_3$ precursor film (BT-1) with a medium heating rate and a hold step for oxycarbonate formation. *In situ* IR spectra in the frequency range for the (b) out-of-plane and (c) asymmetrical stretching bands of $BaCO_3$.

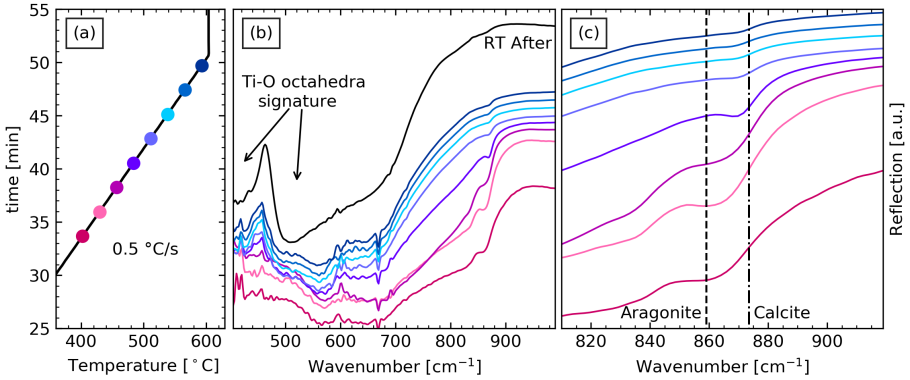

Figure 4.24: a) Temperature profile of a $BaTiO_3$ precursor film (BT-2) heated without the dome for atmosphere control. *In situ* IR spectra in (b) the low frequency range and (c) the frequency range for the out-of-plane $BaCO_3$ band.

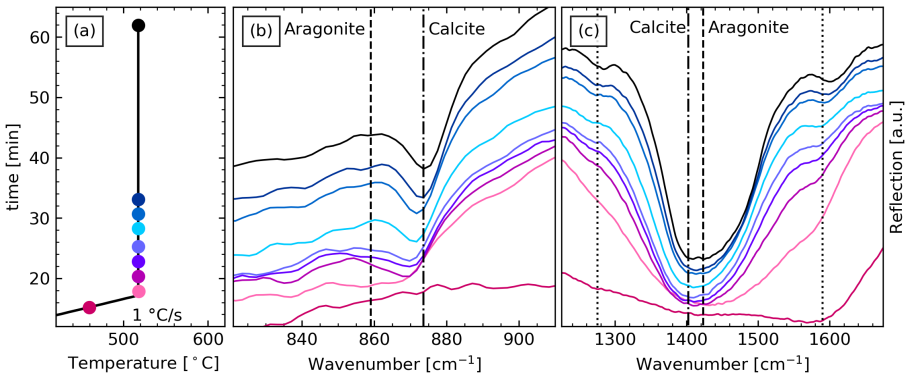

Figure 4.25: (a) Temperature profile of a $BaTiO_3$ precursor film (BT-3) with isothermal oxycarbonate formation. *In situ* IR spectra in the frequency range for the (b) out-of-plane and (c) asymmetrical stretching bands of $BaCO_3$.

the temperature region of the oxycarbonate formation and decomposition are shown in Figure 4.24, while the IR spectra in the full temperature range can be found in Appendix A.2.1. The carbonate oop-band (Figure 4.24(c)) and as-band (not shown) formed above 400 °C in a similar fashion as for sample BT-1 (Figure 4.23(b)). The oop-band formed as a wide feature at the aragonite frequency (859 cm^{-1}) but shifted towards the calcite value (871 cm^{-1}) as the temperature was increased. No shoulder accompanying the as-band was observed for this film. The signature of perovskite absorption associated with the Ti-O octahedra (Figure 4.24(b)) formed at 500 °C and became more pronounced as the temperature was increased. The formation of the perovskite bands was accompanied with the formation of the calcite and as

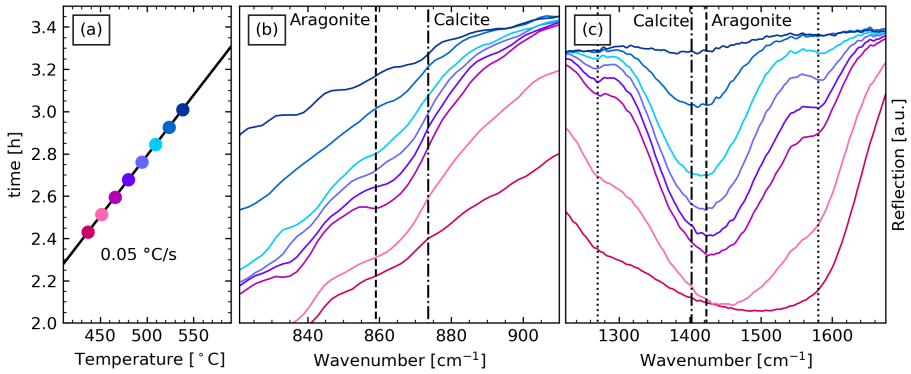

Figure 4.26: (a) Temperature profile of a $BaTiO_3$ precursor film (BT-4) with a low heating rate. *In situ* IR spectra in the frequency range for the (b) out-of-plane and (c) asymmetrical stretching bands of $BaCO_3$.

---

the perovskite band became more pronounced the carbonate oop-band decreased in intensity, showing how the oxycarbonate decomposes to form $BaTiO_3$.

BT-3: Isothermal oxycarbonate annealing

To investigate how the oxycarbonate phase developed during isothermal conditions, a BaTiO3 precursor thick film (BT-3) was heated with 1 °C/s to 520 °C and annealed for 45 min. The IR spectra of sample BT-3 in the region for the oxycarbonate formation and decomposition is shown in Figure 4.25, while the IR spectra in the full temperature range can be found in Appendix A.2.1. Similar to both sample BT-1 (Figure 4.23) and BT-2 (Figure 4.24), the carbonate bands were observed from 520 °C at the start of the hold step. Both the oop-band (Figure 4.25(b)) and the as-band (Figure 4.25(c)) formed as broad features with wavenumbers (861 and 1430 cm^{-1}) assigned to aragonite but shifted to the calcite values (874 and 1402 cm^{-1}) during the hold period. The as-band (Figure 4.25(c)) was accompanied by shoulders at 1280 and 1580 cm^{-1}, but the later shifted towards 1600 cm^{-1} with prolonged hold at 520 °C. The shift in the asymmetric shoulder to higher wavenumber with prolonged hold indicates that a weaker bonding between the carbonate-like compound and the cations is developing. [195]

BT-4: Direct slow heating

IR spectra in the region of the oxycarbonate formation and decomposition of a $BaTiO_3$ precursor thick film (BT-4) heated with a rate of 0.05 °C/s, are shown in Figure 4.26, while the IR spectra in the full temperature range are given in Appendix A.2.1. The decomposition and oxycarbonate formation were similar to sample BT-1 (Figure 4.23), BT-2 (Figure 4.24) and BT-3 (Figure 4.25), but the oxycarbonate phase was less pronounced with slower heating rate. Both the oop-band (Figure

4.26(b)) and the as-band (Figure 4.26(c)) were broad with wavenumbers (861 and 1430 cm^{-1}) assigned to aragonite shifted to the calcite values (871 and 1402 cm^{-1}) during annealing. As for sample BT-3, the as-band (Figure 4.26(c)) was accompanied by shoulders, but unlike sample BT-3, the frequencies of these did not change with continued annealing.

4.4.2 Cation substituted $BaTiO_3$ thick films

The IR spectra of BCT and BCZT thick films in the region for the oxycarbonate formation and decomposition are shown in Figure 4.27 and Figure 4.28, respectively, while the IR spectra in the full temperature range are given in Appendix A.2.1. Both the BCT and BCZT films decomposed in a similar fashion as the $BaTiO_3$ film (BT-I), and the oxycarbonate formation was relatively unaffected by the cation substitution except that the formation temperature was higher for BCZT (Figure 4.28). The kinetics for the decomposition of the oxycarbonate were slower for BCZT compared to $BaTiO_3$ and BCT, and the maximum annealing temperature (approximately 605 °C) was not sufficient to completely decompose the oxycarbonate to form the perovskite phase. The BCT film (Figure 4.27) also had some carbonate residue, but it was more pronounced in the BCZT film, confirming that Zr-substitution increases the nucleation temperature, which was also observed in the synchrotron XRD experiments (Section 4.1.1).

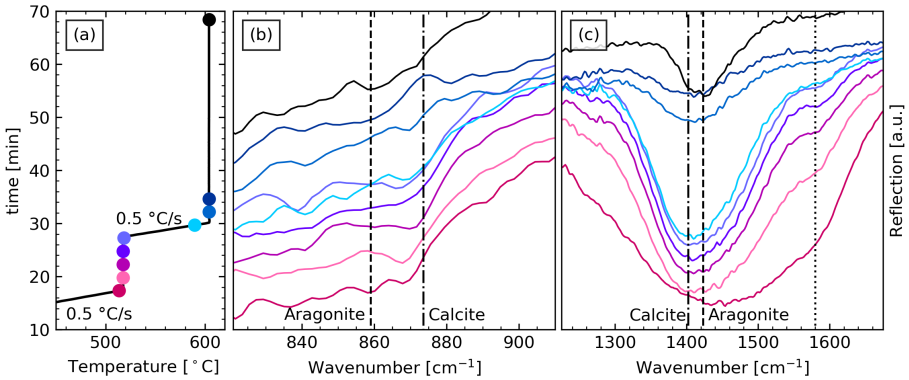

Figure 4.27: (a) Temperature profile of a BCT precursor film with a medium heating rate and a hold step for oxycarbonate formation. *In situ* IR spectra in the frequency range for the (b) out-of-plane and (c) asymmetrical stretching bands of $BaCO_3$.

Table 4.2 summaries the key findings from the *in situ* IR experiments of the thick films. The carbonate oop- and as-bands appeared similar for all samples, although the shift in the oop-band frequency for the $BaTiO_3$ film with isothermal oxycarbonate formation (BT-3) was larger. The shoulders were also stronger for the isothermal oxycarbonate formation in BT-3 and when a low heating rate was used (BT-4). For a heating rate of 0.5 °C/s only the asymmetrical stretching band formed, independent of cation substitution.

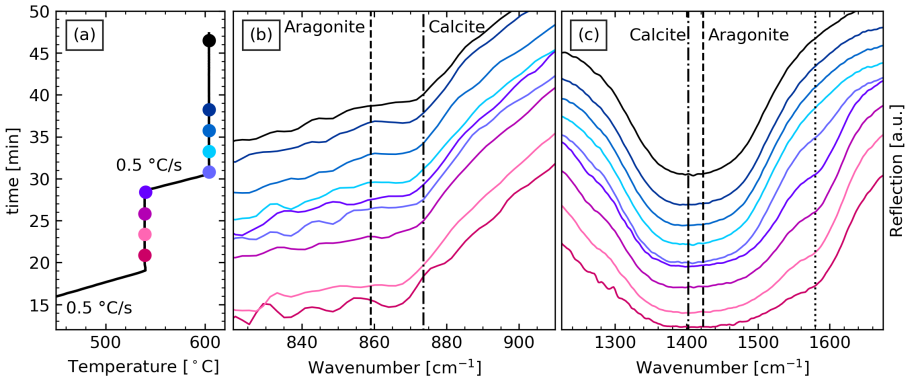

Figure 4.28: (a) Temperature profile of a BCZT precursor film with a medium heating rate and a hold step for oxycarbonate formation. *In situ* IR spectra in the frequency range for the (b) out-of-plane and (c) asymmetrical stretching bands of $BaCO_3$.

Table 4.2: Summary of the frequencies of the oxycarbonate bands from the *in situ* IR experiments of thick $BaTiO_3$-based films.

Sample	**Carbonate oop-band [cm^{-1}]**	**Carbonate as-band [cm^{-1}]**	**Shoulders* [cm^{-1}]**
BT-1	861 → 871	broad 1430 → narrow 1402	1580
BT-2	859 → 871	broad 1430 → narrow 1402	none
BT-3	861 → 874	broad 1430 → narrow 1402	1280 & 1590 → 1600
BT-4	861 → 871	broad 1430 → narrow 1402	1270 & 1580
BCT	861 → 871	broad 1430 → narrow 1402	1580
BCZT	861 → 871	broad 1430 → narrow 1402	1580

*Shoulders were assigned to either $RCOO^-$-group or a carbonate group perturbed by titanium ions. [195]

4.5 Transmission electron microscopy

$BaTiO_3$ thin films on (100) STO made using the different heating programs shown in Figure 3.1 were studied by transmission electron microscopy (TEM) to reveal how repeated annealing influenced the microstructure and texture of multi-layered films. Additionally, the film-substrate interface was of particular interest as both preferred orientation and epitaxy was observed in the films during *in situ* XRD (Section 4.1-4.3).

4.5.1 Epitaxial $BaTiO_3$ thin film on (100) STO

A cross-section of a $BaTiO_3$ thin film on (100) STO made using the epitaxial heating program is shown in Figure 4.29(a). The film thickness was 180 nm, giving an average of 12 nm deposited per layer (15 layers of 0.13 M precursor solution BT-D deposited). The cross-section demonstrates that the film is dense and relatively homogeneous.

Figure 4.29(b) shows the cross-section of the epitaxial film close to the interface in region B. Periodic dislocations were observed at the film-substrate interface with an average distance of 14 nm, which is close to the predicted 16.2 nm spacing for a fully relaxed film based solely on the lattice mismatch (using the lattice parameter in Table 3.4 for the substrate and 4.0037 Å for the film, which is the average parameter for the textured film in Section 4.2.1). The periodicity of the dislocations was

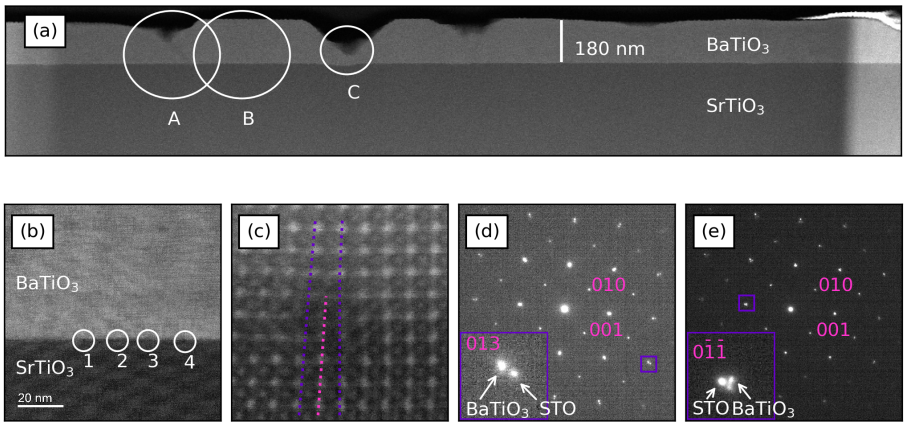

Figure 4.29: (a) HAADF STEM image of a cross section of an epitaxial $BaTiO_3$ thin film on (100) STO. (b) shows periodic dislocations at the substrate interface and (c) shows the termination of a substrate lattice plane at the film interface with an edge dislocation for dislocation 1. Selected area diffraction patterns at the substrate-film interface in (d) region B and (e) region C, where the inserts show the diffraction peaks of both $BaTiO_3$ and STO.

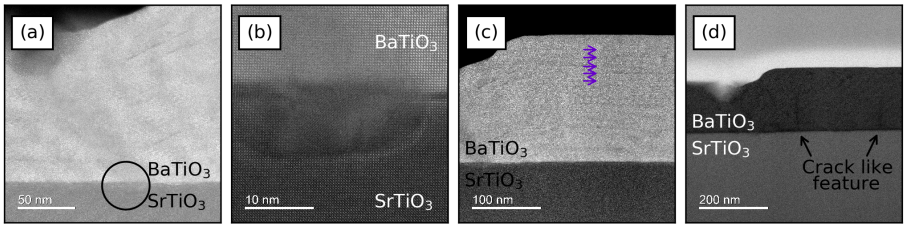

Figure 4.30: HAADF STEM images of a cross section of an epitaxial $BaTiO_3$ thin film on (100) STO, where (a) shows a defect going from the film surface to the substrate and (b) shows the film-substrate interface with the defect, and in (c) the individual film layers are indicated. (d) BF image where film defects are indicated.

similar to the periodicity found for the additional Bragg reflections observed with synchrotron XRD (Figure 4.17). The periodic dislocations show that the epitaxial films investigated in this work were relaxed, and a better term would be cube-on-cube grown films, but for consistency they will be referred to as epitaxial, although they are not epitaxially strained.

One of the dislocations from Figure 4.29(b) (marked "1") is shown in more detail in Figure 4.29(c), where the lines illustrate the edge location that arises from the termination of a substrate lattice plane at the film interface. The selected area diffraction pattern of the epitaxial $BaTiO_3$ film in region B and C are shown in Figure 4.29(d&e). The $BaTiO_3$ diffraction pattern in Figure 4.29(d) from region B shows diffraction from a single epitaxial $BaTiO_3$ crystal, while the diffraction spots in the selected area diffraction pattern in Figure 4.29(e) are split showing that in region C the electron beam probed two $BaTiO_3$ crystal orientations.

The decreased film thickness in region A (Figure 4.29(a)) is shown in more detail in Figure 4.30, where the decrease in film thickness was accompanied by a crack-like feature extending through the film and into the substrate (Figure 4.30(a)). The substrate interface where the crack-like feature terminates is shown in greater detail in Figure 4.30(b), where there is clearly a defect in the substrate. The epitaxial film has several areas of decreased thickness (e.g. regions A and C in Figure 4.29(a)), which were all accompanied by a substrate defect. The defects in the substrate were most likely already present before the film deposition (also observed by synchrotron XRD, Appendix A.1.2) which causes the imperfections in the film and the decrease in film thickness. The different layers of the epitaxial film can partly be distinguished, but the layers were not homogeneous in thickness, as shown in Figure 4.30(c). In Figure 4.30(d) crack-like features occurring occasionally are shown, but they did not extend through the entire film. No defects at the interface between the film and substrate was observed for these features, which closely resembles the threading dislocation lines observed by Fujimoto in fully relaxed $BaTiO_3$ films grown on (100) STO by PLD. [198]

4.5.2 Polycrystalline $BaTiO_3$ thin film on (100) STO

A cross-section of a polycrystalline $BaTiO_3$ thin film on (100) STO made by the polycrystalline heating program is shown in in Figure 4.31(a). This film was 193 nm giving an average of 13 nm built up for each of the 15 layers. The interface between the film and substrate in region A is shown in Figure 4.31(b). At the interface there was an epitaxial layer with a thickness of a few nm, but occasionally the epitaxy extended into grains grown from the substrate interface (Figure 4.31(c)). Edge dislocations were observed in the epitaxial layer caused by termination of substrate lattice planes (Figure 4.31(d)), similar to the periodic dislocations observed for the epitaxial film (Figure 4.29).

Selected area diffraction patterns of the polycrystalline film in regions A and B are shown in Figure 4.31(d&e). The diffraction patterns did not show full diffraction rings for the polycrystalline $BaTiO_3$ film, indicating some degree of preferential orientation, at least close to the substrate interface.

4.5.3 Textured $BaTiO_3$ thin film on (100) STO

A cross-section of a $BaTiO_3$ thin film on (100) STO made by the texture heating program is shown in the HAADF STEM image in Figure 4.32(a). This film was 206 nm giving an average of 13-14 nm for each of the 15 layers of 0.13 M precursor solution (BT-D). The interface between the film and the substrate is shown in more detail in Figure 4.32(b). Similar to the polycrystalline film (Figure 4.31), the textured film also had a thin epitaxial layer close to the substrate interface.

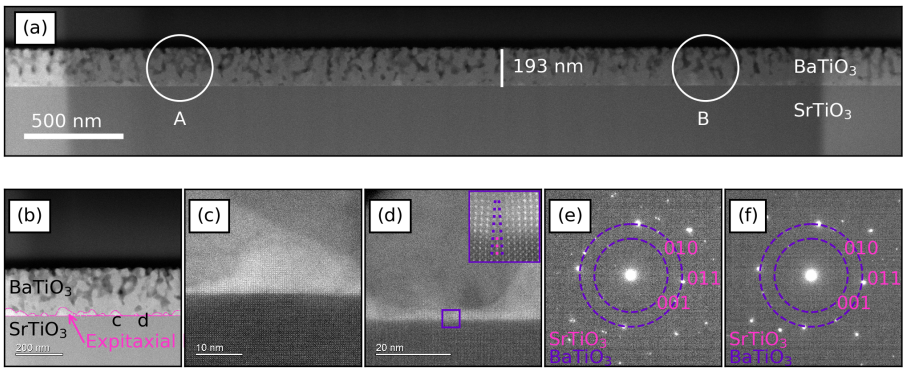

Figure 4.31: (a)HAADF STEM image of a cross section of a polycrystalline $BaTiO_3$ thin film on (100) STO. (b) The film interface in region A where the zoomed images (c) and (d) are taken. (c) Shows an epitaxial grain and (d) shows an epitaxial layer with an edge dislocation which is further illustrated in the insert. Selected area diffraction pattern measured at the substrate-film interface in (e) region A and (f) region B.

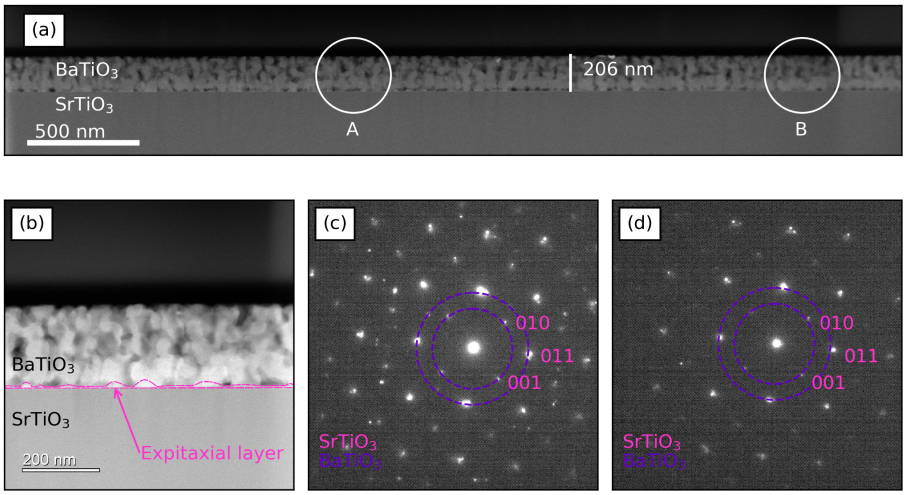

Figure 4.32: HAADF STEM image of (a) cross section of a textured $BaTiO_3$ thin film on (100) STO and (b) interface between film and substrate in region A. Selected area diffraction pattern measured at the substrate-film interface in (c) region A and (d) region B.

Selected area diffraction patterns of the textured $BaTiO_3$ film are shown in Figure 4.32(c&d) from two different regions. Neither diffraction pattern show full diffraction rings for the textured $BaTiO_3$ film, indicating some degree of preferential orientation, at least close to the substrate interface. There are however, more reflections from the film in the diffraction pattern in Figure 4.32(c) than in the diffraction pattern in Figure 4.32(d). In section B, the film seems to be close to epitaxial in the probed area, although with some splitting of the reflections, which means that there was several close to epitaxial crystals probed by the electron beam.

4.6 Ferroelectric properties

Ferroelectric characterization was done on a selection of $BaTiO_3$-based thin films with different degree of texture and thickness, made by the heating programs shown in Figure 3.1. The precursor solutions used to prepare the films for the ferroelectric characterization are listed in Table 4.3, along with the heating program used, number of layers deposited and the total film thickness. The film thickness was measured by either SEM (Appendix A.4) or TEM (Section 4.5).

4.6.1 $BaTiO_3$ thin films

Figure 4.33 shows the in-plane ferroelectric properties of a 474 nm epitaxial $BaTiO_3$ film on a (100) STO substrate for different electrode orientations. The polarization

Table 4.3: Overview of the films used for ferroelectric characterization.

Material Precursor solution	**Heating program**	**# Layers**	**Film thickness [nm]**
$BaTiO_3$ (BT-C)	Epi-HP	15	474 (SEM)
$BaTiO_3$ (BT-D)	Epi-HP	15	180 (TEM)
$BaTiO_3$ (BT-D)	Poly-HP	15	193 (TEM)
$BaTiO_3$ (BT-D)	Tex-HP	15	206 (TEM)
$BaTiO_3$ (BT-C)	Poly-HP	15	626 (SEM)
BCT (BCT-B)	Epi-HP	10	125 (SEM)
BCZT (BCZT-B)	Epi-HP	10	118 (SEM)

versus electrical field (PE-loop) clearly show that the film was ferroelectric due to the hysteresis (Figure 4.33(a)). The switching can also be seen from the capacitance versus electric field loops (CE-loop) in Figure 4.33(b). For both the PE- and CE-loops, the different response of the different electrode orientations reflect the reported domain pattern and in-plane c-axis by Ræder *et al.* [127]

The in-plane ferroelectric properties of epitaxial $BaTiO_3$ thin films with different thickness on (100) STO are displayed in Figure 4.34(a&b). The thickest film (474 nm) displayed a more square hysteresis loop (Figure 4.34(a)) and a larger CE-loop (Figure 4.34(b)) compared to the thinner film which was more slanted. Post-annealing (1000 °C for 3 h) of the thinner film (180 nm) increased the CE-loop and also resulted in a higher polarization for the same electric field, which could be due to reduced porosity after the post-annealing.

Figure 4.35 shows the ferroelectric properties of textured, polycrystalline and epitaxial $BaTiO_3$ thin films on a (100) STO before (Figure 4.35(a)) and after (Figure 4.35(b)) post-annealing at 1000 °C for 3 h. The PE-loops of the epitaxial films showed that this film was ferroelectric, as previously shown in Figure 4.34. The effect of the post-annealing can be seen in the hysteresis loop which reach higher polarization for the same electric field. The polycrystalline and textured films were however not ferroelectric, as they did not display hysteresis loops, neither before nor after the annealing. The PE-loops in Figure 4.34 have different slopes before and after annealing, as these are different films with the electrodes deposited after the annealing. The post-annealing was done to increase the grain size in the polycrystalline and textured films, since small grain sizes can suppress ferroelectricity in $BaTiO_3$ thin films.[6] However, Figure 4.35 clearly shows that there is no improved ferroelectricity for the polycrystalline and textured films despite the significant grain growth that occurred during the post-annealing (Figure 4.35(c-h)).

PV- and CV-loops for a 626 nm polycrystalline $BaTiO_3$ measured with step wise increasing field are shown in Figure 4.36. The polarization increased with increasing field, especially at 100 Hz, but the PV-loops were still far from perfect hysteresis loops, meaning the ferroelectricity of this film was still poor. The tunability also increased with increasing field, which for the last CE-loop was 22 %.

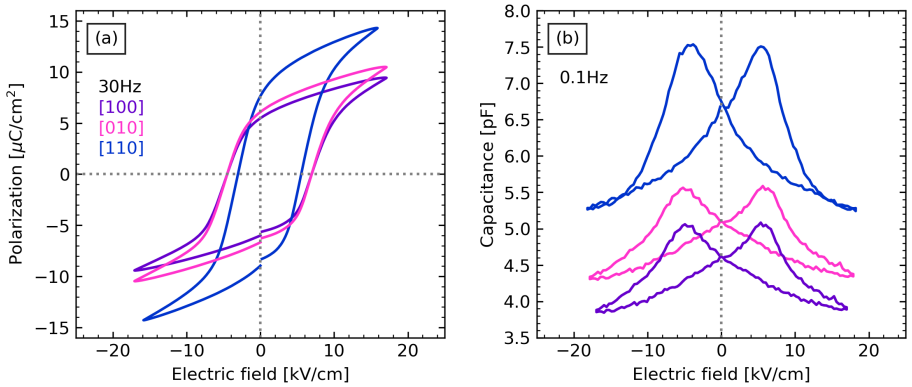

Figure 4.33: In-plane ferroelectric properties of a 474 nm epitaxial $BaTiO_3$ film on a (100) $SrTiO_3$ substrate with different electrode orientations. (a) Polarization versus electrical field hysteresis loop and (b) capacitance versus electrical field loops.

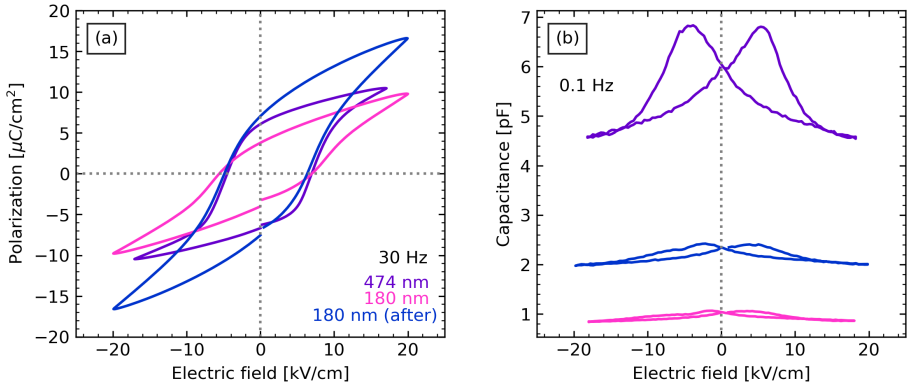

Figure 4.34: In-plane ferroelectric properties of a thick and thin epitaxial $BaTiO_3$ films on a (100) STO compared with the thin film after it was post-annealed at 1000 °C for 3 hours. (a) Polarization versus electrical field hysteresis loops and (b) capacitance versus electrical field loops.

4.6.2 Cation substituted $BaTiO_3$ thin films

The in-plane ferroelectric properties of BCT and BCZT films on (100) STO made by the epitaxial heating program are shown in Figure 4.37, compared to the properties of the 180 nm $BaTiO_3$ film. A thickness dependency for the hysteresis loops was observed even though the data were corrected for film thickness, also seen from Figure 4.34. A significant contribution from leakage current was observed for the cation substituted films (tan δ shown in Appendix A.3), which could be due to the

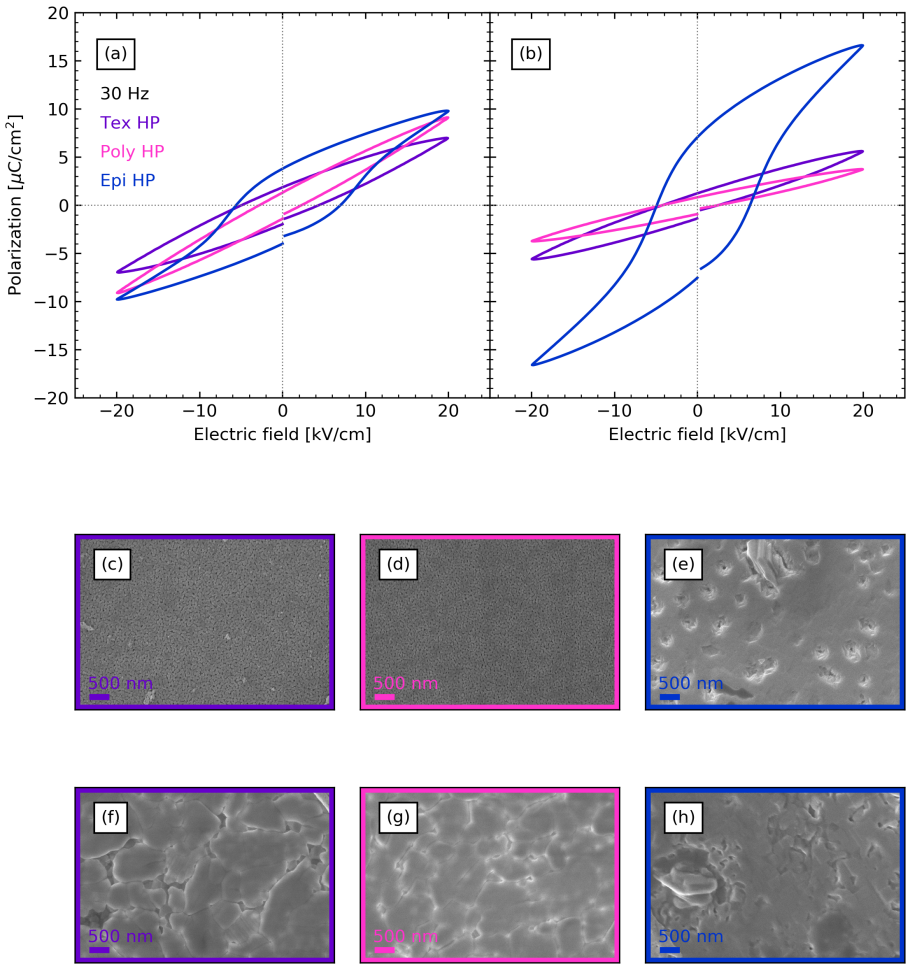

Figure 4.35: In-plane ferroelectric properties of $BaTiO_3$ thin films on a (100) $SrTiO_3$ substrate with different degree of preferential orientation. (a) Polarization verses electric field of the films as prepared and (b) polarization versus electrical field of the films after annealing at 1000 °C for 3 hours. Microstructure of the (c) 206 nm textured, (d) 193 nm polycrystalline and (e) 180 nm epitaxial films as prepared and (f) textured, (g) polycrystalline and (h) epitaxial films after post-annealing.

---

reduced thickness and the porosity of these films, but also from surface charges from water adsorption. The tunability of the 180 nm $BaTiO_3$ film also increased after a post-annealing step at 1000 °C (Figure 4.34) and the same can be expected for the BCT and BCZT films. The increased noise level in the CE-loop of BCT compared to $BaTiO_3$ and BCZT was caused by a different current range used during this measurement (Figure 4.37).

The remnant polarization and cohesive field of the films characterized in this Section are summarized in Table 4.4. The high polarizations observed for the BCT and BCZT films are an effect of the leakage current contributions to the hysteresis loops (Figure 4.37), while for the 626 nm thick $BaTiO_3$ film, the high values are caused by an order of magnitude higher applied electric field.

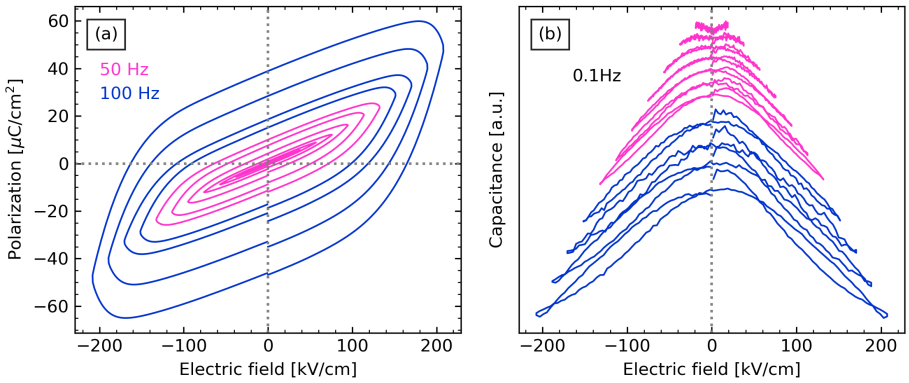

Figure 4.36: In-plane ferroelectric properties of a 626 nm polycrystalline $BaTiO_3$ thin films on a (100) STO. (a) Polarization verses electric field of the films with increasing electric field and (b) capacitance versus increasing electrical field.

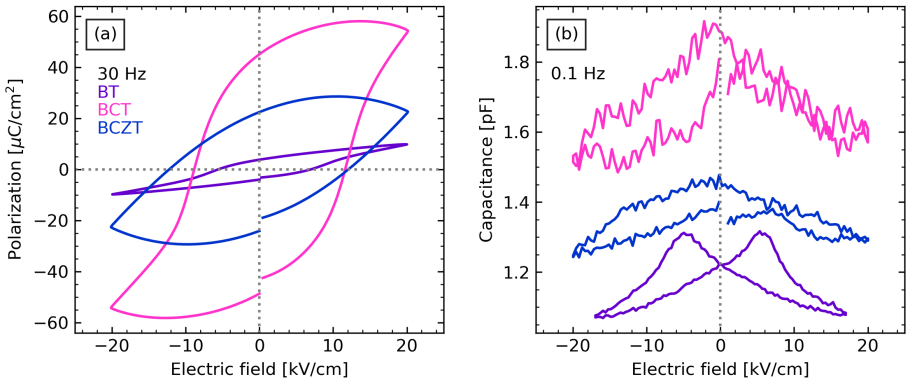

Figure 4.37: In-plane ferroelectric properties of an epitaxial 180 nm $BaTiO_3$, 125 nm BCT and 118 nm BCZT thin film on a (100) STO. (a) Polarization versus electric field of the films and (b) capacitance versus electrical field.

Table 4.4: Summary of the resulting remanent polarisation and cohesive field for the films used for ferroelectric characterization.

Film (Thickness[nm])	**Remanent polarisation [$\mu C/cm^2$]**	**Cohesive field [kV/cm]**
Epitaxial $BaTiO_3$ (474)	6.1 / -6.5	6.5 / -4.5
Epitaxial $BaTiO_3$ (180)	3.9 / -4.1	6.5 / -5.6
Polycryst. $BaTiO_3$ (193)	1.3 / -1.4	4.4 / -2.8
Textured $BaTiO_3$ (206)	2.0 / -2.1	2.3 / -5.0
*Polycryst. $BaTiO_3$ (626)	165 / -163	40 / -46
Epitaxial BCT (125)	47.0 / -50.7	11.6 / -8.9
Epitaxial BCZT (118)	26.4 / -28.3	12.1 / -12.3

*Values given are for the maximum applied voltage

4.7 Infrared spectroscopy of $BaTiO_3$-based thin films and phonon modelling

Near normal IR spectra were recorded on ~60 nm thick $BaTiO_3$-based thin films on various substrates and then the dielectric function was fitted to the reflection spectra as described in Section 3.2.4. The IR reflection spectra of a (100) STO substrate and a $BaTiO_3$ film on STO are shown in Figure 4.38. The different phonon modes used in the fitting of STO are indicated as well as the phonon modes for $BaTiO_3$.

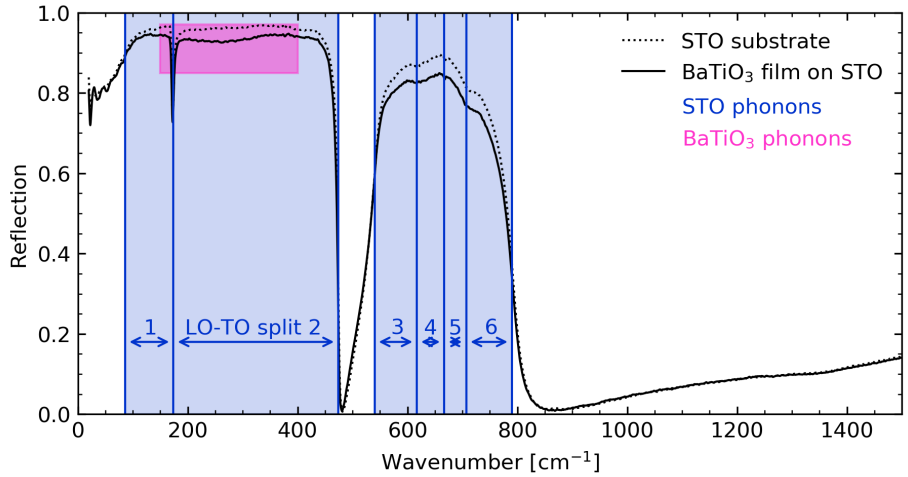

Figure 4.38: Near normal reflection spectra of a STO substrate and a $BaTiO_3$ thin film on STO. The substrate and film phonon modes are indicated.

Due to the similar crystal structure there is a large overlap between the phonon modes of STO and $BaTiO_3$, so only one $BaTiO_3$ phonon mode could be fitted. The reflection spectra of all films, and the values of all parameters used in the fittings are provided in Appendix A.2.2.

The real and imaginary parts of the dielectric function found from the fitting of polycrystalline $BaTiO_3$ thin films on (100) LAO, (100) MgO and (100) STO substrates are shown in Figure 4.39. For the film on STO only one overdamped phonon mode could be fitted, while on LAO two heavily damped phonon modes could be fitted, and on MgO the modes were less damped, especially the mode at 190 cm^{-1}. Because of a soft mode that could not be resolved in the reflection IR spectra, the real part of the dielectric function had different values at low frequencies for the $BaTiO_3$ films on the different substrates.

The real and imaginary parts of the dielectric function found from the fitting of polycrystalline $BaTiO_3$, BCT and BCZT thin films on (100) STO are shown in Figure 4.40. The BCT and BCZT films were practically indistinguishable but had a slightly lower phonon frequency and slightly less damped mode than $BaTiO_3$.

The fitting of near normal incident reflection IR spectra shows how sensitive the fitted dielectric function of the thin films are to the substrate phonon modes and the overlap with the film phonon modes. This is especially true for films less than 100 nm thick, which were used during these measurements.

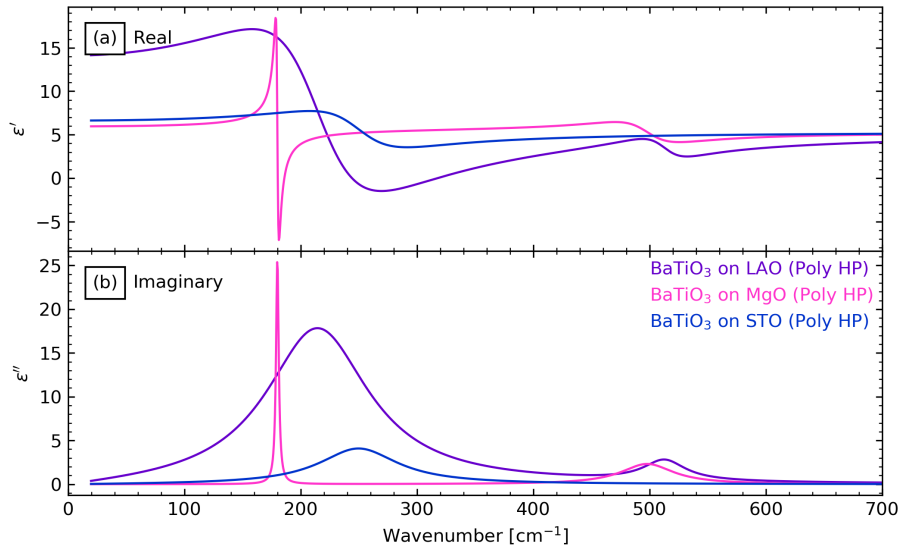

Figure 4.39: The (a) real and (b) imaginary part of the dielectric function found from fitting the IR reflection spectra of $BaTiO_3$ thin films on various substrates.

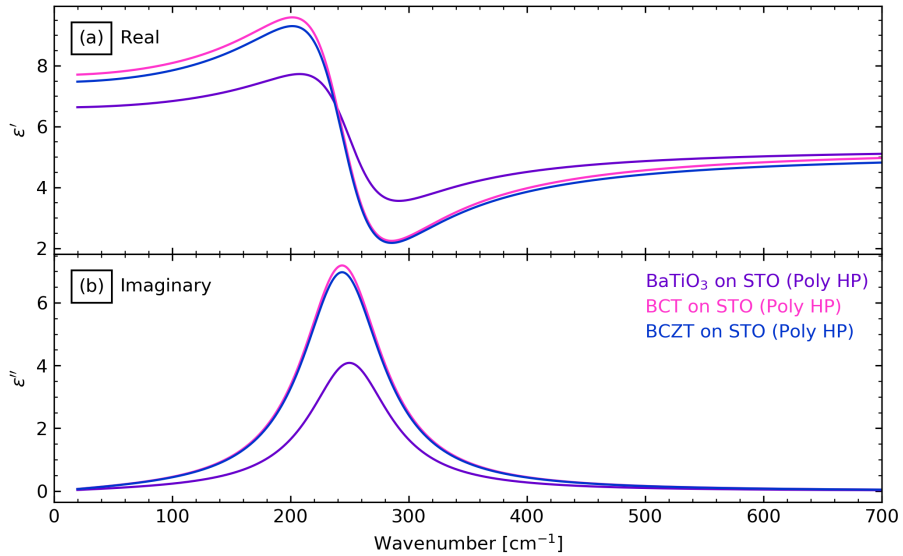

Figure 4.40: The (a) real and (b) imaginary part sf the dielectric function found from fitting the IR reflection spectra of $BaTiO_3$-based thin films on(100) STO.

5 Barium titanate based powders

5.1 The precursor powders

The precursor chemistry was shown to be of importance for the crystallization process and degree of crystallographic texture in the $BaTiO_3$-based thin films in Chapter 4. To further investigate the chemistry of the precursor decomposition, powders prepared from the same precursor solutions used to deposit the films, were characterized by XRD, IR spectroscopy and thermal analysis. Furthermore, the influence of CO_2 in the atmosphere was explored. The powders investigated throughout this chapter were prepared from precursor solutions BT-A, BT-B, BCT-A and BCZT-A.

The IR spectrum of a $BaTiO_3$ precursor powder dried at 200 °C is shown in Figure 5.1(a). Weak vibrational modes of $Ba(NO_3)_2$ can be seen in the spectrum, although the asymmetric stretching mode is split (1340 cm^{-1} and 1400 cm^{-1}), showing that the nitrate ion was bonded to various cations in the precursor powder giving a perturbation. [71,195,196] The symmetric (ss, 1240-1450 cm^{-1}) and asymmetric (as, 1590-1750 cm^{-1}) stretching modes for the carboxylic acid groups from both EDTA, citric acid, and their derivatives are indicated as wide bands. [71,195,196] The width of the bands reflects the bonding to different metal ions. The frequency range for the as-band of the nitrate and carboxylic acid groups overlap, so the intensity of the wide band also has a contribution from the nitrate groups. The characteristic C-OH out-of-plane (oop) bending mode for carboxylic acid groups was observed at 930 cm^{-1}. The C-N stretching mode (1020-1250 cm^{-1}) from the EDTA derivatives was also identified as wide a band. [71, 195, 196]

Figure 5.1(b) compares the IR spectra of $BaTiO_3$, BCT and BCZT precursor powders, showing almost the same features, which is expected since the additives used to prepare the barium and titanium solutions were also used to prepare the calcium and zirconium solutions. Any difference between the precursor powders would be in the metal-oxygen bands, which occur at low wavenumbers and out of range for the spectra in Figure 5.1(b). Therefore, the precursor powders were practically indistinguishable with IR spectroscopy.

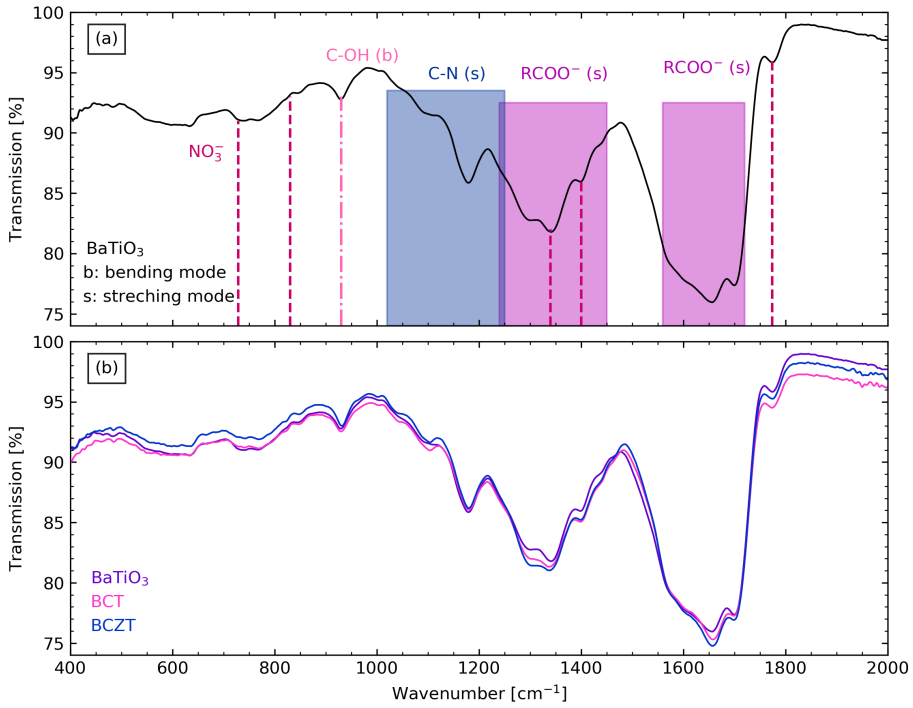

Figure 5.1: (a) IR spectrum of $BaTiO_3$ precursor powder dried at 200 °C. The functional groups in the precursor powder are indicated. (b) IR spectra of the dried $BaTiO_3$, BCT and BCZT precursor powders.

5.2 Precursor powder annealing and decomposition

5.2.1 X-ray diffraction of the phase evolution

A series of the dried $BaTiO_3$ precursor powders were calcined for 2 h at selected temperatures and characterized with XRD and IR spectroscopy. The diffractograms of the calcined powders are shown in Figure 5.2. The powders were amorphous below 550 °C, and $BaTiO_3$ was the only crystalline phase present above 650 °C. At 550 °C, nucleation of the perovskite phase had occurred, evident from the broad reflections which became more intense as the calcination temperature increased. In addition to the perovskite Bragg reflections at 550 °C and 600 °C, weak reflections corresponding to an oxycarbonate phase were present, but this phase disappeared at higher temperatures. Rietveld refinements were performed on the powders with $BaTiO_3$ (600 °C and above) and the lattice parameter and crystallite size obtained are shown in Figure 5.3. The lattice parameters of the $BaTiO_3$ powder series

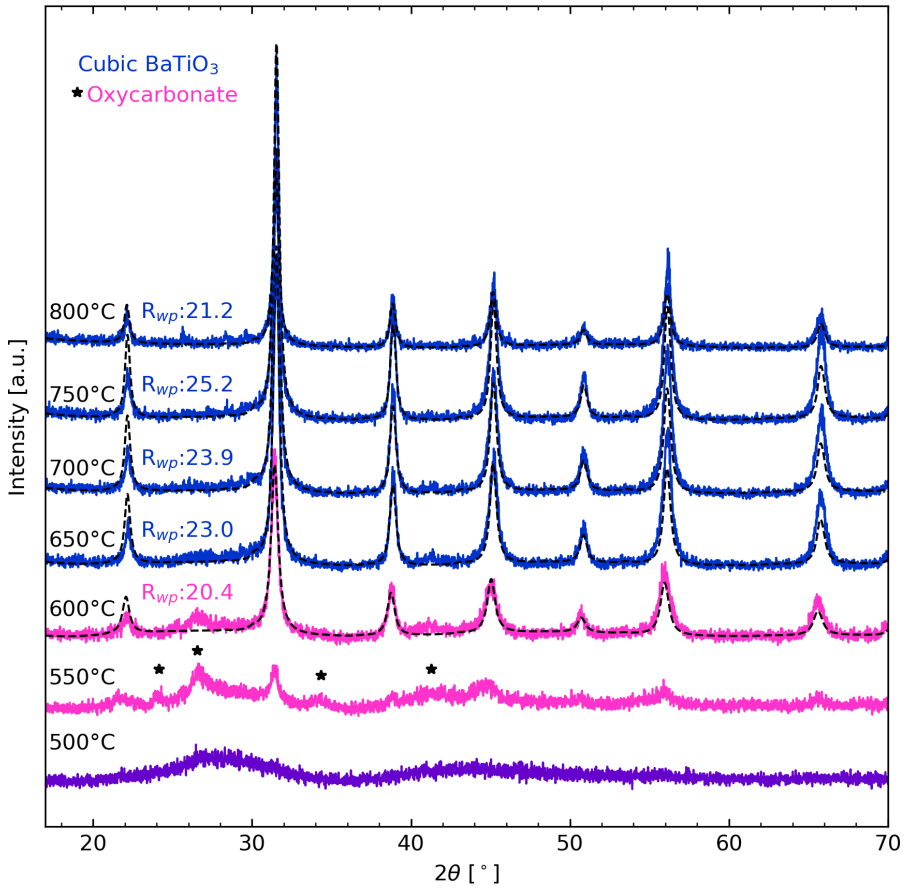

Figure 5.2: XRD patterns of $BaTiO_3$ precursor powders calcined at increasing temperatures for 2 h along with the results of Rietveld refinements. An intermediate oxycarbonate phase can be seen forming alongside the perovskite.

decreased and the crystallite size increased with increasing calcination temperature (Figure 5.3), showing that a higher calcination temperature promotes coarsening of the powders and gives a lattice parameter closer to the bulk value.

Table 5.1 summaries how different heating programs affect the crystallite size and lattice parameter for $BaTiO_3$ powders compared to the values obtained for BCT and BCZT powders (Figure 5.4). All diffractograms where modelled with the cubic phases, since the tetragonal peak splitting could not be resolved, and the R_{wp}-values for refinements with tetragonal symmetry were higher than for cubic. The $BaTiO_3$ powder calcined at 750 °C for 6 h (Figure A.1 in Appendix A.1.1), had a smaller lattice parameter than the powder calcined 750 °C in Figure 5.2-5.3, but the crystallite size was found to be nearly three times the size obtained by a

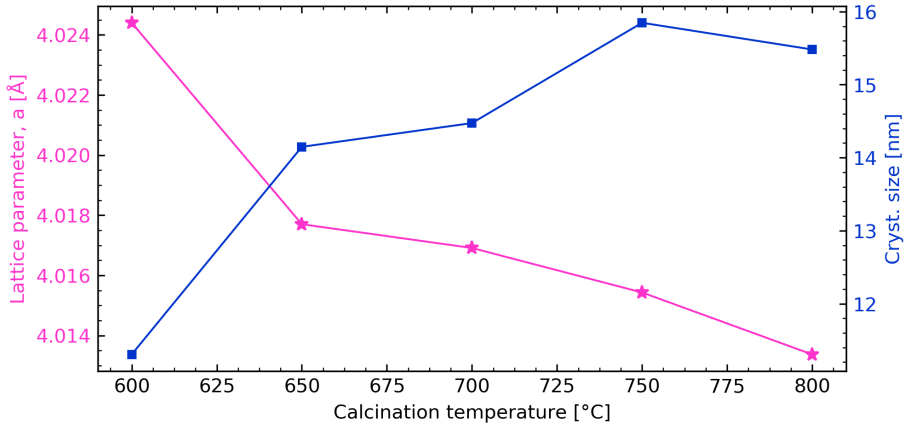

Figure 5.3: Crystallite size and lattice parameter from *ex situ* Rietveld refinements of the $BaTiO_3$ precursor powder series as a function of calcination temperature when held at the calcination temperature for 2 h.

Table 5.1: Overview of results from *ex situ* Rietveld refinement for $BaTiO_3$-based powders calcined at different temperatures and times.

Powder	Calcination program	a [Å]	Cryst.size [nm]	R_{wp}	Figure
$BaTiO_3$	600 °C for 2 h	4.0244(3)	11.3	20.4	5.2
$BaTiO_3$	700 °C for 2 h	4.0169(1)	14.5	23.9	5.2
$BaTiO_3$	800 °C for 2 h	4.0134(8)	15.5	21.2	5.2
$BaTiO_3$	750 °C for 6 h	4.0102(2)	27.2	13.3	A.1
$BaTiO_3$	700 °C for 3 h	4.0140(7)	19.3	21.4	5.4
BCT	700 °C for 3 h	4.0134(1)	20.2	22.1	5.4
BCZT	800 °C for 2 h	4.0127(5)	14.6	13.8	5.4

2 h calcination. The $BaTiO_3$ powder calcined at 700 °C for 3 h also had a smaller lattice parameter than the powder calcined at 700 °C for 2 h, but the crystallite size was larger, showing how the increased annealing time have the same effect on the powders as a higher annealing temperature, namely decreased lattice parameter and increased crystallite size.

The XRD patterns with Rietveld refinement of $BaTiO_3$, BCT and BCZT powders annealed at high temperature for 3 h are shown in Figure 5.4. Because of the slower kinetics and increased nucleation temperature found for the BCZT thin films (Section 4.1.1), the BCZT powder was calcined at 800 °C, while the $BaTiO_3$ and BCT powders were calcined at 700 °C. For all powders, the perovskite was the only phase present and no tetragonal splitting was observed. The lattice parameters and crystallite sizes for BCT and BCZT are compared to $BaTiO_3$ in Table 5.1.

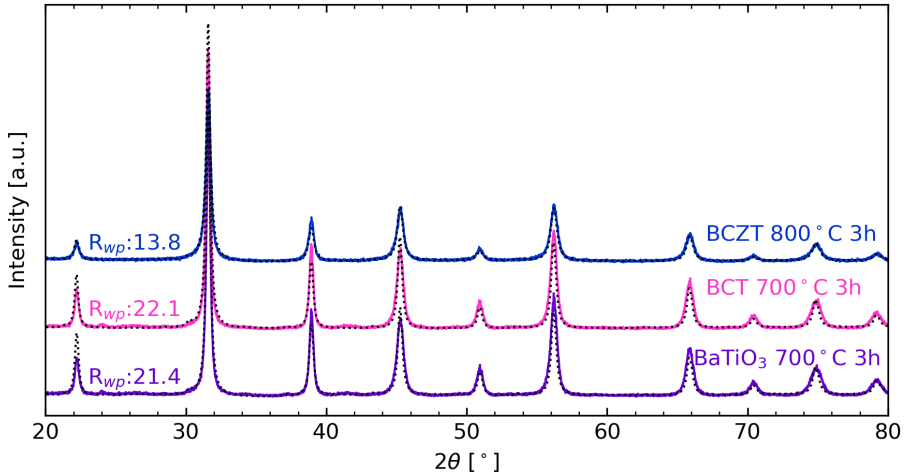

Figure 5.4: XRD patterns of $BaTiO_3$, BCT and BCZT powders annealed at high temperature for 3 h, along with the results from Rietveld refinements.

5.2.2 Infrared spectroscopy of the phase evolution

Figure 5.5 shows the *ex situ* IR spectra of the $BaTiO_3$ precursor powder series calcined at increasing temperatures for 2 h. Between 200-300 °C, the spectra showed the same functional groups as the precursor powder, presented in Figure 5.1. As the temperature was increased from 300 °C to 400 °C , decomposition takes place resulting in the formation of $BaCO_3$ and Ti-rich compounds, in accordance with the findings by Ischenko *et al.* [65, 74] The carbonate as-band (wide band at 1400 cm^{-1}) started to emerge between 300 °C and 400 °C, and then narrowed as the temperature was further increased. The as-band was also accompanied by shoulders on either side (1290 cm^{-1} and 1600 cm^{-1}), marked with arrows for the powder calcined at 500 °C in Figure 5.5, which was also observed for the thick films (Section 4.4). It is proposed that the shoulders correspond to symmetric and asymmetric stretching bands of a $RCOO^-$-group, or from the splitting of the asymmetric stretching band as the $CO_3{}^{2-}$-ion bonds to Ti^{4+}-ions. The carbonate as-band was visible in the spectra up to 650 °C, although the XRD patterns (Figure 5.2) showed phase pure $BaTiO_3$ already at 650 °C. The carbonate as-band is a strongly absorbing vibrational mode, so even trace amounts of carbonate will be visible in the IR spectrum, while the oxycarbonate phase only have weak and broad peaks in the diffractograms, so this difference is not surprising.

The Ti-rich phases were amorphous or in small clusters without long range order since no Bragg reflections could be ascribed to such phases in the X-ray diffractograms (Figure 5.2). The absorption band characteristic for the TiO_6-octahedra in $BaTiO_3$ was present in the IR spectra (Figure 5.5) for powders calcined above 500 °C. Hence, the Ti^{4+} in the Ti-rich phases were not in the octahedral coordina-

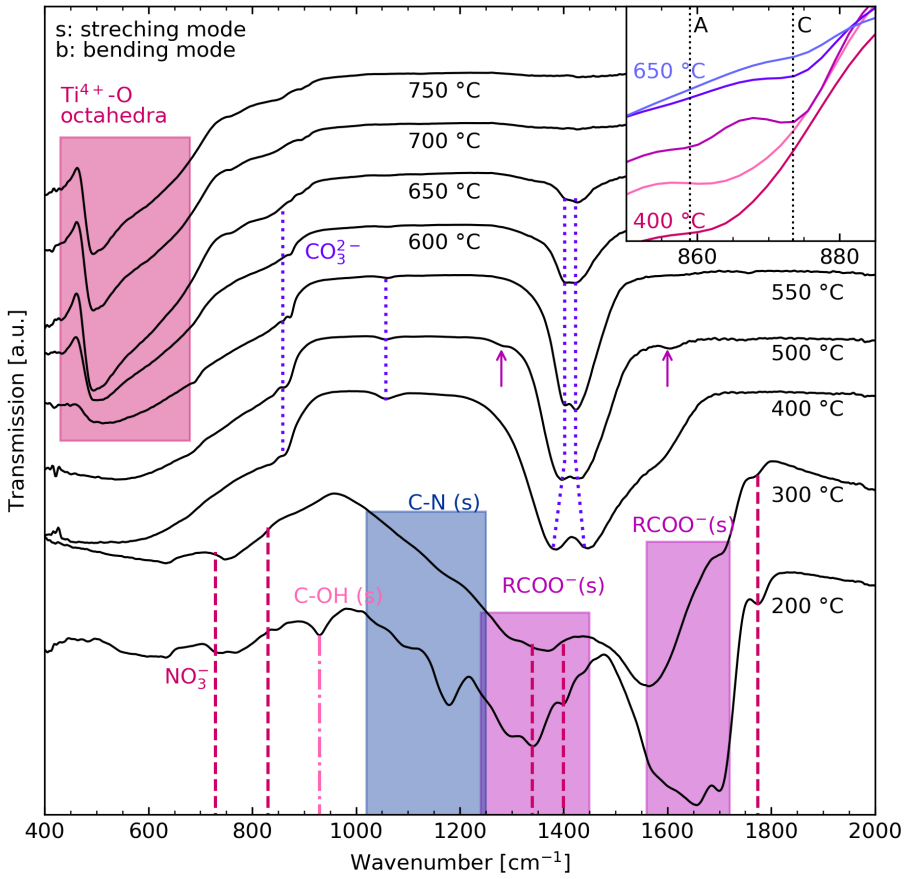

Figure 5.5: IR spectra of $BaTiO_3$ precursor powders calcined at increasing temperatures for 2 h. The functional groups and carbonate bands are indicated, based on the band assignment done for the precursor powder. The insert shows the changes in the out-of-plane carbonate mode with increasing temperature, where the aragonite (A) and calcite (C) bands are indicated.

tion at least not with a long range order as this band was not observed at lower temperatures.

The insert in Figure 5.5 shows part of the IR spectra in the frequency range of the $BaCO_3$ oop-band. This band developed as a broad feature above 400 °C, with a frequency in between that of the aragonite (859 cm^{-1}) and calcite (874 cm^{-1}) $BaCO_3$ polymorphs. [71] As the temperature was increased, the oop-band became more intense. At 550 °C, both aragonite and calcite polymorphs were present. Upon further heating the aragonite band disappeared and only the calcite band was left. The shift in frequency to the value of the calcite-type $BaCO_3$ occurred at the same temperature where the first weak and broad reflections due to the presence of the oxycarbonate phase appeared in the XRD patterns (Figure 5.2). This shows that the oxycarbonate phase is different from the normal aragonite-type $BaCO_3$ and influences the $BaTiO_3$ formation, in accordance with the findings of Ischenko *et al.* [65, 74] and the film results (Chapter 4).

The IR spectra of $BaTiO_3$ precursor powder and dried Ba-solution calcined at 550 °C for 2 h are presented in Figure 5.6. When the dried Ba-solution was calcined alone, only the aragonite polymorph of $BaCO_3$ was formed, while for the $BaTiO_3$ precursor powder, bands of both aragonite and calcite polymorphs were present as previously discussed. This observation shows that the titanium containing pyrolysis products plays a key role in the formation of the oxycarbonate phase.

Figure 5.7 shows the IR spectra of $BaTiO_3$, BCT and BCZT precursor powders calcined to obtain the oxycarbonate phase. Annealing for 1 h at 540 °C was sufficient to obtain the oxycarbonate phase in case of $BaTiO_3$ and BCT, while for BCZT, calcination for 3 h at 550 °C was necessary to observe the oxycarbonate phase and still the $BaCO_3$ as-band (Figure 5.7(c)) was not as intense for the BCZT powder as observed for $BaTiO_3$ and BCT. This difference in intensity shows that the decomposition kinetics of BCZT was slower than for $BaTiO_3$ and BCT, and that zirconium substitution shifts the reaction temperatures upwards. The shift from aragonite to calcite at higher temperatures was the same for all the powders (Figure 5.7), which is in accordance with the *in situ* IR spectroscopy results for thick films in Section 4.4.

5.2.3 Thermal analysis of the phase evolution

Thermal analysis of the $BaTiO_3$, BCT and BCZT precursor powders were carried out with medium (0.2 °C/s) and low (0.02 °C/s) heating rates, since heating rate was observed to influence the decomposition and texture of the films (Section 4.1). The mass loss and the differential scanning calorimetry (DSC) signal for the powders during heating are shown in Figure 5.8. The shape of both the mass loss and DSC curves were similar for the medium (Figure 5.8(a)) and the low (Figure 5.8(b)) heating rates. The different powders showed the same decomposition behaviour independent of cation substitution. This is not surprising considering the similar IR spectra of the precursor powders (Figure 5.1), which showed that the precursor chemistry was similar.

The temperature region for the final mass loss is shown in detail in Figure 5.8(c).

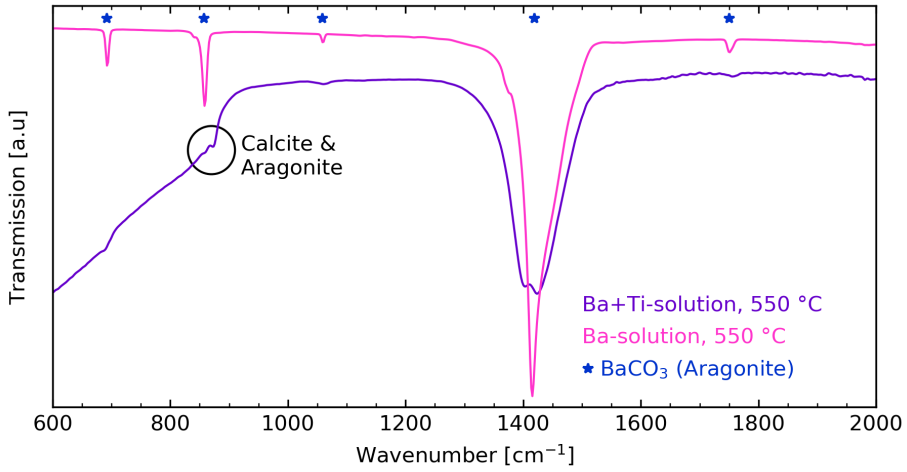

Figure 5.6: IR spectra of $BaTiO_3$ precursor powder and dried Ba-solution calcined at 550 °C for 2 h. The spectra were scaled for clarity.

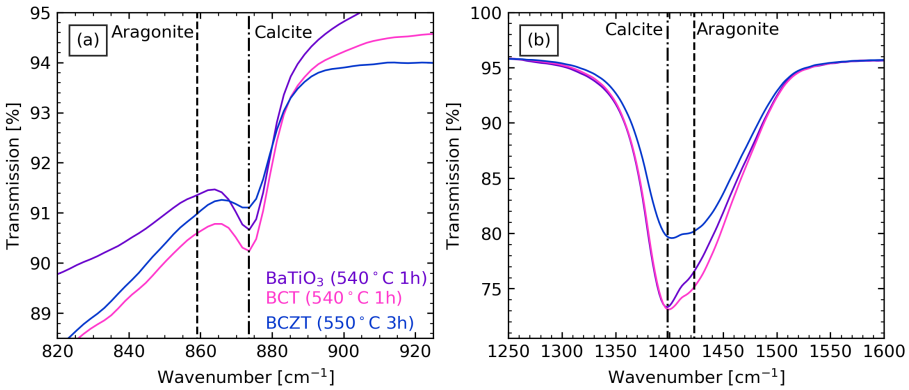

Figure 5.7: IR spectra of $BaTiO_3$, BCT and BCZT powders calcined to obtain the oxycarbonate phase in the frequency range of (a) the out-of-plane vibrational mode of $BaCO_3$ and (b) the asymmetrical absorption band of $BaCO_3$.

The rapid decrease in mass accompanied by a sharp peak in the DSC-curve shifted ∼60 °C lower when the low heating rate was used compared to the medium due to kinetics limitations by faster heating. The mass loss was ∼80 % for all the powders, where differences between the powders were caused by varying water content (from storage) and concentration of the complexing agents and additives in the solutions. The temperatures for the different features in the mass loss curve for all powders and heating rates are listed in Table 5.2. The decomposition giving the final mass loss

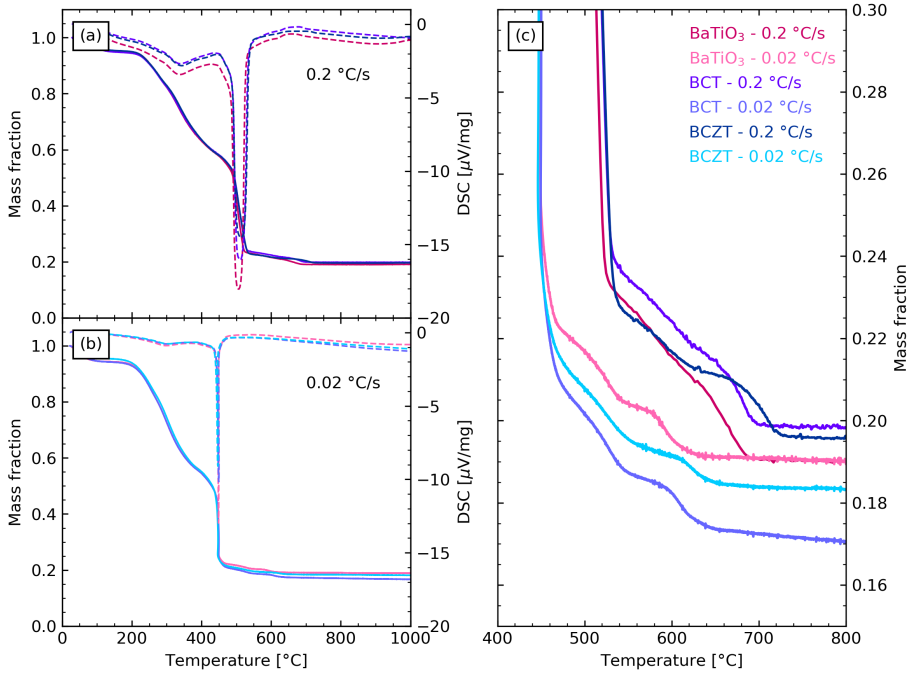

Figure 5.8: Thermal analysis (mass loss) and differential scanning calorimetry (DSC) curves for $BaTiO_3$, BCT and BCZT precursor powders heated with 0.2 °C/s and 0.02 °C/s. The full mass fraction and DSC curve for the (a) 0.2 °C/s measurements and (b) 0.02 °C/s measurements, and (c) shows a detailed view of the final mass loss.

---

occurred in two steps, which was more pronounced with the lower heating rate. The temperature range where the final mass loss occurred is associated with the decomposition of the oxycarbonate phase to form $BaTiO_3$. In the *in situ* IR spectra of the thick films (Section 4.4) the oxycarbonate was accompanied by either a carboxylic acid group or a titanium bonded carbonate group when the thick films were heated with a low heating rate (0.05 °C/s), while for faster heating the absorption bands from this functional group were less pronounced. The presence of a carboxylic acid group or a titanium bonded carbonate group could explain the two steps during the last part of the decomposition of the powders observed by thermal analysis. Both from the *in situ* IR (Section 4.4) and the *in situ* XRD (Section 4.1), it was found that the pyrolysis products were observed to influence the crystallization process and the chemistry of these phases were influenced by the heating profile, and the thermal analysis further supports these findings.

Table 5.2: Summary of the temperatures for the different features in the mass loss curves for the precursor powders during thermal analysis.

Powder	**DSC peak [°C]**	**Stable mass [°C]**	**Decomposition step 1 [°C]**	**Decomposition step 2 [°C]**
$BaTiO_3$ - 0.2 °C/s	505	685	550-615	615-685
$BaTiO_3$ - 0.02 °C/s	450	615	450-530	530-615
BCT - 0.2 °C/s	510	695	560-650	650-695
BCT - 0.02 °C/s	450	640	450-540	540-640
BCZT - 0.2 °C/s	525	725	560-615	615-725
BCZT - 0.02 °C/s	450	645	450-550	550-645

5.3 *In situ* X-ray powder diffraction in variable CO_2 atmosphere

The effect of the partial pressure of CO_2 on the decomposition of the $BaTiO_3$ precursor powders was studied by *in situ* XRD during heating. The same heating program (Figure 3.5(a)) was used for atmospheres with 0, 25, 50, 75, and 100 % CO_2 in synthetic air. All the recorded diffractograms can be found in Appendix A.1.1.

The phases present in each recorded diffractogram as a function of time and CO_2 partial pressure are summarized in Figure 5.9. The results for the 0 % CO_2 (synthetic air) correspond well with the *ex situ* powder XRD results (Figure 5.2). The oxycarbonate formation was unaffected by increasing CO_2 partial pressure, as it formed above 505 °C in all the gas mixtures, except in pure CO_2. However, for the samples heated in a CO_2 rich atmosphere, the aragonite-type $BaCO_3$ formed as a thermodynamically stable phase alongside the oxycarbonate. The temperatures used during the *in situ* powder XRD measurements were not sufficient to remove $BaCO_3$ (aragonite), so once formed the aragonite remained, even after formation of $BaTiO_3$.

The stability of oxycarbonate over $BaTiO_3$ nucleation showed a strong CO_2 dependence even though the formation temperature for the oxycarbonate was unaffected by the CO_2 partial pressure. In synthetic air, the oxycarbonate decomposed below 600 °C, while in a CO_2 rich atmosphere it was still present at 675 °C (Figure 5.9). The increased oxycarbonate stability also affected the $BaTiO_3$ nucleation temperature, which was below 565 °C in synthetic air, but increased to above 650 °C in the CO_2 rich atmosphere. There were no significant differences in the phase evolution of the samples heated in 25-75 % CO_2.

The $BaTiO_3$ nucleation temperature was increased up to 700 °C in a 100 % CO_2 atmosphere. However, only a fraction of the powder sample transformed into $BaTiO_3$, while most of the sample consisted of a black amorphous powder after the experiment, showing that the decomposition of the precursor powder depends on an oxygen containing atmosphere.

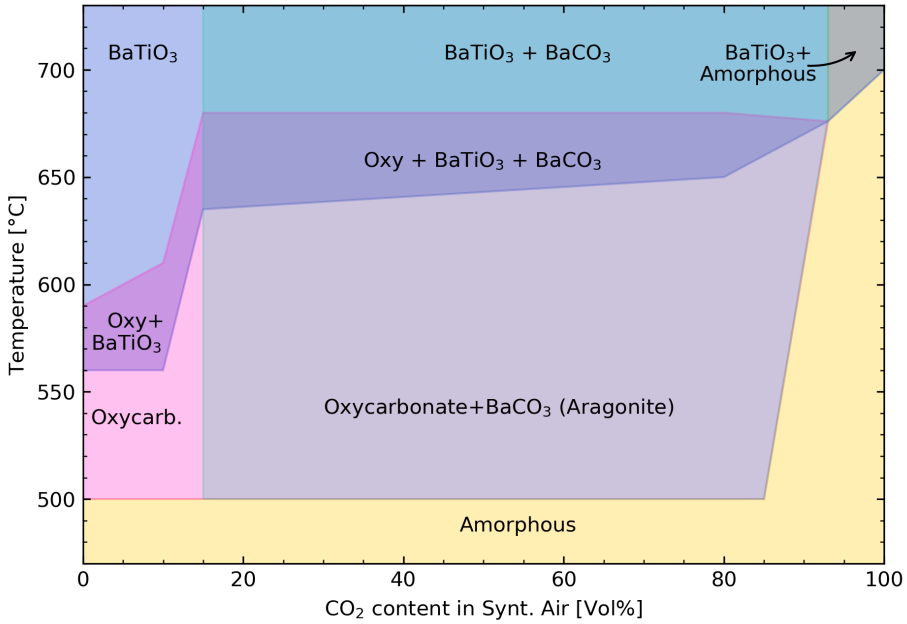

Figure 5.9: Summary of the phases present as a function of both temperature and CO_2 partial pressure during *in situ* XRD measurements of the $BaTiO_3$ precursor powder.

A comparison of the diffractograms of intermediate phases right before $BaTiO_3$ nucleation in various CO_2 partial pressure is shown in Figure 5.10. The diffractogram obtained in 100 % CO_2 is included even though no intermediate phases were observed. The most prominent feature in the diffractograms are the 2-3 reflections in the 2ϑ-range 20-30°.

The *ex situ* diffractogram of a $BaTiO_3$ precursor powder calcined at 585 °C in 50 % CO_2 is shown in Figure 5.11(a), along with the calculated diffractogram from Rietveld refinements. The quantitative phase composition according to the refinement was 27 wt% aragonite and 73 wt% calcite-type $BaCO_3$, with cell parameters listed in Table 5.3. The diffractogram of the sample heated in 50 % CO_2 *in situ* (Figure 5.11(b)) confirms the diffractogram obtained *ex situ*. The sample heated *in situ* to 546 °C in synthetic air (Figure 5.11(c)) shows the presence of only the oxycarbonate phase (with a calcite-like structure) and no aragonite.

Figure 5.12 summarizes the Rietveld refinements of the *in situ* XRD of the powders heated in different CO_2 partial pressures. The lattice parameter for the powder heated in synthetic air decreased slightly with increasing temperature and at the hold step, while the crystallite size increased slightly. The lattice parameter was larger than the bulk values (shown in Figure 5.3), but the crystallite sizes are simi-

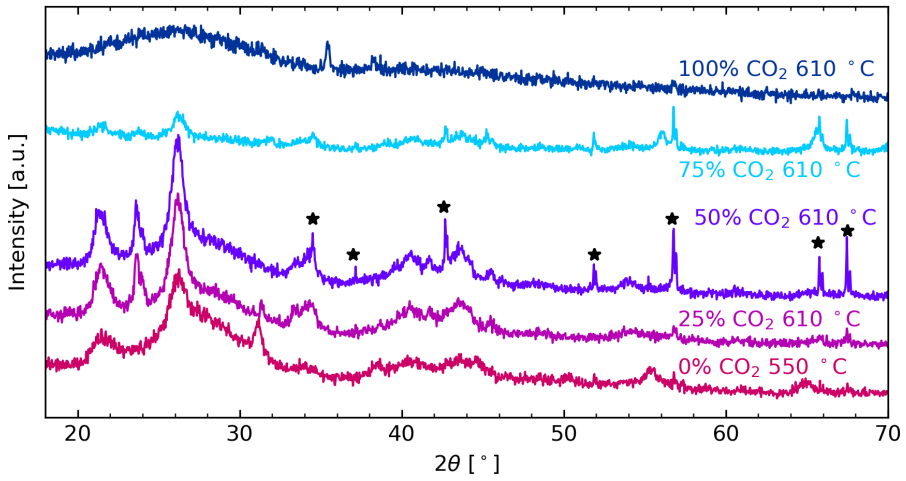

Figure 5.10: XRD patterns of the $BaTiO_3$ precursor powders during *in situ* heating showing the intermediate phases at temperatures right before perovskite nucleation (except the 100 % CO_2 powder, where there were no intermediate phases.) The sharp Bragg reflections from the alumina crucible are marked with an asterisk.

Table 5.3: Results from Rietveld refinement of the carbonate phases that formed during heating of $BaTiO_3$ precursor powders in different CO_2 atmosphere.

Powder	**$BaCO_3$ phase**	**Lattice Parameters [Å]**	**Cryst.size [nm]**	**R_{wp}**
Ex situ 585 °C in 50 % CO_2	Calcite (Trigonal, $R\bar{3}mH$) [65, 69, 74]	a=5.2444(2), c=9.8632(8)	8.0	4.8
	Aragonite (Orthorhombic, Pmcn) [69]	a=6.4584(7), b=5.2802(1), c=8.9239(9)	25.8	
C *In situ* 585 °C in 50 % CO_2	Calcite (Trigonal, $R\bar{3}mH$) [65, 69, 74]	a=5.2217(3), c=10.3453(6)	7.1	9.2
	Aragonite (Orthorhombic, Pmcn) [69]	a=6.6440(7), b=5.3186(4), c=8.9338(2)	18.1	
In situ 546 °C in 0 % CO_2	Calcite (Trigonal, $R\bar{3}mH$) [65, 69, 74]	a=5.2135(2), c=10.3498(8)	5.5	5.6

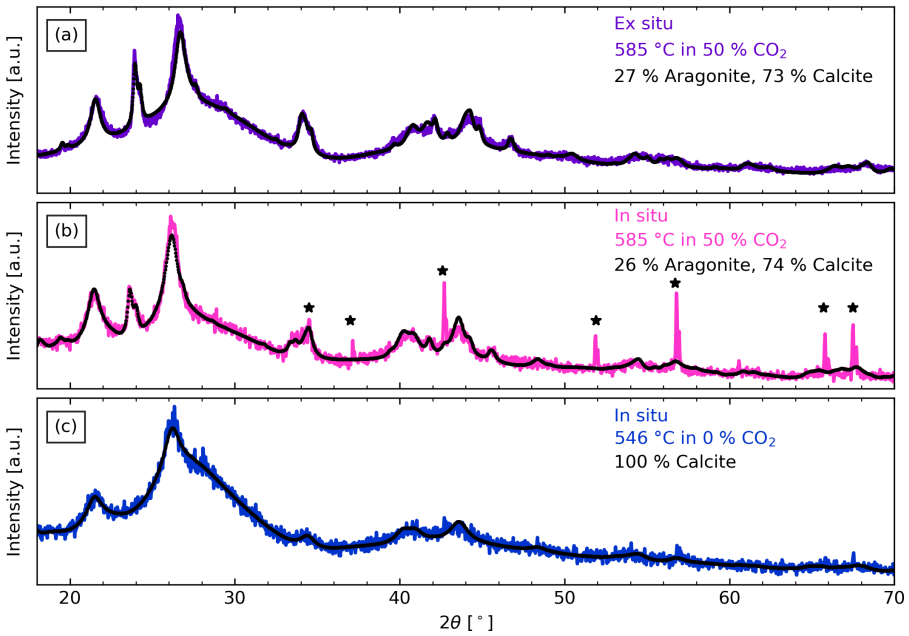

Figure 5.11: XRD patterns and Rietveld refinements of (a) $BaTiO_3$ precursor powder recorded *ex situ* in ambient atmosphere after the powder was heated to 585 °C in 50 % CO_2 for 1 h, (b) $BaTiO_3$ precursor powder heated *in situ* to 585 °C in 50 % CO_2 and (c) $BaTiO_3$ precursor powder heated *in situ* to 546 °C in 0 % CO_2 (synthetic air). The sharp peaks from the alumina crucible are marked with an asterisk.

---

lar to those obtained for the powders calcined *ex situ* (Table 5.1). The powders heated in 25 and 50 % CO_2 atmospheres nucleated at a higher temperature than the powder in synthetic air, and with slightly lower lattice parameters and larger crystallite size. The crystallite sizes of the powders heated on 25 and 50 % CO_2 increased rapidly at first and then more slowly during the hold step, while the lattice parameters decreased slightly. In the powder heated in 75 % CO_2, nucleation resulted in a lattice parameter similar to the ones observed for the powders heated in 25 % and 50 % CO_2, but the lattice parameter decreased while the others increased. The crystallite size had an opposite trend compared to the other powders. The behaviour of the sample heated in 100 % CO_2 was unexpected, but the decrease in crystallite size could be caused by reaction with CO_2 after nucleation. For all samples, both the crystallite size and the lattice parameter decrease during cooling to ambient temperature due to thermal contraction and possibly also shifts in the sample position, although this should be accounted for in the refinement. The *in situ* and *ex situ* refinements at ambient temperature deviate for the 75 and 100 % CO_2 samples because of X-ray absorption by CO_2 (Figure A.7), and the *in situ* values for these samples are therefore less accurate.

Figure 5.13(a) shows IR spectra of the powders heated in different CO_2 partial pressures, measured after cooling. The perovskite signature (between 400-600 cm^{-1}) was clearly visible in all spectra, except the one heated in 100 % CO_2. In addition, there was a strong absorption from $BaCO_3$ in the samples heat treated in 25-75 % CO_2, and both the oop-band and as-band were split indicating that there were both calcite and aragonite-type $BaCO_3$ present. The XRD patterns of the same samples are shown in Figure 5.13(b). The main phase in all diffractograms was $BaTiO_3$, but there were also minor reflections from aragonite-type $BaCO_3$ in the powders heated in 25-75 % CO_2. The crystallinity of the 100 % CO_2 sample was poor compared with the other samples, which can also be seen from the diffractograms.

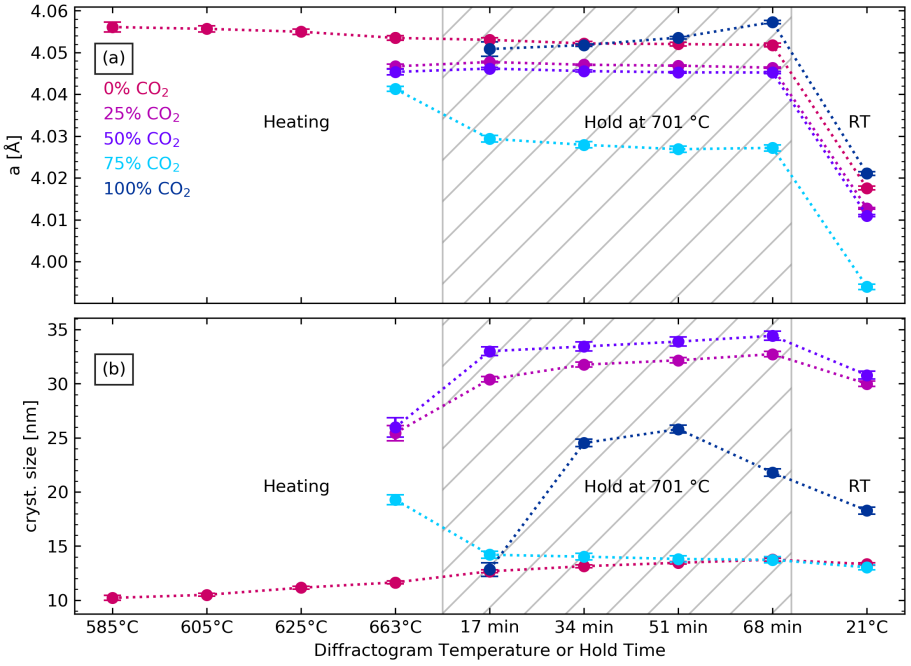

Figure 5.12: (a) The lattice parameter and (b) the crystalline size from the Rietveld refinements as a function of temperature for the powders heated in variable CO_2 partial pressure.

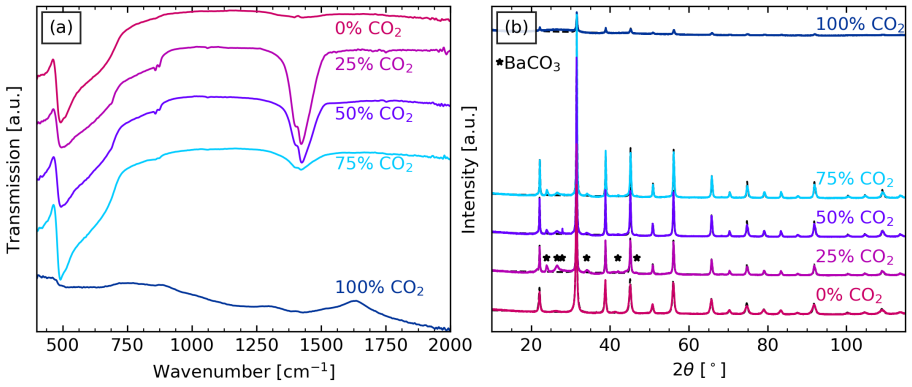

Figure 5.13: (a) IR spectra and (b) XRD patterns and calculated diffractograms from Rietveld refinements of the powders heated in different CO_2 partial pressure measured at ambient temperature afterwards.

6 Potassium sodium niobate films

The influence of the precursor chemistry on aqueous chemical solution deposition of potassium sodium niobate ($K_{0.5}Na_{0.5}NbO_3$, KNN) films has already been reported. [8,9] Moreover, the improved film texture with addition of a salt flux have also been reported [8], but the mechanism was not fully investigated. Therefore, a selection of single-layered KNN-based films from both malic acid (MA) and oxalate (Ox) precursors and with the addition of salt flux (sf) were characterized by *in situ* XRD and IR spectroscopy.

6.1 *In situ* synchrotron X-ray diffraction of KNN thin films

A contour plot of the *in situ* diffractograms as a function of temperature for a KNN-Ox thin film is shown in Figure 6.1. The thermal processing of the precursor film resulted in phase pure KNN, where the nucleation of the perovskite phase occurred at 484 °C. Following the perovskite nucleation, a secondary $K_4Nb_6O_{17}$ phase was present in the temperature range 493-588 °C, although the peaks were weak and hardly visible in the surface plot, except right after nucleation. This secondary phase is commonly observed in KNN films and was observed in films from the same precursor solution reported by Gaukås *et al.* [9] The KNN-Ox film was polycrystalline with full diffraction rings and no signs of any preferential orientation in the single-layered film.

A summary of the nucleation temperatures of KNN as a function of heating rate for the different KNN films, determined by *in situ* XRD, is shown in Figure 6.2(a). All films were heated with a single step annealing program. The presence of the secondary $K_4Nb_6O_{17}$ phase is also indicated by the vertical lines for the KNN-Ox films. No secondary phase was observed in the case of the KNN-MA films, in accordance with the findings of Gaukås *et al.* [9] The nucleation temperatures were higher for the KNN-MA compared to the KNN-Ox films, but the addition of salt flux lowered the nucleation temperature and the temperature region for the secondary phase in the KNN-Ox films was significantly decreased. The results in Figure 6.2(a) correspond well with the findings of Gaukås *et al.* [9] and Pham *et al.* [8] The phase evolution and nucleation temperature for the KNN-MA film did not change when

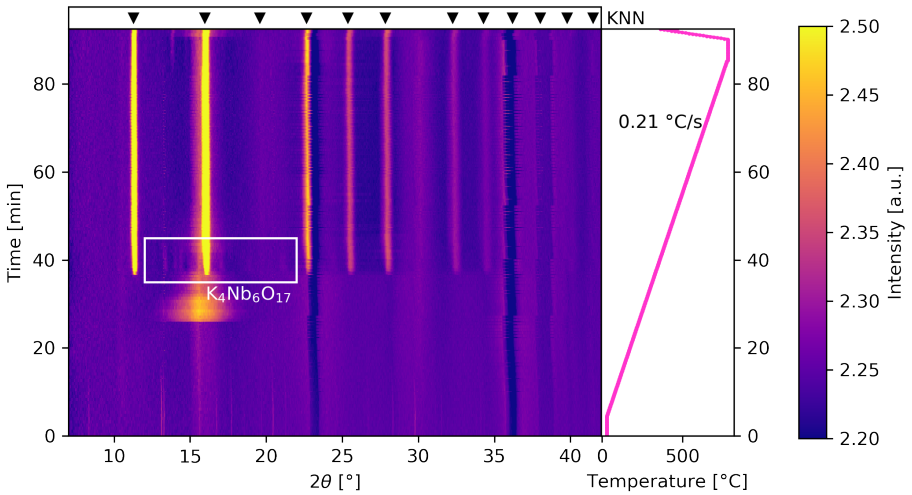

Figure 6.1: Contour plot of the *in situ* diffractograms for a KNN-Ox thin film on (100) STO as a function of time with the corresponding temperature profile. A secondary $K_4Nb_6O_{17}$ phase is also indicated. Any features before KNN crystallization are a result of the gaps in the detector, the data treatment or diffuse scattering from the substrate. The wavelength was 0.78449 Å.

---

a Pt/Si substrate was used instead of STO for a heating rate of 0.2 °C/s. All the KNN thin films characterized *in situ* were polycrystalline, independent of precursor solution, salt flux and heating rate.

The temperature dependence of the lattice parameters from Rietveld refinements on the KNN films are shown in Figure 6.2(b). Cubic KNN was used in the refinements ($Pm\bar{3}m$, ICSD card #186326). The KNN-MA films possessed a higher lattice parameter than the KNN-Ox films, and the addition of salt flux increased this difference. Interestingly, no secondary phases was observed in the KNN-Oxsf film prepared by 5 °C/s heating rate, in contrast to the presence of the secondary phase at 0.2 °C/s. It is however possible that with the higher heating rate the secondary phase formed but was not captured in the recoded diffractograms.

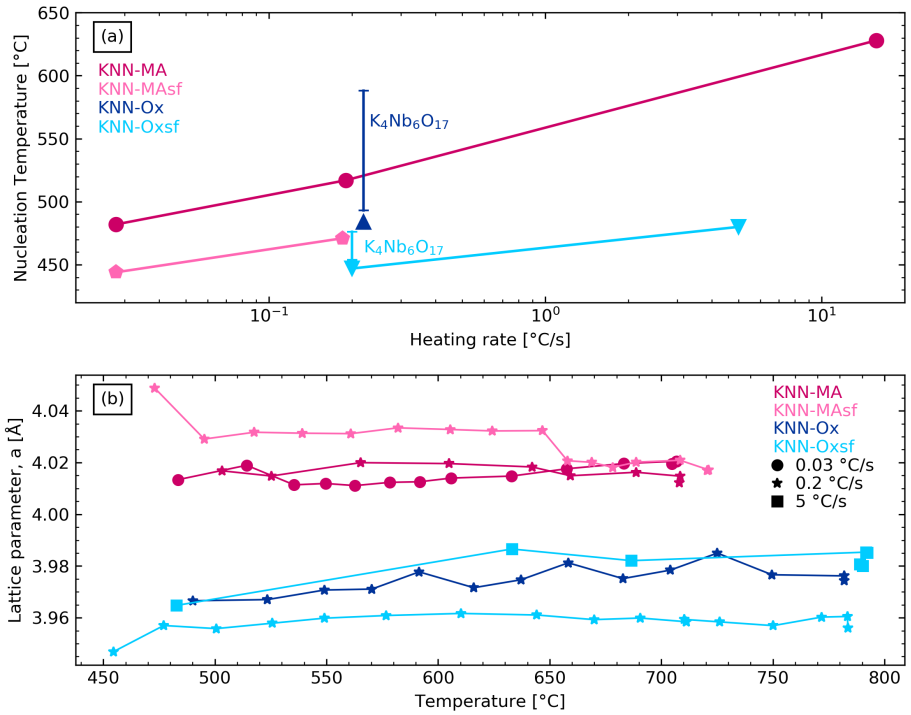

Figure 6.2: (a) Comparison of the nucleation temperature for KNN and temperature region for the presence of a secondary phase (vertical lines) as a function of heating rate annealing of KNN-MA, KNN-Ox thin films on (100) STO, compared to films with the addition of salt flux (sf). (b) Lattice parameters from Rietveld refinements as a function of temperature for KNN thin films on (100) STO.

6.2 *In situ* infrared spectroscopy of KNN thick films

In situ IR spectra of the KNN-MA thick film heated with a heating rate of 0.5 °C/s to the maximum temperature (∼612 °C) and annealed for 20-30 min are shown in Figure 6.3. At low temperature the spectra show the same organic functional groups as observed in the powders from the same precursor solution reported by Gaukås *et al.* [9] As the temperature was increased, decomposition of the organic precursors was initiated, and above 380 °C a broad band (indicated by a horizontal arrow) formed, which Gaukås *et al.* attributed to a residual carbonaceous material. [9] When the temperature reached the hold step, the organic part of the film had decomposed, and only a broad band at (400-900 cm^{-1}) corresponding to Nb-O octahedra was present. In the spectrum recorded of the KNN-MA film after cooling (without the dome), a strong Nb-O band was observed confirming the formation of KNN.

The *in situ* IR spectra of the KNN-MAsf thick film is shown in Figure 6.4. The same features as in the KNN-MA spectrum can be seen at low temperature, and the phase evolution was similar to the KNN-MA film, up to the temperature where the Nb-O band forms. This band appeared at a lower temperature (546 °C) in the KNN-MAsf film, compared to 612 °C for the KNN-MA film. However, with the addition of a salt flux, a strong carbonate band (asymmetrical stretching band) was observed at ∼1430 cm^{-1} at the same time as the Nb-O perovskite band appeared. The appearance of a carbonate band after annealing at maximum temperature was caused by carbonate deposition on the dome windows, evidenced by the spectrum recorded of the KNN-MAsf film after cooling (without the dome), where there was no sign of the carbonate. The spectrum after cooling confirms the formation of KNN.

The IR spectra of a KNN-Ox film are displayed in Figure 6.5, while the IR spectra of a KNN-Oxsf film are presented in Figure 6.6. Above 280 °C and 300 °C, the C-O and C=O absorption bands at 1240 cm^{-1}, 1375 cm^{-1}, and 1680-1710 cm^{-1}, identified by Gaukås *et al.* [9], appeared for both the KNN-Ox and KNN-Oxsf films, respectively. With further increasing temperature, the C-O and C=O bands decreased and the as-band from the carbonates emerged as the perovskite Nb-O band appeared. The carbonates were observed to be build up on the dome windows confirming volatility of these species. The total removal of carbonate was confirmed by considering the IR spectra of the KNN-Ox and KNN-Oxsf films (Figure 6.5 and 6.6) recorded after cooling (without the dome). The salt flux seems to have less effect in the phase evolution of the oxalate films compared to the malic acid films.

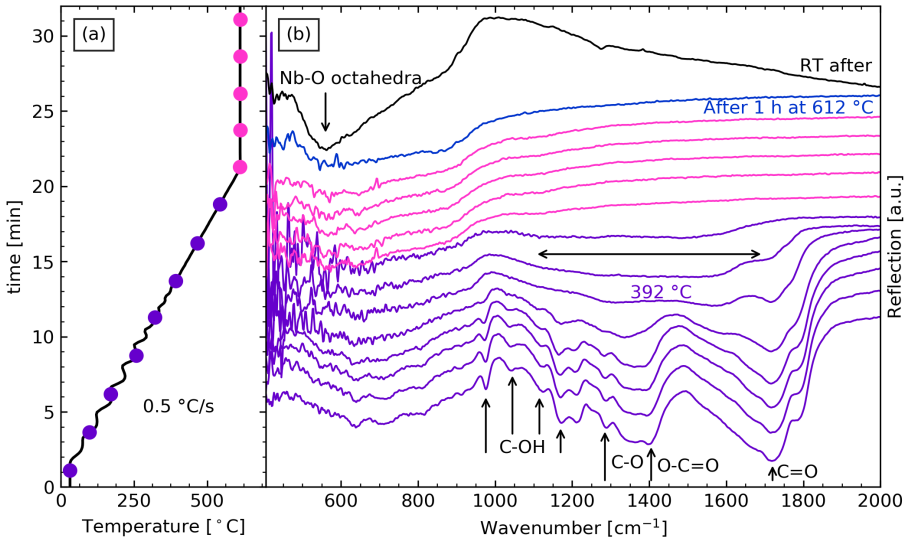

Figure 6.3: (a) Temperature profile and (b) *in situ* IR spectra during annealing of a KNN-MA thick film.

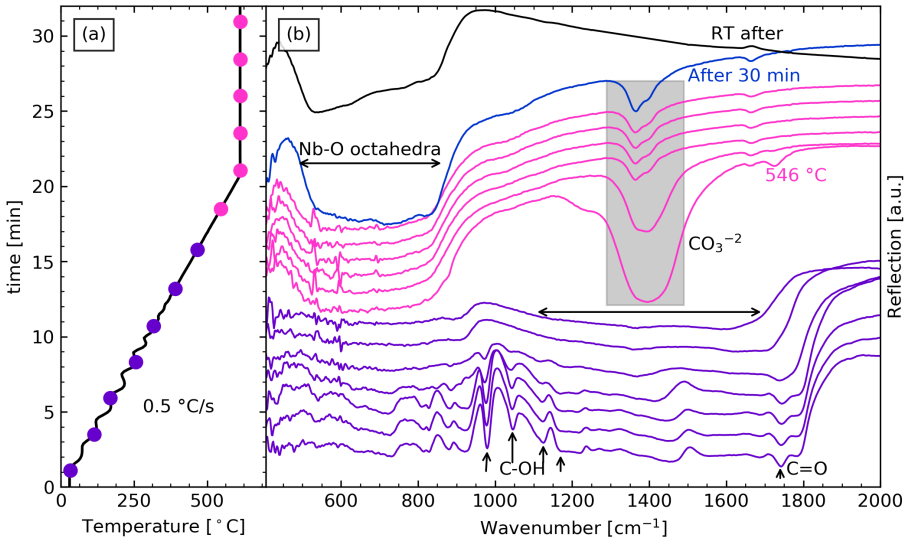

Figure 6.4: (a) Temperature profile and (b) *in situ* IR spectra during annealing of a KNN-MAsf thick film.

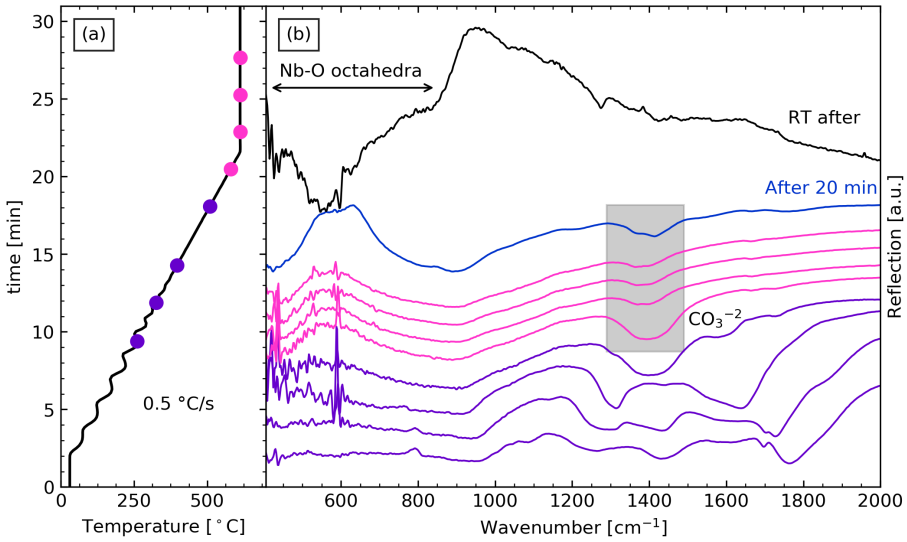

Figure 6.5: (a) Temperature profile and (b) *in situ* IR spectra during annealing of a KNN-Ox thick film.

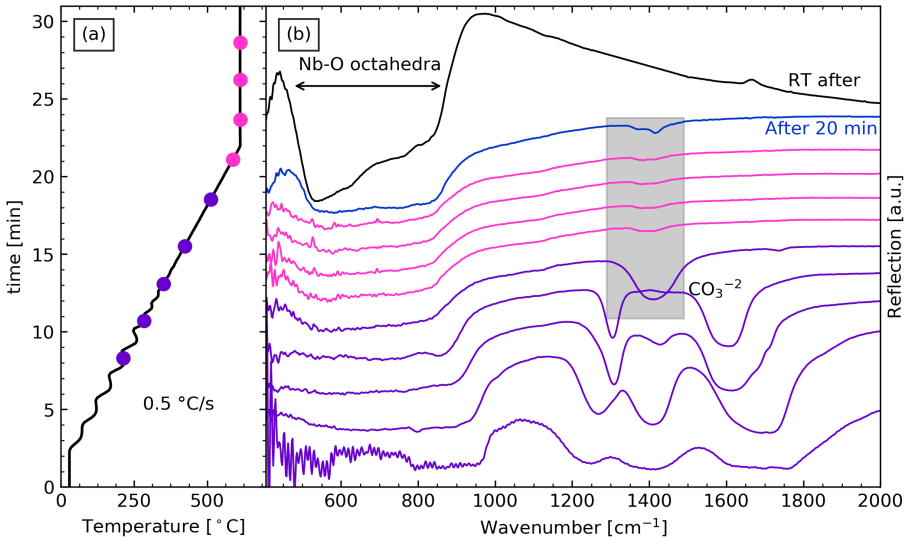

Figure 6.6: (a) Temperature profile and (b) *in situ* IR spectra during annealing of a KNN-Oxsf thick film.

Discussion

7 Tailoring of high quality films by aqueous chemical solution deposition

7.1 Barium titanate based thin films

The decomposition and crystallization process of $BaTiO_3$-based thin films was investigated with *in situ* characterization tools, where a range of selected processing parameters were varied. In addition, *complementary ex situ* characterization was also carried out to study the thin films microstructure, preferred orientation and ferroelectric properties. The basis for the investigation was $BaTiO_3$ thin films, and the effect of cation substitution, substrate orientation and type of substrates were analysed. Powders from the same precursor solutions were investigated to reveal additional information about the precursor chemistry, decomposition and pyrolysis reactions. The important aspects for fabricating phase pure highly textured $BaTiO_3$ films are discussed.

7.1.1 Precursor chemistry, decomposition and pyrolysis reactions

The precursor chemistry is an important aspect of film fabrication by CSD, and considerations should be taken to ensure a stable solution with the desired cations are achieved. With water as the solvent additives such as complexing agents might be necessary to ensure sufficient solubility of the cations. In this work, stable aqueous solutions of barium, calcium, zirconium and titanium were prepared, where the cations were complexed with citric acid and in addition EDTA for the alkaline earth cations. Most transition metals form stable complexes with citric acid in water, but basic cations like the alkali earths only form weak complexes [199], so for the most basic alkaline earths, e.g. barium, it was previously reported that EDTA as a complexing agent was necessary in combination with citric acid. [200]

The Ba-solution used in this work was prepared based on the work of Sletnes *et al.* [200] and Rioja-Monllor *et al.* [201] and the Ti-solution based on the work of Haugen *et al.* [202] and Christensen *et al.* [203] The Ca-solution was prepared following the recipe for the Ba-solution, and Zr was complexed with the same molar

ratio of citric acid as in the Ti-solution, even though citric acid and EDTA are not necessary for stabilizing solutions of Ca and Zr. [128] The addition of complexing agents to the Ca and Zr-solutions were done to ensure a similar concentration of organics and pH as the Ba- and Ti-solutions, so the concentration and chemistry of the resulting perovskite precursor solution were not changed significantly with cation substitution.

Concentration of the precursor solutions will influence the crystalline film thickness. Multilayer polycrystalline films prepared from precursors with concentrations of 0.13 M and 0.26 M and heated with the same program, had thicknesses of 193 and 626 nm for 15 layers, respectively (Section 4.5.1). Hence, film thickness is not linearly dependent on the precursor concentration, which could be related to the viscosity of the solutions.

Transformation pathway: decomposition and pyrolysis

The decomposition of the $BaTiO_3$ precursor films followed the oxycarbonate forming route as reviewed in Section 2.4.1, so most likely a type of mixed metal citric acid complex formed in the precursor solution. The decomposition and pyrolysis reactions can be divided into the following steps, which are illustrated in Figure 7.1;

Drying (150-200 °C): In this temperature range water evaporates and an organic network forms, where the barium and titanium ions are bonded in close proximity by the surrounding complexing agents. The dried film was resolvable in water showing that no gelling occurred, as opposed to precursor solutions with organic solvents or added chelating agents, where the as-deposited film forms a gel right after deposition and is therefore not resolvable (Section 2.2.1).

Decomposition (200-460 °C): At the start of this period the nitrate decomposes, the ammonia evaporates and the organics present in the film start to decompose. However, the wide $RCOO^-$ stretching bands are still present, as seen from the *in situ* IR spectra of the films (Section 4.4) and the IR spectra of the powders (Section 5.2.2), showing that a variety of organic groups are still present in the film. The symmetric and asymmetric stretching bands of the $RCOO^-$ groups become more narrow and shifts toward the asymmetric carbonate frequency as temperature is increased, demonstrating the preference for carbonate formation in this system.

Organic removal and carbonate formation (460-530 °C): The sharp decrease in the mass fraction seen from thermal analysis of the powder precursor (Figure 5.8) corresponds to a narrow temperature range in which the remaining organic compounds are removed and barium carbonate forms. No other functional groups can be seen in the IR spectra at these temperatures (Section 4.4 and 5.2.2). The organic removal (pyrolysis) can be expressed through the following proposed reaction (after Ischenko *et al.* [74]);

$$\text{Organic network} \longrightarrow \text{BaCO}_3\text{-like} + \text{Ba}_y\text{TiO}_{2+y} \tag{7.1}$$

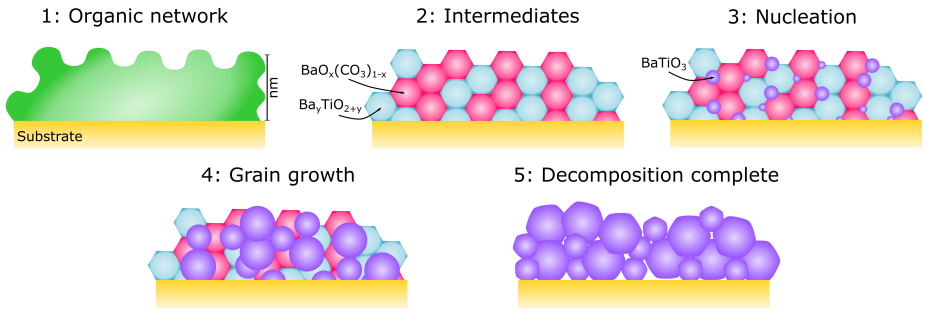

Figure 7.1: Illustration of the decomposition as well as nucleation and growth process in $BaTiO_3$ single layer films from aqueous CSD. 1: At intermediate temperatures the film is an amorphous organic network. 2: The oxycarbonate phase forms, which is proposed to consist of nanosized domains of oxycarbonate and Ti-rich $BaTiO_3$-like phases. 3: Nucleation of $BaTiO_3$ occurs homogeneously at the interfaces between the oxycarbonate and the Ti-rich $BaTiO_3$-like phases. 4: Growth of $BaTiO_3$ occurs through consumption of the oxycarbonate and the Ti-rich $BaTiO_3$-like phases. 5: Decomposition continues until the film is phase pure $BaTiO_3$.

---

which occurs at the start of this temperature region, leaving only $BaCO_3$-like and amorphous Ti-rich $BaTiO_3$-like phases without any long range order in the films. As the temperature is further increased the formation of carbonate starts according to the following proposed reaction;

$$BaCO_3\text{-like} \longrightarrow BaO_x(CO_3)_{1-x} \tag{7.2}$$

The IR carbonate bands form first as broad features with a frequency corresponding to aragonite-type $BaCO_3$ but quickly shifts towards the calcite frequency as temperature is further increased, and then weak reflections corresponding to calcite-type $BaCO_3$ appears in the XRD patterns (Section 4.1-4.3 and 5.2.1). This carbonate formation takes place in the first step of the two-step decomposition seen by thermal analysis on the powders (Figure 5.8 and Table 5.2). Oxycarbonate formation is accompanied by formation of shoulders corresponding to a Ti-carbonate-like phase in the IR spectra. The organic removal and carbonate formation correspond to going from Step 1 in Figure 7.1, where the film in an amorphous organic network, to Step 2 where the film consist of oxycarbonate and titanium rich $BaTiO_3$-like phases. Based on the work of Ischenko *et al.* [74] it is proposed that the oxycarbonate and Ti-rich $BaTiO_3$-like phases are nanosized domains, as the crystallinity of the oxycarbonate is poor and no diffraction can be seen from the Ti-rich phase.

$BaTiO_3$ nucleation and growth (530-600 °C): Nucleation of $BaTiO_3$ in the films occur by decomposition of the oxycarbonate phase through the following reac-

tion proposed by Ischenko *et al.* [74];

$$Ba_yTiO_{2+y} + BaO_x(CO_3)_{1-x} \longrightarrow BaTiO_3 + CO_2\,(g) \tag{7.3}$$

The metastable nature of the oxycarbonate phase ensures complete decomposition. This reaction corresponds the second step in the two-step decomposition evident from thermal analysis on the powders (Figure 5.8 and Table 5.2). The nucleation of $BaTiO_3$ occurs homogeneously throughout the film as the oxycarbonate and Ti-rich phases are intimately mixed, and $BaTiO_3$ growth occurs through the decomposition reaction in Equation 7.3. The nucleation and growth process is illustrated in Steps 3-5 in Figure 7.1.

Phase pure $BaTiO_3$ (above 600 °C): After the oxycarbonate is fully decomposed, the film consists of phase pure $BaTiO_3$. The factors influencing the microstructure, preferential orientation (texture) in the film, lattice parameter and properties of the film depends on the decomposition reactions and annealing conditions, which will be discussed further in Section 7.1.2-7.1.4.

The oxycarbonate phase

The oxycarbonate phase is frequently reported in literature during wet chemical synthesis of $BaTiO_3$, where a mixed metal complex formed in the precursor solution (Section 2.4.1). The characteristic features for this phase reported in literature, such as weak and broad reflections in the XRD patterns due to poor crystallinity, a shift in the absorption frequency from the aragonite- to calcite-type $BaCO_3$ seen by both IR and Raman spectroscopy and a metastable nature, were also observed in this work. The oxycarbonate phase has a structure resembling the calcite-type $BaCO_3$, as the IR absorption bands (Section 4.4 and Section 5.2.2) were consistent with the calcite frequencies, and the Rietveld refinement of powders with the oxycarbonate phase (Figure 5.11) gave a good fit for calcite-type $BaCO_3$ with nanosized crystallites and a slightly higher a/c-ratio (Table 5.3) than the reference structure [69]. However, in the IR spectra (Section 4.4 and Section 5.2.2), the calcite absorption bands were accompanied by shoulders assigned to the symmetric and asymmetric carbonate band perturbed by bonding with titanium in a Ti-carbonate-like group. These shoulders formed alongside the calcite band, which likely means that they are connected to or part of the structure of the oxycarbonate phase.

Arima *et al.* [100], Kikihana *et al.* [101] and Fang *et al.* [102] attributed the formation of the oxycarbonate phase in Pechini-based synthesis of $BaTiO_3$ to the formation of a stable mixed metal citric acid complex. The complex maintained the structure upon heating which resulted in $BaTiO_3$ nucleation from decomposition of the oxycarbonate rather than from solid state reaction of $BaCO_3$ and TiO_2 (Section 2.4.1). The precursor chemistry in this work is different from the Pechini-based routes as there is no polyester formation (or the gelling seen for other CSD routes), but the formation mechanism for the oxycarbonate seems to be similar. Ischenko *et al.* [65] proposed two different stabilizing mechanisms for the oxycarbonate phase, where the first is stabilization of the high temperature calcite-type of $BaCO_3$ with

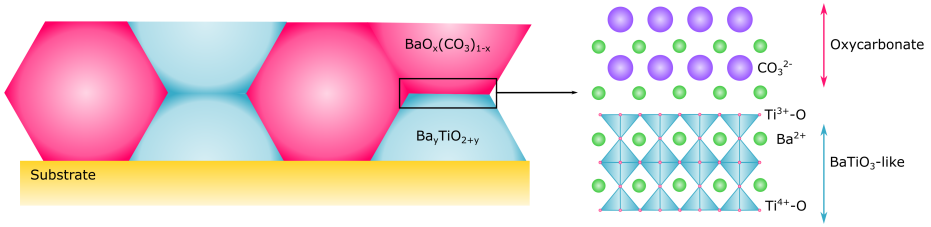

Figure 7.2: Illustration of the interface layers between the oxycarbonate and Ti-rich $BaTiO_3$-like phases, where the calcite structure of the oxycarbonate is stabilized by topotaxial formation from the oxygen deficient interface with the Ti-rich $BaTiO_3$-like structure (adapted from [65]).

---

the substitution of the CO_3^{2-} anions with O^{2-}, which expands the lattice from the hexagonal close packing found in the aragonite-type $BaCO_3$ and therefore stabilizes the less densely packed calcite structure.

The second stabilizing mechanism proposed by Ischenko *et al.* [65] is topotaxial templating of the calcite-type $BaCO_3$ on oxygen deficient Ti-O interface layers, derived from similar mechanisms found in the Ruddlesden-Popper phases ($A_4{}^{II}B_3{}^{IV}O_{10}$). [65] Cubic close-packed ordering of barium, similar to the barium packing in the calcite-type $BaCO_3$, can be supported at the interface with cubic $BaTiO_3$. In the model proposed by Ischenko *et al.*, the oxycarbonate ($BaO_x(CO_3)_{1-x}$) was grown from layers of Ba^{2+} at the interface with layers of Ti^{3+} and O^{2-} that are already present from the Ti-rich $BaTiO_3$-like structure. The proposed local structure is illustrated in Figure 7.2. The oxidation state of titanium in the interface layers is reduced to compensate for the oxygen deficiency [65], but further way from this Ba/Ti-O interface, the Ti-O layers are closer to those found in $BaTiO_3$, with Ti^{4+}. However, in the Ti-rich phase there with no long range ordering as nanosized domains are proposed based on the work of Ischenko *et al.* [65, 74].

This proposed model explains the features of the oxycarbonate phase observed in this work; poor crystallinity due to nanosized domains/clusters, seemingly amorphous titanium compounds due to oxygen deficiency and size, and the requirement of titanium for the oxycarbonate formation as seen from the IR spectra in Figure 5.6. The intimate mixing of barium and titanium in the organic network formed during decomposition could be the reason why this topotaxial templating occurs, which gives rise to the oxycarbonate formation over the formation of separate $BaCO_3$ (aragonite) and TiO_2 particles (e.g. the solid state reaction transformation path in Section 2.4.1). The shoulders in the IR spectra of both the powders and films, at 1280 cm^{-1} and 1590 cm^{-1}, could be due to perturbations of the carbonate group by titanium at the interface between the carbonate and Ti-rich domains.

A key aspect of the model presented by Ischenko *et al.* [65] is the reduced oxidation state of titanium in the interface layers. Titanium in the 3+ oxidation state does not occur often under ambient conditions, but Ischenko *et al.* [65] supported their model with the X-ray photoelectron spectroscopy (XPS) analysis by Cho [110]

on the Pechini-based precursor decomposed at 500 °C for 2 h, which revealed that up to 40 % of the titanium in the decomposed product was reduced to 3+, while at higher temperature this oxidation state was no longer observed.

Influence of the heating rate on the transformation pathway for $BaTiO_3$

The effect of the heating rate on the decomposition of $BaTiO_3$-based films was investigated by *in situ* IR spectroscopy (Section 4.4) and XRD (Section 4.1.1) of the films and supported by thermal analysis of the powders (Section 5.2.3). A shift in the temperature for the different stages of the decomposition presented earlier was observed, where slower heating led to decreased reaction temperatures and more narrow temperature ranges for the different stages of the decomposition. The oxycarbonate phase observed in this work showed similar characteristics for both the films and powders with respect heating rate during decomposition.

The decomposition and pyrolysis temperatures increase with faster heating caused by kinetic limitations of the reactions. The fastest heating rates (>3 °C/s) were only investigated with *in situ* XRD, so only crystallization was observed. In the heating rate range 3-10 °C/s, the nucleation temperatures were significantly increased compared to slower heating and the oxycarbonate and $BaTiO_3$ nucleated simultaneously, showing how the kinetic limitations merge the different decomposition stages presented earlier. For ultra-high heating rates (>10 °C/s), the organic removal and $BaTiO_3$ nucleation can be assumed to occur simultaneously, where $BaTiO_3$ nucleation occurs directly from the amorphous precursor without the formation of oxycarbonate. Even though secondary phases are avoided with the ultra-high heating rates, the microstructure of these films was undesirable as the large amount of organics combust at once causing significant gas evolution, which gives pinholes in the film, as seen for the film heated with 20 °C/s in Figure 4.3(d).

Effect of CO_2 partial pressure on the decomposition of the precursor film

The effect of CO_2 on the decomposition of the $BaTiO_3$ precursors was observed by *in situ* XRD of a thin film (Figure 4.9) and of powders (Section 5.3). Increased partial pressure of CO_2 in the atmosphere stabilizes the oxycarbonate phase over $BaTiO_3$ nucleation by drastically limiting the decomposition reaction in Equation 7.3. For high CO_2 partial pressures (> 25 vol%) the perovskite nucleation temperature increased more than 100 °C. Moreover, the temperature region for coexistence of oxycarbonate and perovskite increased in these high CO_2 partial pressures, which means that even if the decomposition reaction in Equation 7.3 can take place the high partial pressure of CO_2 serves as a kinetic limitation on this reaction.

A second effect of a high CO_2 partial pressure is the formation of the thermodynamically stable aragonite-type $BaCO_3$, which once formed require temperatures above 700 °C to be removed. No secondary Ti-rich phases were observed alongside the perovskite once aragonite-type $BaCO_3$ formed, so the titanium remains as unreacted Ba_yTiO_{2+y}. The aragonite-type $BaCO_3$ formed at the same temperature as the oxycarbonate, so the CO_2 stabilizes a second reaction during the organic removal

step described by this modified version of Equation 7.2;

$$\mathrm{BaCO_3\text{-like} \xrightarrow[\text{I: Air}]{} BaO_x(CO_3)_{1-x}} \qquad \mathrm{BaCO_3\text{-like} \xrightarrow[\text{II: } CO_2]{} BaCO_3 + BaO_x(CO_3)_{1-x}} \tag{7.4}$$

leading to the formation of aragonite-type $BaCO_3$ along with the oxycarbonate phase. The formation of a broad aragonite absorption band before the shift towards calcite formation when the films were annealed in air might be caused by locally enhanced CO_2 partial pressure from decomposing organics, which upon removal decrease the CO_2 partial pressure before the aragonite-type $BaCO_3$ can fully crystallize.

The effect of cation substitution on the decomposition and pyrolysis reactions

The effects of cation substitution on the decomposition and pyrolysis reactions were minor compared to the effects of the heating rate and CO_2, as previously discussed. The mechanisms for formation of oxycarbonate were also unaffected, as was the oxycarbonate structure, since the IR absorption bands of the films (Figure 4.27 and 4.28) and of the powders (Figure 5.7) did not shift in frequency and no other bands appeared compared to the $BaTiO_3$ powders and films. Hence, the calcium truly is in a solid solution with barium in the carbonate phases, and zirconium is similarly coordinated and chemically bonded as titanium.

Calcium substitution did increase the nucleation temperature for the oxycarbonate phase to some extent, which is expected as calcium is less basic than barium and therefore forms less stable carbonates. This effect is also seen by *in situ* XRD of the thin films (Figure 4.6), where the decomposition temperature of the oxycarbonate phase is somewhat reduced compared to the $BaTiO_3$ film, but the thermal analysis of the powders (Figure 5.8 and Table 5.2) indicates that the temperature region for the oxycarbonate decomposition was shifted upwards compared to $BaTiO_3$. These conflicting results could be due to favourable nucleation conditions for the perovskite on the STO substrate for the BCT thin film, while in the powder no such lowered nucleation energy was present.

The effect of zirconium substitution is the most pronounced as the kinetics of the decomposition and pyrolysis reactions is delayed to higher temperatures. This can be seen from the thermal analysis of the powders (Figure 5.8 and Table 5.2), where the temperature for the major organic removal and the end of mass loss is shifted higher in temperature compared to both the $BaTiO_3$ and the BCT powders. Additionally, decomposition of the precursor film and the formation of the oxycarbonate were slower in the BCZT powders, since both a higher temperature and a longer annealing time were necessary for forming this phase as shown in Figure 4.6. The slower kinetics in the BCZT films can be explained by the the lower activation energy required for titanate formation compared to zirconate formation reported in literature. [204, 205] For solid state reactions between $BaCO_3$, TiO_2 and ZrO_2 to form BZT, $BaTiO_3$ formation was reported to start above 700 °C, while $BaZrO_3$

formation started above 800 °C. [205] In addition to the increased formation temperature, the kinetics of $BaZrO_3$ formation was observed to be slower than $BaTiO_3$ formation. [205]

7.1.2 Crystallization: texture and microstructure of the films

In order to achieve a high degree of preferential orientation of films from CSD, both the heating profile and pyrolysis reactions are important. As stated in Section 2.2.2, the transformation pathway, e.g. the phases that form in the system, can influence the nucleation and growth of the crystalline films. With classical nucleation and growth, a high heating rate delays the nucleation to higher temperatures, where heterogenous nucleation at the substrate is more favourable, which will increase the likelihood of crystallographic texture. [6] However, intermediate phases can alter the nucleation into a non-classical regime by acting as nucleation sites or templates for the crystalline film. Thus, the pyrolysis reactions influence the crystallization behaviour and can also determine the crystallographic texture in the film. [6]

Nucleation of the $BaTiO_3$-based films in this work occurred at the interface between the $BaO_x(CO_3)_{1-x}$ and Ba_yTiO_{2+y} domains by the decomposition reaction presented in Equation 7.3 and illustrated in Figure 7.1. The proposed nanosized domains of the oxycarbonate and Ti-rich phases ensures even distribution of nucleation sites through the film, resulting in homogenous nucleation of $BaTiO_3$. The annealing condition will influence the growth process, affecting both degree of preferential orientation in the film, the microstructure and lattice parameters, all of which will be discussed in the following sections.

Mechanisms for formation of texture in a single deposited layer

The degree of preferential orientation of $BaTiO_3$ single layer films by aqueous CSD depends on the heating rate for the single-step annealed films, as seen from the *in situ* XRD results in Section 4.1.1. For $BaTiO_3$ films on (100) STO, the nucleation temperature versus heating rate shown in Figure 4.3 revealed a decreasing nucleation temperature with decreasing heating rate for the textured films, while the azimuthal intensity distribution for the (100) reflection for these films (Figure 4.4) showed an increasing degree of (100) preferred orientation with slower heating. The heating rate limit for achieving texture was found to be ∼3 °C/s, but the diffractograms and azimuthal intensity distribution for the (100) reflection show that this transition is gradual without any sharp limit. The same heating rate dependency for texture was also observed using LAO, MgO and Pt/Si substrates, while fused silica as a substrate gave no texture. A suitable crystal lattice as template therefore seems to be a requirement for achieving $BaTiO_3$ thin films with texture in a single layer, while the degree of preferred orientation depends on the heating rate for single step annealing.

For multi-step annealing, the mechanisms for obtaining texture become more complex as it is no longer solely dependent on the heating rate, but rather the whole temperature profile. It was shown in Figure 4.7 that the total annealing time below the nucleation threshold of both oxycarbonate and $BaTiO_3$ determines

whether preferred orientation developed. Based on the proposed structure of the intermediate phases (Figure 7.2), possible orientation of the Ti-rich $BaTiO_3$-like domains relative to the substrate could be governing the $BaTiO_3$ orientation, but the heating rate during crystallization is important as well. Film III and Film V (Figure 4.7) were textured even though a fast heating rate (25 °C/s) was used during crystallization, and both films had been held for a certain time at a temperature significantly below the nucleation thresholds. Film III had full diffraction rings in addition to the diffraction spots from the (100) preferred orientation, but due to the prolonged annealing at low temperature for Film V the diffraction pattern of this film showed a high degree of texture. Film VI illustrates how the heating rate during crystallization enhances the degree of preferential orientation, as this film had the highest degree of texture for the $BaTiO_3$ films investigated, which can be seen from the diffraction patterns in Figure 4.11. For the single-step annealing, a low heating rate induce more texture, but also entail a longer time at intermediate temperature, so the mechanisms for texture formation are the same independent of the type of temperature profile.

The pyrolysis reactions are of utmost importance for the texture formation in the $BaTiO_3$ films. The temperature profile will determine which reactions are taking place. Ideally for a high degree of texture, the low temperature annealing should allow the removal of all organics, so only the intermediate oxycarbonate and Ti-rich phases remain. These reactions occur in the temperature range 400-500 °C, and the film should be annealed sufficiently to allow these phases to adhere to the substrate orientation before crystallization. The annealing can be done either by using a low heating rate for the initial heating, or by holding at a suitable temperature. The hold temperature needs to be significantly below the nucleation threshold, as illustrated by Film II in Figure 4.7, where the temperature was chosen to be at the nucleation threshold for $BaTiO_3$, resulting in a film with no texture.

Mechanisms for formation of texture in multi-layered films

Repeated annealing also causes preferential orientation in the films. Single layered films made by a similar heating program as the polycrystalline heating program in Figure 3.1, was studied by *in situ* XRD (Section 4.1.1), and no texture was observed. However, corresponding multi-layered films characterized by TEM shows a certain degree of preferred orientation (Figure 4.31), as district diffraction spots are seen for the film, but no rings. The multilayer film also has an epitaxial layer, which formed during the first annealing, since signs of epitaxy can be seen in the textured and polycrystalline single layered films by *in situ* XRD. The epitaxial layer is only a few nm thick, but epitaxial grains are also seen for the polycrystalline film, where the grains extends further into the film than the average thickness of one deposited layer. The extension of the epitaxy shows that the epitaxial grains grow from the substrate as constitutive layers are annealed. The lack of full diffraction rings in the selected area diffraction patterns for this multilayer film (Figure 4.31) demonstrates that there is a certain degree of interlayer epitaxy, even when this heating program does not result in texture for a single layer.

The texture heating program (Figure 3.1) gives a high degree texture in both

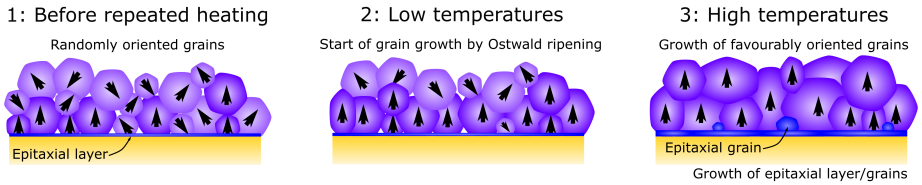

Figure 7.3: Illustration of the proposed formation mechanism of crystallographic texture and epitaxial layers in thin film during repeated annealing. 1: Polycrystalline first layer with randomly oriented grains and a thin epitaxial layer at the substrate interface. 2: The growth of favourably oriented grains by Ostwald ripening starts at low temperatures. 3: The grain growth continues at high temperature and the epitaxial layer increases in thickness and epitaxial grains grow from the substrate.

---

single and multi-layered films. The multi-layered film studied by TEM is close to epitaxial in certain areas according to the selected area diffraction patterns (Figure 4.32). There is also an epitaxial layer at the substrate interface, which corresponds well with the high degree of preferential orientation and signs of epitaxy seen in the single-layered film heated with a similar heating program during *in situ* XRD (Figure 4.1).

The illustration in Figure 7.3 shows the proposed structural changes by repeated annealing in the first deposited layer in a film heated so that each layer is initially polycrystalline after deposition (Step 1 in Figure 7.3). In the initial stage of the repeated annealing at low temperatures (Step 2 in Figure 7.3), the grain growth of favourably oriented grains by Ostwald ripening starts, which continues at higher temperatures (Step 3 in Figure 7.3). The maximum temperature is too low to enable the extensive grain growth associated with the final stage of a sintering process, but this was observed for the films post-annealed at a high temperature (1000 °C) in Figure 4.35. As more layers are deposited, the following layers will template after the orientation of underlying grains. However, epitaxy only occurs in a thin layer at the substrate interface or in grains grown from the substrate as the temperatures are not sufficient to overcome grain boundaries [1, 206], but it is possible that the large grains in the post-annealed multilayer films (Figure 4.35) have epitaxy extending further into the films.

The induced texture diminish the difference between the multi-layered films heated with the polycrystalline and the texture heating program (Section 4.5), which explain why these films have a similar microstructure and ferroelectric response (Section 4.6).

For all the single-layered $BaTiO_3$ films studied in this work, the oxycarbonate phase was not present above 620 °C, giving phase pure films. But, the formation of oxycarbonate could be detrimental to multi-layer $BaTiO_3$ films if each layer is not fully crystallized. Khomyakova *et al.* [128] reported that in aqueous CSD of multilayer BCZT films, the oxycarbonate formation led to phase segregation and a secondary $CaZrTi_2O_7$ phase if each layer was not fully crystallized before deposition

of the next. The same reaction mechanisms as presented in Khomyakova *et al.* [128] should hold for the $BaTiO_3$ films as well, where Ba is depleted from the perovskite phase by local high CO_2 pressure from the oxycarbonate decomposition, leading to areas with Ba-deficient Ba_yTiO_{2+y} phases and $BaCO_3$ (aragonite-type). A thorough understanding and control over the decomposition reactions and the transformation pathway for the precursors are therefore of outmost importance for producing high quality multilayer thin films with high degree of texture from CSD.

Microstructure and lattice parameters

The film microstructure and grain size were shown to depend on the heating rate during crystallization for the single-layered films. If a high heating rate was used, the films had small spherical grains, full coverage and a large lattice parameter (Microstructure 1 in Figure 7.4), whereas a low heating rate gave larger interconnected grains with incomplete coverage with a lattice parameter close to the bulk value (Microstructure 2 in Figure 7.4), independent of cation substitution and substrate. The grain growth seems to follow classical nucleation theory, even if the intermediate phases determining the texture, alters the transformation pathway and nucleation into a non-classical regime. Classically, small grains are predicted for fast heating, when the nucleation rate is high, and the entire film should crystallize simultaneously. [6] A low heating rate should give lower nucleation rate, but the grain coarsen by the prolonged annealing time, which is exactly what is observed for the single layered films in Section 4.1.1, where the films heated with a low heating rate resulted in a microstructure of grains with necking and texture.

The lattice parameters of the $BaTiO_3$ thin films provided in Figure 4.8 and Table 4.1 deviates from the bulk values due to both finite size effects and strain. The strain in the films stems from both the lattice mismatch and the difference in thermal expansion coefficient relative to the substrate. According to Table 3.4, $BaTiO_3$ has a larger lattice parameter than the substrates, except for MgO, which should result in compressive strain. But $BaTiO_3$ has a larger thermal expansion

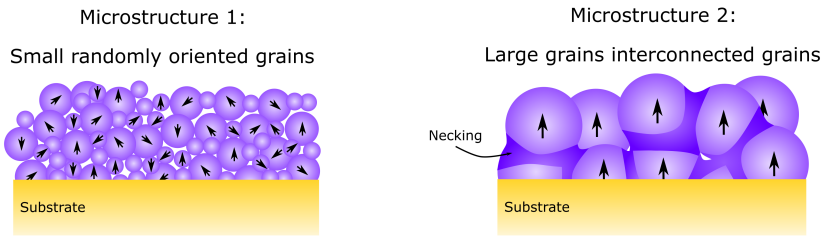

Figure 7.4: Illustration of the two types of microstructures for thin films prepared by aqueous CSD. 1: Small spherical randomly oriented grains form when a high heating rate is used during crystallization. 2: Large oriented interconnected grains forms when a slow heating rate is used during crystallization leading to certain degree of preferred orientation in the film.

coefficient than all the substrates [46], which should give tensile strain in the film during cooling. The strain in the films after cooling then depends on how much the lattice mismatch contributes and how clamped the film contraction was by the substrate. Relaxation also contributes to the observed lattice parameters, as lattice matching with the substrate can only be retained in a few unit cells. [13] A single layer film were in the range 12-42 nm, dependent on the precursor concentration and porosity, giving non-uniform strain in the films. In general, the lattice parameters were higher for the polycrystalline films and decreased with increasing degree of texture, meaning that the lattice parameter is governed by the degree of preferential orientation in the films and strain, where the thermal contribution dominates over lattice mismatch due to the film thickness.

The influence of the substrate and effect of cation substitution on the crystallization process

Both the oxycarbonate and $BaTiO_3$ showed a heating rate dependency for the nucleation on STO (Section 4.1.1). The similar crystal structure of STO and $BaTiO_3$ leads to lower nucleation energies at the substrate interface for the intermediate Ti-rich $BaTiO_3$-like phases (Ba_yTiO_{2+y}) but also for $BaTiO_3$, resulting in lower nucleation temperature for both and decreased oxycarbonate stability on STO compared to Pt/Si (Figure 4.5). This lowered nucleation temperature demonstrates that heterogeneous nucleation at the substrate interface takes place. Considering the proposed composition of the oxycarbonate; calcite-like $BaO_x(CO_3)_{1-x}$ and oxygen deficient Ba_yTiO_{2+y}, such heterogeneous nucleation with a preferred orientation possibly adhering the STO lattice could be expected, especially for the Ba_yTiO_{2+y}.

The nucleation temperature of oxycarbonate on Pt/Si is higher than on STO and is unaffected by the heating rate, hence nucleation occurs at temperatures similar to the powders (Chapter 5). The crystallization of $BaTiO_3$ on Pt/Si follows the same trend as on STO, where preferred orientation is governed by the pyrolysis products. With a transformation pathway where the pyrolysis products act as templates for the $BaTiO_3$ nucleation, the nature of the precursor phases would govern the resulting preferred orientation in the crystalline film. The nucleation temperature for $BaTiO_3$ on fused silica and Pt/Si were only $\sim$10 °C higher than on STO, showing that the effect of heterogenous nucleation on STO was more pronounced for the oxycarbonate phase compared to $BaTiO_3$, especially for heating rates lower than 0.2 °C/s. The crystallization of $BaTiO_3$ films on MgO and LAO was only investigated *ex situ*, but since the same heating programs were used as for the films on STO, and the films on MgO and LAO showed the same degree of texture and also showed the same tendency for epitaxy (Section 7.1.3), these substrates can be assumed to not change the crystallization process significantly.

Calcium substitution somewhat increases the nucleation temperature for both the oxycarbonate and the perovskite, while zirconium substitution significantly increases the oxycarbonate nucleation and decomposition temperature, while the perovskite nucleation barely increased. The slower kinetics for formation with zirconium substitution are also reflected in the texture formation, only the lowest heating rate (0.03 °C/s) gave texture in the BCZT films.

7.1.3 Epitaxy and cube-on-cube growth in the films

The epitaxial films investigated in this work were relaxed as evident by the periodic edge dislocations observed with TEM (Figure 4.29). A more suitable term for these films would be cube-on-cube grown since they are not epitaxially strained by the substrate, which was also mentioned in Section 4.5, but for consistency the films will be referred to as epitaxial. However, the epitaxial layer of a few nm seen in the films on STO, independent of the temperature profile and number of deposited layers, is thin enough to support epitaxial strain (e.g. true epitaxy). Edge dislocations were also observed in the polycrystalline film (Figure 4.31), but it is not verified if the dislocations seen in the epitaxial layers have the same periodicity as the dislocations seen in the epitaxial films (Figure 4.29), therefore no judgement can be made about relaxation versus epitaxial strain in these layers.

Conditions for achieving epitaxy

A requirement for film epitaxy (cube-on-cube growth) is that the substrate has a compatible crystal lattice. STO and LAO are both perovskites the crystal structures are compatible with $BaTiO_3$, and the lattice mismatch are 2.6 and 5.4 % respectively. While MgO and Pt/Si have cubic structures where the lattice mismatch are 4.9 and 2.2 %, respectively. Calculated based on the substrate lattice parameters in Table 3.4 and using 4.0037 Å for $BaTiO_3$ (the average parameter for the film in Figure 4.11). The *in situ* XRD (Section 4.3) revealed that epitaxy (cube-on-cube growth) is possible for $BaTiO_3$ thin films on STO if the film was heated with a high enough heating rate through crystallization (> 1 °C/s) and to a high temperature (> 960 °C). The high heating rate is necessary in order to limit the amount of homogeneous nucleation occurring before crossing the temperature threshold where cube-on-cube growth is favoured. Otherwise, the film will be a mixture of polycrystalline and epitaxial (such as Film VIII in Section 4.3).

$BaTiO_3$ films on Pt/Si, MgO and LAO were prepared with the epitaxial heating program, where both the diffraction and microstructure (Appendix A.1.2 and A.4, respectively) indicated epitaxy in the films, but not completely, resulting in a partial polycrystalline character. The BCT film prepared with the epitaxial heating program had the same microstructure as $BaTiO_3$, while the BCZT had a rougher appearance, possibly due to the annealing temperature (Figure 4.21). These films, demonstrate that that epitaxy was possible on all the crystalline substrates investigated in this work and, but completely epitaxial films were only possible on STO, which could be due to temperature limitations on the heating setup. Since $BaTiO_3$ and STO are most similar of the material systems and substrates investigated, the cube-on-cube growth threshold for $BaTiO_3$ on STO could be lower than $BaTiO_3$ on LAO, MgO and Pt/Si, or BCZT on STO. Therefore, it is proposed that complete epitaxial transformation can be achieved by increasing the annealing temperature.

A possible reaction scheme for the formation of epitaxial (cube-on-cube grown) films is presented in Figure 7.5. Dependent on the heating rate, $BaTiO_3$ nucleates randomly either in an organic matrix (fast heating) or from the oxycarbonate phase (slower heating or separate hold step), shown as Step 1 in Figure 7.5. Then

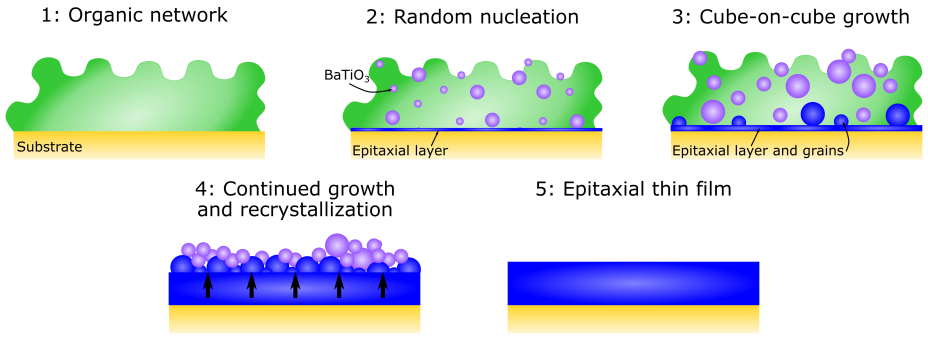

Figure 7.5: Illustration of the proposed formation mechanism of epitaxial thin films from aqueous CSD. 1: At low temperatures the film is amorphous. 2: Above the nucleation threshold, homogenous nucleation of $BaTiO_3$ will occur and an epitaxial layer at the substrate interface will form. 3: Due to the high heating rate, crystallization is incomplete as the threshold for cube-on-cube growth is exceeded resulting in formation of epitaxial grains and growth of the epitaxial layer. 4: During the high temperature annealing the epitaxial layer will grow at the expense of the epitaxial and randomly oriented grains, resulting in 5: an epitaxial thin film.

---

a high heating rate is necessary to prevent complete crystallization or growth of the nanosized $BaTiO_3$ grains until a high enough temperature is reached that enables cube-on-cube growth at the substrate, Steps 2-3 in Figure 7.5. The epitaxial film is first formed at the substrate interface, but with the rapidly increasing temperature and prolonged annealing at high temperature this layer grows by consumption/recrystallization of the overlaying grains, independent of their orientation, Steps 4-5 in Figure 7.5. As shown for Film VIII in Figure 4.18, there is a temperature threshold that must be exceeded for complete transformation of the film to epitaxial. Additionally, the film must be annealed for a certain time to complete the transformation, but the 5 min annealing used in the epitaxial heating program (Figure 3.1) was enough to achieve complete epitaxial transformation of the $BaTiO_3$ films studied in this work.

Relaxation by periodic dislocation

The TEM imaging revealed that the multilayer epitaxial films had periodic dislocations at the substrate interface (Figure 4.29), where the periodicity of the dislocations is close to the distance predicted by theory based on the lattice mismatch. [13] The dislocation periodicity is also in the same range as the periodic distance calculated from the additional reflections observed by synchrotron XRD for a single layer epitaxial film (Figure 4.17). It is proposed that the additional reflections seen by synchrotron XRD are due to the periodic dislocations arising from relaxation of the film, meaning that the dislocations are highly ordered and formed during crystallization of the first deposited layer. Similar reflection objects have been observed

in relation to ferroelectric domain pattern in other materials [207], but as they were present in the films at significantly higher temperatures than the expected Curie temperature of the films, they could not be caused by ferroelectric domains.

Lattice parameter and strain

In Section 4.3, the lattice parameter for an epitaxial single layer (∼25 nm) $BaTiO_3$ film on STO (Film VII in Figure 4.16), was calculated from the (310) and (311) reflections, where the (310) reflection gave a significantly lower lattice parameter then the (311) reflection (3.9522 Å and 4.0171 Å, respectively with uncertainty ±0.0025 Å). The (310) reflection has a larger contribution from lattice planes parallel to the substrate surface and therefore a good indication of the in-plane lattice parameter, which shows how the film is compressively strained from the substrate. The lattice parameter from (311) is larger, as these lattice planes also have a contribution from the out-of-plane parameter, which fits with the expansion compensating from the in-plane strain. In contrast, the lattice parameter calculated from a textured single layer $BaTiO_3$ film on STO (Figure 4.11) was more or less equal for the (310) and (311) reflections (4.0005 Å and 4.0068 Å, respectively uncertainty ±0.0025 Å), demonstrating less strain imposed from the substrate.

Multilayer epitaxial 180 nm thick $BaTiO_3$ films from the same aqueous CSD synthesis route as presented in this work were also prepared by Ræder *et al.* [127] The lattice parameters of multilayer $BaTiO_3$ films were found to be 4.010 Å in-plane and 4.000 Å out-of-plane [29], which contrasts with the parameters found in this work for a ∼25 nm film. Ræder *et al.* concluded that the c-axis was in-plane, giving rise to in-plane polarization caused by the mismatch in thermal expansion coefficients between $BaTiO_3$ and the STO substrates. [127] During cooling from the annealing temperature (1000 °C) the film is clamped to the contraction of the substrate, which induces compressive strain. Since the same experimental procedure and a similar heating programs were used in this work as by Ræder *et al.*, the same polarization state and strain situation can be assumed for the multilayer films reported in this work. The contrasting in-plane and out-of-plane lattice parameters reported here for a single layer film and by Ræder *et al.* for multilayer films might be an effect of different degree of relaxation as the film thickness is a factor of 10 larger for the multilayer films, where the lattice parameters reported will be an average for all layers. The experimental measurement conditions in this work and by Ræder *et al.* could potentially also contribute to the different observed lattice parameters.

7.1.4 Ferroelectric behaviour

The ferroelectric properties of the $BaTiO_3$-based thin films were highly dependent on the microstructure and degree of preferential orientation, but the remnant polarizations and cohesive fields were in the same range as typically reported for $BaTiO_3$ films from CSD (Section 2.4). Only the epitaxial (cube-on-cube grown) films gave a square hysteresis loop, while the response from the multilayer films made by the texture and polycrystalline heating programs was nearly linear. The grain sizes of the films made by the texture and polycrystalline heating programs are in the range

of the critical grain size observed in literature (Section 2.3), therefore these films were post-annealed to enable the grain growth, but the ferroelectric response did not improve. The electric fields applied to the films were lower than what is typically used for measurements of $BaTiO_3$ ceramics [12, 39, 208], but as shown for the polycrystalline film in Figure 4.36, increasing the field did not result in a more square hysteresis loop, but it did increase the tunability. The slim CE-loops measured for this polycrystalline film (Figure 4.36) has also been reported in literature for $BaTiO_3$ films on LAO made by a CSD process, where the ferroelectric repose was measured with interdigitated electrodes. [136] Dimos *et al.* observed an increased tunability when the annealing temperature was higher as this increased the grain sizes in the polycrystalline film, but the CE-loops remained slim. [136]

The limited in-plane response from the polycrystalline and textured films, could also be due to different orientation of the polar axis (c-axis) in these films, giving less in-plane response. The TEM investigation only shows that these films have a preferred orientation, but this does not need to be consistent with the substrate orientation. As these films were less clamped by the substrate contraction during the fabrication, which Ræder *et al.* reported to be responsible for the in-plane polarization [127], a different preferred orientation could occur.

The thickness dependence on the ferroelectric response observed for the epitaxial $BaTiO_3$ films could be an effect of decreased porosity and more uniform thickness in the thicker film. Which would also explain the increased tunability after post-annealing, as the porosity was decreased, seen from the microstructure in Figure 4.35. The leakage contribution to the PE-loops arise both from the film but also from surface charges and capacitance of the substrate. Other contributions than from the film were assumed to be neglectable, but this can also not be the case as surface charges from e.g. water adsorption could be contributing. Also, defective electrode fingers would give a more "leaky" appearance, although this should have been accounted for in the corrections.

7.2 KNN thin films

Phase purity is a common challenge during synthesis, ceramics processing and thin film fabrication of KNN-based materials, due to the volatility of the alkali metals. Adding excess alkali is common practise to compensate for the effect of the volatility. Here, the alkali excess was 5 at% and the thin and thick films investigated with *in situ* XRD and IR spectroscopy were phase pure after the heat treatment.

7.2.1 Effect of niobium precursor

The type of niobium precursor, malic acid-based (MA) or oxalate-based (Ox), determines the decomposition reactions during annealing of the KNN films, and therefore also the governs the crystallization. The nucleation temperature in the films studied with *in situ* XRD (Figure 6.2) was higher in the MA films than in the Ox. The nucleation temperature also decreased with decreasing heating rate, and this trend seems to be stronger in the MA films, although different heating rates were used, and the two are not directly comparable. The organic functional groups and the phase evolution in the *in situ* IR spectra of the thick films in this work (Section 6.2), confirms the *ex situ* findings on powders by Gaukås *et al.* [9]

In this work, all the single layer KNN films were phase pure, independent of type of precursor, which contrasts to the results reported by Gaukås *et al.* Multilayer KNN films based on MA were found to be phase pure, while in KNN films from the Ox precursor a secondary $K_4Nb_6O_{17}$ phase was observed. [9] Thermal analysis and *ex situ* IR spectroscopy of MA and Ox powders revealed that the complete decomposition of the precursors was delayed with the MA precursor so that perovskite nucleation occurred while there was still organic residue left and at a higher temperature in the powders, compared to the Ox system, where decomposition was complete before perovskite nucleation. The delayed nucleation was suggested as a mechanism for suppressing the secondary phase formation, leading to phase pure films. [9] However, since all the single layer KNN films studied in this work were phase pure, the observation of secondary phases in the multilayer films of Ox by Gaukås *et al.* [9] and Pham *et al.* [8] is likely due to the incomplete annealing before deposition of the next layer, and fully crystallizing each layer would probably result in phase pure multilayer films from both precursors.

7.2.2 Effect of salt flux

The *in situ* IR spectra (Section 6.2) showed that addition of salt flux leads to the formation of carbonates at intermediate temperatures, as the carbonate asymmetric stretching bands appear in the spectra. The carbonates (and hydroxides [8]) are reported to form as K_2O and Na_2O reacts with CO_2 and H_2O in the atmosphere. The alkali species are volatile, and the carbonate and hydroxides can decompose to

release alkali from the system according to:

$$\begin{aligned} K_2CO_3\,(s,l) &\longrightarrow 2K\,(g) + {}^1/_2\,O_2\,(g) + CO_2\,(g) \\ 2KOH\,(s,l) &\longrightarrow 2K\,(g) + {}^1/_2\,O_2\,(g) + H_2O\,(g) \end{aligned} \tag{7.5}$$

where sodium is neglected for simplicity. [8] Alkali evaporation results in the presence of secondary phases, such as the $K_4Nb_6O_{17}$ phase seen as an intermediate phase in this work (Figure 6.2). The addition of the salt flux was suggested by Pham *et al.* to give an ionic liquid which dissolves the carbonates and the hydroxides and in the ionic liquid the activity of the alkali species reduced, leading to decreased alkali volatility and less secondary phases. [8] This explains the reduced temperature region seen for the $K_4Nb_6O_{17}$ phase with *in situ* XRD (Figure 6.2) for the KNN-Ox films with salt flux.

The lattice parameters obtained from the Rietveld refinement of the KNN films were significantly larger for the KNN-MA films compared to the KNN-Ox films. The salt flux also had different effects on the KNN-MA and KNN-Ox films. For the KNN-MA film, a larger lattice parameter was observed at nucleation compared to the value after annealing, while in the KNN-Ox films the lattice parameter increased during the annealing compared to nucleation. A possible explanation is heterogeneous but randomly oriented in-plane strained nucleation at the substrate for the KNN-Ox film followed by relaxation during annealing, while the KNN-MA nucleation is homogeneous and possibly with carbonate incorporation in the lattice, which is removed during annealing. Such a nucleation scheme would also explain the larger lattice parameters observed for KNN-MA than the KNN-Ox films, independent of salt flux addition in the system.

7.2.3 Texture and epitaxy in the KNN films

None of the KNN films had diffraction spots instead of the diffraction rings showing a low degree of texture. However, a signature of texture was seen in the KNN-MA film heated fast (5 °C/s) without salt, where there was somewhat higher intensity on the (100) diffraction ring at 90° (azimuthal direction) and weak (310) and (311) reflections from the film in the diffraction pattern. This is in contrast to the work of Gaukås *et al.* [9] and Pham *et al.* [8] where both reported texture in the multilayer KNN films. Gaukås *et al.* suggested that mixed heteroepitaxial and oriented homogenous nucleation and growth occurred in the first layer. However, both Gaukås *et al.* and Pham *et al.* reported on multi-layered films, where several layers were pyrolysed followed by a final crystallization step, while in this work only single layer films were studied. In the $BaTiO_3$ system repeated annealing was found to induced texture in multilayer films, even if the same heating did not give texture in a single layer. The texture observed by Gaukås *et al.* and Pham *et al.* could therefore be formed by the same mechanism as presented in Section 7.1.2 and illustrated in Figure 7.3, where texture and epitaxy are caused by the repeated annealing. Improved texture with the addition of salt (reported by Pham *et al.* [8]), would then be due to orientation of the first layers, and heterogeneous nucleation/precipitation from the ionic liquid in consecutive layers.

7.3 Possibilities and challenges with the *in situ* characterization tools

Understanding the complex decomposition and crystallization reactions taking place during aqueous CSD of oxide thin films is crucial for achieving high quality phase pure films with a tailored degree of crystallographic texture and microstructure. The work presented in this thesis emphasizes the information about the decomposition and crystallization gained by two complementary *in situ* characterization techniques. This information is necessary in order to optimize the film annealing temperature profile and processing conditions. The work on the $BaTiO_3$ films showed how versatile these tools are with respect to analysis of texture and varying processing conditions, while the work on the KNN films shows how the *in situ* studies revealed mechanisms for the phase evolution and texture development, which were not observed by *ex situ* investigations.

In Section 2.6.1 various *in situ* IR spectroscopy setups were reviewed, but none were found for studying decomposition reactions during heating of films. The adaptation of a diffuse reflection cell intended for continuous heating of powders in combination with the use of a reflective substrate enabled continuous characterization of the decomposition and pyrolysis process for films from aqueous CSD. Although the measurements were successful, several improvements could be made to the setup. The most important is designing a new flat KBr window, instead of using the dome, which would improve the signal to noise ratio more than 10 times (Appendix A.2.1). A flat window would allow thinner films to be studied, better resolution of the perovskite absorption band frequency region and less saturation from the organic functional groups in the precursor film. However, optimization of the film to window distance would be necessary to avoid cracking of the window due to thermal expansion, but the distance should not be too large as this will refract the beam and reduce the throughput signal.

The *in situ* IR cell used in this work is also compatible with Raman spectroscopy, although a flat lid with a silica window would be necessary, showing the versatility of the setup. Raman spectroscopy is also suited for studying phase transitions in ferroelectrics and could be a useful supplement for characterizing films from aqueous CSD.

Thin films are usually characterized by IR spectroscopy with a near normal incident angle to remove the incident angle dependency of the reflection spectra. Hence, an alternative design with a heating plate could also be useful and would remove the requirement of a reflective substrate. However, the phonon modelling in Section 4.7, showed how weak the phonon modes of these thin films are compared to the substrate modes. Additionally, a lower wavenumber range is necessary to fully utilize the information from the crystalline films.

The design of the *in situ* synchrotron XRD heating setup is first of its kind and allows the effect of a wide range of processing parameters to be studied. The fast heating rates and high temperature available is comparable with the RTP commonly used for thin film fabrication, so both the mechanisms for slow and fast crystallization can be investigated. Additionally, X-ray 2D detectors are important

for revealing the orientation relationship between the film and the substrate, as polycrystalline, textured and epitaxial films were investigated. The fact that the mechanisms for cube-on-cube growth were revealed and the periodic dislocations could be seen even though the range of motion were limited to tilt and x,y,z translations, shows just how powerful the setup is for studying highly oriented films. Moreover, the possibility for atmosphere control during decomposition was demonstrated and the heating plate design also open for the possibility of studying the effect of external stimuli, such as electric field, with heating during XRD measurements, where texture and orientation can be monitored.

The main challenge with the heating setup for *in situ* synchrotron XRD is thermal expansion of the insulation during heating, but a protocol for data treatment was developed to deal with this challenge, outlined in Appendix C. Proper alignment of the films before measurements, inspecting the recoded data while measuring to ensure sufficient signal from the substrate and a consistent procedure for designing each experiment are important to simplify data processing. Additionally, measuring the room temperature and hold data at different detector heights improve the quality of the data and the detector position should be chosen such that the gaps in the detector does not overlap with an important film or substrate reflections. The time resolution is limited by the number of translational steps used, but with experience these can be limited.

Although there is room for improvement for both the *in situ* setups for characterization of thin films from aqueous CSD developed in the FASTS project, the results presented in this work shows how valuable information can be obtained by studying the decomposition, pyrolysis and crystallization process *in situ*. Studying the reactions with continuous annealing reveal a more accurate picture of the mechanisms at play, which reduces the amount of trial and error needed for optimizing the processing conditions during annealing of the thin films.

7.4 How to make phase pure textured perovskite thin films by aqueous chemical solution deposition

Aqueous chemical solution deposition is an inexpensive, versatile and simple synthesis route for fabricating oxide thin films. Aqueous CSD routes for a wide range of materials exist, but this discussion will be limited to material systems related to $BaTiO_3$ and KNN or with the perovskite structure.

Over the past years aqueous CSD synthesis routes for films from several ferroelectric material systems have been developed in our group, including the perovskites $Bi_{0.5}Na_{0.5}TiO_3$ (BNT) by Christensen *et al.* [203, 209], $K_{0.5}Na_{0.5}NbO_3$ by Gaukås *et al.* [9], Pham *et al.* [8] and the results presented in this work, $BaTiO_3$ by Ræder *et al.* [127] and Bakken *et al.* [210] and $BaTiO_3$-based perovskites such as BCZT by Khomyakova *et al.* [128] and the results presented in this work, but also the tungsten bronze $Sr_xBa_{1-x}Nb_2O_6$ (SBN) by Blichfeld *et al.* [190] Other works reporting on the use of aqueous CSD include; Van Bael *et al.* [22] reported on the synthesis of $(Bi,La)_4Ti_3O_{12}$, $SrBi_2Ta_2O_9$ and $PbZr_{1-x}Ti_xO_3$ films, Bretos *et al.* [211] on $(Pb,Ca)TiO_3$ films, Pollefeyt *et al.* [212] on $SrTiO_3$ buffer layers, Hardy *et al.* [129, 130] investigated $Ba(Zr,Ti)O_3$ films, De Dobbelaere *et al.* [213] fabricated $PbTiO_3$ films, Van de Velde *et al.* [214] reported on TiO_2 thin films and Lu *et al.* [151] and Zhang *et al.* [152] prepared KNN films.

The different systems present various processing challenges, but phase pure films from all material systems were fabricated, demonstrating the possibilities with the aqueous CSD route for thin film fabrication. In this Section a general approach to film fabrication by aqueous CSD will be outlined based on the experience from this work and selected literature.

The precursor solution and cation solubility

The precursor solution might be the most important element in the aqueous CSD process, and care should be taken when preparing the solution. Dependent on the solubility of the cations, it might be necessary to prepare separate solutions before mixing in stoichiometric ratios like for the $BaTiO_3$ system (reported in this work). The solubility of the cations can also be affected by the pH, so care should be taken to avoid precipitation. [6]

For the alkali and alkaline earth cations, nitrates usually have high solubility, but the solubility can also be increased by addition of complexing agents, illustrated by the addition of EDTA and citric acid to form a stable dissolved Ba-complex. [199] Citrates [211], acetates [22], carbonates [129, 130] and hydroxides [129, 130] are also reported for the alkaline earths. Transition metals usually form stable citric acid complexes, where Ti [22, 127–129, 210–214], Zr [22, 129, 130], Ta [22] and Nb [22] all have successfully been complexed with citric acid (often in combination with hydrogen peroxide), but Nb complexed with malic acid or ammonium oxalate was also reported [8, 9, 129, 203]. Lead citrate [211, 213] and bismuth acetate [22] and

nitrate [203,209] have been reported as precursors, either stabilized or mixed directly into the B-cation solution.

After deposition it is important to properly dry the film, as water based solutions are (usually) non-gelling, and storage of the films without drying will result in dewetting. The viscosity and concentration of the precursor solution will determine the crystalline film thickness but deposition parameters and porosity (determined by the temperature profile) will also influence the thickness.

Transformation pathway and secondary phases

The precursor chemistry also to a large degree govern what phases might form during decomposition and pyrolysis, e.g. the transformation pathway for the desired crystalline phase. Knowing the mechanisms for formation of secondary phases, how thermodynamically stable they are, and how they are affected by the processing conditions is crucial for obtaining phase pure films after crystallization.

Carbonates are a likely secondary phase due to the organic additives (citric acid), but the stability of carbonates depends on the material system. For the alkaline earth carbonates are usually observed during processing of the films. [127–130, 210, 211] Especially for $BaTiO_3$, formation of carbonates is hard to avoid due to the high thermodynamic stability of $BaCO_3$ and the abundance of CO_2, both in the precursor solution but also in the atmosphere. However, for the precursor chemistry presented in this work, a metastable oxycarbonate is formed instead of thermodynamically stable $BaCO_3$ [127, 128, 210], although this is dependent on the local partial pressure of CO_2 and temperature (Section 5.3). For phase pure $BaTiO_3$-based films, the concentration of CO_2 in the atmosphere should be limited to avoid $BaCO_3$ formation (Section 5.3), but formation of oxycarbonate is desired as it will increase the likelihood of texture and a desirable microstructure (Section 7.1.2), even if it delays the perovskite nucleation. However, in the KNN system, the presence of carbonate indicate lowered alkali volatility which reduces the amount of secondary phase in the crystalline film. [8] In the KNN system, Gaukås *et al.* reported on increased amounts of secondary phases when the films were decomposed in pure oxygen [9], which could be caused by an decreased alkali volatility or enhanced combustion. Ambient atmosphere however, gave phase pure films [9], demonstrating the effect the processing conditions have on the decomposition and crystallization. Moreover, CO_2 in the processing atmosphere could be beneficial for KNN films for carbonate stabilization and therefore reducing alkali volatility.

In the BNT system, Christensen *et al.* reported that the reduction of Bi^{3+} to bismuth metal is the major challenge as, bismuth metal leads to formation of bismuth rich secondary pyrochlore phases. [203, 209] If bismuth metal forms at low temperatures, it will segregate and grow by Oswald ripening, and upon reoxidation to Bi^{3+}, the pyrochlore will form in the bismuth enriched areas. The key to limit the pyrochlores was sufficient local oxygen partial pressure and avoiding prolonged annealing at the temperatures below the temperature for bismuth reoxidization. [203, 209]

During fabrication of $PbTiO_3$ films, De Dobbelaere *et al.* [213] reported on the formation of Pb_2O_3 when the annealing temperature was increased from 600 to

700 °C, but only on SiO_2 substrates (not on $SrTiO_3$ and Pt/Si), which was attributed to the poor crystallinity of $PbTiO_3$ on SiO_2. Pb-related secondary phases were not observed in the (Pb,Ca)TiO_3 films on Pt/Si reported by Bretos *et al.* [211], which shows how the substrate can also influence the formation of secondary phases.

What these examples demonstrate is that even though these systems have a great deal in common, the secondary phase formation occurs differently, but is often related to the A-type of cation. Since the transformation pathway and secondary phase formation occur by different mechanisms, knowledge about the chemistry of the material system is crucial for designing the temperature profile for decomposition and crystallization. There are also other considerations to take when designing the temperature profile, such as nucleation and growth, desired microstructure and mechanisms for texture.

Nucleation and crystallization

The nucleation and growth behaviour of $BaTiO_3$-based films were outlined in Section 7.1.2. All the perovskite systems, KNN, BNT and BCZT follow the same homogenous nucleation and growth and the crystallization temperatures are in the range 450-550 °C. However, annealing at a higher temperature was found to improve the crystallinity of the films, so high temperature annealing (> 700 °C) is recommended. The addition of a salt flux in the KNN system decreased the nucleation temperature, and shifted the nucleation towards heterogeneous at the substrate as the perovskite formed by precipitation from the salt melt, especially for KNN films from a oxalate based precursor.

The tungsten bronze SBN had a significantly higher nucleation temperature than the perovskites, but no crystalline secondary phases was observed during decomposition [190], although secondary phase formation depend on the Sr/Ba ratio in the tungsten bronze.

Crystallographic texture and microstructure

The nucleation and growth mechanism of $BaTiO_3$-based films investigated in this work were outlined in Section 7.1.2. The crystalline phase forms by homogenous nucleation in the temperature range 500-570 °C, in accordance with the observations by Ræder *et al.* [127] and Khomyakova *et al.* [128] In other perovskite systems, the nucleation temperatures were reported as 450 °C [8, 9] and 520-550 °C [151, 152] for KNN, 500 °C for BNT [203, 209], in the range 540-620 °C for (Pb,Ca)TiO_3 where higher Ca-content leads to increased decomposition temperatures [213]. Although the nucleation temperatures generally are low, a high temperature annealing (> 700 °C) is recommended as increased crystallinity is generally reported. Homogeneous nucleation seems to be the case in all of these perovskites, judging from the reported microstructure, and similar microstructure dependence on the temperature program as outlined for the $BaTiO_3$-based films investigated in this work (Section 7.1.2) could be expected. This mechanism was illustrated in Figure 7.3, where a high heating rate during nucleation gives small spherical randomly oriented grains, while a slower heating rate or repeated annealing gives texture, and larger interconnected or

columnar grains. However, the different morphology of the $PbTiO_3$ films on different substrates shows that the microstructure is not solely governed by nucleation. [213]

The formation of crystallographic texture was discussed in Section 7.1.3 for the $BaTiO_3$-based films, which either formed as a result of low temperature annealing and ordering of the nanosized titanate domains, or as a consequence of Ostwald ripening and recrystallization during repeated annealing as consecutive layers were deposited. The first mechanism is limited to film-substrate systems with compatible crystal structures, observed for SBN on (100) STO [190] and the $BaTiO_3$-based films in this work, but texture investigations are usually not conducted for single-layered films. However, the texture induced by repeated annealing was observed for several perovskites; $SrTiO_3$ on LAO [212], KNN on (100) STO [8, 9], (110) STO [8], (111) STO [8] and Pt/Si [151, 152] and $PbTiO_3$ on Pt/Si and STO [213].

In general, to increase the likelihood of texture formation, the substrate should have a similar crystal lattice and lattice parameter as the film material. Issues, such as incompatibility between the film and substrate or diffusion from the substrate, can be avoided with a suitable protective layer, such as layers of $BaTiO_3$ between the Pt/Si substrates and BNT films to reduce the effects of Pt-Bi inter-diffusion. [209]

Cube-on-cube growth was observed for the $BaTiO_3$-based films on STO, MgO and LAO (Section 7.1.3), when a high annealing temperature and a high heating rate was used, resulting in fully relaxed epitaxial films. Highly textured films were also observed for $SrTiO_3$ thin films on LAO fabricated in wet Ar in 5 % H_2, where a heating rate of 8 °C/min was used up to 1100 °C and the films were annealed for 2 h. [212] Combined with the faceted microstructure of the $SrTiO_3$ films [212], the high degree of orientation could suggest cube-on-cube growth of these films, even if the heating rate was significantly lower than the 5 °C/s threshold found for the $BaTiO_3$-based films in this work. Provided a suitable substrate is used, the same cube-on-cube growth mechanism is proposed to be possible in most of the perovskite systems reviewed in this Section, but the temperature and heating rate threshold for enabling this growth mode will vary for the different material systems and based on the lattice mismatch with the substrate.

Designing the temperature profile

Knowing what causes the formation of secondary phases will help either avoid or decompose them, so the first part of the temperature profile should be chosen based on which secondary phases might form and how to limit the cation volatility or segregation as a result of secondary phase formation. Secondly, the annealing temperature should be chosen to be higher than the nucleation temperature, as this will improve the crystallinity of the film. Fully crystallizing each layer is recommended to avoid secondary phases from cation segregation in the final multilayer film. Additionally, the desired microstructure and texture forming mechanism should be considered. The texture is induced either from a compatible substrate, where the orientation is important to have favourable lattice matching between the film and substrate. Or texture is induced by repeated annealing, either by Oswald ripening or homoepitaxial nucleation of the consecutive layers, giving a columnar microstructure. Finally, cube-on-cube grown films are possible from aqueous CSD but require high annealing

temperature and lattice matching.

A multilayer polycrystalline film, with small grains with random orientation is harder to achieve, due to the repeated annealing induced texture. However, if such a microstructure is desired, each layer should only be pyrolysed at a low enough temperature so that crystallization is completely avoided, even with repeated annealing, but high enough so that most of the organic removal has occurred. Then a final annealing should be done at a high temperature to crystallize the film and a high heating rate should be used for direct homogenous nucleation.

8 Conclusion

The results for both the $BaTiO_3$ and KNN system presented in this work, demonstrate the successful development of flexible *in situ* characterization tools for studying oxide thin films during aqueous CSD. Both the *in situ* XRD and *in situ* IR setups are capable of measuring films during annealing, where the processing parameters such as temperature, heating rate and atmosphere can be varied to mimic industrial fabrication conditions.

The *in situ* IR and XRD investigations revealed that $BaTiO_3$ forms through an intermediate oxycarbonate phase during decomposition of the precursor, where the oxycarbonate formation can be related to the complexes in the precursor solution. This oxycarbonate phase is close to $BaCO_3$ with a crystal structure resembling the calcite polymorph, which is stabilized by oxygen substitution, giving the proposed stoichiometry $BaO_x(CO_3)_{1-x}$. A second stabilizing mechanism for the formation of the oxycarbonate phase was proposed; templating of calcite-type $BaCO_3$ with a Ti-rich $BaTiO_3$-like phase, as the oxycarbonate phase only formed when titanium was present in the system. The oxycarbonate was metastable in ambient atmosphere, but increased CO_2 partial pressure was shown to increase the oxycarbonate stability over $BaTiO_3$. For multilayer films, each deposited layer should be fully crystallized, otherwise the formation of the oxycarbonate phase leads to cation segregation and secondary phases.

The formation of crystallographic texture occurred by two different proposed mechanisms. The first depends on the nature of the intermediate phases. Prolonged annealing in the temperature range 400-500 °C, either by a low heating rate or a hold step, was demonstrated to result in amorphous $BaCO_3$-like and Ti-rich $BaTiO_3$-like phases in the film. These phases can adhere to the substrate orientation, provided the substrate have a compatible crystal structure. $BaTiO_3$ was shown to nucleate by reaction of the oxycarbonate and Ti-rich $BaTiO_3$-like phases, where the orientation of $BaTiO_3$ depends on the intermediates. A low heating rate during nucleation enhanced the texture, and a high temperature annealing (> 650 °C) is recommended as it increases the crystallinity. Texture in multilayer films can also form by the repeated annealing as favourably oriented grains in the previously deposited layers will grow by Ostwald ripening as constitutive layers are deposited, independent of the substrate.

$BaTiO_3$-based films showed cube-on-cube growth using a high annealing temperature (>1000 °C) and a high heating rate (>1 °C/s) during nucleation. The fast heating ensured limited homogenous nucleation of $BaTiO_3$ before reaching the

temperature threshold for where cube-on-cube growth was favoured. These films appeared epitaxial by synchrotron XRD, but transmission electron microscopy showed that these films were relaxed by formation of edge dislocations. Electrical characterizations demonstrated the ferroelectric nature of these films, as they displayed hysteresis and switching.

The *in situ* characterization of the KNN films, demonstrated that the mechanisms revealed for the nucleation, growth and texture development in the $BaTiO_3$-based films are more general, even though the decomposition reactions are highly dependent on the precursor chemistry in case of KNN. Thin films from aqueous CSD typically show homogenous nucleation as the crystalline phase nucleates from an amorphous organic network. The microstructure was highly dependent on the heating rate, while crystallographic texture depended on the intermediate phases or is induced by repeated annealing. Cube-on-cube growth is possible dependent on annealing temperature, heating rate and lattice matching with the substrate.

9 Outlook

The generalized guidelines outlined in this thesis will serve as an important staring point when establishing new aqueous CSD routes for oxide thin films. The importance of the precursor solution chemistry and temperature profile during annealing was demonstrated for the $BaTiO_3$-based and KNN material systems, which could ease development of aqueous fabrication of thin film industrially. Mechanisms for texture and epitaxy were proposed, which is important as functional properties are usually enhanced by inducing a preferred orientation of the thin films. Understanding what governs the decomposition and crystallization reactions will simplify the optimization needed for tailoring the film for a given application. Additionally, the films investigated in this work show that the functional properties, microstructure and degree of preferred orientation achieved using aqueous CSD are comparable to those produced by non-aqueous CSD. Hence, the CSD process can be made more environmentally-friendly without compromising on the film quality.

The *in situ* XRD and IR spectroscopy methods used in this work, highlights the strength of *in situ* characterization. Continued measurements revealed additional information that was not observed or would have been time consuming to investigate with *ex situ* studies. The decomposition and crystallization reactions during aqueous CSD are complex. Hence, the insight gained by *in situ* studies for the dependency between precursor chemistry, annealing conditions and the resulting film is crucial for producing high quality films.

References

[1] D. W. Richerson, *Modern ceramic engineering : properties, processing, and use in design*. CRC Press Boca Raton, 3rd ed., 2006.

[2] S. R. Elliott, *The physics and chemistry of solids*. Wiley New York, 1998.

[3] J. Rodel, W. Jo, K. T. P. Seifert, E. M. Anton, T. Granzow, and D. Damjanovic, "Perspective on the development of lead-free piezoceramics," *Journal of the American Ceramic Society*, vol. 92, no. 6, pp. 1153–1177, 2009.

[4] M. Acosta, N. Novak, V. Rojas, S. Patel, R. Vaish, J. Koruza, G. A. Rossetti, and J. Rodel, "$BaTiO_3$-based piezoelectrics: Fundamentals, current status, and perspectives," *Applied Physics Reviews*, vol. 4, no. 4, pp. 1–53.

[5] G. H. Haertling, "Ferroelectric thin-films for electronic applications," *Journal of Vacuum Science & Technology A: Vacuum Surfaces and Films*, vol. 9, no. 3, pp. 414–420, 1991.

[6] R. W. Schwartz, T. Schneller, and R. Waser, "Chemical solution deposition of electronic oxide films," *Comptes Rendus Chimie*, vol. 7, no. 5, pp. 433–461, 2004.

[7] N. Bassiri-Gharb, Y. Bastani, and A. Bernal, "Chemical solution growth of ferroelectric oxide thin films and nanostructures," *Chemical Society Reviews*, vol. 43, no. 7, pp. 2125–2140, 2014.

[8] K.-N. Pham, N. H. Gaukås, M. Morozov, T. Tybell, P. E. Vullum, T. Grande, and M.-A. Einarsrud, "Epitaxial $K_{0.5}Na_{0.5}NbO_3$ thin films by aqueous chemical solution deposition," *Royal Society Open Science*, vol. 6, no. 1, pp. 1–10, 2019.

[9] N. H. Gaukås, S. M. Dale, T. M. Ræder, A. Toresen, R. Holmestad, J. Glaum, M.-A. Einarsrud, and T. Grande, "Controlling phase purity and texture of $K_{0.5}Na_{0.5}NbO_3$ thin films by aqueous chemical solution deposition," *Materials*, vol. 12, no. 13, pp. 1–16, 2019.

[10] A. Pramanick, A. D. Prewitt, J. S. Forrester, and J. L. Jones, "Domains, domain walls and defects in perovskite ferroelectric oxides: A review of present understanding and recent contributions," *Critical Reviews in Solid State and Materials Sciences*, vol. 37, no. 4, pp. 243–275, 2012.

[11] L. Jin, F. Li, and S. Zhang, "Decoding the fingerprint of ferroelectric loops: Comprehension of the material properties and structures," *Journal of the American Ceramic Society*, vol. 97, no. 1, pp. 1–27, 2014.

[12] H. Jaffe and D. A. Berlincourt, "Piezoelectric transducer materials," *Proceedings of the Institute of Electrical and Electronics Engineers*, vol. 53, no. 10, pp. 1372–1386, 1965.

[13] M. Ohring, *Epitaxy*. Elsevier Amsterdam, 2nd ed., 2002.

[14] D. Damjanovic, "Ferroelectric, dielectric and piezoelectric properties of ferroelectric thin films and ceramics," *Reports on Progress in Physics*, vol. 61, no. 9, pp. 1267–1324, 1998.

[15] T. M. Shaw, S. Trolier-McKinstry, and P. C. McIntyre, "The properties of ferroelectric films at small dimensions," *Annual Review of Materials Science*, vol. 30, pp. 263–298, 2000.

[16] M. A. M. Roji, G. Jiji, and T. A. B. Raj, "A retrospect on the role of piezoelectric nanogenerators in the development of the green world," *Rsc Advances*, vol. 7, no. 53, pp. 33642–33670, 2017.

[17] G. Z. Zhang, M. Y. Li, H. L. Li, Q. Wang, and S. L. Jiang, "Harvesting energy from human activity: Ferroelectric energy harvesters for portable, implantable, and biomedical electronics," *Energy Technology*, vol. 6, no. 5, pp. 791–812, 2018.

[18] A. Marino, G. G. Genchi, E. Sinibaldi, and G. Ciofani, "Piezoelectric effects of materials on bio-lnterfaces," *Acs Applied Materials & Interfaces*, vol. 9, no. 21, pp. 17663–17680, 2017.

[19] S.-W. Yu, S.-T. Kuo, W.-H. Tuan, Y.-Y. Tsai, and C.-H. Su, "Ion release from three lead-free piezoelectric ceramics and their physical and cytotoxicity characteristics," *Materials Letters*, vol. 65, no. 23, pp. 3522–3524, 2011.

[20] S.-W. Yu, S.-T. Kuo, W.-H. Tuan, Y.-Y. Tsai, and S.-F. Wang, "Cytotoxicity and degradation behavior of potassium sodium niobate piezoelectric ceramics," *Ceramics International*, vol. 38, no. 4, pp. 2845–2850, 2012.

[21] M. S. Bhuiyan, M. Paranthaman, and K. Salama, "Solution-derived textured oxide thin films - a review," *Superconductor Science & Technology*, vol. 19, no. 2, pp. 1–21, 2006.

[22] M. K. Van Bael, D. Nelis, A. Hardy, D. Mondelaers, K. Van Werde, J. D'Haen, G. Vanhoyland, H. Van den Rul, J. Mullens, L. C. Van Poucke, F. Frederix, and D. J. Wouters, "Aqueous chemical solution depotion of ferroelectric thin films," *Integrated Ferroelectrics*, vol. 45, pp. 113–122, 2002.

[23] W. D. Callister and D. G. Rethwisch, *Materials science and engineering: an introduction*, vol. 7. Wiley New York, 2007.

[24] U. Hasenkox, S. Hoffmann, and R. Waser, "Influence of precursor chemistry on the formation of $MTiO_3$ (M = Ba, Sr) ceramic thin films," *Journal of Sol-Gel Science and Technology*, vol. 12, no. 2, pp. 67–79, 1998.

[25] J. Ricote, R. Poyato, M. Alguero, L. Pardo, M. L. Calzada, and D. Chateigner, "Texture development in modified lead titanate thin films obtained by chemical solution deposition on silicon-based substrates," *Journal of the American Ceramic Society*, vol. 86, no. 9, pp. 1571–1577, 2003.

[26] M. Figlarz, B. Gérand, A. Delahaye-Vidal, B. Dumont, F. Harb, A. Coucou, and F. Fievet, "Topotaxy, nucleation and growth," *Solid State Ionics*, vol. 43, pp. 143–170, 1990.

[27] R. J. D. Tilley, *Perovskites : Structure-Property Relationships*. Wiley New York, 2016.

[28] F. Jona and G. Shirane, "Ferroelectric crystals," *ZAMM - Journal of Applied Mathematics and Mechanics*, vol. 43, no. 10-11, pp. 512–512, 1963.

[29] J. Petzelt and S. Kamba, "Far infrared and terahertz spectroscopy of ferroelectric soft modes in thin films: A review," *Ferroelectrics*, vol. 503, no. 1, pp. 19–44, 2016.

[30] W. Cochran, "Crystal stability and the theory of ferroelectricity," *Advances in Physics*, vol. 9, no. 36, pp. 387–423, 1960.

[31] B. Ravel, E. A. Stern, R. I. Vedrinskii, and V. Kraizman, "Local structure and the phase transitions of $BaTiO_3$," *Ferroelectrics*, vol. 206, no. 1, pp. 407–430, 1998.

[32] Q. Zhang, T. Cagin, and W. A. Goddard, "The ferroelectric and cubic phases in $BaTiO_3$ ferroelectrics are also antiferroelectric," *Proceedings of the National Academy of Sciences*, vol. 103, no. 40, pp. 14695–14700, 2006.

[33] J. Harada, J. D. Axe, and G. Shirane, "Neutron-scattering study of soft modes in cubic $BaTiO_3$," *Physical Review B*, vol. 4, no. 1, pp. 155–162, 1971.

[34] J. Holakovský, "A new type of the ferroelectric phase transition," *Physica Status Solidi B*, vol. 56, no. 2, pp. 615–619, 1973.

[35] J. T. Last, "Infrared-absorption studies on barium titanate and related materials," *Physical Review*, vol. 105, no. 6, pp. 1740–1750, 1957.

[36] M. T. Buscaglia, V. Buscaglia, M. Viviani, J. Petzelt, M. Savinov, L. Mitoseriu, A. Testino, P. Nanni, C. Harnagea, Z. Zhao, and M. Nygren, "Ferroelectric properties of dense nanocrystalline $BaTiO_3$ ceramics," *Nanotechnology*, vol. 15, no. 9, pp. 1113–1117, 2004.

[37] M. E. Lines and A. M. Glass, *Principles and applications of ferroelectrics and related materials*. Oxford university press, 1977.

[38] A. Rae, M. Chu, and V. Ganine, *Dielectric Ceramic Materials*. Ceramic Transactions, The American Ceramic Society Westerville.

[39] M. M. Vijatovic, J. D. Bobic, and B. A. Stojanovic, "History and challenges of barium titanate: Part I," *Science of Sintering*, vol. 40, no. 2, pp. 155–165, 2008.

[40] X. Y. Deng, X. H. Wang, H. Wen, L. L. Chen, L. Chen, and L. T. Li, "Ferroelectric properties of nanocrystalline barium titanate ceramics," *Applied Physics Letters*, vol. 88, no. 25, pp. 1–3.

[41] M. H. Frey and D. A. Payne, "Grain-size effect on structure and phase transformations for barium titanate," *Phys Rev B Condens Matter*, vol. 54, no. 5, pp. 3158–3168, 1996.

[42] S. Ikegami, I. Ueda, and T. Nagata, "Electromechanical properties of $PbTiO_3$ ceramics containing La and Mn," *Journal of the Acoustical Society of America*, vol. 50, no. 4, pp. 1060–, 1971.

[43] D. Damjanovic, T. R. Gururaja, and L. E. Cross, "Anisotropy in piezoelectric properties of modified lead titanate ceramics," *American Ceramic Society Bulletin*, vol. 66, no. 4, pp. 699–703, 1987.

[44] D. A. Berlincourt, C. Cmolik, and H. Jaffe, "Piezoelectric properties of polycrystalline lead titanate zirconate compositions," *Proceedings of the Institute of Radio Engineers*, vol. 48, no. 2, pp. 220–229, 1960.

[45] X. N. Zhu, W. Zhang, and X. M. Chen, "Enhanced dielectric and ferroelectric characteristics in Ca-modified $BaTiO_3$ ceramics," *AIP Advances*, vol. 3, no. 8, p. 295–300, 2013.

[46] D. Taylor, "Thermal-expansion data 8: Complex oxides, ABO_3, the perovskites," *Transactions and Journal of the British Ceramic Society*, vol. 84, no. 6, pp. 181–188, 1985.

[47] L.-Y. Li and X.-G. Tang, "Effect of electric field on the dielectric properties and ferroelectric phase transition of sol–gel derived $(Ba_{0.9}Ca_{0.10})TiO_3$ ceramics," *Materials Chemistry and Physics*, vol. 115, no. 2, pp. 507–511, 2009.

[48] A. B. Haugen, J. S. Forrester, D. Damjanovic, B. Li, K. J. Bowman, and J. L. Jones, "Structure and phase transitions in $0.5(Ba_{0.7}Ca_{0.3}TO_3)$-$0.5(BaZr_{0.2}Ti_{0.8}O_3)$ from -100 °C to 150 °C," *Journal of Applied Physics*, vol. 113, no. 1, pp. 1–5, 2013.

[49] V. R. Mastelaro, H. R. Favarim, A. Mesquita, A. Michalowicz, J. Moscovici, and J. A. Eiras, "Local structure and hybridization states in $Ba_{0.9}Ca_{0.10}Ti_{1-x}Zr_xO_3$ ceramic compounds: Correlation with a normal or relaxor ferroelectric character," *Acta Materialia*, vol. 84, pp. 164–171, 2015.

[50] S. Lahiry and A. Mansingh, "Dielectric properties of sol–gel derived barium strontium titanate thin films," *Thin Solid Films*, vol. 516, no. 8, pp. 1656–1662, 2008.

[51] K. A. Razak, A. Asadov, J. Yoo, E. Haemmerle, and W. Gao, "Structural and dielectric properties of barium strontium titanate produced by high temperature hydrothermal method," *Journal of Alloys and Compounds*, vol. 449, no. 1–2, pp. 19–23, 2008.

[52] N. Nanakorn, P. Jalupoom, N. Vaneesorn, and A. Thanaboonsombut, "Dielectric and ferroelectric properties of $Ba(Ti_{1-x}Zr_x)O_3$ ceramics," *Ceramics International*, vol. 34, no. 4, pp. 779–782, 2008.

[53] X. P. Jiang, M. Zeng, H. L. W. Chan, and C. L. Choy, "Relaxor behaviors and tunability in $BaTi_{0.35}Zr_{0.65}O_3$ ceramics," *Materials Science and Engineering: A*, vol. 438–440, pp. 198–201, 2006.

[54] A. Dixit, S. B. Majumder, P. S. Dobal, R. S. Katiyar, and A. S. Bhalla, "Phase transition studies of sol-gel deposited barium zirconate titanate thin films," *Thin Solid Films*, vol. 447, pp. 284–288, 2004.

[55] S.-E. Park, S. Wada, L. Cross, and T. R. Shrout, "Crystallographically engineered $BaTiO_3$ single crystals for high-performance piezoelectrics," *Journal of applied physics*, vol. 86, pp. 2746–2750, 1999.

[56] Z. Yu, C. Ang, R. Y. Guo, and A. S. Bhalla, "Piezoelectric and strain properties of $Ba(Ti_{1-x}Zr_x)O_3$ ceramics," *Journal of Applied Physics*, vol. 92, no. 3, pp. 1489–1493, 2002.

[57] V. V. Shvartsman and D. C. Lupascu, "Lead-free relaxor ferroelectrics," *Journal of the American Ceramic Society*, vol. 95, no. 1, pp. 1–26, 2012.

[58] S. Annie, R. Jean, and M. Mario, "The crossover from a ferroelectric to a relaxor state in lead-free solid solutions," *Journal of Physics: Condensed Matter*, vol. 16, no. 6, pp. 963–970, 2004.

[59] T. Mitsui and W. B. Westphal, "Dielectric and X-ray studies of $Ca_xBa_{1-x}TiO_3$ and $Ca_xSr_{1-x}TiO_3$," *Physical Review*, vol. 124, no. 5, pp. 1354–1359, 1961.

[60] D. Fu, Y. Kamai, N. Sakamoto, N. Wakiya, H. Suzuki, and M. Itoh, "Phase diagram and piezoelectric response of $(Ba_{1x}Ca_x)(Zr_{0.1}Ti_{0.9})O_3$ solid solution," *Journal of Physics: Condensed Matter*, vol. 25, no. 42, pp. 1–5, 2013.

[61] R. Shannon, "Revised effective ionic radii and systematic studies of interatomic distances in halides and chalcogenides," *Acta Crystallographica Section A*, vol. 32, no. 5, pp. 751–767, 1976.

[62] M. J. Choi, J. R. Lim, J. S. Choi, J. H. Eom, B. J. Park, K. S. Kim, D. Kim, and S. G. Yoon, "Microstructural and electrical properties of lead-free $0.5Ba(Zr_{0.2}Ti_{0.8})O_3$-$0.5(Ba_{0.7}Ca_{0.3})TiO_3$ (BZT-BCT) epitaxial films grown on Si (001) substrates," *Scripta Materialia*, vol. 108, pp. 96–99, 2015.

[63] W. Liu and X. Ren, "Large piezoelectric effect in Pb-free ceramics," *Physical Review Letters*, vol. 103, no. 25, pp. 1–4, 2009.

[64] I. Barin and G. Platzki, *Thermochemical data of pure substances*. VCH Weinheim, 3rd ed., 1995.

[65] V. Ischenko, J. Woltersdorf, E. Pippel, R. Koferstein, and H. P. Abicht, "Formation of metastable calcite-type barium carbonate during low-temperature decomposition of (Ba,Ti)-precursor complexes," *Solid State Sciences*, vol. 9, no. 3-4, pp. 303–309, 2007.

[66] G. H. Aylward and T. J. V. Findlay, *SI chemical data*. Wiley New York, 6th ed., 2008.

[67] J. J. Lander, "Polymorphism and anion rotational disorder in the alkaline earth carbonates," *The Journal of Chemical Physics*, vol. 17, no. 10, pp. 892–901, 1949.

[68] K. O. Strømme, "On the crystal structures of the high-temperature forms of strontium and barium carbonate and structurally related compounds," *Acta Chemica Scandinavica Series A Physical and Inorganic Chemistry*, vol. 29a, pp. 105–110, 1975.

[69] S. M. Antao and I. Hassan, "$BaCO_3$: high-temperature crystal structures and the Pmcn $\rightarrow$ R_3m phase transition at 811 °C," *Physics and Chemistry of Minerals*, vol. 34, no. 8, pp. 573–580, 2007.

[70] T. Nishino, "Characterization of γ-$BaCO_3$," *Solid State Ionics*, vol. 32-33, pp. 394–397, 1989.

[71] K. Nakamoto, *Infrared and Raman Spectra of Inorganic and Coordination Compounds, Part A: Theory and Applications in Inorganic Chemistry*, vol. Pt. A. Wiley New York, 5th ed., 1997.

[72] F. A. Miller and C. H. Wilkins, "Infrared spectra and characteristic frequencies of inorganic ions," *Analytical Chemistry*, vol. 24, no. 8, pp. 1253–1294, 1952.

[73] R. A. Nyquist and R. O. Kagel, *Infrared spectra of inorganic compounds : (3800-45cm^{-1})*. Academic Press London, 1971.

[74] V. Ischenko, E. Pippel, R. Koferstein, H. P. Abicht, and J. Woltersdorf, "Barium titanate via thermal decomposition of Ba,Ti-precursor complexes: The nature of the intermediate phases," *Solid State Sciences*, vol. 9, no. 1, pp. 21–26, 2007.

[75] P. Durán, D. Gutierrez, J. Tartaj, M. A. Bañares, and C. Moure, "On the formation of an oxycarbonate intermediate phase in the synthesis of $BaTiO_3$ from (Ba,Ti)-polymeric organic precursors," *Journal of the European Ceramic Society*, vol. 22, no. 6, pp. 797–807, 2002.

[76] S. Gablenz, H. P. Abicht, E. Pippel, O. Lichtenberger, and J. Woltersdorf, "New evidence for an oxycarbonate phase as an intermediate step in $BaTiO_3$ preparation," *Journal of the European Ceramic Society*, vol. 20, no. 8, pp. 1053–1060, 2000.

[77] T. M. Stawski, W. J. C. Vijselaar, O. F. Gobel, S. A. Veldhuis, B. F. Smith, D. H. A. Blank, and J. E. ten Elshof, "Influence of high temperature processing of sol-gel derived barium titanate thin films deposited on platinum and strontium ruthenate coated silicon wafers," *Thin Solid Films*, vol. 520, no. 13, pp. 4394–4401, 2012.

[78] R. Ashiri, A. Nemati, M. S. Ghamsari, and M. M. Dastgahi, "Nanothickness films, nanostructured films, and nanocrystals of barium titanate obtained directly by a newly developed sol-gel synthesis pathway," *Journal of Materials Science-Materials in Electronics*, vol. 25, no. 12, pp. 5345–5355, 2014.

[79] S. Halder, T. Schneller, and R. Waser, "Crystallization temperature limit of (Ba,Sr)TiO_3 thin films prepared by a non oxocarbonate phase forming CSD route," *Journal of Sol-Gel Science and Technology*, vol. 33, no. 3, pp. 299–306, 2005.

[80] D. S. Paik, A. V. P. Rao, and S. Komarneni, "Ba-titanate and barium/strontium titanate thin films from hydroxide precursors: Preparation and ferroelectric behavior," *Journal of Sol-Gel Science and Technology*, vol. 10, no. 2, pp. 213–220, 1997.

[81] R. W. Schwartz, P. G. Clem, J. A. Voigt, E. R. Byhoff, M. Van Stry, T. J. Headley, and N. A. Missert, "Control of microstructure and orientation in solution-deposited $BaTiO_3$ and $SrTiO_3$ thin films," *Journal of the American Ceramic Society*, vol. 82, no. 9, pp. 2359–2367, 1999.

[82] S. Y. Chen, H. W. Wang, and L. C. Huang, "Role of an intermediate phase $(Ba,Sr)_2Ti_2O_5CO_3$ in doped $(Ba_{0.7}Sr_{0.3})TiO_3$ thin films," *Materials Chemistry and Physics*, vol. 77, no. 3, pp. 632–638, 2003.

[83] Y. P. Ding, C. Y. Jin, and Z. Y. Meng, "The effects and mechanism of chemical additives on the pyrolysis evolution and microstructure of sol-gel derived $Ba_{1-x}Sr_xTiO_3$ thin films," *Thin Solid Films*, vol. 375, no. 1-2, pp. 196–199, 2000.

[84] K. Szot, S. Hoffmann, W. Speier, U. Breuer, M. Siegert, and R. Waser, "Segregation phenomena in thin films of $BaTiO_3$," *Integrated Ferroelectrics*, vol. 33, no. 1-4, pp. 303–310, 2001.

[85] S. Hoffmann and R. Waser, "Control of the morphology of csd-prepared $(Ba,Sr)TiO_3$ thin films," *Journal of the European Ceramic Society*, vol. 19, no. 6-7, pp. 1339–1343, 1999.

[86] R. Ashiri, "A mechanistic study of nanoscale structure development, phase transition, morphology evolution, and growth of ultrathin barium titanate nanostructured films," *Metallurgical and Materials Transactions a-Physical Metallurgy and Materials Science*, vol. 45A, no. 9, pp. 4138–4154, 2014.

[87] M. C. Gust, N. D. Evans, L. A. Momoda, and M. L. Mecartney, "*In-situ* transmission electron microscopy crystallization studies of sol-gel-derived barium titanate thin films," *Journal of the American Ceramic Society*, vol. 80, no. 11, pp. 2828–2836, 1997.

[88] M. C. Gust, L. A. Momoda, N. D. Evans, and M. L. Mecartney, "Crystallization of sol-gel-derived barium strontium titanate thin films," *Journal of the American Ceramic Society*, vol. 84, no. 5, pp. 1087–1092, 2001.

[89] L. Radonjic, M. Todorovic, and J. Miladinovic, "Structural evolution of nanostructured barium titanate thin film sol-gel derived," *Journal of Sol-Gel Science and Technology*, vol. 45, no. 2, pp. 125–132, 2008.

[90] A. Manso-Silvan, L. Fuentes-Cobas, R. J. Martin-Palma, M. Hernandez-Velez, and J. M. Martinez-Duart, "$BaTiO_3$ thin films obtained by sol-gel spin coating," *Surface & Coatings Technology*, vol. 151, pp. 118–121, 2002.

[91] C. Ando, T. Suzuki, Y. Mizuno, H. Kishi, S. Nakayama, and M. Senna, "Evaluation of additive effects and homogeneity of the starting mixture on the nuclei-growth processes of barium titanate via a solid state route," *Journal of Materials Science*, vol. 43, no. 18, pp. 6182–6192, 2008.

[92] R. Ashiri, "On the solid-state formation of $BaTiO_3$ nanocrystals from mechanically activated $BaCO_3$ and TiO_2 powders: innovative mechanochemical processing, the mechanism involved, and phase and nanostructure evolutions," *Rsc Advances*, vol. 6, no. 21, pp. 17138–17150, 2016.

[93] K. Tsuzuku and M. Couzi, "*In situ* investigation of chemical reactions between $BaCO_3$ and anatase or rutile TiO_2," *Journal of Materials Science*, vol. 47, no. 10, pp. 4481–4487, 2012.

[94] M. T. Buscaglia, M. Bassoli, and V. Buscaglia, "Solid-state synthesis of ultrafine $BaTiO_3$ powders from nanocrystalline $BaCO_3$ and TiO_2," *Journal of the American Ceramic Society*, vol. 88, no. 9, pp. 2374–2379, 2005.

[95] A. Lotnyk, S. Senz, and D. Hesse, "Formation of $BaTiO_3$ thin films from (110) TiO_2 rutile single crystals and $BaCO_3$ by solid state reactions," *Solid State Ionics*, vol. 177, no. 5-6, pp. 429–436, 2006.

[96] U. Manzoor and D. K. Kim, "Synthesis of nano-sized barium titanate powder by solid-state reaction between barium carbonate and titania," *Journal of Materials Science & Technology*, vol. 23, no. 5, pp. 655–658, 2007.

[97] W. Ousibenomar, S. S. Xue, R. A. Lessard, A. Singh, Z. L. Wu, and P. K. Kuo, "Structural and optical characterization of $BaTiO_3$ thin-films prepared by metal-organic deposition from barium 2-ethylhexanoate and titanium dimethoxy dineodecanoate," *Journal of Materials Research*, vol. 9, no. 4, pp. 970–979, 1994.

[98] J. D. Tsay, T. T. Fang, T. A. Gubiotti, and J. Y. Ying, "Evolution of the formation of barium titanate in the citrate process: the effect of the pH and the molar ratio of barium ion and citric acid," *Journal of Materials Science*, vol. 33, no. 14, pp. 3721–3727, 1998.

[99] P. Duran, F. Capel, D. Gutierrez, J. Tartaj, M. A. Banares, and C. Moure, "Metal citrate polymerized complex thermal decomposition leading to the synthesis of $BaTiO_3$: effects of the precursor structure on the $BaTiO_3$ formation mechanism," *Journal of Materials Chemistry*, vol. 11, no. 7, pp. 1828–1836, 2001.

[100] M. Arima, M. Kakihana, Y. Nakamura, M. Yashima, and M. Yoshimura, "Polymerized complex route to barium titanate powders using barium-titanium mixed-metal citric acid complex," *Journal of the American Ceramic Society*, vol. 79, no. 11, pp. 2847–2856, 1996.

[101] M. Kakihana, M. Arima, Y. Nakamura, M. Yashima, and M. Yoshimura, "Spectroscopic characterization of precursors used in the pechini-type polymerizable complex processing of barium titanate," *Chemistry of Materials*, vol. 11, no. 2, pp. 438–450, 1999.

[102] T. T. Fang, M. S. Wu, and J. D. Tsai, "C-13 NMR study of the solution chemistry of barium titanium citrate gels prepared using the pechini process," *Journal of the American Ceramic Society*, vol. 85, no. 12, pp. 2984–2988, 2002.

[103] S. Kumar, G. L. Messing, and W. B. White, "Metal-organic resin derived barium-titanate 1: Formation of barium titanium oxycarbonate intermediate," *Journal of the American Ceramic Society*, vol. 76, no. 3, pp. 617–624, 1993.

[104] S. Kumar and G. L. Messing, "Metal-organic resin derived barium-titanate 2: Kinetics of $BaTiO_3$ formation," *Journal of the American Ceramic Society*, vol. 77, no. 11, pp. 2940–2948, 1994.

[105] M. H. Frey and D. A. Payne, "Synthesis and processing of barium-titanate ceramics from alkoxide solutions and monolithic gels," *Chemistry of Materials*, vol. 7, no. 1, pp. 123–129, 1995.

[106] H. S. Gopalakrishnamurthy, M. S. Rao, and T. R. N. Kutty, "Thermal-decomposition of titanyl oxalates 1: Barium titanyl oxalate," *Journal of Inorganic & Nuclear Chemistry*, vol. 37, no. 4, pp. 891–898, 1975.

[107] D. Hennings and W. Mayr, "Thermal-decomposition of (Ba,Ti) citrates into barium-titanate," *Journal of Solid State Chemistry*, vol. 26, no. 4, pp. 329–338, 1978.

[108] M. Arima, M. Kakihana, M. Yashima, and M. Yoshimura, "Polymerized complex synthesis of pure $BaTiO_3$ at reduced temperature," *European Journal of Solid State and Inorganic Chemistry*, vol. 32, no. 7-8, pp. 863–871, 1995.

[109] D. Hennings, G. Rosenstein, and H. Schreinemacher, "Hydrothermal preparation of barium titanate from barium-titanium acetate gel precursors," *Journal of the European Ceramic Society*, vol. 8, no. 2, pp. 107–115, 1991.

[110] W. S. Cho, "Structural evolution and characterization of $BaTiO_3$ nanoparticles synthesized from polymeric precursor," *Journal of Physics and Chemistry of Solids*, vol. 59, no. 5, pp. 659–666, 1998.

[111] O. O. Vasyl'kiv, A. V. Ragulya, and V. V. Skorokhod, "Synthesis and sintering of nanocrystalline barium titanate powder under nonisothermal conditions. II phase analysis of the decomposition products of barium titanyl-oxalate and the synthesis of barium titanate," *Powder Metallurgy and Metal Ceramics*, vol. 36, no. 5-6, pp. 277–282, 1997.

[112] C. Borderon, D. Averty, R. Seveno, and H. W. Gundel, "Preparation and characterization of barium strontium titanate thin films by chemical solution deposition," *Ferroelectrics*, vol. 362, pp. 1–7, 2008.

[113] X. F. Chen, W. Q. Lu, W. G. Zhu, S. Y. Lim, and S. A. Akbar, "Structural and thermal analyses on phase evolution of sol-gel (Ba,Sr)TiO_3 thin films," *Surface & Coatings Technology*, vol. 167, no. 2-3, pp. 203–206, 2003.

[114] J. G. Cheng, X. J. Meng, B. Li, J. Tang, S. L. Guo, J. H. Chu, M. Wang, H. Wang, and Z. Wang, "Ferroelectricity in sol-gel derived $Ba_{0.8}Sr_{0.2}TiO_3$ thin films using a highly diluted precursor solution," *Applied Physics Letters*, vol. 75, no. 14, pp. 2132–2134, 1999.

[115] J. C. Lee and S. G. Yoon, "Characterization of $(Ba_{1-x},Sr_x)TiO_3$ thin films deposited on $Pt/Ti/SiO_2/Si$ substrates with different Ti buffer layer thicknesses," *Journal of Vacuum Science & Technology B*, vol. 17, no. 5, pp. 2182–2185, 1999.

[116] Z.-L. Cai, Z.-M. Wang, H.-H. Wang, Z.-X. Cheng, B.-W. Li, X.-L. Guo, H. Kimura, and A. Kasahara, "An investigation of the nanomechanical properties of $0.5Ba(Zr_{0.2}Ti_{0.8})O_3$-$0.5(Ba_{0.7}Ca_{0.3})TiO_3$ thin films," *Journal of the American Ceramic Society*, vol. 98, no. 1, pp. 114–118, 2015.

[117] Y. Chen, T. Y. Zhang, Q. G. Chi, J. Q. Lin, X. Wang, and Q. Q. Lei, "Low temperature growth of (100)-oriented $Ba(Zr_{0.2}Ti_{0.8})O_3$-$0.5(Ba_{0.7}Ca_{0.3})TiO_3$ thin films using a $LaNiO_3$ seed layer," *Journal of Alloys and Compounds*, vol. 663, pp. 818–822, 2016.

[118] A. Jalalian, A. M. Grishin, X. L. Wang, Z. X. Cheng, and S. X. Dou, "Large piezoelectric coefficient and ferroelectric nanodomain switching in $Ba(Zr_{0.2}Ti_{0.8})O_3$-$0.5(Ba_{0.7}Ca_{0.3})TiO_3$ nanofibers and thin films," *Applied Physics Letters*, vol. 104, no. 10, pp. 1–5, 2014.

[119] G. Kang, K. Yao, and J. Wang, "(1-x)$Ba(Zr_{0.2}Ti_{0.8})O_3$-x$(Ba_{0.7}Ca_{0.3})TiO_3$ ferroelectric thin films prepared from chemical solutions," *Journal of the American Ceramic Society*, vol. 95, no. 3, pp. 986–991, 2012.

[120] W. Li, J. Hao, H. Zeng, and J. Zhai, "Dielectric and piezoelectric properties of the $Ba_{0.92}Ca_{0.08}Ti_{0.95}Zr_{0.05}O_3$ thin films grown on different substrate," *Current Applied Physics*, vol. 13, no. 7, pp. 1205–1208, 2013.

[121] W. L. Li, T. D. Zhang, D. Xu, Y. F. Hou, W. P. Cao, and W. D. Fei, "$LaNiO_3$ seed layer induced enhancement of piezoelectric properties in (100)-oriented (1-x)BZT−xBCT thin films," *Journal of the European Ceramic Society*, vol. 35, no. 7, pp. 2041–2049, 2015.

[122] Z. Wang, Z. Cai, H. Wang, Z. Cheng, J. Chen, X. Guo, and H. Kimura, "Lead-free $Ba(Zr_{0.2}Ti_{0.8})O_3$-$0.5(Ba_{0.7}Ca_{0.3})TiO_3$ thin films with enhanced electric properties fabricated from optimized sol-gel systems," *Materials Chemistry and Physics*, vol. 186, pp. 528–533, 2017.

[123] W. F. Bai, B. Shen, F. Fu, and J. W. Zhai, "Dielectric, ferroelectric, and piezoelectric properties of textured BZT-BCT lead-free thick film by screen printing," *Materials Letters*, vol. 83, pp. 20–22, 2012.

[124] L. N. Gao, J. W. Zhai, and X. Yao, "Study of dielectric characteristics of graded $Ba_{1-x}Ca_xZr_{0.05}Ti_{0.95}O_3$ thin films grown by a sol-gel process," *Journal of Sol-Gel Science and Technology*, vol. 45, no. 1, pp. 51–55, 2008.

[125] Y. Lin, G. Wu, N. Qin, and D. Bao, "Structure, dielectric, ferroelectric, and optical properties of (1-x)$Ba(Zr_{0.2}Ti_{0.8})O_3$-x$(Ba_{0.7}Ca_{0.3})TiO_3$ thin films prepared by sol-gel method," *Thin Solid Films*, vol. 520, no. 7, pp. 2800–2804, 2012.

[126] Z. Tao, F. Che, Y. M. Han, F. Wang, Z. C. Yang, W. Qi, Y. Wu, and K. L. Zhang, "Out-of-plane and in-plane piezoelectric behaviors of $Ba(Zr_{0.2}Ti_{0.8})O_3$-$0.5(Ba_{0.7}Ca_{0.3})TiO_3$ thin films," *Progress in Natural Science-Materials International*, vol. 27, no. 6, pp. 664–668, 2017.

[127] T. M. Raeder, K. Bakken, J. Glaum, M. A. Einarsrud, and T. Grande, "Enhanced in-plane ferroelectricity in $BaTiO_3$ thin films fabricated by aqueous chemical solution deposition," *Aip Advances*, vol. 8, no. 10, pp. 1–9.

[128] E. Khomyakova, S. Wenner, K. Bakken, T. Grande, J. Glaum, and M.-A. Einarsrud, "On the formation mechanism of BCZT thin films by aqueous chemical solution deposition," *Journal of the European Ceramic Society (Submitted)*, 2020.

[129] A. Hardy, J. D'Haen, H. Van den Rul, M. K. Van Bael, and J. Mullens, "Crystallization of alkaline earth zirconates and niobates from compositionally flexible aqueous solution-gel syntheses," *Materials Research Bulletin*, vol. 44, no. 4, pp. 734–740, 2009.

[130] A. Hardy, S. Van Elshocht, W. Knaepen, J. D'Haen, T. Conard, B. Brijs, W. Vandervorst, G. Pourtois, J. Kittl, C. Detavernier, M. Heyns, M. K. Van Bael, H. Van den Rul, and J. Mullens, "Crystallization resistance of barium titanate zirconate ultrathin films from aqueous CSD: a study of cause and effect," *Journal of Materials Chemistry*, vol. 19, no. 8, pp. 1115–1122, 2009.

[131] J. P. George, J. Beeckman, W. Woestenborghs, P. F. Smet, W. Bogaerts, and K. Neyts, "Preferentially oriented $BaTiO_3$ thin films deposited on silicon with thin intermediate buffer layers," *Nanoscale Research Letters*, vol. 8, no. 1, pp. 1–7, 2013.

[132] T. Hosokura, A. Ando, and T. Konoike, "Orientation-controlled $BaTiO_3$ thin films fabricated by chemical solution deposition," *Rsc Advances*, vol. 5, no. 118, pp. 97563–97567, 2015.

[133] B. I. Edmondson, S. Kwon, C. H. Lam, J. E. Ortmann, A. A. Demkov, M. J. Kim, and J. G. Ekerdt, "Epitaxial, electro-optically active barium titanate thin films on silicon by chemical solution deposition," *Journal of the American Ceramic Society*, pp. 1–10, 2019.

[134] B. C. Luo, D. Y. Wang, M. M. Duan, and S. Li, "Orientation-dependent piezoelectric properties in lead-free epitaxial $0.5Ba_{0.7}Ca_{0.3}TO_3$-$0.5BaZr_{0.2}Ti_{0.8}O_3$ thin films," *Applied Physics Letters*, vol. 103, no. 12, pp. 1–5, 2013.

[135] M. Shi, J. G. Zhong, R. Z. Zuo, Y. D. Xu, L. Wang, H. L. Su, and C. Gu, "Effect of annealing processes on the structural and electrical properties of the lead-free thin films of $(Ba_{0.9}Ca_{0.1})(Ti_{0.9}Zr_{0.1})O_3$," *Journal of Alloys and Compounds*, vol. 562, pp. 116–122, 2013.

[136] D. Dimos, M. Raymond, R. Schwartz, H. Al-Shareef, and C. Mueller, "Tunability and calculation of the dielectric constant of capacitor structures with interdigital electrodes," *Journal of Electroceramics*, vol. 1, no. 2, pp. 145–153, 1997.

[137] Y. Saito, H. Takao, T. Tani, T. Nonoyama, K. Takatori, T. Homma, T. Nagaya, and M. Nakamura, "Lead-free piezoceramics," *Nature*, vol. 432, no. 7013, pp. 84–87, 2004.

[138] L. Egerton and D. M. Dillon, "Piezoelectric and dielectric properties of ceramics in the system potassium—sodium niobate," *Journal of the American Ceramic Society*, vol. 42, no. 9, pp. 438–442, 1959.

[139] A. Safari and E. K. Akdoğan, *Piezoelectric and Acoustic Materials for Transducer Applications*. Springer US Boston, 2008.

[140] C. W. Ahn, S. Y. Lee, H. J. Lee, A. Ullah, J. S. Bae, E. D. Jeong, J. S. Choi, B. H. Park, and I. W. Kim, "The effect of k and na excess on the ferroelectric and piezoelectric properties of $K_{0.5}Na_{0.5}NbO_3$ thin films," *Journal of Physics D-Applied Physics*, vol. 42, no. 21, pp. 1–6.

[141] H. Brunckova, L. Medvecky, P. Hvizdos, and J. Durisin, "Structural and nanomechanical properties of sol-gel prepared (K, Na)NbO_3 thin films," *Surface and Interface Analysis*, vol. 47, no. 11, pp. 1063–1071, 2015.

[142] A. Chowdhury, J. Bould, M. G. S. Londesborough, and S. J. Milne, "Fundamental issues in the synthesis of ferroelectric $Na_{0.5}K_{0.5}NbO_3$ thin films by sol-gel processing," *Chemistry of Materials*, vol. 22, no. 13, pp. 3862–3874, 2010.

[143] C. Kang, J.-H. Park, D. Shen, H. Ahn, M. Park, and D.-J. Kim, "Growth and characterization of $K_{0.5}Na_{0.5}NbO_3$ thin films by a sol–gel method," *Journal of Sol-Gel Science and Technology*, vol. 58, no. 1, pp. 85–90, 2011.

[144] J. Kwak, A. I. Kingon, and S.-H. Kim, "Lead-free $Na_{0.5}K_{0.5}NbO_3$ thin films for the implantable piezoelectric medical sensor applications," *Materials Letters*, vol. 82, pp. 130–132, 2012.

[145] F. Lai, J.-F. Li, Z.-X. Zhu, and Y. Xu, "Influence of li content on electrical properties of highly piezoelectric (Li,K,Na)NbO_3 thin films prepared by sol-gel processing," *Journal of Applied Physics*, vol. 106, no. 6, pp. 1–7, 2009.

[146] Y. Nakashima, W. Sakamoto, H. Maiwa, T. Shimura, and T. Yogo, "Lead-free piezoelectric (K,Na)NbO_3 thin films derived from metal alkoxide precursors," *Japanese Journal of Applied Physics*, vol. 46, no. No. 14, pp. 311–313, 2007.

[147] V. X., O. Raymond, D. A. Ochoa, J. E. García, and L. Mestres, "Growth and physical properties of highly oriented La-doped (K,Na)NbO_3 ferroelectric thin films," *Thin Solid Films*, vol. 577, pp. 35–41, 2015.

[148] X. Yan, W. Ren, X. Wu, P. Shi, and X. Yao, "Lead-free (K,Na)NbO_3 ferroelectric thin films: Preparation, structure and electrical properties," *Journal of Alloys and Compounds*, vol. 508, no. 1, pp. 129–132, 2010.

[149] X. Wu, L. Wang, W. Ren, X. Yan, P. Shi, X. Chen, and X. Yao, "Preparation and properties of (110) oriented lead-free sodium potassium niobate thin films by MOD method," *Ferroelectrics*, vol. 367, no. 1, pp. 61–66, 2008.

[150] J. Luo, W. Sun, Z. Zhou, Y. Bai, Z. J. Wang, G. Tian, D. Chen, X. Gao, F. Zhu, and J.-F. Li, "Domain evolution and piezoelectric response across thermotropic phase boundary in (K,Na)NbO_3-based epitaxial thin films," *ACS Applied Materials & Interfaces*, vol. 9, no. 15, pp. 13315–13322, 2017.

[151] T. Lu, K. Zhu, J. Liu, J. Wang, and J. Qiu, "Lead-free (K,Na)NbO_3 thin films derived from chemical solution deposition modified with EDTA," *Journal of Materials Science: Materials in Electronics*, vol. 25, no. 2, pp. 1112–1116, 2014.

[152] D. Zhang, F. Zheng, X. Yang, L. Feng, X. Huang, H. Liu, and M. Cao, "Preparation and ferroelectric properties of $K_{0.5}Na_{0.5}NbO_3$ thin films derived from non-alcohol niobium salt sol-gel process," *Integrated Ferroelectrics*, vol. 154, no. 1, pp. 97–102, 2014.

[153] Y. Du and S. M. George, "Molecular layer deposition of nylon 66 films examined using *in Situ* FTIR spectroscopy," *The Journal of Physical Chemistry C*, vol. 111, no. 24, pp. 8509–8517, 2007.

[154] H. Hu, S. Cai, H. Li, L. Huang, L. Shi, and D. Zhang, "*In Situ* DRIFTs investigation of the low-temperature reaction mechanism over Mn-doped Co_3O_4 for the selective catalytic reduction of NO_x with NH_3," *The Journal of Physical Chemistry C*, vol. 119, no. 40, pp. 22924–22933, 2015.

[155] P. Innocenzi, T. Kidchob, J. M. Bertolo, M. Piccinini, M. C. Guidi, and C. Marcelli, "Time-resolved infrared spectroscopy as an *In Situ* tool to study the kinetics during self-assembly of mesostructured films," *The Journal of Physical Chemistry B*, vol. 110, no. 22, pp. 10837–10841, 2006.

[156] R. Kas, O. Ayemoba, N. J. Firet, J. Middelkoop, W. A. Smith, and A. Cuesta, "*In-Situ* infrared spectroscopy applied to the study of the electrocatalytic reduction of CO_2: Theory, practice and challenges," *ChemPhysChem*, vol. 20, no. 22, pp. 2904–2925, 2019.

[157] J. A. Lercher, V. Veefkind, and K. Fajerwerg, "*In situ* IR spectroscopy for developing catalysts and catalytic processes," *Vibrational Spectroscopy*, vol. 19, no. 1, pp. 107–121, 1999.

[158] S. Meng, P. Wang, L. Chen, G. Gao, and J. Zhang, "*In situ* characterization of phase transition of amorphous poly(9,9-di-n-octyl-2,7-fluorene) thin film during thermal annealing," *Chemical Research in Chinese Universities*, vol. 35, no. 1, pp. 157–162, 2019.

[159] D. Wang, L. Zhang, K. Kamasamudram, and W. S. Epling, "*In Situ*-DRIFTs study of selective catalytic reduction of NO_x by NH_3 over Cu-exchanged SAPO-34," *ACS Catalysis*, vol. 3, no. 5, pp. 871–881, 2013.

[160] S. Wang, Z. Chen, B. He, Z. Yan, H. Wang, L. Liu, and X. Wang, "*In Situ*-DRIFTs investigation on ceox catalyst supported by fly-ash-made porous cordierite ceramics for low-temperature NH_3-SCR of NO_x," *Catalysts*, vol. 9, no. 6, p. 496, 2019.

[161] D. Cozzolino, *Infrared Spectroscopy : Theory, Developments and Applications*. Nova Science Publishers New York, 2013.

[162] A. M. Almanza-Workman, S. Raghavan, and R. P. Sperline, "*In Situ* ATR-FTIR analysis of surfactant adsorption onto silicon from buffered hydrofluoric acid solutions," *Langmuir*, vol. 16, no. 8, pp. 3636–3640, 2000.

[163] S. J. Hug and D. Bahnemann, "Infrared spectra of oxalate, malonate and succinate adsorbed on the aqueous surface of rutile, anatase and lepidocrocite measured with *in situ* ATR-FTIR," *Journal of Electron Spectroscopy and Related Phenomena*, vol. 150, no. 2, pp. 208–219, 2006.

[164] M.-S. Zheng and S.-G. Sun, "*In situ* FTIR spectroscopic studies of CO adsorption on electrodes with nanometer-scale thin films of ruthenium in sulfuric acid solutions," *Journal of Electroanalytical Chemistry*, vol. 500, no. 1, pp. 223–232, 2001.

[165] S. Zhuiykov, "*In situ* FTIR study of oxygen adsorption on nanostructured RuO_2 thin-film electrode," *Ionics*, vol. 15, no. 4, pp. 507–512, 2009.

[166] V. Goian, F. Kadlec, C. Kadlec, B. Dabrowski, S. Kolesnik, O. Chmaissem, D. Nuzhnyy, M. Kempa, V. Bovtun, M. Savinov, J. Hejtmánek, J. Prokleška, and S. Kamba, "Spectroscopic studies of the ferroelectric and magnetic phase transitions in multiferroic $Sr_{1-x}Ba_xMnO_3$," *Journal of Physics: Condensed Matter*, vol. 28, no. 17, pp. 1–7, 2016.

[167] S. Kamba, M. Kempa, V. Bovtun, J. Petzelt, K. Brinkman, and N. Setter, "Soft and central mode behaviour in $PbMg_{1/3}Nb_{2/3}O_3$ relaxor ferroelectric," *Journal of Physics: Condensed Matter*, vol. 17, no. 25, pp. 3965–3974, 2005.

[168] P. Innocenzi, T. Kidchob, L. Malfatti, S. Costacurta, M. Takahashi, M. Piccinini, and A. Marcelli, "*In-situ* study of sol-gel processing by time-resolved infrared spectroscopy," *Journal of Sol-Gel Science and Technology*, vol. 48, no. 1-2, pp. 253–259, 2008.

[169] W. Eberhardt, "Synchrotron radiation: A continuing revolution in X-ray science - diffraction limited storage rings and beyond," *Journal of Electron Spectroscopy and Related Phenomena*, vol. 200, pp. 31–39, 2015.

[170] J. C. Lindon, G. E. Tranter, and D. Koppenaal, *Encyclopedia of Spectroscopy and Spectrometry*. Elsevier Science Amsterdam, 3 ed., 2016.

[171] S. Bauer, A. Rodrigues, and T. Baumbach, "Real time *in situ* X-ray diffraction study of the crystalline structure modification of $Ba_{0.5}Sr_{0.5}TiO_3$ during the post-annealing," *Scientific Reports*, vol. 8, no. 1, p. 5664–5673, 2018.

[172] W. Matz, N. Schell, W. Neumann, J. Bøttiger, and J. Chevallier, "A two magnetron sputter deposition chamber for *in situ* observation of thin film growth by synchrotron radiation scattering," *Review of Scientific Instruments*, vol. 72, no. 8, pp. 3344–3348, 2001.

[173] B. Bein, H.-C. Hsing, S. J. Callori, J. Sinsheimer, P. V. Chinta, R. L. Headrick, and M. Dawber, "*In situ* X-ray diffraction and the evolution of polarization during the growth of ferroelectric superlattices," *Nature Communications*, vol. 6, no. 1, pp. 1–8, 2015.

[174] K. Ellmer, R. Mientus, V. Wei , and H. Rossner, "*In situ* energy-dispersive X-ray diffraction system for time-resolved thin-film growth studies," *Measurement Science and Technology*, vol. 14, no. 3, pp. 336–345, 2003.

[175] K. Ellmer, R. Mientus, V. Weiß, and H. Rossner, "Setup for *in situ* X-ray diffraction studies of thin film growth by magnetron sputtering," *Nuclear Instruments and Methods in Physics Research Section A: Accelerators, Spectrometers, Detectors and Associated Equipment*, vol. 467-468, pp. 1041–1044, 2001.

[176] J. Q. Zheng, X. K. Wang, M. C. Shih, S. Williams, J. So, S. J. Lee, P. Dutta, R. P. H. Chang, and J. B. Ketterson, "*In situ* synchrotron studies of the structural properties of Y-Ba-Cu-O thin films during growth," *Applied Physics Letters*, vol. 58, no. 20, pp. 2303–2305, 1991.

[177] M. Roelsgaard, A.-C. Dippel, K. A. Borup, I. G. Nielsen, N. L. N. Broge, J. T. Roh, O. Gutowski, and B. B. Iversen, "Time-resolved grazing-incidence pair distribution functions during deposition by radio-frequency magnetron sputtering," *IUCrJ*, vol. 6, no. 2, pp. 299–304, 2019.

[178] G. Kaune, S. Hartnauer, and R. Scheer, "*In situ* XRD investigation of $Cu_2ZnSnSe_4$ thin film growth by thermal co-evaporation," *physica status solidi (a)*, vol. 211, no. 9, pp. 1991–1996, 2014.

[179] F. Bertram, C. Deiter, K. Pflaum, M. Suendorf, C. Otte, and J. Wollschläger, "*In-situ* X-ray diffraction studies on post-deposition vacuum-annealing of ultra-thin iron oxide films," *Journal of Applied Physics*, vol. 110, no. 10, pp. 1–5, 2011.

[180] A. Davydok, T. W. Cornelius, C. Mocuta, E. C. Lima, E. B. Araujo, and O. Thomas, "*In situ* X-ray diffraction studies on the piezoelectric response of PZT thin films," *Thin Solid Films*, vol. 603, pp. 29–33, 2016.

[181] K. M. O. Jensen, A. B. Blichfeld, S. R. Bauers, S. R. Wood, E. Dooryhee, D. C. Johnson, B. B. Iversen, and S. J. L. Billinge, "Demonstration of thin film pair distribution function analysis (tfPDF) for the study of local structure in amorphous and crystalline thin films," *IUCrJ*, vol. 2, no. 5, pp. 481–489, 2015.

[182] A.-C. Dippel, M. Roelsgaard, U. Boettger, T. Schneller, O. Gutowski, and U. Ruett, "Local atomic structure of thin and ultrathin films via rapid high-energy X-ray total scattering at grazing incidence," *IUCrJ*, vol. 6, no. 2, pp. 290–298, 2019.

[183] T. Miyadera, Y. Shibata, T. Koganezawa, T. N. Murakami, T. Sugita, N. Tanigaki, and M. Chikamatsu, "Crystallization dynamics of organolead halide perovskite by real-time X-ray diffraction," *Nano Letters*, vol. 15, no. 8, pp. 5630–5634, 2015.

[184] K. Nittala, S. Mhin, J. L. Jones, D. S. Robinson, J. F. Ihlefeld, and G. L. Brennecka, "*In situ* X-ray diffraction of solution-derived ferroelectric thin films for quantitative phase and texture evolution measurement," *Journal of Applied Physics*, vol. 112, no. 10, pp. 1–10, 2012.

[185] K. Nittala, S. Mhin, K. M. Dunnigan, D. S. Robinson, J. F. Ihlefeld, P. G. Kotula, G. L. Brennecka, and J. L. Jones, "Phase and texture evolution in solution deposited lead zirconate titanate thin films: Formation and role of the Pt_3Pb intermetallic phase," *Journal of Applied Physics*, vol. 113, no. 24, pp. 1–11, 2013.

[186] CRYSTAL GmbH, "Crystal Data Sheet." URL: `https://crystal-gmbh.com/en/products/substrates/oxides.php`, (2020, February 02).

[187] W. P. Davey, "Precision measurements of the lattice constants of twelve common metals," *Physical Review*, vol. 25, no. 6, pp. 753–761, 1925.

[188] A. Bergamin, G. Cavagnero, G. Mana, and G. Zosi, "Lattice parameter and thermal expansion of monocrystalline silicon," *Journal of Applied Physics*, vol. 82, no. 11, pp. 5396–5400, 1997.

[189] V. Baidakov, V. Fokin, I. Gutzow, J. Schmelzer, G. Johari, A. Karamanov, V. Leko, B. Pevzner, I. Polyakova, and C. Schick, *Glass: Selected Properties and Crystallization*. Walter de Gruyter GmbH & Company KG Berlin, 2014.

[190] A. B. Blichfeld, K. Bakken, D. Chernyshov, J. Glaum, T. Grande, and M.-A. Einarsrud, "Experimental setup for high-temperature *in situ* studies of crystallization of thin films with atmosphere control," *Journal of Synchrotron Radiation (In preparation)*.

[191] V. Dyadkin, P. Pattison, V. Dmitriev, and D. Chernyshov, "A new multipurpose diffractometer PILATUS at SNBL," *Journal of Synchrotron Radiation*, vol. 23, pp. 825–829, 2016.

[192] L. Lutterotti, "Total pattern fitting for the combined size–strain–stress–texture determination in thin film diffraction," *Nuclear Instruments and Methods in Physics Research Section B: Beam Interactions with Materials and Atoms*, vol. 268, no. 3, pp. 334–340, 2010.

[193] P. Brüesch, *Phonons: theory and experiments, Experiments and interpretation of experimental results*, vol. 2 of *Springer series in solid-state sciences*. Springer Berlin, 1986.

[194] C. H. Nguyen, R. Nigon, T. M. Raeder, U. Hanke, E. Halvorsen, and P. Muralt, "Probing-models for interdigitated electrode systems with ferroelectric thin films," *Journal of Physics D: Applied Physics*, vol. 51, no. 17, pp. 1–16, 2018.

[195] K. Nakamoto, *Infrared and Raman Spectra of Inorganic and Coordination Compounds, Part B: Applications in coordination, organometallic, and bioinorganic chemistry*, vol. Pt. B. Wiley New York, 5th ed., 1997.

[196] B. H. Stuart, *Infrared Spectroscopy : Fundamentals and Applications*. Analytical Techniques in the Sciences, Wiley New York, 2004.

[197] P. Linstrom and W. Mallard, *NIST Chemistry WebBook, NIST Standard Reference Database Number 69*. National Institute of Standards and Technology (retrieved 2020 February 08).

[198] M. Fujimoto, "Defects in epitaxially grown perovskite thin films," *Journal of Crystal Growth*, vol. 237, pp. 430–437.

[199] T. O. L. Sunde, T. Grande, and M.-A. Einarsrud, *Modified Pechini Synthesis of Oxide Powders and Thin Films*. Springer International Publishing New York, 2016.

[200] M. Sletnes, S. L. Skjærvø, M. Lindgren, T. Grande, and M.-A. Einarsrud, "Luminescent Eu^{3+}-doped $NaLa(WO_4)(MoO_4)$ and Ba_2CaMoO_6 prepared by the modified pechini method," *Journal of Sol-Gel Science and Technology*, vol. 77, no. 1, pp. 136–144, 2016.

[201] L. Rioja-Monllor, S. Ricote, C. Bernuy-Lopez, T. Grande, R. O'Hayre, and M.-A. Einarsrud, "High-performance $La_{0.5}Ba_{0.5}Co_{1/3}Mn_{1/3}Fe_{1/3}O_{3d}BaZr_{1z}Y_zO_{3d}$ cathode composites via an exsolution mechanism for protonic ceramic fuel cells," *Inorganics*, vol. 6, no. 3, pp. 1–14, 2018.

[202] A. B. Haugen, I. Kumakiri, C. Simon, and M.-A. Einarsrud, "TiO_2, TiO_2/Ag and TiO_2/Au photocatalysts prepared by spray pyrolysis," *Journal of the European Ceramic Society*, vol. 31, no. 3, pp. 291–298, 2011.

[203] M. Christensen, M.-A. Einarsrud, and T. Grande, "Fabrication of lead-free $Bi_{0.5}Na_{0.5}TiO_3$ thin films by aqueous chemical solution deposition," *Materials*, vol. 10, no. 2, pp. 1–17, 2017.

[204] R. C. Ropp, *Encyclopedia of the alkaline earth compounds*. Elsevier Oxford, 2013.

[205] J. Bera and S. K. Rout, "On the formation mechanism of $BaTiO_3$–$BaZrO_3$ solid solution through solid-oxide reaction," *Materials Letters*, vol. 59, no. 1, pp. 135–138, 2005.

[206] T. A. Ring, *Fundamentals of Ceramic Powder Processing and Synthesis*. Elsevier Science Amsterdam, 1996.

[207] E. Wintersberger, N. Hrauda, D. Kriegner, M. Keplinger, G. Springholz, J. Stangl, G. Bauer, J. Oswald, T. Belytschko, C. Deiter, F. Bertram, and O. H. Seeck, "Analysis of periodic dislocation networks using X-ray diffraction and extended finite element modeling," *Applied Physics Letters*, vol. 96, no. 13, pp. 1–3, 2010.

[208] M. M. Vijatovic, J. D. Bobic, and B. D. Stojanovic, "History and challenges of barium titanate: Part II," *Science of Sintering*, vol. 40, no. 3, pp. 235–244, 2008.

[209] M. Christensen, *Fabrication of Lead-Free $Bi_{0.5}Na_{0.5}TiO_3$ Thin Films by Aqueous Chemical Solution Deposition*. PhD thesis, Norwegian university of science and technology (NTNU, NTNU, Trondheim, Norway, 2017.

[210] K. Bakken, A. B. Blichfeld, D. Chernyshov, T. Grande, J. Glaum, and M.-A. Einarsrud, "Mechanisms for texturing in $BaTiO_3$ thin films from aqueous chemical solution deposition," *Journal of Sol-Gel Science and Technology (Submitted)*, 2020.

[211] I. Bretos, R. Jiménez, M. L. Calzada, M. K. Van Bael, A. Hardy, D. Van Genechten, and J. Mullens, "Entirely aqueous solution-gel route for the preparation of $(Pb_{1-x}Ca_x)TiO_3$ thin films," *Chemistry of Materials*, vol. 18, no. 26, pp. 6448–6456, 2006.

[212] G. Pollefeyt, S. Clerick, P. Vermeir, P. Lommens, K. De Buysser, and I. Van Driessche, "Influence of aqueous precursor chemistry on the growth process of epitaxial $SrTiO_3$ buffer layers," *Inorganic Chemistry*, vol. 53, no. 10, pp. 4913–4921, 2014.

[213] C. De Dobbelaere, A. Hardy, J. D'Haen, H. Van den Rul, M. K. Van Bael, and J. Mullens, "Morphology of water-based chemical solution deposition (CSD) lead titanate films on different substrates: Towards island formation," *Journal of the European Ceramic Society*, vol. 29, no. 9, pp. 1703–1711, 2009.

[214] N. Van de Velde, M. Arin, P. Lommens, D. Poelman, and I. Van Driessche, "Characterization of the aqueous peroxomethod for the synthesis of transparent TiO_2 thin films," *Thin Solid Films*, vol. 519, no. 11, pp. 3475–3479, 2011.

Appendices

A Additional Results

A.1 X-ray diffraction results

A.1.1 Powder X-ray diffraction

$BaTiO_3$ powder

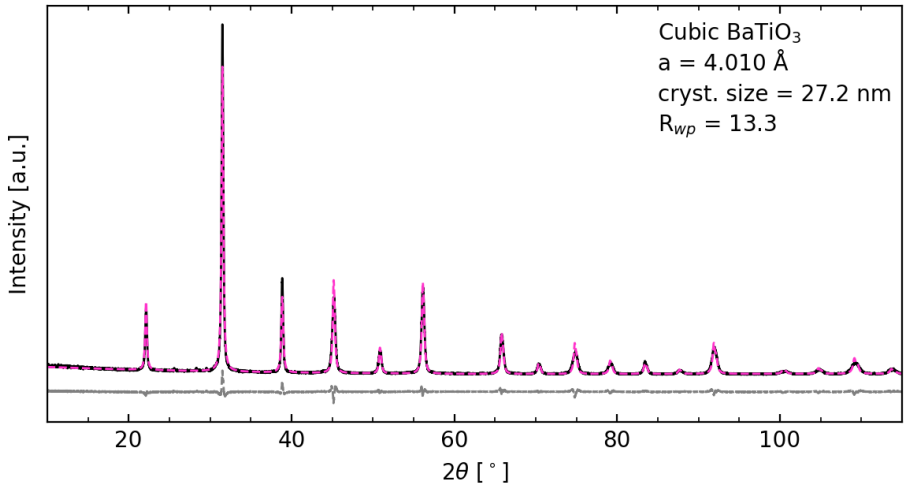

Figure A.1: XRD pattern of $BaTiO_3$ powder calcined at 750 °C for 6 h with the results of Rietveld refinements.

***In situ* annealing of $BaTiO_3$ powder with varying CO_2 partial pressure**

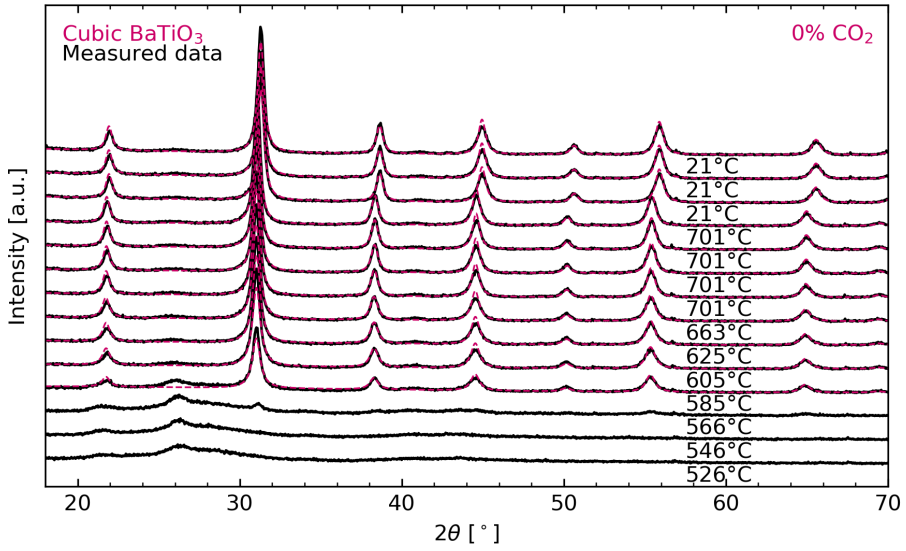

Figure A.2: *In situ* XRD and result from Rietveld refinement for $BaTiO_3$ precursor powder heated in 0 % CO_2 and synthetic air.

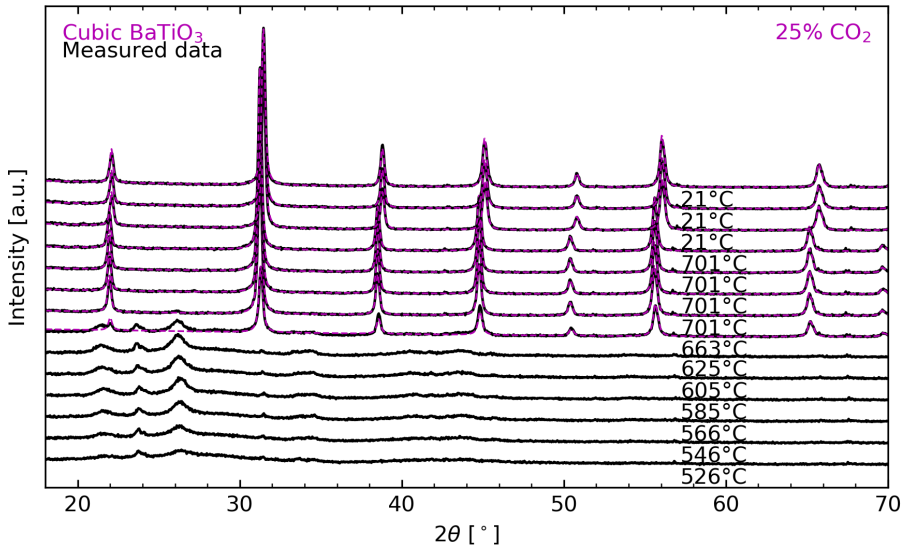

Figure A.3: *In situ* XRD and result from Rietveld refinement for $BaTiO_3$ precursor powder heated in 25 % CO_2 and synthetic air.

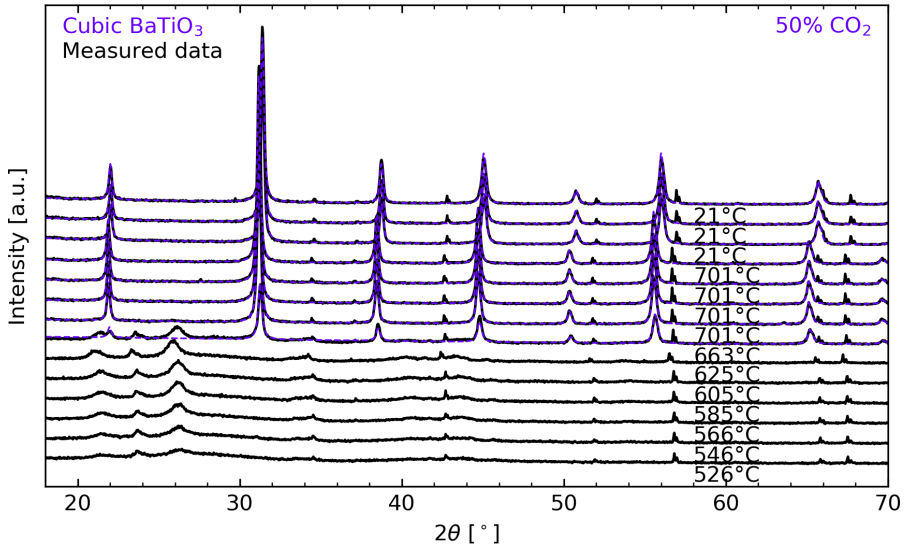

Figure A.4: *In situ* XRD and result from Rietveld refinement for $BaTiO_3$ precursor powder heated in 50 % CO_2 and synthetic air.

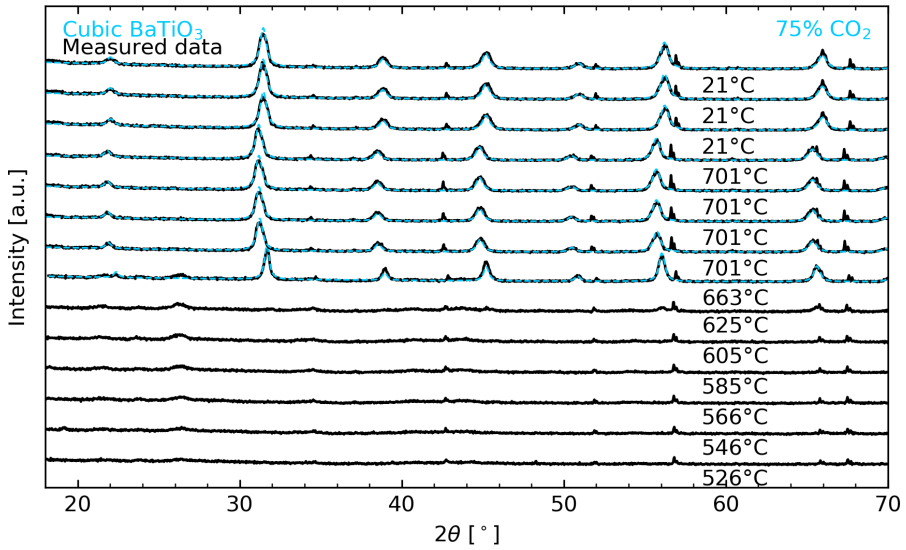

Figure A.5: *In situ* XRD and result from Rietveld refinement for $BaTiO_3$ precursor powder heated in 75 % CO_2 and synthetic air.

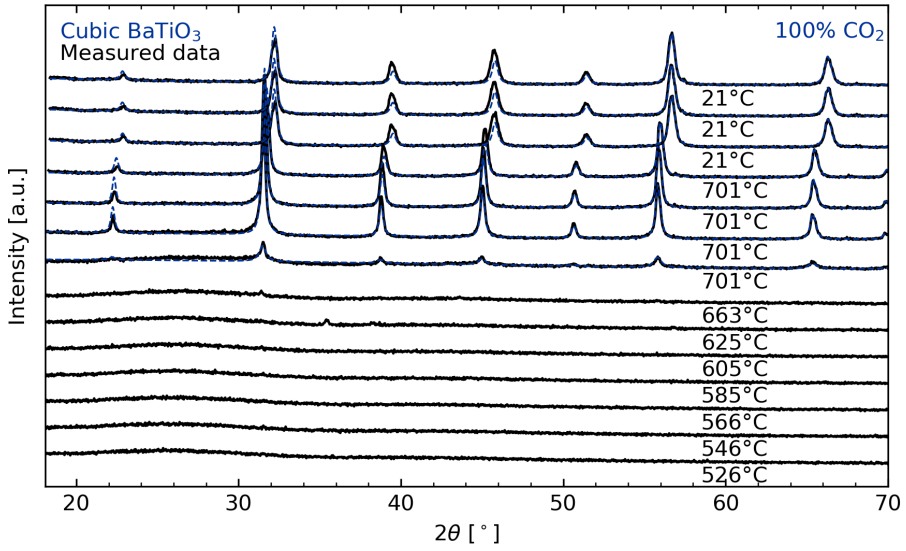

Figure A.6: *In situ* XRD and result from Rietveld refinement for $BaTiO_3$ precursor powder heated in 100 % CO_2 and synthetic air.

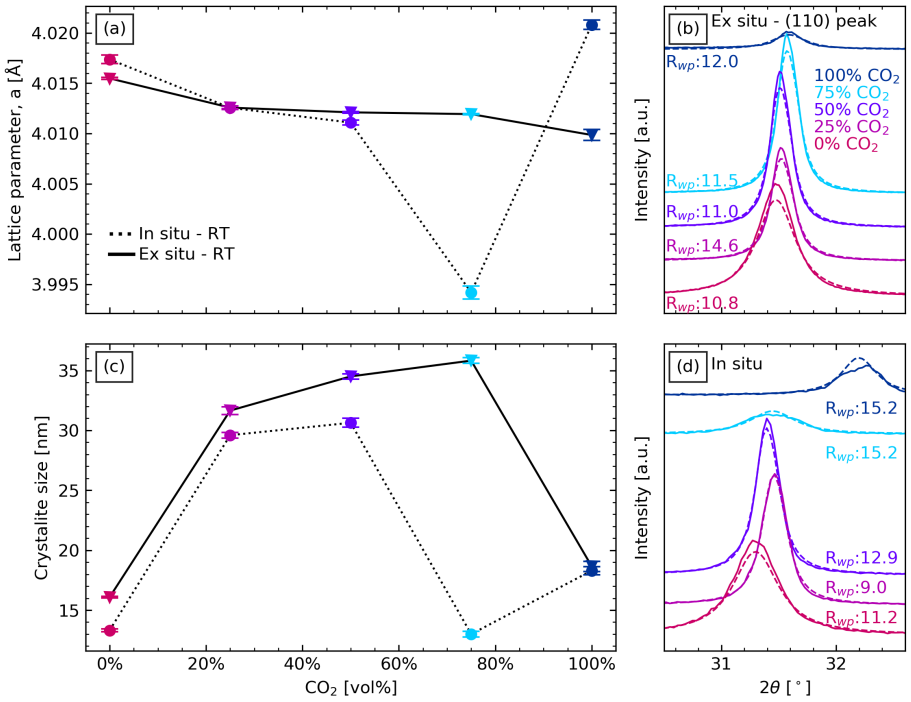

Figure A.7: Comparison of the (a) lattice parameter and (c) crystallite size from Rietveld refinements done for ambient temperature diffractograms (b) *ex situ* and (d) *in situ* for the powders heated in variable CO_2 partial pressure.

A.1.2 Synchrotron X-ray diffraction

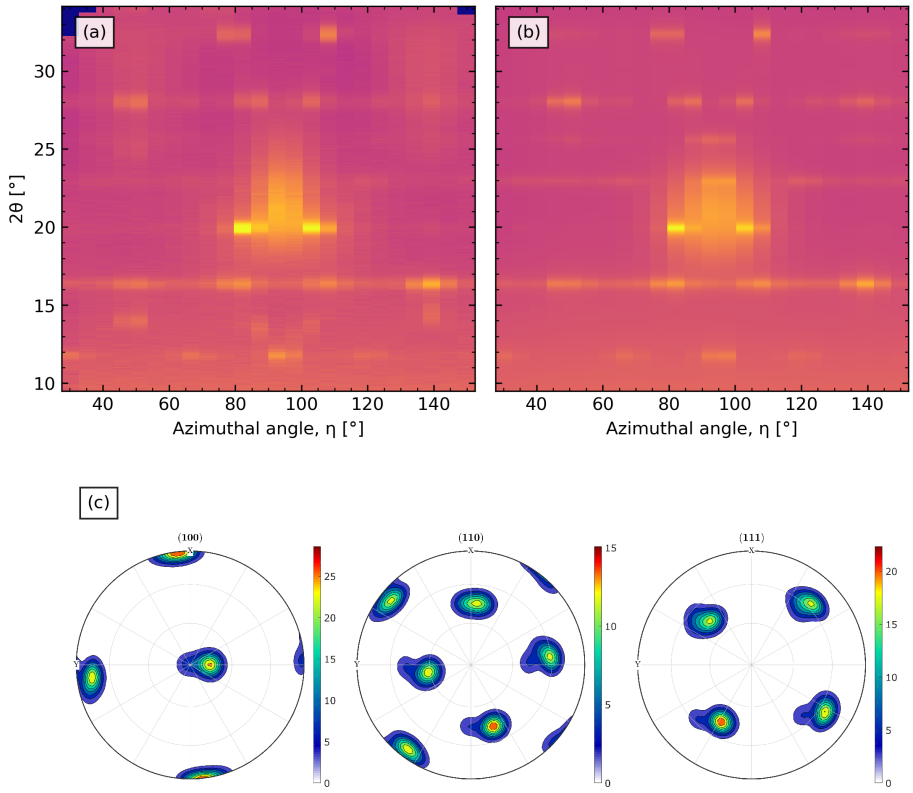

Figure A.8: The (a) experimental and (b) calculated 2D diffractograms from a Rietveld refinement with a E-WIMV texture component for a single-layer crystalline $BaTiO_3$ thin film on (100) MgO after single step heating with 0.2 °C/s to 710 °C. (c) Pole figures calculated based on ODFs from the Rietveld refinement of the same film. The wavelength was 0.78006 Å.

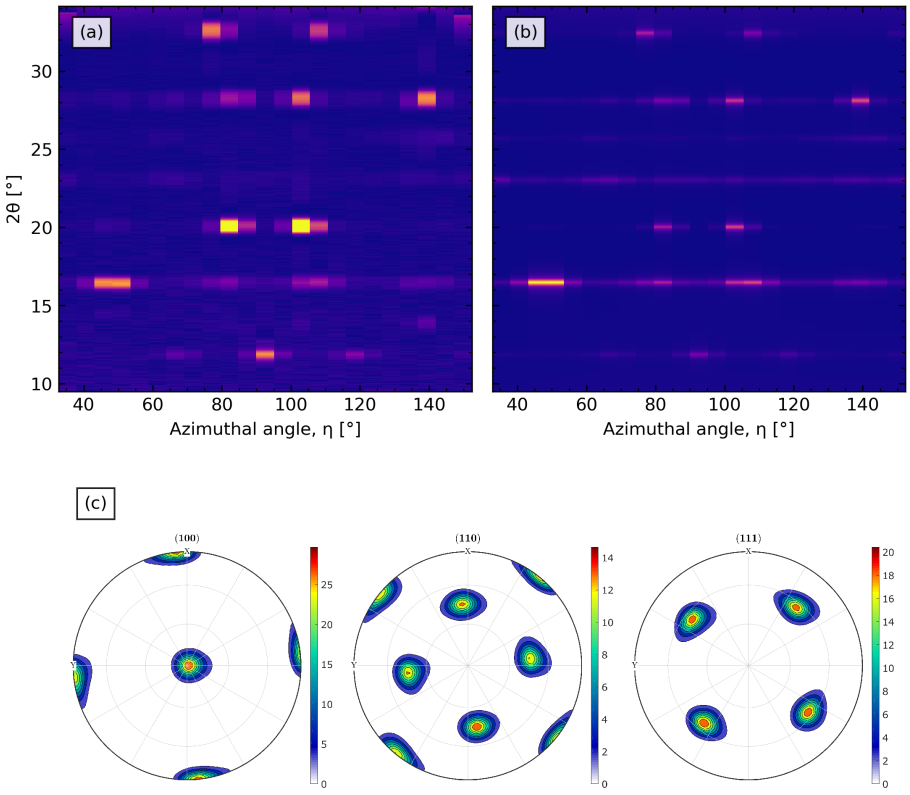

Figure A.9: The (a) experimental and (b) calculated 2D diffractograms from a Rietveld refinement with a E-WIMV texture component for a single-layer crystalline $BaTiO_3$ thin film on (100) LAO after single step heating with 0.2 °C/s to 710 °C. (c) Pole figures calculated based on ODFs from the Rietveld refinement of the same film. The wavelength was 0.78006 Å.

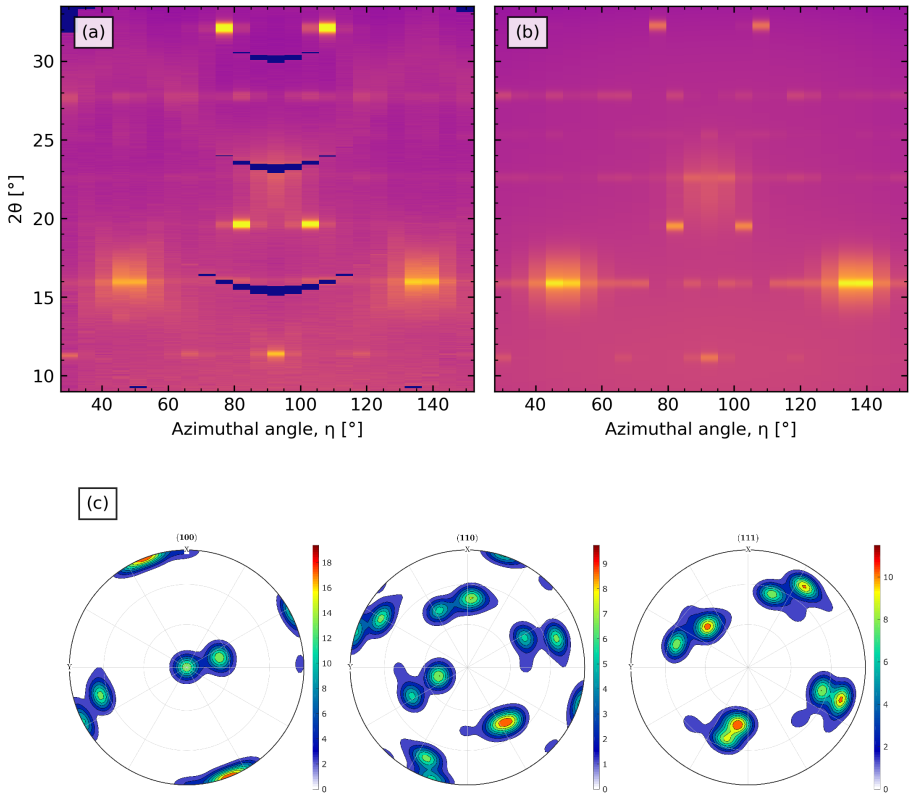

Figure A.10: The (a) experimental and (b) calculated 2D diffractograms from a Rietveld refinement with a E-WIMV texture component for a single-layer crystalline BCT thin film on (100) STO after single step heating with 0.1 °C/s to 706 °C. (c) Pole figures calculated based on ODFs from the Rietveld refinement of the same film. The wavelength was 0.77624 Å.

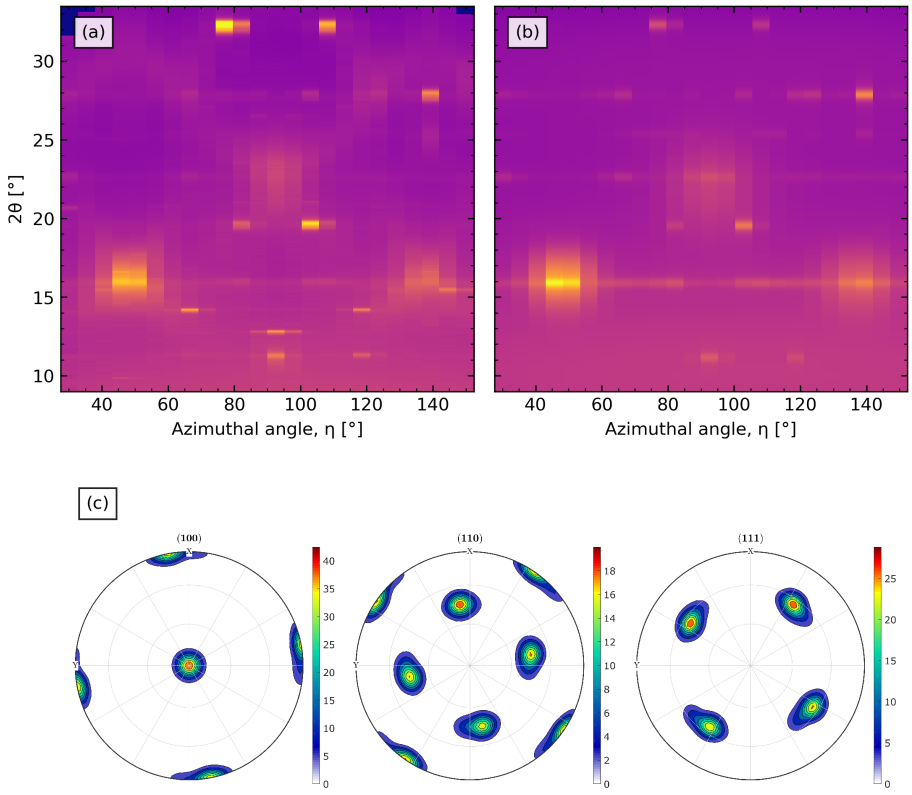

Figure A.11: The (a) experimental and (b) calculated 2D diffractograms from a Rietveld refinement with a E-WIMV texture component for a single-layer crystalline BCZT thin film on (100) STO after single step heating with 0.03 °C/s to 800 °C. (c) Pole figures calculated based on ODFs from the Rietveld refinement of the same film. The wavelength was 0.78242 Å.

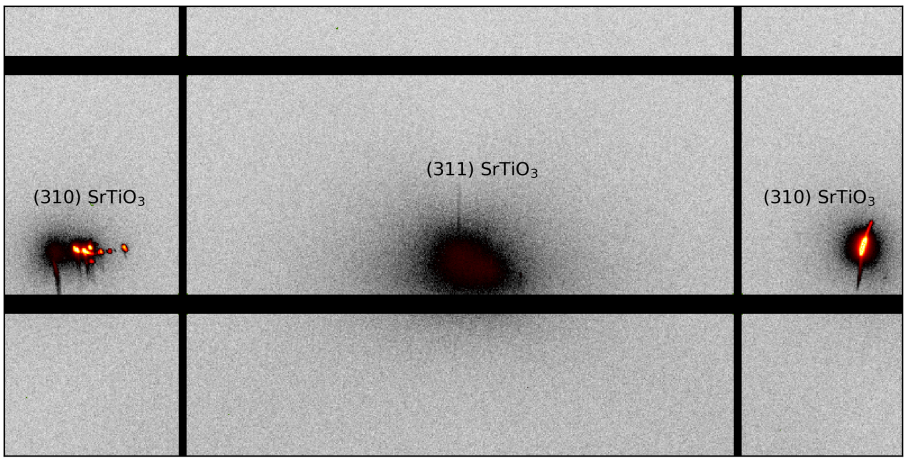

Figure A.12: The reflections of a (100) STO substrate measured with synchrotron XRD. The splitting of one of the (310) reflections are caused by defects in the single crystal substrate.

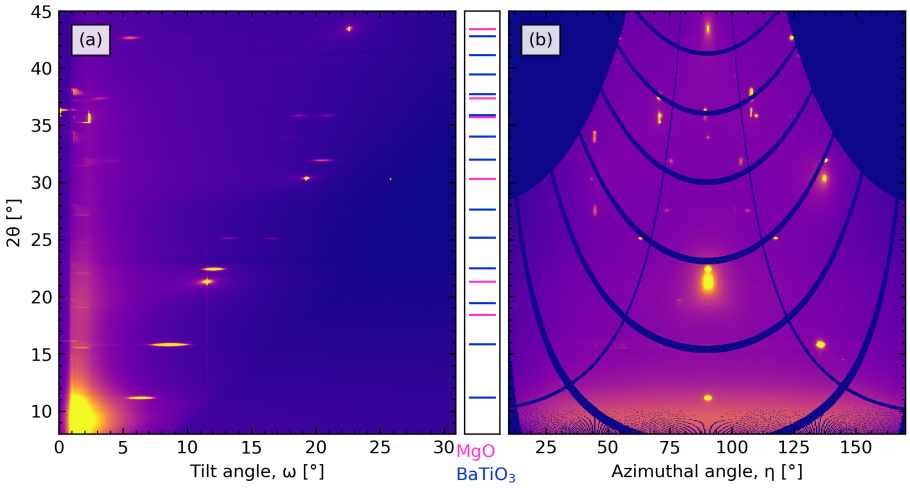

Figure A.13: Diffraction from a 60 nm highly textured $BaTiO_3$ thin film on (100) MgO is presented in two perpendicular angular directions; (a) tilt (ω) and (b) azimuthal (η). The wavelength was 0.78006 Å.

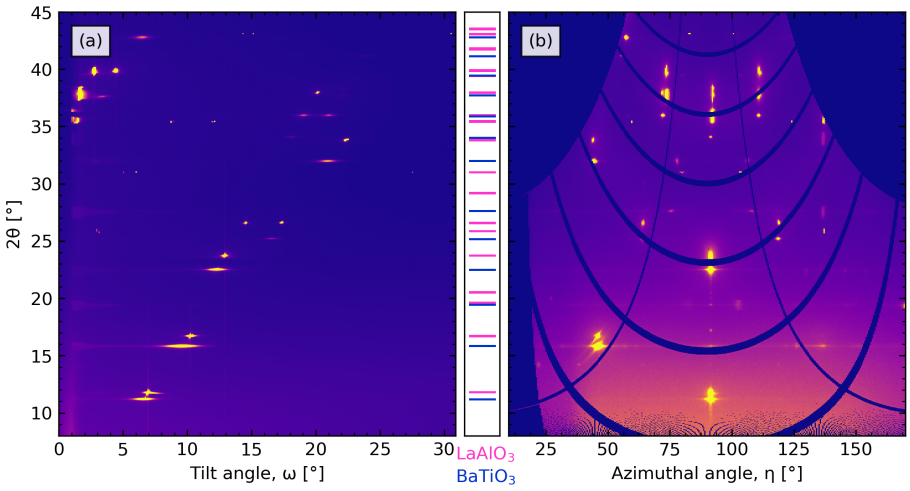

Figure A.14: Diffraction from a 60 nm highly textured $BaTiO_3$ thin film on (100) LAO is presented in two perpendicular angular directions; (a) tilt (ω) and (b) azimuthal (η). The wavelength was 0.78006 Å.

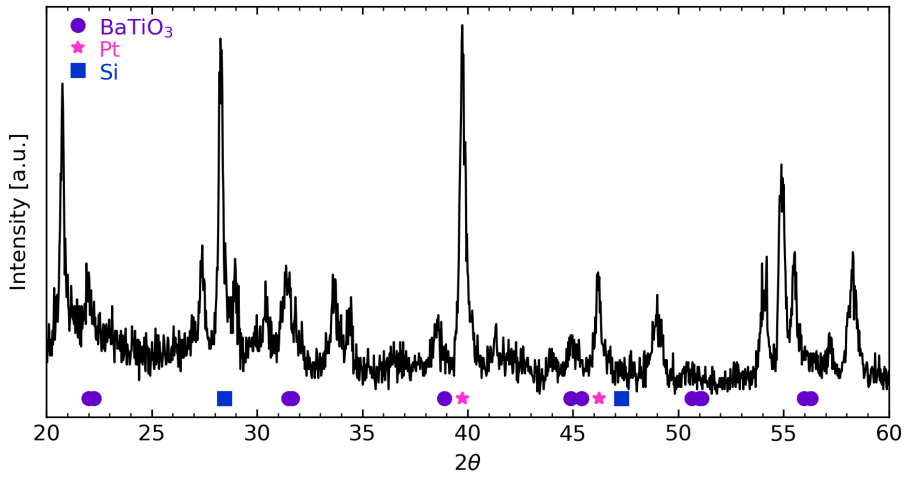

Figure A.15: GI-XRD pattern from a 60 nm $BaTiO_3$ film on Pt/Si heated with the epitaxial heating program.

A.2 Infrared spectroscopy

A.2.1 *In situ* infrared spectroscopy of $BaTiO_3$-based films

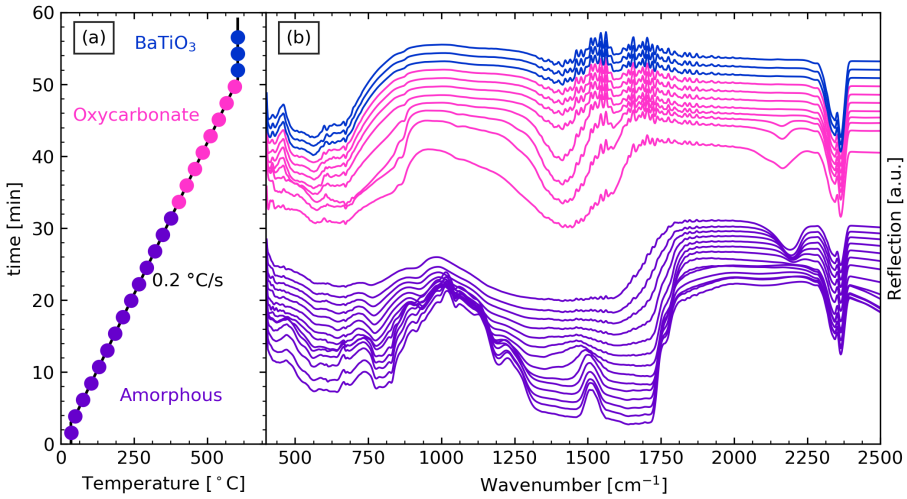

Figure A.16: (a) Temperature profile and (b) *in situ* IR spectra during annealing of a $BaTiO_3$ precursor film (BT-2) heated without the dome for atmosphere control.

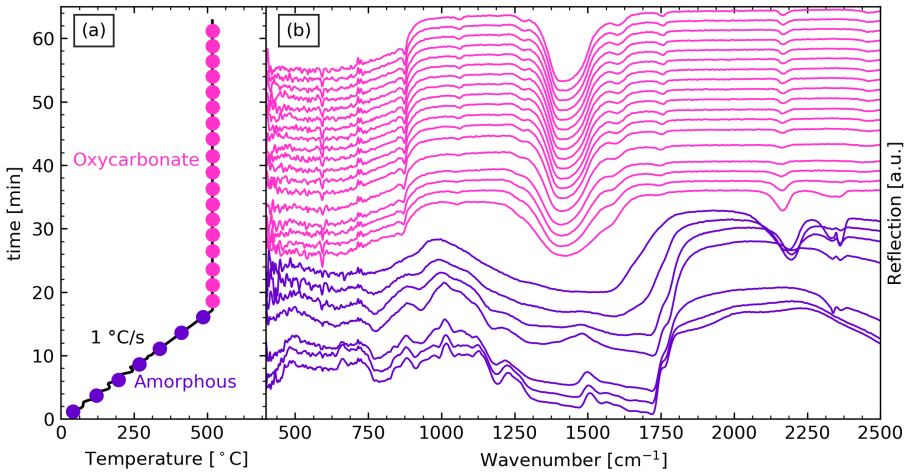

Figure A.17: (a) Temperature profile and (b) *in situ* IR spectra during annealing of a $BaTiO_3$ precursor film (BT-3) with isothermal oxycarbonate annealing.

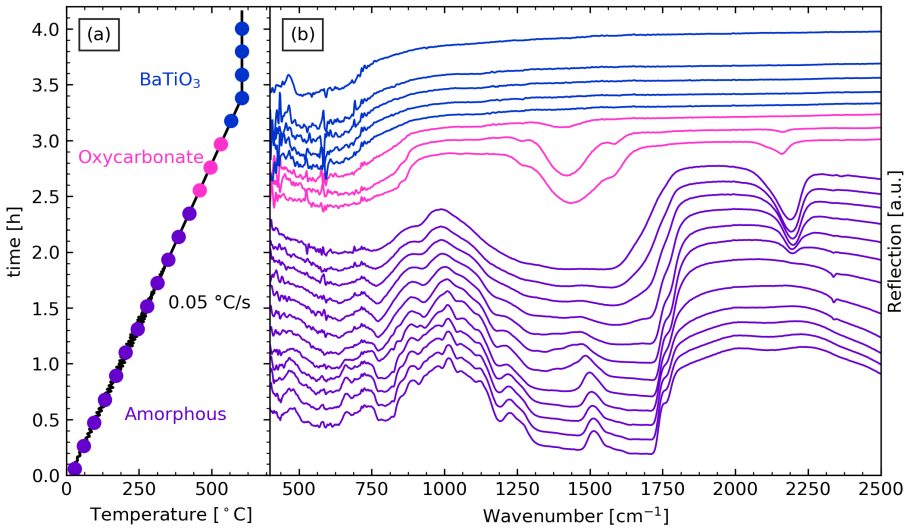

Figure A.18: (a) Temperature profile and (b) *in situ* IR spectra during annealing of a $BaTiO_3$ precursor film (BT-4) with direct slow heating.

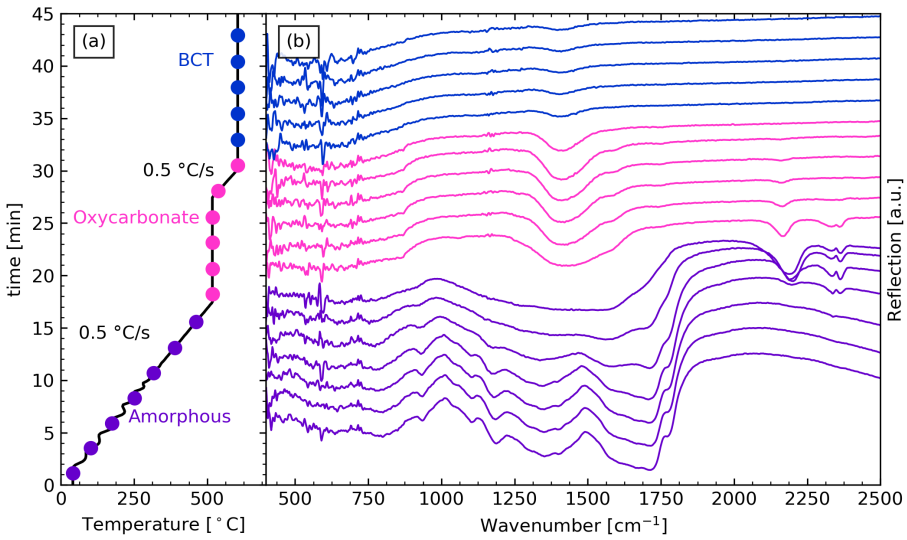

Figure A.19: (a) Temperature profile and (b) *in situ* IR spectra during annealing of a BCT precursor film with a medium heating rate and a hold step for oxycarbonate formation.

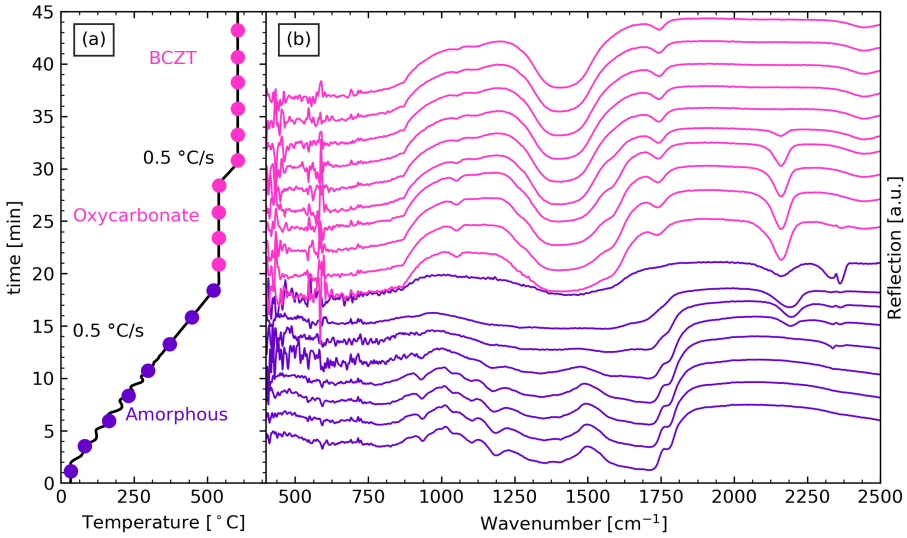

Figure A.20: (a) Temperature profile and (b) *in situ* IR spectra during annealing of a BCZT precursor film with a medium heating rate and a hold step for oxycarbonate formation.

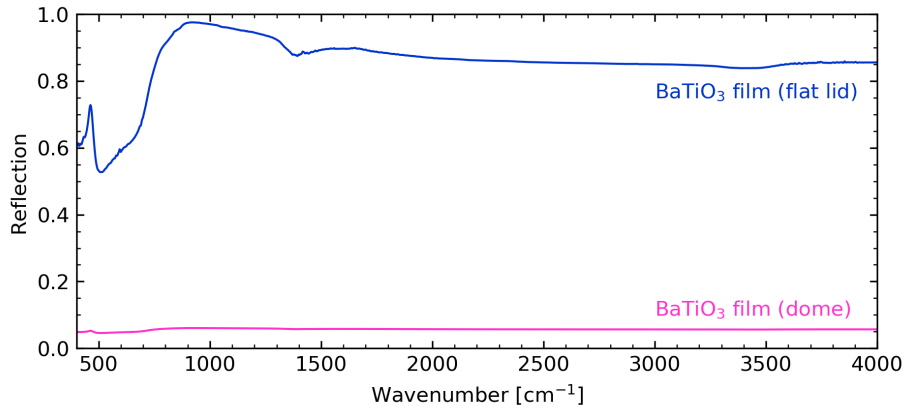

Figure A.21: Increased signal during *in situ* IR spectroscopy using a flat lid instead of the dome for atmosphere control. Measured on the same $BaTiO_3$ thin films at ambient temperature.

A.2.2 Near-normal infrared spectroscopy of thin films and phonon modelling

The value of ϵ_∞ was set to 5.2047 for the STO substrate, 3.19529 for MgO and 4.28235 LAO.

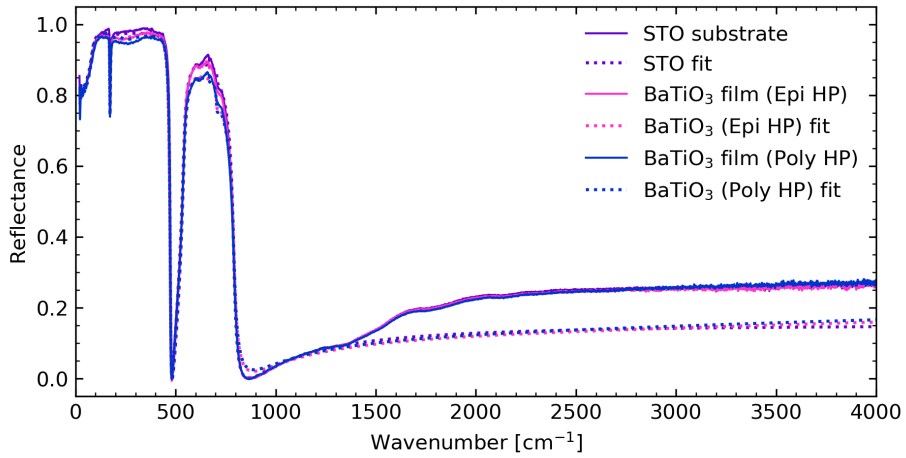

Figure A.22: Reflection IR spectra and calculated fit for $BaTiO_3$ thin films on (100) STO.

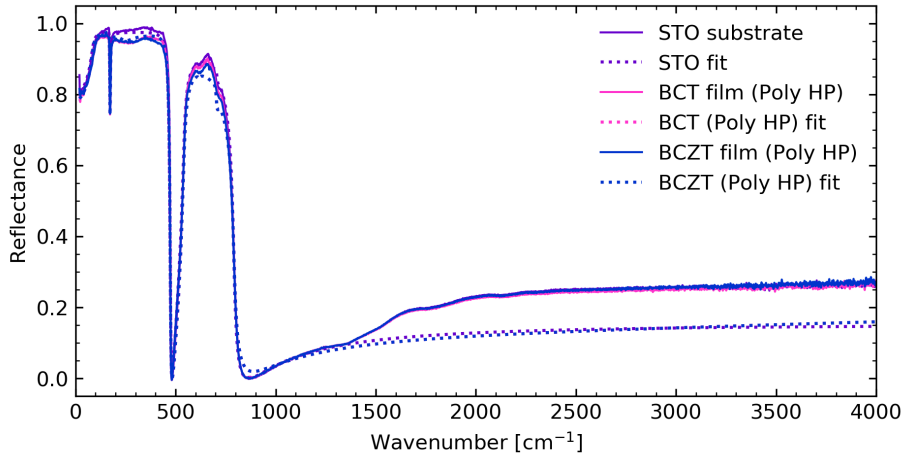

Figure A.23: Reflection IR spectra and calculated fit for BCT and BCZT thin films on (100) STO.

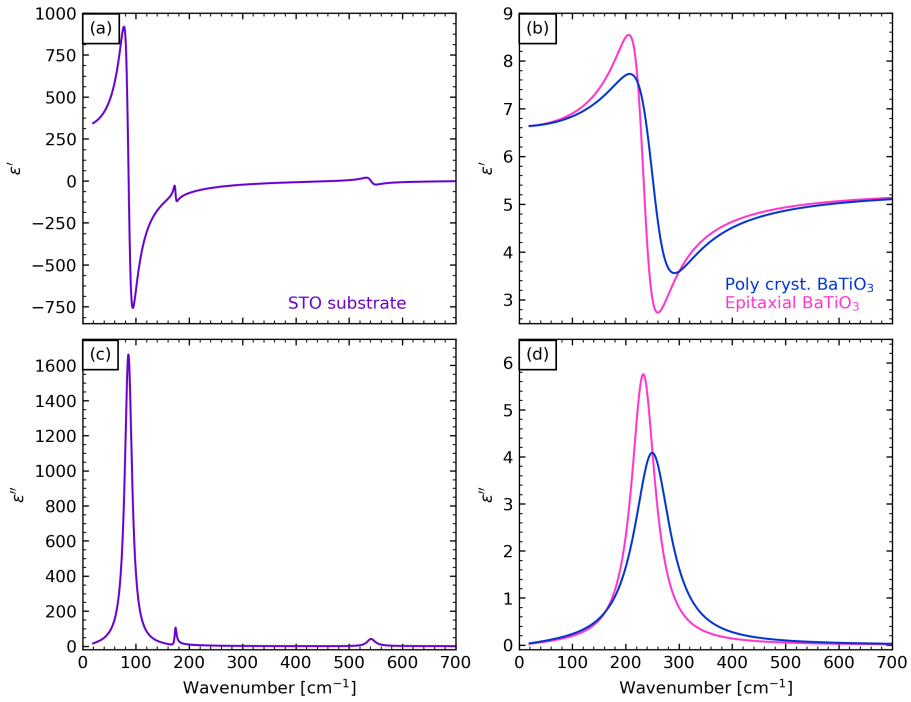

Figure A.24: Comparison between the (a&b) real and (c&d) imaginary part of the fitted dielectric function for a STO substrate (a&c) and 60 nm polycrystalline versus epitaxial $BaTiO_3$ films on STO (b&d).

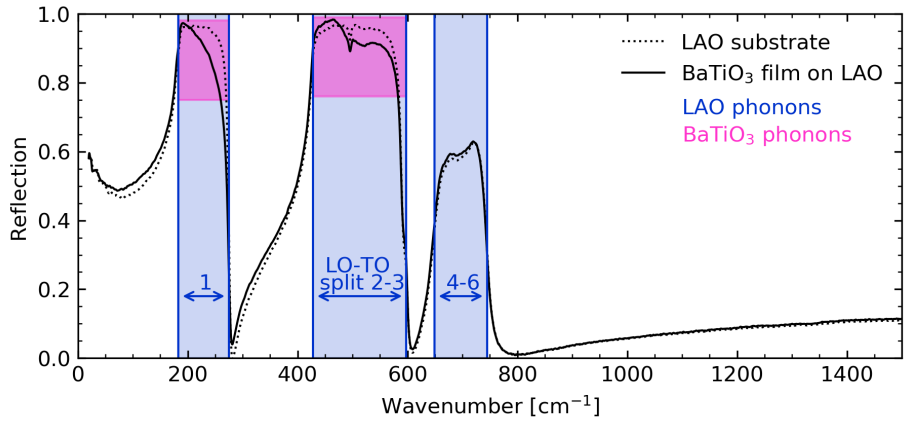

Figure A.25: Reflection IR spectra of a LAO substrate and a $BaTiO_3$ thin films on LAO, where the fitted phonon modes of both LAO and the $BaTiO_3$ film are indicated.

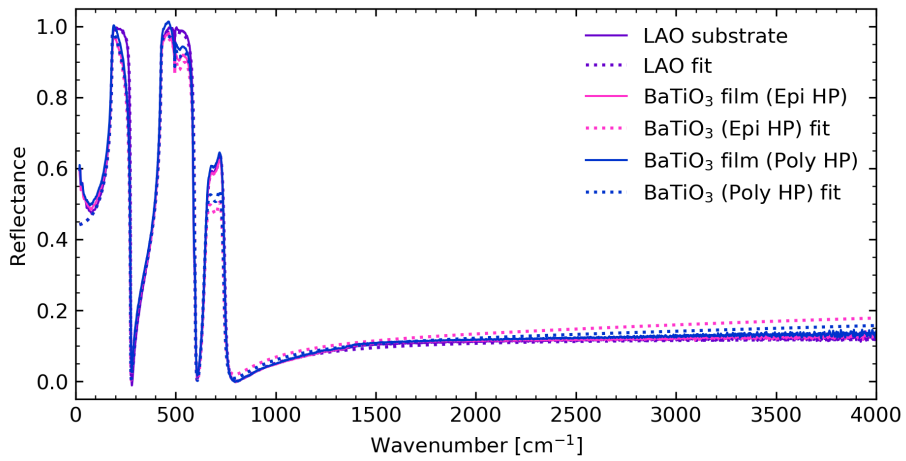

Figure A.26: Reflection IR spectra and calculated fit for $BaTiO_3$ thin films on (100) LAO.

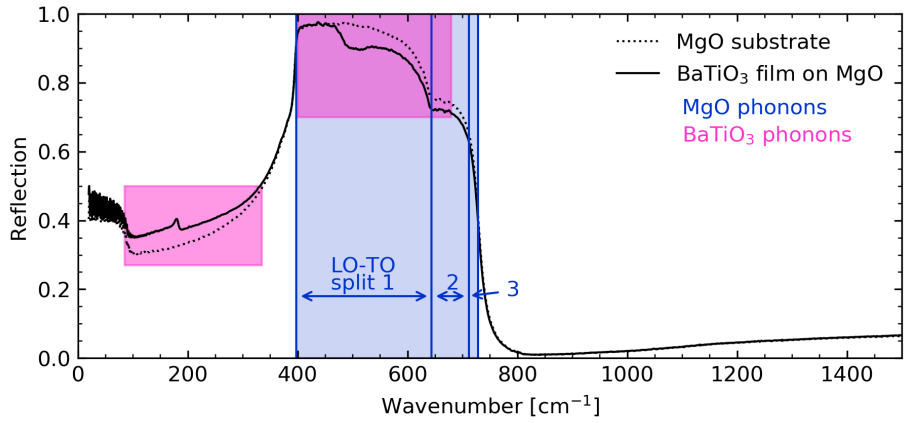

Figure A.27: Reflection IR spectra of a MgO substrate and a $BaTiO_3$ thin films on MgO, where the fitted phonon modes of both MgO and the $BaTiO_3$ film are indicated.

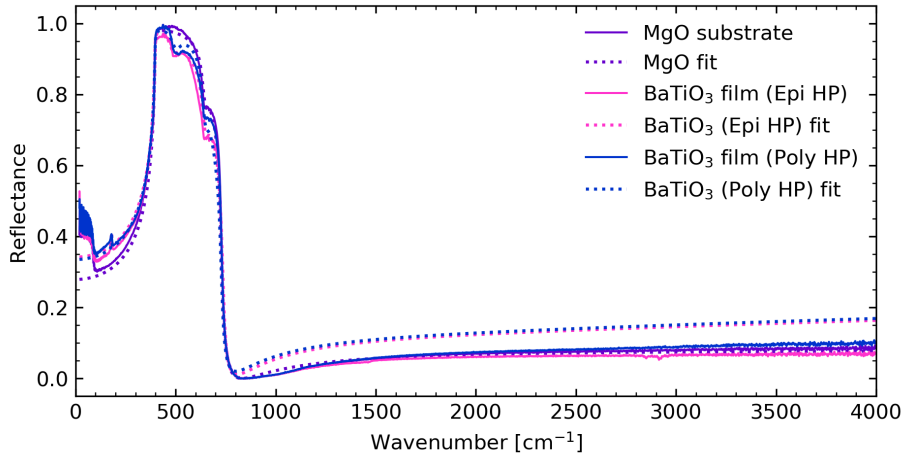

Figure A.28: Reflection IR spectra and calculated fit for $BaTiO_3$ thin films on (100) MgO.

Table A.1: Parameters from fitting of near-normal IR spectroscopy of STO substrate.

Modes	ω_{TO} [$\mathbf{cm^{-1}}$]	γ_{TO}	ω_{LO} [$\mathbf{cm^{-1}}$]	γ_{LO}
1	86.44	16.58	172	2.889
2	174	4.207	474.51	6.727
3	540.91	18.22	617.45	8.376
4	617.5	8.395	667	0
5	667	0	707	12.839
6	707	13.265	790.287	17.412

Table A.2: Parameters from fitting of near-normal IR spectroscopy of $BaTiO_3$-based films on STO substrates.

Films	$\boldsymbol{\omega}$ [$\mathbf{cm^{-1}}$]	$\boldsymbol{\gamma}$	**S**	ϵ_∞
Epitaxial $BaTiO_3$	234.62	1.327	54.29	5.3
Polycryst. $BaTiO_3$	253.17	1.327	82.81	5.3
Polycryst. BCT	247.11	2.39	82.812	5.3
Polycryst. BCZT	247.11	2.392	83.234	5.3

Table A.3: Parameters from fitting of near-normal IR spectroscopy of LAO substrate.

Modes	ω_{TO} [$\mathbf{cm^{-1}}$]	γ_{TO}	ω_{LO} [$\mathbf{cm^{-1}}$]	γ_{LO}
1	183	1.104	275	1.974
2	428	2.805	495.92	0.416
3	495.96	0.402	597.534	7.115
4	649.34	23.002	695	66.7106
5	700	59.784	710	29.06
6	710.77	27.369	745.72	12.87

Table A.4: Parameters from fitting of near-normal IR spectroscopy of $BaTiO_3$ films on LAO substrates.

Films	ω_1 [$\mathbf{cm^{-1}}$]	γ_1	S_1	ω_2 [$\mathbf{cm^{-1}}$]	γ_2	S_2	ϵ_∞
Epitaxial $BaTiO_3$	221.06	8.358	138.62	513.21	0.201	43.97	5.3
Polycryst. $BaTiO_3$	221.06	8.588	108.12	513.21	0.201	43.97	5.3

Table A.5: Parameters from fitting of near-normal IR spectroscopy of MgO substrate.

Modes	ω_{TO} [$\mathbf{cm^{-1}}$]	γ_{TO}	ω_{LO} [$\mathbf{cm^{-1}}$]	γ_{LO}
1	397.55	2.97	643.7	40.08
2	645.82	42.77	712.52	138.71
3	718	140.61	728	17.96

Table A.6: Parameters from fitting of near-normal IR spectroscopy of $BaTiO_3$ films on MgO substrates.

Films	ω_1 [$\mathbf{cm^{-1}}$]	γ_1	S_1	ω_2 [$\mathbf{cm^{-1}}$]	γ_2	S_2	ϵ_∞
Epitaxial $BaTiO_3$	180	0.4	2.8	489.67	0.333	52.97	5.3
Polycryst. $BaTiO_3$	180	0.4	2.8	498.77	0.258	55.62	5.3

A.3 Electrical characterization

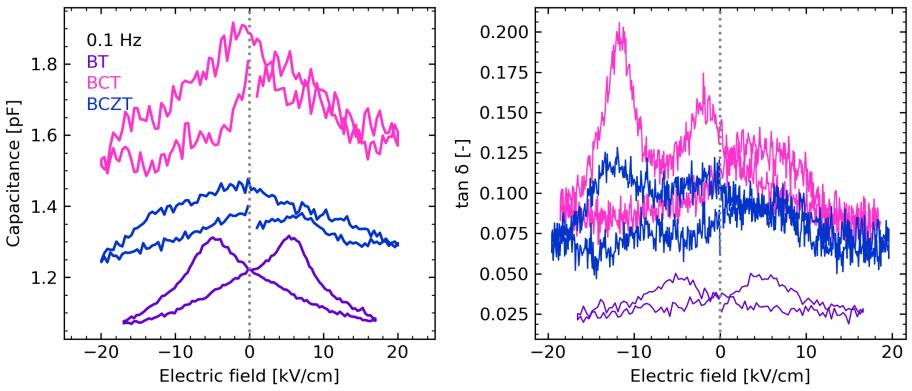

Figure A.29: (a) Capacitance and (b) tan δ versus electrical field for $BaTiO_3$, BCT and BCZT thin films on (100) STO.

A.4 Electron microscope imaging

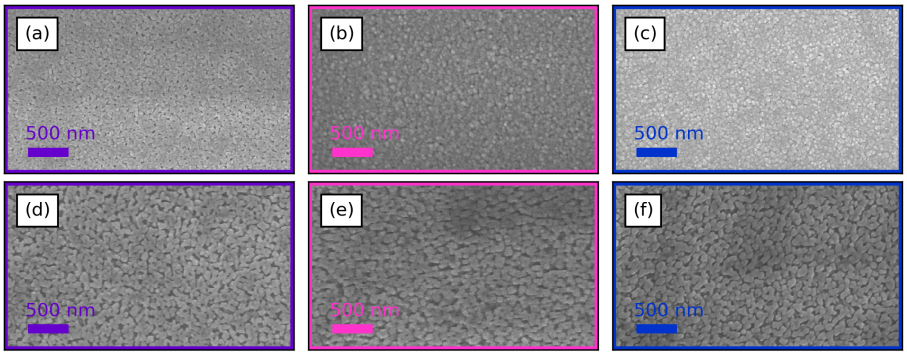

Figure A.30: Microstructure of polycrystalline (a) $BaTiO_3$, (b) BCT and (c) BCZT and textured (d) $BaTiO_3$, (e) BCT and (f) BCZT thin films on (100) STO.

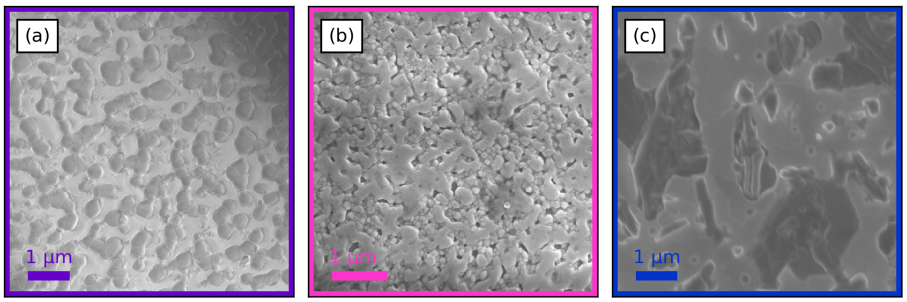

Figure A.31: Microstructure of $BaTiO_3$ films on (a) (100) MgO, (b) (100) LAO and (c) Pt/Si prepared with the epitaxial heating program.

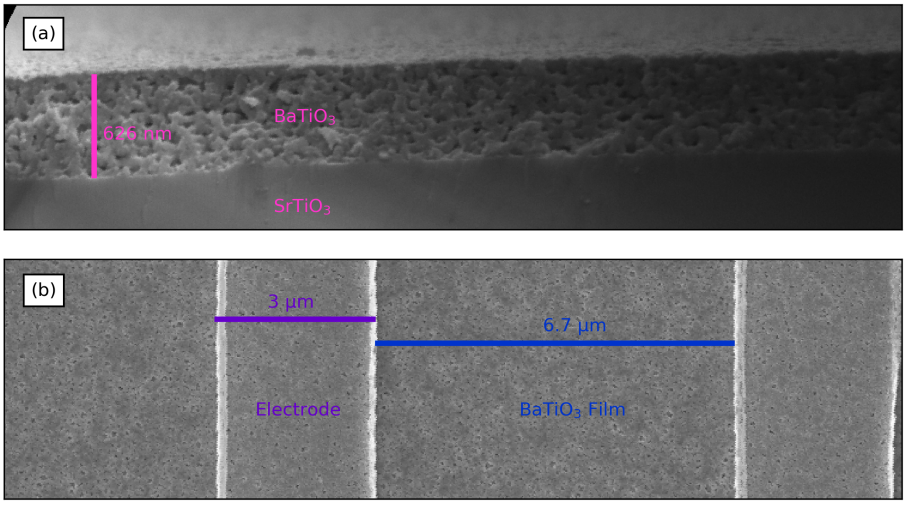

Figure A.32: (a) Cross-section showing film thickness and (b) surface of a polycrystalline $BaTiO_3$ film showing the microstructure and electrode dimensions. The electrodes retain the film surface morphology.

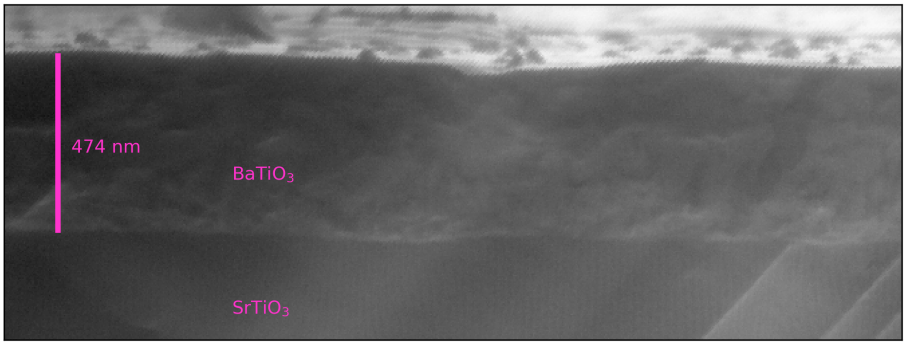

Figure A.33: Cross-section showing film thickness of an epitaxial $BaTiO_3$ film.

B Scientific Paper Draft 1

Mechanisms for texturing in $BaTiO_3$ thin films from aqueous chemical solution deposition

K. Bakken, A. B. Blichfeld, D. Chernyshov, T. Grande, J. Glaum and M.-A. Einarsrud

Submitted to Journal of Sol-Gel Science and Technology (2020)

This paper is awaiting publication and is not included.

C Scientific Paper Draft 2

Experimental setup for high-temperature *in situ* studies of crystallization of thin films with atmosphere control

A. B. Blichfeld, K. Bakken

Drafted manuscript

This paper is awaiting publication and is not included.